Johannes Gutenberg-Universität,
Mainz

The search for the neutron electric dipole moment

Dissertation
zur Erlangung des Grades
„Doktor der Naturwissenschaften“

im Promotionsfach Kernchemie

am Fachbereich Chemie, Pharmazie und Geowissenschaften
der Johannes Gutenberg-Universität
in Mainz

Johannes Zenner
geb. in Oberwesel

Villigen, den 14. August 2013

Datum der mündlichen Prüfung:
08. Juli 2013

Abstract

A permanent electric dipole moment of the neutron violates time reversal as well as parity symmetry. Thus it also violates the combination of charge conjugation and parity symmetry if the combination of all three symmetries is a symmetry of nature. The violation of these symmetries could help to explain the observed baryon content of the Universe. The prediction of the Standard Model of particle physics for the neutron electric dipole moment is only about $10^{-32}\, e \cdot \mathrm{cm}$. At the same time the combined violation of charge conjugation and parity symmetry in the Standard Model is insufficient to explain the observed baryon asymmetry of the Universe. Several extensions to the Standard Model can explain the observed baryon asymmetry and also predict values for the neutron electric dipole moment just below the current best experimental limit of $d_\mathrm{n} < 2.9 \times 10^{-26}\, e \cdot \mathrm{cm}$, (90% C.L.) that has been obtained by the Sussex–RAL–ILL collaboration in 2006. The very same experiment that set the current best limit on the electric dipole moment has been upgraded and moved to the Paul Scherrer Institute. Now an international collaboration is aiming at increasing the sensitivity for an electric dipole moment by more than an order of magnitude.

This thesis took place in the frame of this experiment and went along with the commissioning of the experiment until first data taking. After a short layout of the theoretical background in chapter 1, the experiment with all subsystems and their performance are described in detail in chapter 2. To reach the goal sensitivity the control of systematic errors is as important as an increase in statistical sensitivity. Known systematic effects are described and evaluated in chapter 3. During about ten days in 2012, a first set of data was measured with the experiment at the Paul Scherrer Institute. An analysis of this data is presented in chapter 4, together with general tools developed for future analysis efforts. The result for the upper limit of an electric dipole moment of the neutron is $|d_\mathrm{n}| \leq 6.4 \times 10^{-25}\, e \cdot \mathrm{cm}$ (95%C.L.).

Chapter 5 presents investigations for a next generation experiment, to build electrodes made partly from insulating material. Among other advantages, such electrodes would reduce magnetic noise, generated by the thermal movement of charge carriers.

The last chapter summarizes this work and gives an outlook.

Zusammenfassung

Ein permanentes elektrisches Dipolmoment des Neutrons stellt sowohl eine Verletzung der Zeitumkehr- als auch der Paritätssymmetrie dar. Somit verletzt es auch die Kombination von Ladungsumkehr und Paritätssymmetrie unter der Annahmen, dass die Kombination aller drei Symmetrien in der Natur nicht verletzt ist. Im Rahmen des Standard Modells der Teilchenphysik wird ein elektrisches Dipolmoment des Neutrons von $10^{-32}\, e \cdot \mathrm{cm}$ vorhersagt. Gleichzeitig ist eben dieses Modell nicht in der Lage die beobachtet Asymmetrie von Materie und Antimaterie im Universum zu erklären. Erweiterungen des Standard Modells hingegen versuchen nicht nur diese Asymmetrie zu erklären, sie sagen gleichzeitig oft auch grössere Werte für das elektrische Dipolmoment des Neutrons vorher. Diese reichen bis an das momentane obere Limit von $d_\mathrm{n} < 2.9 \times 10^{-26}\, e \cdot \mathrm{cm}$, (90% C.L.) heran, welches 2006 von der Sussex–RAL–ILL Kollaboration publiziert wurde. Das Experiment, mit welchem dieses Limit gemessen wurde, steht nun am Paul Scherrer Institut. Eine international Kollaboration hat es sich zum Ziel gesetzt, die Sensitivität der Messung um mehr als eine Grössenordnung zu verbessern.

Die vorliegende Arbeit fand im Rahmen dieser Bemühungen statt und erlaubte es, das Experiment von der Installation bis zur ersten Datennahme zu begleiten. Nach einer kurzen Erläuterung des theoretischen Hintergrunds in Kapitel 1, folgt eine detaillierte Beschreibung aller Komponenten des Experiments sowie eine Abschätzung ihres Leistungsvermögens in Kapitel 2. Systematische Effekte müssen in gleicher Weise kontrolliert werden, in welcher die statistische Sensitivität verbessert wird. Daher werden in Kapitel 3 die bekannten systematischen Fehler vorgestellt und abgeschätzt. 2012 wurden während etwa zehn Tagen die ersten Daten zur Bestimmung des elektrischen Dipolmoments aufgenommen. Eine Analyse dieser Daten wird in Kapitel 4 vorgestellt und resultiert in einem oberen Limit von $|d_\mathrm{n}| \leq 6.4 \times 10^{-25}\, e \cdot \mathrm{cm}$ (95%C.L.).

Kapitel 5 befasst sich mit der Entwicklung von Elektroden für ein zukünftiges Experiment, welche zu einem grossen Teil aus nichtleitenden Materialien bestehen. Diese haben unter anderem den Vorteil, dass sie wesentlich weniger magnetisches Rauschen verursachen, welches durch die thermische Bewegung elektrischer Ladungen entsteht.

Im letzten Kapitel werden die Resultate dieser Arbeit diskuttiert und zusammengafasst.

Contents

List of Figures

List of Tables

Chapter 1

Introduction

1.1 Motivation

One of the biggest questions in today's physics is the dominance of matter over antimatter, the so called Baryon Asymmetry of the Universe (BAU). Our current understanding of the creation of the Universe starts with the Big Bang. In the Standard Model of cosmology the Big Bang produces the same amounts of matter and antimatter. Particles and antiparticles therefore should have almost completely annihilated as long as matter density in the early Universe was high enough for the two species to interact. Yet we live in a matter dominated Universe where almost no traces of antimatter can be found, showing that at some point a clear imbalance between matter and antimatter must have developed. Possible explanations involve the breaking of symmetries like the combined charge conjugation and parity symmetry (CP) or time reversal symmetry (T) that are closely linked to a permanent electric dipole moment (edm) of particles. The small amount of CP-violation that is found in the Standard Model of particle physics (SM) is insufficient to explain the observed BAU and would also lead to electric dipole moments that are too small to be detected in any experiment in the near future. Furthermore, the SM cannot give answers to other fundamental questions of todays physics like:

- What is dark matter ?
- What is dark energy ?
- Why is gravity so much weaker than the other forces (hierarchy problem) ?
- ...

Extensions of the Standard Model not only can help to resolve some of these questions, they can also lead to additional CP-violation and predict electric dipole moments of particles like the neutron that are close to the current experimental sensitivity. The search for the neutron electric dipole moment (nedm), is therefore one of the most promising experiments to discover CP-violation beyond the SM and help to understand our Universe.

1.2 Symmetries

As this work is describing an experiment, searching explicitly for the breaking of symmetries of fundamental forces in nature, a short introduction to the importance of symmetries in physics will be given. The amount of literature available on this topic already demonstrates the importance of this concept in theoretical physics. This section is based on the excellent overview article by F. Gieres [Gie97].

What is symmetry? A physical model is called symmetric under a certain operation, if its properties are invariant under this operation, i.e. one cannot tell whether the transformation has been performed or not.

One of the simplest every day examples is the symmetry of a geometric object; a perfect sphere under the operation of a rotation around the center of the sphere. If the surface has no special marks, an observer can not tell if the sphere has been rotated: the sphere is symmetric under the operation of rotation. This would be an example of continuous symmetry. If we would now take a cube instead of a sphere, the cube would only be symmetric for certain angles of rotation and we would have a discrete symmetry. Like wise a physical equation (law) is symmetric under a transformation if the observables described by the equation are unaffected by the transformation (e.g. a change of space time coordinates).

Symmetry in physics The principle of symmetries is one of the major foundations of modern physics. Not only can symmetries help to simplify the discovery of the solution to a physical problem, but each continuous symmetry with n parameters is directly linked to the conservation of n physical properties, as described in the theorem of Emmy Noether in 1918 [Noe18]. Often the formulation of a physical law is only possible because of symmetries, as the general structure of a physical theory is basically determined by its underlying symmetries. For example, the number of gauge bosons of the strong interaction is determined by the number of generators of the underlying symmetry group, the SU(3).

Force	C	P	T
Electric field $\boldsymbol{E}$	$-\boldsymbol{E}$	$-\boldsymbol{E}$	$\boldsymbol{E}$
Magnetic field $\boldsymbol{B}$	$-\boldsymbol{B}$	$\boldsymbol{B}$	$-\boldsymbol{B}$
Momentum $\boldsymbol{p}$	$\boldsymbol{p}$	$-\boldsymbol{p}$	$-\boldsymbol{p}$
Angular momentum $\boldsymbol{l}$	$\boldsymbol{l}$	$\boldsymbol{l}$	$-\boldsymbol{l}$
Charge density ϱ	$-\varrho$	ϱ	ϱ

Table 1.1: Transformation of observables under C, P, and T

Force	C	P	T	CP	CPT
Gravitation	✓	✓	✓	✓	✓
Strong	✓	✓	✓	✓	✓
Electromagnetic	✓	✓	✓	✓	✓
Weak	✗	✗	(✗)	(✗)	✓

Table 1.2: C, P, and T symmetry of fundamental forces. The weak force is the only known interaction to maximally violate P. It also has shown minor violations of CP (see Sec. 1.3.2) and therefore also T via the CPT theorem.

In the context of this thesis, symmetries and their behavior under three discrete transformations are of great importance:

T-Symmetry $T : t \mapsto -t$ is the symmetry under the reversal of time.

C-Symmetry $C : p \mapsto \bar{p}$ is the symmetry under the exchange of every particle with its antiparticle.

P-Symmetry $P : \boldsymbol{r} \mapsto -\boldsymbol{r}$ is the symmetry under flipping the spatial coordinates.

The transformation of some quantities under C, P, and T transformation is shown in Tab. 1.1.

These symmetries are linked by the CPT theorem, which states that all laws of physics are invariant under the combined transformation of C,P and T. Most of the fundamental interactions are symmetric under C,P, or T (see Tab. 1.2). The weak force is the only known interaction that (maximally) violates P symmetry as discovered in 1957 by Wu et al. in the decay of ^{60}Co [WAH$^+$57], and also CP (see Sec. 1.3.2 for more details).

Broken symmetries As beautiful and useful as symmetries are, the most interesting phenomena in physics occur actually in the breaking of symmetries. One speaks of explicitly broken symmetries if the equations

describing a system are not invariant under a certain symmetry. For an atom in an electric or magnetic field, additional terms in the Hamiltonian (Stark and Zeemann effect) will violate its rotation symmetry. Spontaneous symmetry breaking on the other hand occurs, if the Hamiltonian of a system has more symmetries, than valid solutions to the Hamiltonian. While the Higgs mechanism is an example of the latter[1], the search for the nedm (or edms in general) is a search for an explicit breaking of T (and therefore also CP).

1.3 Theory

In the first part of this section a short overview of the theoretical background for CP-violation, edms, and the BAU will be given. Many instructive overview articles exist that cover these topics in great detail (e.g. [DS11, PR05, Fuk12]). In the second part of this section ultracold neutrons (UCN), used in many state of the art experiments searching for an edm of the neutron, are shortly characterized. More details about UCN physics can be found e.g. in [GRL91, Ign90].

1.3.1 The baryon asymmetry problem

If during the Big Bang the same number of baryons and antibaryons had been produced, most of the matter would have annihilated in the early Universe and almost only photons would have been left. The dominance of matter over antimatter is usually expressed in the $\eta_{10} = 10^{10}\eta$ parameter which is defined as

$$\eta = \frac{n_B - n_{\overline{B}}}{n_\gamma}, \tag{1.1}$$

the ratio of the number of baryons (n_B) minus the number of antibaryons ($n_{\overline{B}}$) divided by the number of photons (n_γ) in the Universe. Within the current models used to describe the creation of our Universe, this ratio is as small as $\eta_{10} = 10^{-8}$ [RT99]. This is many orders of magnitude smaller than the value that has been observed

$$\eta_{10} = 6.15 \pm 0.15$$

using satellite based measurements of the cosmic microwave background like the WMAP[2] mission [K+11]. Preconditions needed to explain this imbalance

[1] The potential of the Higgs field has more symmetry than the solution of lowest energy.
[2] Wilkinson Microwave Anisotropy Probe

have been phrased already by A.D. Sakharov [Sak67] in 1967:

1. Violation of baryon number conservation (B=$n_B - n_{\overline{B}} \neq 0$) in order to change the net number of baryons over time;

2. C and CP-violation so that processes violating B can lead to an asymmetry in the baryon numbers;

3. A departure from the thermal equilibrium in the early Universe, as in a thermal equilibrium, CPT conservation would restore the symmetry.

1.3.2 CP-violation in the Standard Model of particle physics

So far CP-violation has only been found in the electroweak sector. This can be incorporated in the SM through a CP-violating phase in the CKM[3] matrix, describing the mixing of quark flavors when taking part in the weak interaction. Although CP-violation also exists in the strong sector through the Θ-term (see Sec. 1.3.5), no experimental evidence has been found yet for CP-violation in strong interactions. In 1964 the first direct CP-violating process was observed in the decay of the neutral K meson by James Cronin and Val Fitch [CCFT64] when they observed the decay of the K_2 state into two pions with a branching ratio of 2×10^{-3}. More recently CP-violation has also been found in the neutral B meson by the Belle [AAA+01] and BaBar [LPT+12] experiments and in the neutral D meson by the LHCb experiment [AABA+12]. However the amount of CP-violation is many orders of magnitude too small to explain the observed BAU. This motivates the search for CP-violation that might come from physics beyond the SM.

1.3.3 Electric dipole moments and CP-violation

The classic definition of an electric dipole moment of a charge distribution with charge density $\varrho(\boldsymbol{x})$ is the integral

$$\boldsymbol{d} = \int d^3x \boldsymbol{x} \varrho(\boldsymbol{x}). \tag{1.2}$$

This is a vector and the only existing (axial) vector in a particle is its spin. Thus an edm, like the magnetic moment, must be aligned with the spin $\boldsymbol{\sigma}$, so that

[3] named after Nicola Cabibbo, Makoto Kobayashi and Toshihide Masukawa.

$$\boldsymbol{d} \propto d\frac{\boldsymbol{\sigma}}{|\boldsymbol{\sigma}|}. \tag{1.3}$$

Any permanent edm of a particle violates P and T-symmetry and therefore also CP-symmetry if CPT is a good symmetry of nature. This can be easily seen if we look at the Hamiltonian of a particle with an electric ($\boldsymbol{d}$) and magnetic ($\boldsymbol{\mu}$) dipole moment in an electric $\boldsymbol{E}$ and magnetic $\boldsymbol{B}$ field under P or T transformation

$$\mathcal{H} = -d\frac{\boldsymbol{\sigma}}{|\boldsymbol{\sigma}|}\boldsymbol{E} - \mu\frac{\boldsymbol{\sigma}}{|\boldsymbol{\sigma}|}\boldsymbol{B}. \tag{1.4}$$

Looking at Tab. 1.1, it is clear that $\mathcal{H}$ violates P and T symmetry if $d \neq 0$.

1.3.4 Searches for permanent electric dipole moments in different systems

The search for permanent electric dipole moments is currently among the most promising experiments to find new sources of CP-violation. Therefore, it is not surprising that around the world more than 30 different experiments are searching for electric dipole moments in different systems. The systems that are probed for a permanent edm are, besides the neutron, searches with protons (deuterons), muons, and heavy paramagnetic or diamagnetic atoms and molecules (see Tab. 1.3). In this context it is important to notice that only the muon is a fundamental particle. Therefore careful theoretical calculations are required to deduce the electric dipole moment of fundamental particles like quarks or electrons from these measurements.

System	Current best edm limit $[e \cdot \text{cm}]$	
μ	1.8×10^{-19} 95% C.L.	[BBB$^+$09]
n	2.9×10^{-26} 90% C.L.	[BDG$^+$06]
^{199}Hg	3.1×10^{-29} 95% C.L.	[GSL$^+$09]
^{205}Tl	9×10^{-25} 90% C.L.	[RCSD02]
YbF	1.1×10^{-22} 90% C.L.	[HKS$^+$11]

Table 1.3: Current edm limits in different systems. Only the muon is a fundamental particle. Theoretical models are needed to translate the other results into upper limits of fundamental particles.

1.3.5 Electric dipole moment of the neutron in the SM

In the SM there exist two different sources of CP-violation that could lead to an nedm, further also denoted as d_n:

Electroweak Via the CP-violating phase in the CKM matrix, the neutron can get a very small CP-violating electric dipole moment of the order of $d_{\mathrm{n}} = 10^{-32}\, e \cdot \mathrm{cm}$.

QCD In the Lagrangian of the strong interaction exists the QCD vacuum polarization term, also called Θ-term. This term violates P and CP-symmetry and could result in $d_{\mathrm{n}} = \Theta \times 10^{-16}\, e \cdot \mathrm{cm}$.

Electroweak interaction The electroweak contributions to d_{n} come from possible edms of the valence quarks as well as from interactions of quarks (valence and sea quarks) within the neutron

$$d_{\mathrm{n}} = d_{\mathrm{n}}^{\mathrm{quark}} + d_{\mathrm{n}}^{\mathrm{ia}}. \tag{1.5}$$

As for the quark sector, possible edm contributions are only possible on the three loop level. They are of the order of $d_{\mathrm{n}}^{\mathrm{quark}} = 10^{-34} e \cdot \mathrm{cm}$. Therefore the dominant factor for d_{n} comes from a two loop weak interaction diagram shown in Fig. 1.1. This has been calculated to be of the order of $d_{\mathrm{n}}^{\mathrm{ia}} = 10^{-32} e \cdot \mathrm{cm}$ [KZ82].

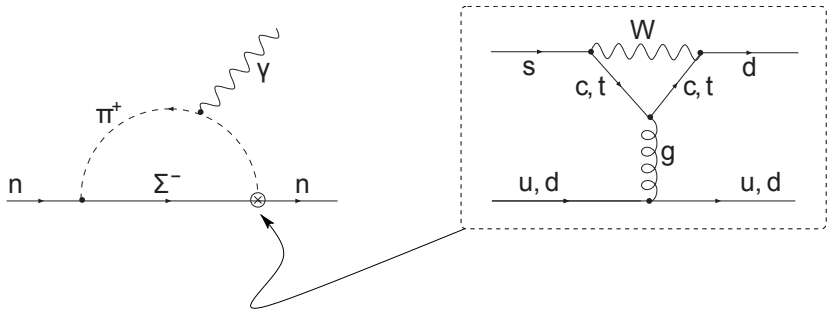

Figure 1.1: Feynman diagram for the dominant contribution of the nedm in the SM. Here the right vertex is the CP violating penguin diagram [KZ82].

The total edm contribution to the neutron from the electroweak interaction is therefore only $d_{\mathrm{n}} \approx 10^{-32} e \cdot \mathrm{cm}$. This is far below any experimental sensitivity in the near future.

Strong interaction The Lagrangian of the strong interaction contains a CP-violating term with an angular parameter $0 \leq \Theta \leq 2\pi$:

$$\begin{aligned}\mathcal{L} &= \mathcal{L}_{CP} + \mathcal{L}_{\not{C}\not{P}} \\ &= \mathcal{L}_{CP} + \Theta\frac{n_f g^2}{32\pi^2} F_{\mu\nu}\tilde{F}^{\mu\nu}.\end{aligned}$$

Here $F_{\mu\nu} = \partial_\mu A^a_\nu + \partial_\nu A^a_\mu + i[A_\mu, A\nu]$ and $\tilde{F}_{\mu\nu} = 1/2\epsilon_{\mu\nu\alpha\beta}F^{\alpha\beta}$ are the gluon field strength tensor and the dual field strength tensor. The first term $\mathcal{L}_{CP}$ describes the gluons, quarks, and their interactions, the second term describes the interaction of the gluons with the vacuum. This term corresponds to $\boldsymbol{E}_a \cdot \boldsymbol{B}_a$ while $\mathcal{L}_{CP}$ corresponds to $\boldsymbol{E}_a^2 - \boldsymbol{B}_b^2$. Here $\boldsymbol{E}_a$ and $\boldsymbol{B}_a$ are the electric and magnetic-like fields. With Tab. 1.1 we can see that $\mathcal{L}_{\not{C}\not{P}}$ is odd under P and T transformations. From dimensional arguments this so called Θ-term would result in an nedm of the order $d_\mathrm{n} \approx \Theta \times 10^{-16}\, e \cdot \mathrm{cm}$ [PR05]. As this is far above the current experimental lower limit of the nedm the only solution for this dilemma is that the parameter Θ, which is an angle an therefore can take values between 0 and 2π, is smaller than 10^{-10}. As there is no natural reason for this parameter to be that small, this issue is referred to as the strong CP problem.

1.3.6 Extensions to the Standard Model

Although hints for physics beyond the SM have been found[4], most experimental tests of the SM are in perfect agreement with theoretical predictions. Many extensions to the SM, however, introduce new sources of CP-violation and allow, among others, the explanation of the observed BAU (e.g. [Plü98]). These extensions predict nedm-values 'just around the corner' and therefore provide a strong motivation to conduct further searches for electric dipole moments in all accessible systems. For many of these models the search for edms is providing the most stringent constrains on parameters, and already the current limits have ruled out many earlier models.

1.4 Ultracold neutrons

The ongoing search for the electric dipole moment of the neutron is strongly associated with the deployment of UCN. Almost all modern experiments

[4] Among the prominent examples being the existence of dark matter, the anomaly in the Muon g factor, or neutrino oscillations.

searching for the edm of the neutron use UCN and a short characterization of their features is given in this chapter, which follows loosely the argumentations of [GRL91].

As the cross section of reactions with neutrons strongly depends on their velocity, they are usually classified by their energies. A general overview is given in Tab. 1.4. Each energy regime can also be translated into a mean velocity, the de Broglie wavelength, or the mean temperature via

$$E = \frac{1}{2}mv^2 = \frac{h^2}{2m\lambda^2} = \frac{3}{2}k_B T. \tag{1.6}$$

This is also illustrated in Figure 1.2.

Name	Energy E	Velocity v	Wavelength λ	Temperature T
Ultracold	300 neV	$8\,\mathrm{m}\cdot\mathrm{s}^{-1}$	50 nm	3 mK
Cold	1 meV	$500\,\mathrm{m}\cdot\mathrm{s}^{-1}$	3 nm	8 K
Thermal	0.0254 eV	$2.2\times10^{3}\,\mathrm{m}\cdot\mathrm{s}^{-1}$	0.2 nm	290 K
Epithermal	10 eV	$43\times10^{3}\,\mathrm{m}\cdot\mathrm{s}^{-1}$	0.009 nm	77000 K
Fast	10 keV	$1.380\times10^{6}\,\mathrm{m}\cdot\mathrm{s}^{-1}$	0.0003 nm	77 MK

Table 1.4: Commonly used names for classification of neutrons by energy together with typical values for energy, velocity, wavelength, and temperature.

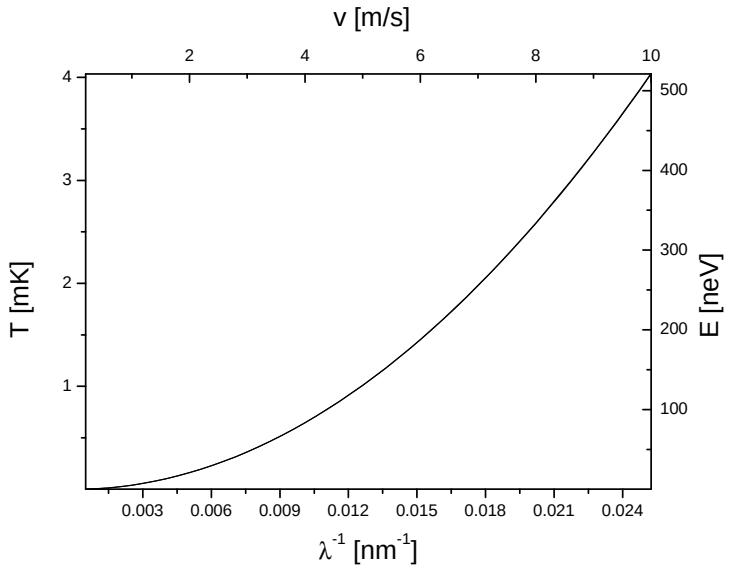

Figure 1.2: Illustration of (1.6), showing the correlation between velocity v, energy E, wavelength λ, and temperature T for neutrons in the UCN regime.

The low energy and therefore large wavelength of UCN result in unique properties: They are reflected under all angles of incidence from certain materials. This allows the building of traps to store these neutrons. Thus experiments with long observation times, in principle up to the lifetime of the free neutron, are possible in order to determine the properties of the neutron with very high precision. Like all neutrons, UCN interact via all four fundamental forces. Due to their low energy, the potentials describing the interactions are on the same energy scale as the kinetic energy of the UCN which leads to effects that usually can be disregarded in neutron physics.

1.4.1 Weak interaction

The weak interaction is responsible for the radioactive β-decay of the neutron. The free neutron decays within a lifetime of $\tau_{\mathrm{n}} = 880.1 \pm 1.1\,\mathrm{s}$ [eaPDG12][5] into a proton, an electron, and an electron antineutrino:

$$n \rightarrow p + e^- + \bar{\nu_e} + 782\,\mathrm{keV}. \tag{1.7}$$

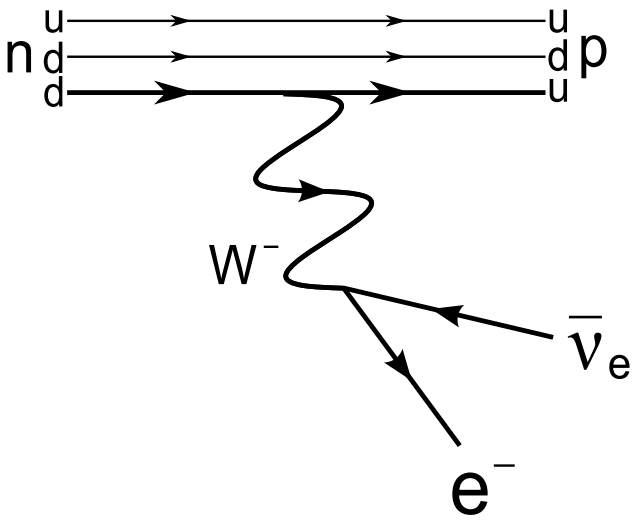

Figure 1.3: Feynman diagram of the neutron β-decay on the quark level. One of the d-quarks changes into a u-quark via exchange of a W^--boson, which decays into an electron and an electron antineutrino.

Apart from the spatial distribution of the decay products, described by the correlation parameters (*a,A,B,C*) that can be investigated in the neutron

[5]The world average for the lifetime of the neutron, as published by the particle data group, changed in the last year by many standard deviations. This is due to the fact that several experiments gave different results that are incompatible. For an historical overview and a detailed discussion of recent results see [WG11].

β-decay, the lifetime of the neutron is of great interest. As these parameters contain information about cosmological models, like the p/n ratio, as well as precision tests of the SM, e.g. the unitarity of the CKM matrix, many experiments are performed to measure these parameters (for an overview see e.g. [DS11]). In the nEDM-experiment the weak interaction is of vanishingly low interest.

1.4.2 Gravitational interaction

Gravity can normally be neglected in particle physics as it is too weak to influence any measurement. For UCN however, the gravitational interaction is of the same order of magnitude as the kinetic energy. The gravitational potential is given by

$$V_g = m_\mathrm{n} g h, \tag{1.8}$$

with $m_\mathrm{n} g = 102\,\mathrm{neV} \cdot \mathrm{m}^{-1}$. This means that UCN can only rise a few meters in the Earth's gravitational field and it is easy to modify their energy by letting them fall or rise a few meters. This is used in the nEDM-experiment e.g. to increase the detection efficiency by dropping the stored UCN by $\sim 1.6\,\mathrm{m}$ (see Sec. 2.4.7).

1.4.3 Electromagnetic interaction

The neutron is a fermion that carries a spin of $1/2\,\hbar$ and therefore has a magnetic moment μ_n through which it interacts with magnetic fields. The interaction energy with a static magnetic field $\boldsymbol{B}$ is

$$V_m = -\boldsymbol{\mu}_\mathbf{n} \boldsymbol{B}, \tag{1.9}$$

with $\mu_\mathrm{n} = 60\,\mathrm{neV} \cdot \mathrm{T}^{-1}$. In an inhomogeneous field an additional force is experienced by the neutron. Differentiation of (1.9) gives

$$\boldsymbol{F_m} = -\boldsymbol{\nabla} V_m = \pm |\boldsymbol{\mu}_\mathbf{n}| \boldsymbol{\nabla B}. \tag{1.10}$$

The sign corresponds to the relative orientation between spin and magnetic field. The magnetic interaction of UCN is used in the nEDM-experiment to polarize UCN and to detect their polarization at the end of a measuring cycle (see Sec. 2.4.8).

Equation (1.10) holds only if the UCN moves adiabatically through the magnetic field. This is the case if the Larmor precession frequency $f_\mathrm{L} = \frac{\mathbf{2}\boldsymbol{\mu}_\mathbf{n}}{h}\boldsymbol{B}$ is much smaller than the change of the magnetic field in the rest frame of the UCN. Due to their low speed this condition is relatively easy to fulfill for UCN.

The interaction of the neutron with an electric field is governed by its charge. So far the results from experiments searching for the electric charge of the neutron are compatible with zero and the present upper limit is $q_n < 1.8 \times 10^{-21} e$ (95% C.L.) [BGKM88]. This result was obtained a quarter of a century ago and new experiments are planned to improve this limit by an order of magnitude [FKL+08, PSKI+10]. A direct force on UCN due to an electric charge cannot be investigated with the experiment described in this thesis. The next higher order, the measurement of the electric dipole moment, is explained in detail in Sec. 2.1.

1.4.4 Strong interaction

Due to the strong interaction, neutrons and protons are bound within the nucleus of atoms. The short range of the strong interaction only affects the neighboring nuclei. The effective potential has spherical symmetry and can be approximated by a Woods-Saxon potential. It has a depth of about $V \approx -40\,\mathrm{MeV}$ and scales with the number of nucleons A like $R \approx 1.25 \times A^{\frac{1}{3}}\,\mathrm{fm}$. Comparing the binding energy as well as the dimensions of the potential with the typical energies and wavelengths λ of UCN (see Tab. 9), it is worthwhile to note, that these differ by many orders of magnitude. Therefore it is not possible to use perturbation theory to describe the scattering process. A 'pseudo potential' as introduced by Fermi describing the nuclear potential with a δ function, however, allows the use of the first order Born approximation. The scattering of a neutron with a nucleus can be described as a superposition of an incoming plane wave and a scattered spherical wave:

$$\psi = e^{\imath \boldsymbol{kr}} + f(\Theta)\frac{e^{\imath \boldsymbol{kr}}}{r}, \tag{1.11}$$

with the angle dependent scattering amplitude $f(\Theta)$. As the wavelength of the UCN is much larger than the interaction length of the strong interaction ($\lambda \gg R$), no angular momentum can be transferred and the process is dominated by s-wave scattering. Thus the scattering amplitude becomes independent of the scattering angle and is described only by the scattering length a

$$f(\Theta) = \text{const.} = -a. \tag{1.12}$$

Although it is in principle possible to calculate the scattering length if the nuclear potential can be described precisely enough, usually experimental data is used to determine a. If we now consider the scattering with many nuclei we can simply take the sum of all pseudo potentials of nuclei at the position r_i with the scattering length a_i to get

$$V(\boldsymbol{r}) = \frac{2\pi\hbar^2}{m_\mathrm{N}} \sum_i a_i \delta\left(\boldsymbol{r_i} - \boldsymbol{r}\right), \tag{1.13}$$

with the mass of the neutron m_N. Comparing the wavelength of a UCN with the lattice of typical condensed matter we see that the resulting wave will be an interference of all scattered spherical waves and the potential can finally be described by

$$V(\boldsymbol{r}) = \frac{2\pi\hbar^2}{m_\mathrm{N}} \sum_i N_i a_i, \tag{1.14}$$

with N_i the number density and a_i the scattering length of material i. In UCN physics this potential is often referred to as the optical potential as a neutron with an energy $E < V$ will be reflected from certain materials under any incidence angle like a light beam from a mirror. Often a critical velocity, v_c, is defined as the velocity that corresponds to $v_c = \sqrt{2E/m_\mathrm{N}}$ and therefore represents the maximum velocity of a neutron that can be confined within an optical potential V.

However, UCN can also be lost when being reflected from a wall. Upon reflection, the wavefunction of the UCN has a finite probability density inside the material, from which it is reflected. UCN losses arise from two processes:

1. Upscattering: Interaction processes in which the UCN gets an energy transfer from the scattering material. Like in the production process (see Sec. 1.4.5), the UCN will absorb a phonon from the lattice of the reflecting material. Usually this gain in energy is so large that the neutron will no longer be reflected by any material wall and thus is not considered a UCN. The up-scattering probability is described by the material cross section σ_{us} and depends on the wall temperature.

2. Absorption: A UCN can be captured by a nucleus of the reflecting material. The absorption probability is described by an absorption cross section σ_a.

These processes add up to the loss cross section $\sigma = \sigma_{us} + \sigma_a$ which follows a v^{-1} dependency.

To include these losses in the description of UCN scattering developed above, the optical potential is extended by an imaginary part

$$U(\boldsymbol{r}) = V(\boldsymbol{r}) - \imath W = \hbar \sum_i N_i \left(\frac{2\pi\hbar}{m_\mathrm{N}} a_i - \frac{\imath}{2}\sigma_i v \right). \tag{1.15}$$

The ratio η = W/V is a measure for the loss per bounce probability of a material.

The strong interaction of UCN plays a crucial role in the nEDM-experiment. By choosing proper materials (with high V and low W) for the nEDM-spectrometer we are able to guide UCN into a storage chamber and observe their interaction with magnetic and electric fields for a long time. An overview of material properties used in the experiment is given in Table 1.5.

Material	V [neV]	η = W/V [10^{-4}]
Diamond like carbon (DLC)	249 ± 14 [ABD$^+$07]	3.1 ± 0.9 [ABD$^+$06]
Deuterated polystyrene (dPS)	161 ± 10 [BDH$^+$08]	3 ± 1 [BDH$^+$08]
Deuterated polyethene(dPE)	214 ± 10 [BDH$^+$08]	≈ 5 [May98]
Nickel molybdenum (NiMo)	215 ± 10 [Lau13]	4 ± 1 [Göl12]
SiO_2 (quartz)	95 [BDH$^+$08]	4 ± 1 [BDH$^+$08]

Table 1.5: UCN storage properties for materials used in the nEDM-experiment. The real part of the potential V defines the maximal energy of the UCN that can be stored. The ratio η = W/V is a measure for the loss per bounce due to up scattering and capture processes.

1.4.5 Production of ultracold neutrons

As the free neutron decays, the only neutrons available for UCN production are bound in nuclei and need to be liberated from those. To produce a high density of UCN, a strong neutron source is needed. There are two different types of neutron sources in use that create a high flux and can be used for UCN production: nuclear reactors and spallation sources. The first uses nuclear fission mostly of uranium ^{235}U. The reactor at the Institut Laue-Langevin (ILL), Grenoble, France is at the moment the world's strongest continuous neutron source with a thermal flux of up to $1.5 \times 10^{15}\,\mathrm{cm}^{-2} \cdot \mathrm{s}^{-1}$ [LL]. Some nuclear reactor types (like the TRIGA reactor at the University in Mainz) can be pulsed to create high neutron fluxes for a short time. A possible advantage for many UCN experiments that store neutrons.

Spallation sources are accelerator based neutron sources. A beam of high energy protons is shot onto a neutron rich target material like lead or mercury to create neutrons. This is called a spallation process. The world's strongest neutron source of this type is the Spallation Neutron Source (SNS) at Oak Ridge, USA creating a pulsed neutron flux [Lab]. Once liberated from the nuclei, the neutrons have to be decelerated into the ultracold regime. The following exemplary description of the two UCN sources that are closely

related to the experiment described in this document will give an overview of the different techniques used in producing UCN.

The PF2 UCN source at ILL

The current version of the nEDM experiment was situated for about 20 years at the ILL and the current best limit on the neutron EDM was measured at this UCN source. The reactor based ILL UCN source is a so called thermal source, that uses the very cold neutrons present in the tail of the Maxwell-Boltzmann distributed velocity of moderated neutrons.

Neutrons created in the fission process reach the vertical cold source, a vessel filled with liquid Deuterium (lD_2) at a temperature of about 20 K (see Fig. 1.4). After moderation the cold neutrons are extracted vertically via a 12 m long curved guide that is coated with Nickel. Fast neutrons and γ-rays are not following the curvature of the guide, and only the low energy part of the neutron spectrum with velocities below $50\,\mathrm{m}\cdot\mathrm{s}^{-1}$ is guided to a Doppler shift device: the 'Turbine'. It consists of a wheel spinning with 230 rpm and fitted with nickel coated curved blades that move away from the incoming neutron beam. Neutrons are reflected and lose momentum as the blades move away from the incoming neutron beam with $25\,\mathrm{m}\cdot\mathrm{s}^{-1}$. This technique was developed by A. Steyerl in 1968 [SNS+86].

The UCN source at PSI

The UCN source at the Paul Scherrer Institute (PSI) (see Fig. 1.6) uses a spallation neutron source to generate neutrons and a solid deuterium converter to produce UCN. The high intensity proton beam of PSI with an energy of 590 MeV and a beam current of 2.2 mA is used for the spallation process. It is produced in a three-stage accelerator complex (see Fig. 1.5) and is usually meant to produce pions, muons, and neutrons at the spallation target (SINQ). The full beam can be deflected by a fast kicker magnet onto the UCN spallation target. The source has a duty cycle of 0.83%, e.g. one proton kick onto the UCN source for 4 s every 480 s. This is defined via the integral beam current on target and was originally designed to give 1% duty cycle. As the beam current of the proton accelerator was increased since the initial design phase from 2 mA to 2.2 mA, the duty cycle was decreased and will further decrease for an upgraded beam current of 2.4 mA. This however has no influence on the total sensitivity of the nEDM-experiment as the UCN production scales linearly with the beam current [Göl12].

In the spallation target, consisting of 760 lead-filled zirconium alloy tubes,

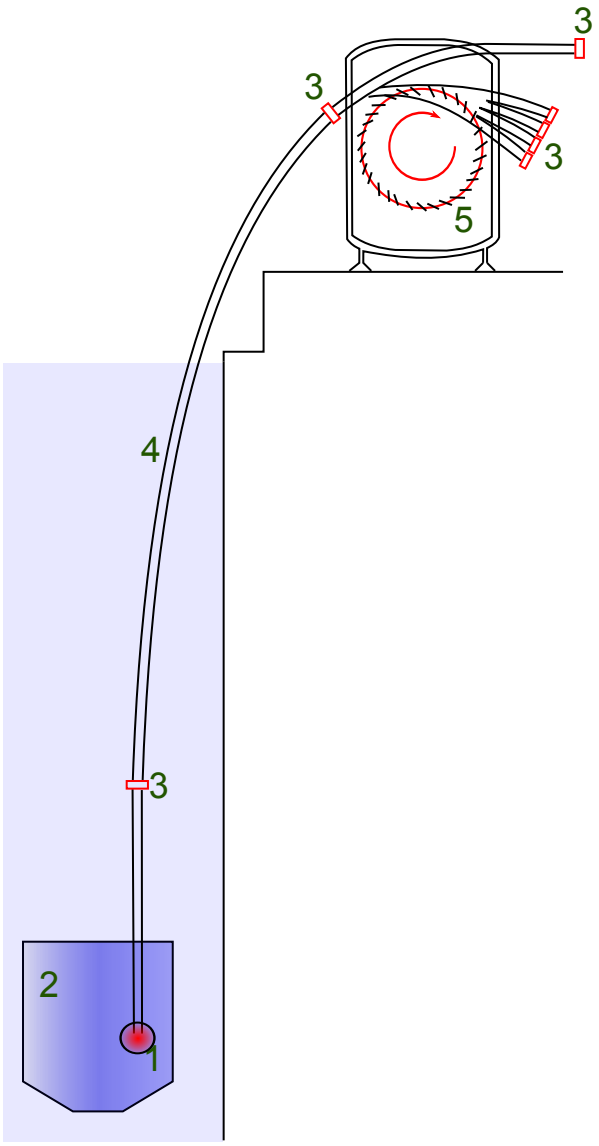

Figure 1.4: A scheme of the ILL PF2 UCN source. (1) Vertical cold source, (2) D_2O tank, (3) shutter, (4) neutron guide, (5) turbine. For details see text.

about eight to ten neutrons per incoming proton are produced. The neutrons have a broad energy spectrum up to the initial proton energy ($\mathcal{O}(1\,\mathrm{MeV})$) and are first moderated to room temperature ($\mathcal{O}(10^{-1}\,\mathrm{eV})$) using heavy water ($D_2O$). They enter a solid deuterium (sD_2) crystal at 5 K situated in the center of the D_2O moderator vessel, about 0.4 m above the center of the spallation target, and will be further moderated towards the cold neutron regime ($\mathcal{O}(1\,\mathrm{meV})$).

The actual UCN conversion takes place in the sD_2 crystal, where cold neutrons are down-scattered into the UCN regime by phonon excitations (see below). UCN are then filled into a storage vessel that is coated with DLC (see Tab. 1.5). By opening (one of) the beam line shutters, UCN can be distributed to three different beam lines via the NiMo-coated UCN guides. The optical potential of the wall coating limits the maximum energy of UCN that can be used in experiments.

Superthermal UCN production The idea of a superthermal UCN source was proposed in 1975 by Golub and Pendlebury [GP75]. Instead of acting purely as a moderator in which the neutrons thermalize by undergoing many scattering processes with single atoms, they can also excite the atomic grid of the crystal and create phonons.

If a suitable converter like sD_2 is used, the phonon density overlaps with the energy of the incoming cold neutron thus leaving the neutron with almost no energy after the phonon excitation. The reversed process, the absorption of a phonon by a neutron can be greatly suppressed by cooling the converter material. Therefore the UCN never get into thermal equilibrium with the converter but have a much lower energy: The deuterium crystal has a temperature of 5 K while the UCN are in the millikelvin regime. More details on superthermal UCN production can be found in [Liu02].

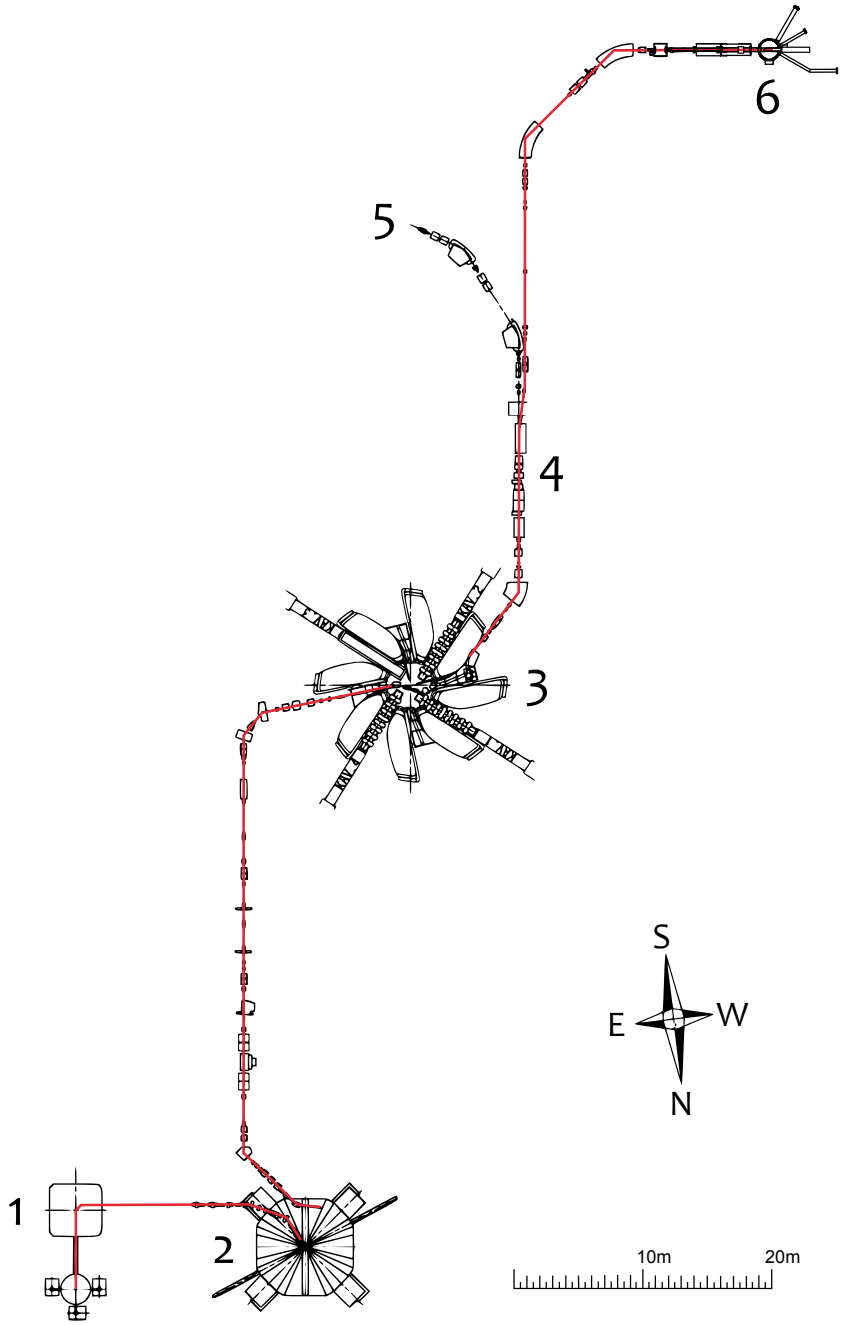

Figure 1.5: The PSI proton accelerator producing the 590 MeV proton beam with a beam current of 2.2 mA. (1) Cockroft-Walton cascade (870 keV), (2) injector cyclotron (72 MeV), (3) main cyclotron (590 MeV), (4) kicker magnet, (5) beamline towards targets for meson and neutron production (not shown), (6) UCN source with spallation target.

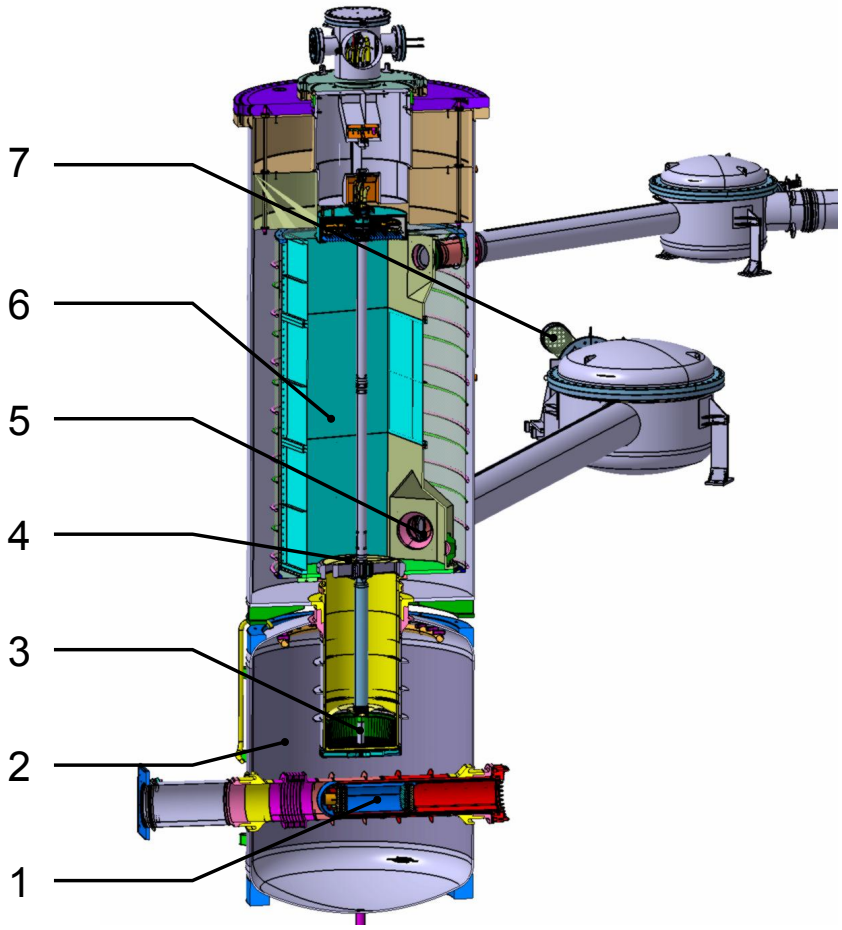

Figure 1.6: CAD drawing of the UCN source. The source has a total height of about 7 m. (1) Spallation target, (2) D_2O moderator, (3) sD_2 converter, (4) main UCN shutter, (5) UCN beam line shutter, (6) UCN storage volume, (7) south beam line towards nEDM-experiment.

Chapter 2

The nEDM experiment

2.1 The experimental technique

The nedm is determined using stored UCN in parallel ($\uparrow\uparrow$) and antiparallel ($\uparrow\downarrow$) magnetic ($\boldsymbol{B}$) and electric ($\boldsymbol{E}$) fields. A neutron with a magnetic ($\boldsymbol{\mu_{\mathrm{n}}}$) and an electric ($\boldsymbol{d_{\mathrm{n}}}$) dipole moment will in these cases precess with a frequency f_{n} of

$$f_{\mathrm{n}\uparrow\uparrow/\uparrow\downarrow} = \frac{2}{h} \times \left| \boldsymbol{\mu}_{\mathrm{n}} \boldsymbol{B} \pm \boldsymbol{d}_{\mathrm{n}} \boldsymbol{E} \right|, \tag{2.1}$$

where h is the Planck constant and the plus sign corresponds to parallel fields. The nedm is extracted from the difference in the precession frequencies ($\Delta f_{\mathrm{n}} = f_{\mathrm{n}\uparrow\uparrow} - f_{\mathrm{n}\uparrow\downarrow}$) of the two cases via

$$\boldsymbol{d_{\mathrm{n}}} = \frac{h \Delta f_{\mathrm{n}}}{2\left(\boldsymbol{E}_{\uparrow\uparrow} + \boldsymbol{E}_{\uparrow\downarrow}\right)} + \frac{\boldsymbol{\mu}_{\mathrm{n}}\left(\boldsymbol{B}_{\uparrow\uparrow} - \boldsymbol{B}_{\uparrow\downarrow}\right)}{2\left(\boldsymbol{E}_{\uparrow\uparrow} + \boldsymbol{E}_{\uparrow\downarrow}\right)}. \tag{2.2}$$

The precession frequency f_{n} is determined using Ramsey's method of separated oscillatory fields. From (2.2) the most important requirement of this experimental method can be seen: In our case, the two measurements (parallel and antiparallel fields) are not taking place at the same time. Thus it is of uttermost importance that the magnetic field between the two measurements does not change. For the same magnetic field strength of the parallel and antiparallel case ($\boldsymbol{B}_{\uparrow\uparrow} = \boldsymbol{B}_{\uparrow\downarrow}$ and $\boldsymbol{E}_{\uparrow\uparrow} = -\boldsymbol{E}_{\uparrow\downarrow}$) the last term of (2.2) cancels, so that

$$d_{\mathrm{n}} = \frac{h \Delta f_{\mathrm{n}}}{4E}, \tag{2.3}$$

and one directly measures d_{n}. A small change in the magnetic field can mimic a nedm due to the neutron's (relatively) strong coupling to the magnetic

field via its magnetic moment. This triggers not only the demand for precise magnetometry (see Sec. 2.4.9 and 2.4.10). Systematic effects are also related to magnetic field changes correlated to the change of the electric field (see Sec. 3).

2.1.1 Ramsey's method of separated oscillatory fields

The nEDM-experiment is based on the method of separated oscillatory fields developed by Norman F. Ramsey[1]. In contrast to the molecular beam experiments of Ramsey the oscillatory fields are not spatially separated but in time. The basic steps are illustrated in Fig. 2.1.

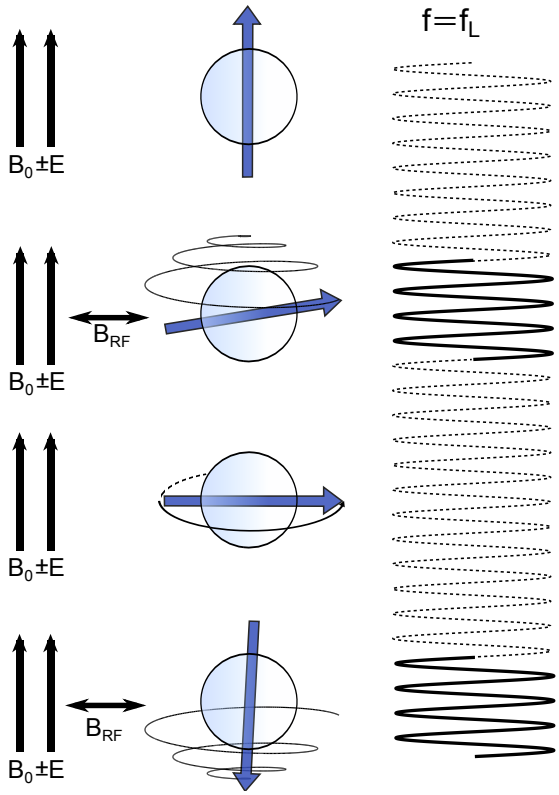

Figure 2.1: Illustration of Ramsey's method of separated oscillatory fields as used in the nEDM experiment. For a detailed explanation see text.

Polarized UCN are filled into a storage chamber with their spin aligned either parallel (N_{up}) or antiparallel (N_{down}) to the static holding field B_0. For a time t, an alternating magnetic field B_{RF} is applied perpendicular to

[1] for which he won the Noble Prize in Physics in 1989.

B_0. The frequency is close to the Larmor precession frequency of the UCN $f_\mathrm{L} = \gamma_\mathrm{n} \mathrm{B}_0$. Here γ_n is the gyromagnetic ratio of neutrons that has a value of about $29.16\,\mathrm{Hz} \cdot \mu\mathrm{T}^{-1}$. The product of amplitude and duration of this field is chosen such, that the spin of the UCN is flipped by $\pi/2$ and is therefore called a $\pi/2$-pulse.

After the pulse the neutrons precess for a time $T \gg t$ in the magnetic and electric field configuration with the frequency given by (2.1). At the end of the free precession time a second $\pi/2$-pulse is applied in phase with the first. If the frequency of B_RF is exactly the Larmor frequency and if no additional phase has been built up due to the interaction of an electric dipole moment with the electric field, the two pulses will exactly add up. The UCN will end up in a final state with all spins in the opposite orientation compared to the initial population. The actual precession frequency of the neutrons can be measured by detuning the applied B_RF frequency and measuring one or even better, both of the two spin states of the UCN (see Fig. 2.2). As this is a comparison of the UCN frequency f_L with the external reference f_RF, a precises atomic clock is needed to generate B_RF.

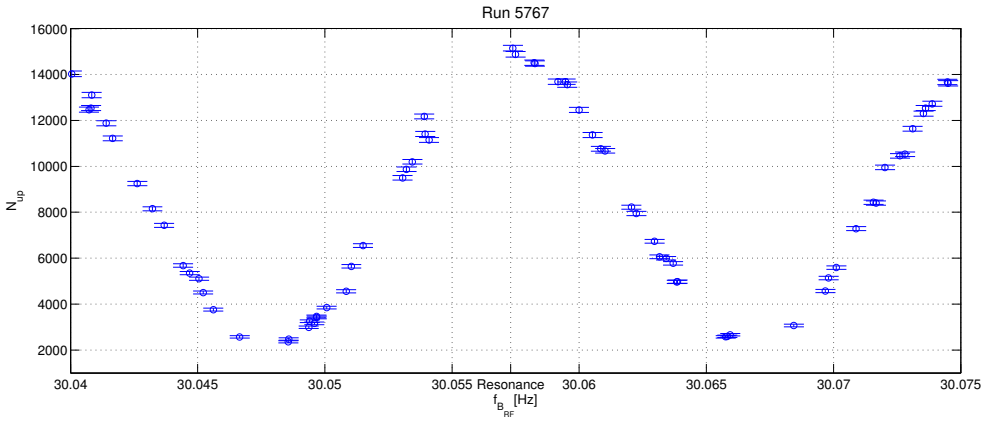

Figure 2.2: A typical Ramsey resonance pattern as measured in the nEDM spectrometer. This measurement was performed for $T = 30\,\mathrm{s}$ and without an electric field applied. The resonance frequency is $30.05731(2)\,\mathrm{Hz}$, and the initial spin state was 'down'.

Under the influence of an electric dipole moment the pattern in Fig. 2.2 would shift to a higher (lower) frequency for a parallel (antiparallel) field configuration. The maximum sensitivity on such a frequency shift of the neutrons is achieved at the steepest slope of the pattern. Here a small change in frequency would lead to a large difference in the observed count rate.

2.1.2 Expected statistical sensitivity

The change in UCN counts as a function of $f = f_{\mathrm{L}} - f_{\mathrm{RF}}$ for a Ramsey type measurement close to the resonance for one spin component (e.g. N_{up}) can be described as

$$N_{\mathrm{up}}(\Delta f) = N_{\mathrm{up}} \left[1 - \alpha \cos\left(fT\right)\right], \tag{2.4}$$

with $N_{\mathrm{up}} = {}^{(N_{\mathrm{max}}+N_{\mathrm{min}})}/_{2}$ (see also Fig. 2.2 where $N_{\mathrm{max}} \approx 14500$ and $N_{\mathrm{min}} \approx 2000$), $\alpha = {}^{(N_{\mathrm{max}}-N_{\mathrm{min}})}/_{(N_{\mathrm{max}}+N_{\mathrm{min}})}$, and the free precession time T. Looking at the change in the number of counts as a function of the frequency change that we would expect from the influence of the edm in an electric field we see that

$$\frac{\partial N_{\mathrm{up}}(f)}{\partial f} = N_{\mathrm{up}} \alpha T \sin\left(fT\right), \tag{2.5}$$

has a maximum (${}^{\partial N_{\mathrm{up}}(f)}/_{\partial f} = N_{\mathrm{up}}\alpha T$) at $fT = {}^{\pi}/_{2}$, so at half of the resonance as previously mentioned. At this position of the pattern, the sensitivity of this measurement for a frequency change as a function of a change in the number of UCN counts is then

$$\sigma_f = \frac{\partial f}{\partial N_{\mathrm{up}}(f)} \Delta N_{\mathrm{up}} = \frac{1}{\alpha T \sqrt{N_{\mathrm{up}}}}, \tag{2.6}$$

with the statistical error in the UCN counts of $\sqrt{N_{\mathrm{up}}}$. As in the experiment we measure not only N_{up} but $N = N_{\mathrm{up}} + N_{\mathrm{down}} = 2N_{\mathrm{up}}$ (at half the resonance) a factor of two must be taken into account. In the edm measurement we look at the frequency difference Δf between parallel and antiparallel electric field configuration and get for the sensitivity of the frequency shift

$$\sigma_{\Delta f} = \sqrt{2(\sigma_f)^2}. \tag{2.7}$$

Using (2.3) we get the sensitivity for an electric dipole moment of such a measurement

$$\sigma_{d_{\mathrm{n}}} = \frac{\hbar}{2E\alpha T \sqrt{N}}. \tag{2.8}$$

For a repetition of the experiment the sensitivity scales with the inverse square root of the number of repetitions.

2.2 History of nEDM experiments

Already in 1950 Ramsey and Purcell discussed that the nedm would be a signature of T-violation and pronounced a first upper limit of $d_{\mathrm{n}} < 3 \times 10^{-18}\, e \cdot \mathrm{cm}$ [PR50]. Many improved experiments where triggered afterwards and increased the sensitivity on the nedm by orders of magnitude (see Fig. 2.3).

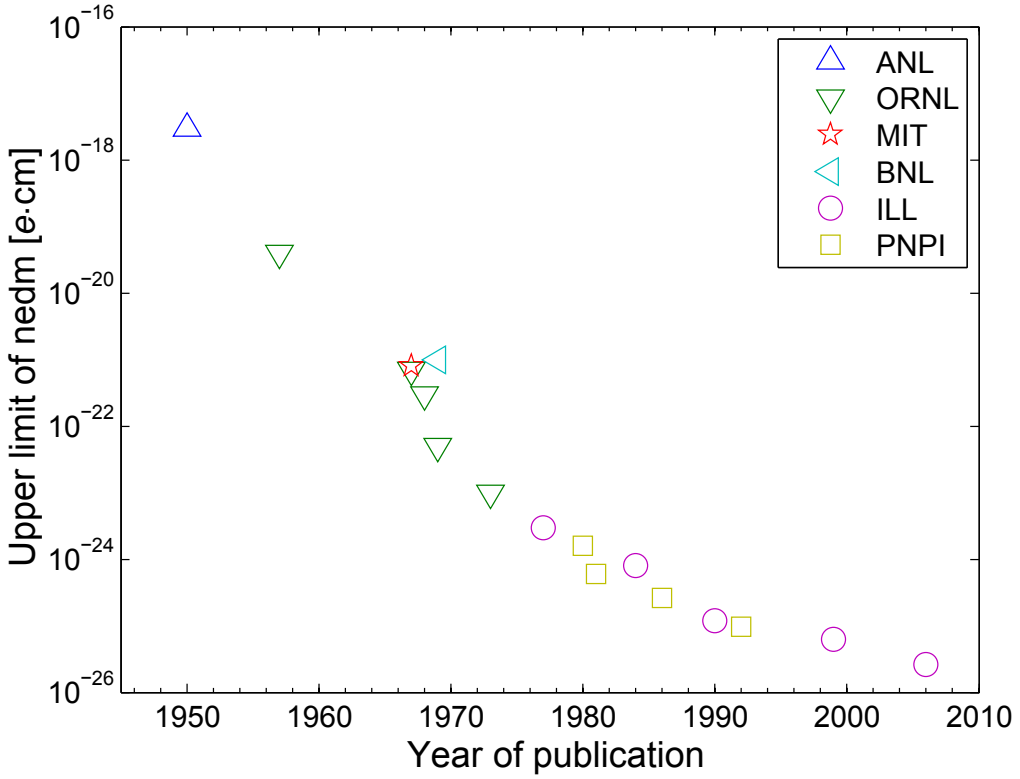

Figure 2.3: Over the last half century the upper limit on the neutron electric dipole moment was decreased by many orders of magnitude (Argonne National Laboratory (ANL), Oak Ridge National Laboratory (ORNL), Massachusetts Institute of Technology (MIT), Brookhaven National Laboratory (BNL), Institut Laue-Langevin (ILL), Petersburg Nuclear Physics Institute (PNPI)). Until 1980 nedm results shown here were achieved using scattering or magnetic resonance of cold neutron beams. The results after 1980 where achieved using stored ultracold neutrons. The flattening of the decrease of upper limits around 1990 is due to the statistical limitation of current UCN sources. (Data from [PR50, SPR57, SN67, MDBR67, BMDR69, CNS$^+$69, DMR73, DMP$^+$77, ABB$^+$80, ABB$^+$81, PSG$^+$84, A$^+$86, SCP$^+$90, ABB$^+$92, HBG$^+$99, HP06]).

Up to the 1970s cold neutron beams were used to measure the electric

dipole moment. A typical setup of such an experiment is shown in Fig. 2.4. Cold neutron beams can be produced with a high neutron density. However as the neutrons have a high velocity compared to UCN the observation time is much shorter. Even more severe is a velocity dependent systematic effect known as the motional field or $\boldsymbol{v} \times \boldsymbol{E}$ effect (see sec. 3.1.2). In the rest frame of the neutron the electrical field $\boldsymbol{E}$ is seen as an additional magnetic field

$$\boldsymbol{B}_{\boldsymbol{v}\times\boldsymbol{E}} = \frac{\boldsymbol{v} \times \boldsymbol{E}}{c^2}, \tag{2.9}$$

which changes direction with the electric field and mimics an edm signal. The best ever achieved nedm result at a beam of $d_\mathrm{n} < 3 \times 10^{-24}\, e \cdot \mathrm{cm}$ (90 % C.L.) [DMP$^+$77] was limited by this systematic effect.

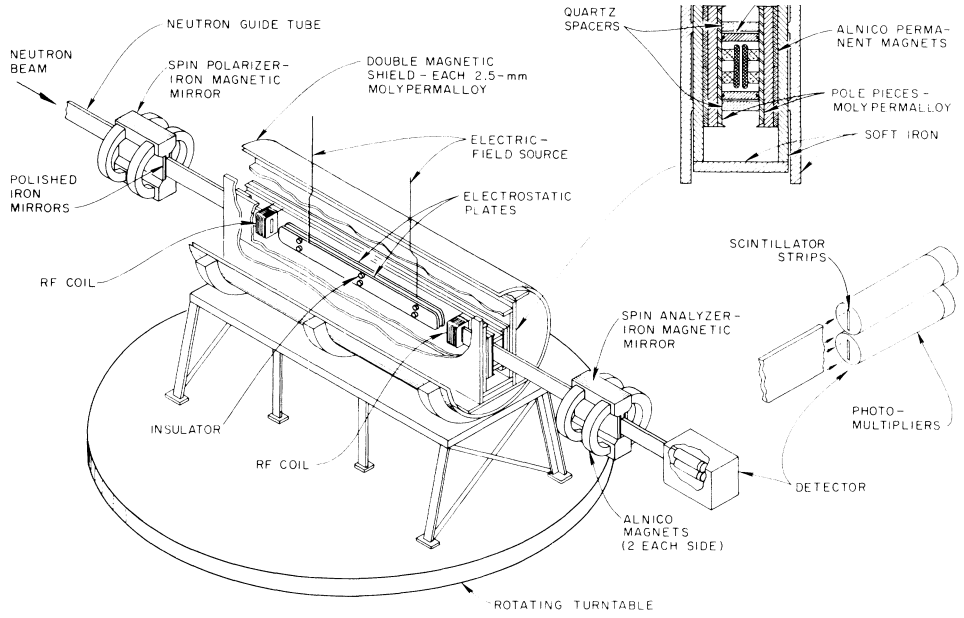

Figure 2.4: The spectrometer used by Dress et. al. to measure the best ever achieved cold neutron beam nedm result. The scheme can be taken as a general example for the idea of a beam based nedm experiment. A beam of polarized cold neutrons traverses a region with parallel or antiparallel electric and magnetic fields. The precession frequency of the neutrons in this region is measured by applying an amplitude modulated magnetic field at each end of the homogeneous field region (from [DMP$^+$77]).

Starting in the 1980s a series of nedm searches were performed at the Petersburg Nuclear Physics Institute (PNPI), Russia and at the Institut Laue-Langevin (ILL), France, using stored UCN. The possibility to store neutrons increases the free precession time from some milliseconds to

hundreds of seconds and reduces velocity dependent systematic effects like the motional magnetic field at the cost of drastically reduced neutron count rates[2]. The current best limit on the nedm of $d_{\mathrm{n}} < 2.9 \times 10^{-26}\, e \cdot \mathrm{cm}$ (90 % C.L.) [BDG+06], published in 2006, was actually limited by statistical uncertainties and not by systematic effects.

2.2.1 Current nEDM experiments

Besides the experiment described in this thesis there are at least seven other collaborations around the world trying to measure the electric dipole moment of the neutron (see Fig. 2.5). They all aim for an improvement of the current best limit by at least an order of magnitude in sensitivity. Although having different approaches on magnetometry or the actual realization of the experiment like cryogenic techniques, most of these experiments use a refined method of the room temperature approach that is described in this work. Essential to most of the experiments is the close relation with the development of new sources for UCN to increase the UCN density and therefore the statistical sensitivity.

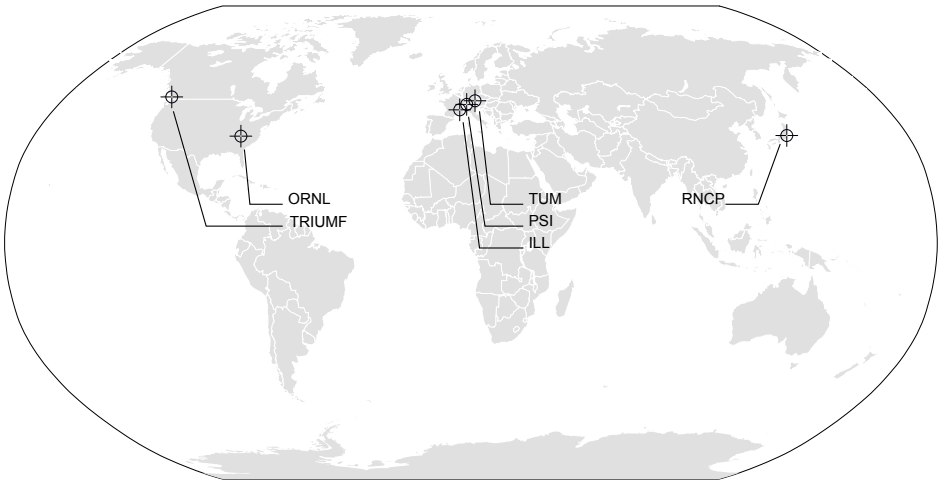

Figure 2.5: Laboratories around the world hosting experiments that search for an edm of the neutron.

Among the experiments that will try to further improve the room temperature approach is the n^{2}EDM-experiment, the successor of the

[2]Comparing the sensitivity of [DMP+77] with the nEDM at PSI with regard to neutron density and free precession time, one can see, that the average count rate in a cold beam of $2800\,\mathrm{s}^{-1}$ is about a factor 1000 higher. However, the increase in free precession time from about 0.02 s to 200 s leads to a 300 times higher sensitivity.

nEDM-experiment, developed within this collaboration. It will feature a double precession chamber to measure both electric field configurations at the same time, and optical atomic magnetometers, based on ^{3}He, ^{199}Hg, and ^{133}Cs . A similar experiment is being build up in Germany at the new UCN source at Technische Universität München(TUM) [Fie]. This experiment focuses on ^{199}Hg and SQUIDs[3] for magnetic field monitoring. A third similar experiment is being developed in Japan [MAH+12] and will be operated at a UCN source at the Research Center for Nuclear Physics(RNCP) and later shall be moved to the source at TRIUMF[4] in Canada.

A different class of experiments is the search for an nedm using cryogenic techniques. Liquid helium is used to convert polarized cold neutrons to UCN. The measurement of the electric dipole moment is performed in the very same liquid helium environment. Two different groups are working on cryogenic experiments. In the United States, a spectrometer is set up at Oak Ridge National Laboratory (ORNL) [I+07] that will use small amounts of ^{3}He within the liquid He as co-magnetometer and neutron detector. At ILL in France, the successor of the nEDM-experiment is developed. The 'CryoEDM' experiment [vdG09] will use SQUID devices for magnetometry and a solid state ^{6}Li based neutron detector. While there are general advantages of the cryogenic approach like the use of superconducting shields and possible high UCN densities, it is also technically challenging and time consuming as the cool-down and warm-up of such large cryostats takes time.

A very different approach is envisaged in a crystal diffraction experiment carried out at the ILL [FJK+10]. This experiment is trading the long observation time of UCN for the high electric field inside the lattice of non-centrosymmetric crystals. A cold neutron beam is reflected from a quartz crystal close to the Bragg condition and the spin rotation due to a possible edm of the neutron is measured. The sensitivity of the experiment needs to be improved to reach the same sensitivity as current UCN based edm experiments and it seems challenging to improve the current upper limit by a large factor with this technique.

2.3 The nEDM-experiment at PSI

In 2009 the nEDM-experiment was lifted from its stand at ILL where it had been situated for about 20 years and moved to PSI. It is now situated at

[3] Superconducting quantum interference device.

[4] Tri University Meson Facility.

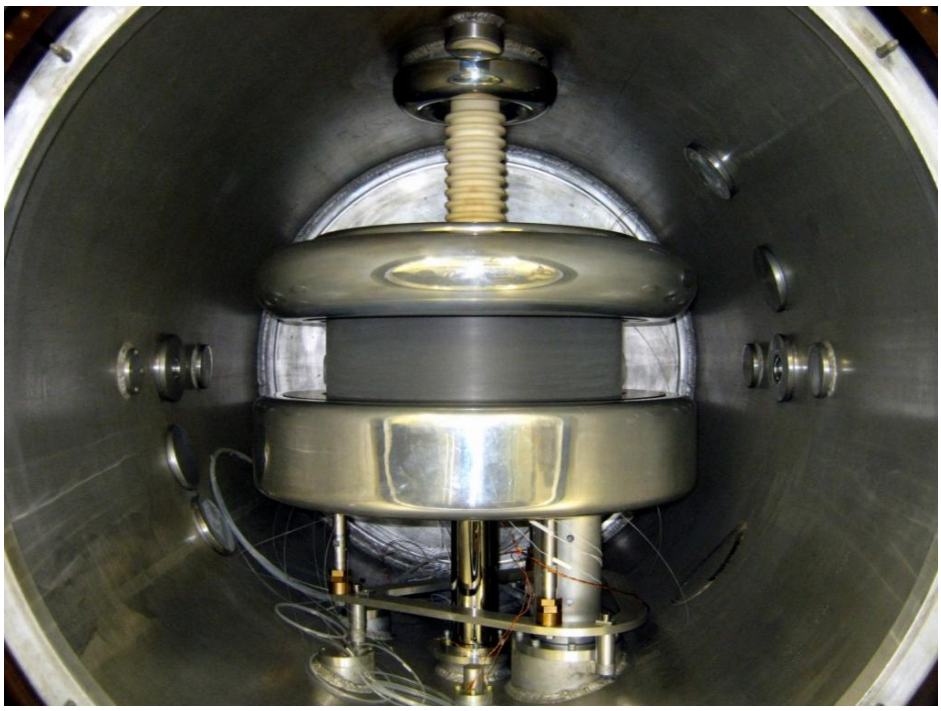

Figure 2.6: A view into the open nEDM-experiment. The precession chamber consisting of two electrodes and an insulator ring, is resting on an adjustable tripod. From the top the high voltage vacuum feed-through and from the bottom the coated UCN glass guide and the mercury magnetometer system are entering the vacuum tank. The optical fibers visible belong to the Cesium magnetometer system.

N 47° 32' 11.152" E 8° 13' 19.535" in the WNAA building next to the UCN source (see Fig. 2.7). The PSI is an institute that houses large scale facilities, with a wide range of research topics. Thus it is unavoidable to have some larger magnets in the vicinity of the nEDM-experiment that will modify the magnetic field. One of the biggest influences is created by the SULTAN[5] magnet. It is situated in close vicinity of the nEDM-experiment, just across the street, and creates magnetic fields up to 12 T. This magnetic field is not constant, but usually ramps up in the morning and down in the evening. During this time the magnetic field inside the precession chamber changes too much, invalidating any measurement.

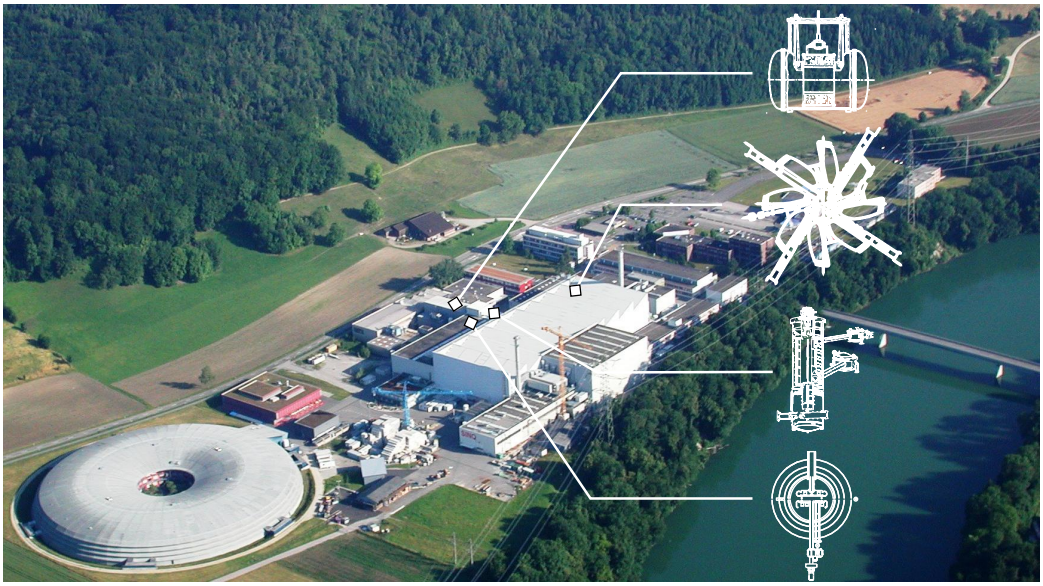

Figure 2.7: The area west of the PSI next to the river Aare. Marked are the positions (from top to bottom) of the SULTAN magnet, the main cyclotron, the UCN source, and the nEDM-experiment. The round building, that contains a synchrotron source, in the lower left corner can be used for scale: it has an outer diameter of 138 m.

The coordinate system of the nEDM-experiment at PSI In this document the coordinate system shown in Fig. 2.8 and Fig. 2.10 will be used. The origin of the coordinate system is the center of the precession chamber at the height of the mercury magnetometer readout beam. The x-axis is along

[5]German acronym for **Su**pral**e**iter **T**est **An**lage

the readout beam pointing towards the UCN source. The y-axis is along the cylindrical axes of the vacuum tank, pointing towards the SULTAN magnet. The z-axis is antiparallel to the direction of gravitational acceleration.

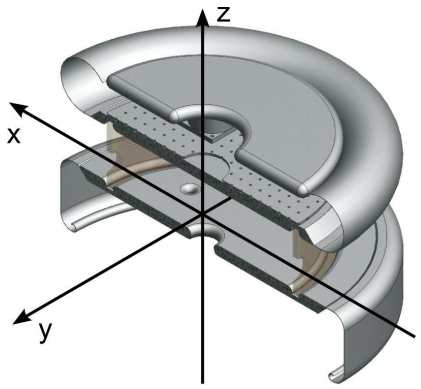

Figure 2.8: Coordinate system of the nEDM-experiment. The origin is in the center of the precession chamber, at the height of the readout light beam of the mercury magnetometer.

2.3.1 Operation of the experiment

A typical experiment performed with the nEDM spectrometer consists of a **run** that can take between some minutes up to a few days. Each run consists of several **cycles**. In each cycle up to 16 different **steps** are performed. The steps are the same in each cycle, but parameters like the electric field, the frequency of alternating magnetic fields, the duration of a step or even the magnetic field configuration can be changed automatically from cycle to cycle. Each step can contain up to 14 actions to be taken by the FPGA based DAQ board. These are defined in a μTimer table. An example of such a μTimer table is given in Fig. 2.9. It is also possible to define two different μTimers, that will be executed sequentially in every cycle, dividing each cycle in two sub cycles (0,1). This way it is e.g. possible to perform an additional measurement with the Hg comagnetometer after a short UCN measurement, until the UCN source is ready again.

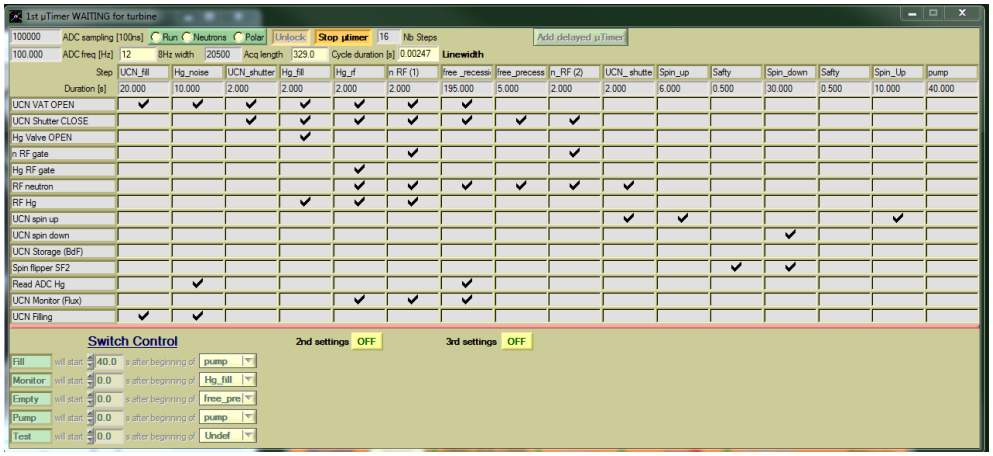

Figure 2.9: Operator interface of an exemplary µTimer table as used in the nEDM data taking in autumn 2012. The check marks in the table activate one or more of the 14 actions that can be performed by the µTimer. Also the switch control is embedded into this window (see Sec. 2.4.5).

2.4 The subsystems of the experiment

There are several subsystems depicted in Figure 2.10, that are needed to operate the experiment. A description will be given of all these subsystems, focusing on their purpose, use, and important performance parameters.

2.4.1 Thermohouse

The thermohouse (see Fig. 2.11) is used to create a controlled environment for the experiment.

The demands are to have a stabilized temperature inside regardless of large temperature fluctuations outside[6], as well as some protection against dust and other pollutions coming from the experimental area. The thermohouse is a two-level construction made from non-ferromagnetic materials, mainly wood. The house is 4.2 m wide, 7 m deep and 8.8 m high. Both floors have an individual thermal stabilization system that consists of an air condition and a feedback system. On the ground floor most of the electronics and the computers are located. Usually the experiment is controlled from here. The temperature is stabilized to $\Delta T = \pm 1\,\mathrm{K}$ to

[6]The surrounding experimental hall is neither insulated nor heated, so it can have large temperature changes of several K between day and night and even bigger changes between the seasons. During a cold winter actually several water pipes of the air conditioning system did freeze!

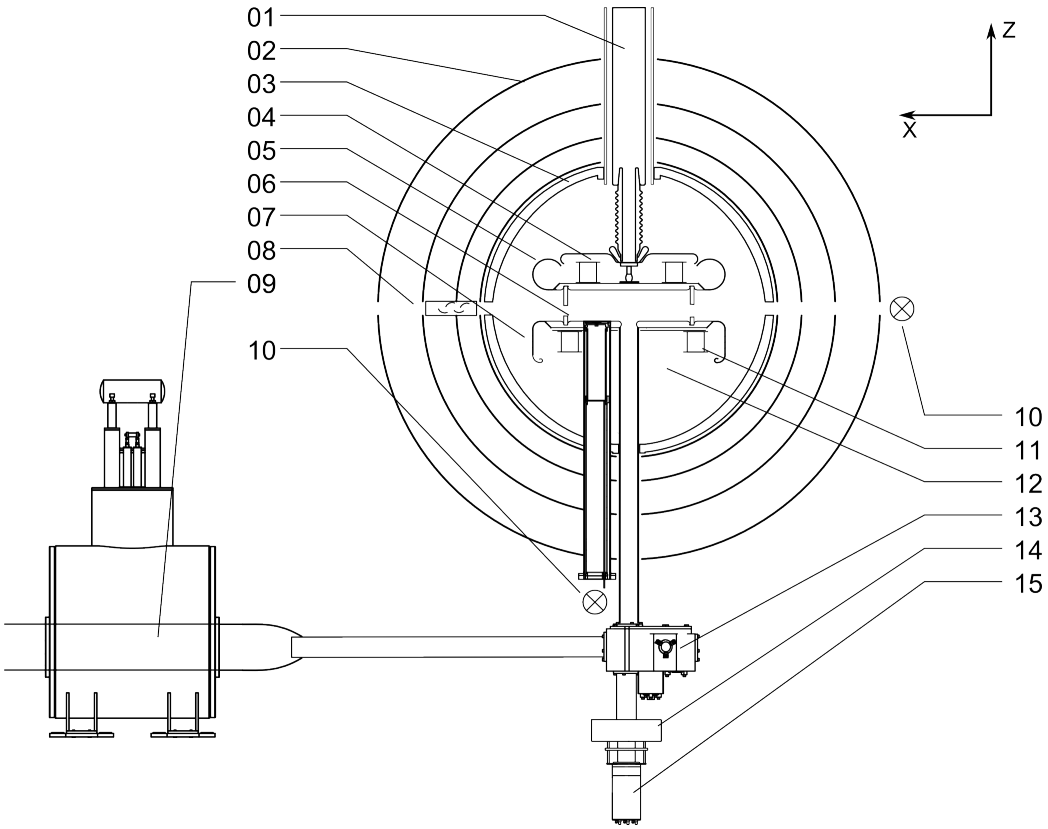

Figure 2.10: Sketch of the nEDM-experiment, as it is installed at PSI, showing the most important parts. (01) High voltage vacuum feedthrough, (02) four-layer magnetic shield, (03) vacuum tank with main magnetic coil and 33 corrections coils, (04) high voltage cesium magnetometer array, (05) high voltage electrode, (06) insulator ring, (07) ground electrode, (08) photo multiplier tube, (09) superconducting polarizer magnet, (10) ^{204}Hg discharge lamp, (11) ground cesium magnetometer array, (12) vacuum, (13) neutron switch, (14) spin analyzer, (15) neutron detector.

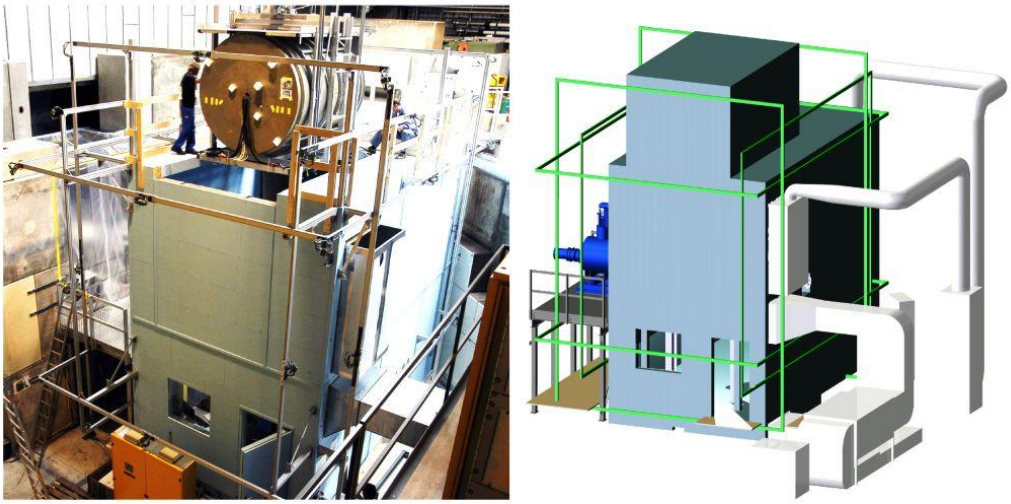

Figure 2.11: Comparison of a picture of the thermohouse taken during the installation of the spectrometer in August 2009 and a CAD drawing of the thermohouse. The air conditioning channels are not fully assembled. The large coils of the surrounding field compensation are also visible and highlighted in green in the CAD drawing.

ensure stable operation of all data acquisition systems, etc. The spectrometer is mounted on an aluminum support structure and is situated on the first floor. This is needed to bring the experiment above the UCN beamline height which is about 3.3 m above the concrete floor of the hall. The upper floor has its own door and can only be reached via stairs and a small lock, that is used to keep the room clean. It is stabilized to $\Delta T = \pm 0.1\,\mathrm{K}$ in order to have stable magnetic conditions. A change in temperature will change the dimensions of the vacuum tank (expansion coefficient: $\alpha_{\mathrm{Al}} \approx 23 \times 10^{-6}\,\mathrm{K}^{-1}$) together with the magnetic field coils and the magnetic shield (expansion coefficient: $\alpha_{\mathrm{MuMetal}} \approx 10 \times 10^{-6}\,\mathrm{K}^{-1}$) and thus the magnetic field.

A set of temperature sensors monitors the actual temperature in the thermohouse at different locations around the shield. Figure 2.12 shows a typical overnight measurement of these sensors. The overall spread of the different sensors is due to an unknown offset of each individual sensor. The measured temperature stability is actually even $\Delta T = \pm 0.01\,\mathrm{K}$. The magnetic field in the center of a cosine-theta coil[7] of length l and diameter

[7] This type of coil has an equal horizontal spacing along the z-axis of about 2 cm between turns of rectangular shaped windings.

a is proportional to $B \propto l\,(l^2 + a^2)^{-1/2}$ [BCL98]. Thus the change of the magnetic field due to thermal expansion is $\Delta B \approx 2 \times 10^{-8}\,\mu\mathrm{T} = 20\,\mathrm{fT}$, and the influence of the distance change between magnetic shield and tank is one order of magnitude lower. This is below the expected sensitivity of the experiment (see Fig. 5.1) and can be neglected.

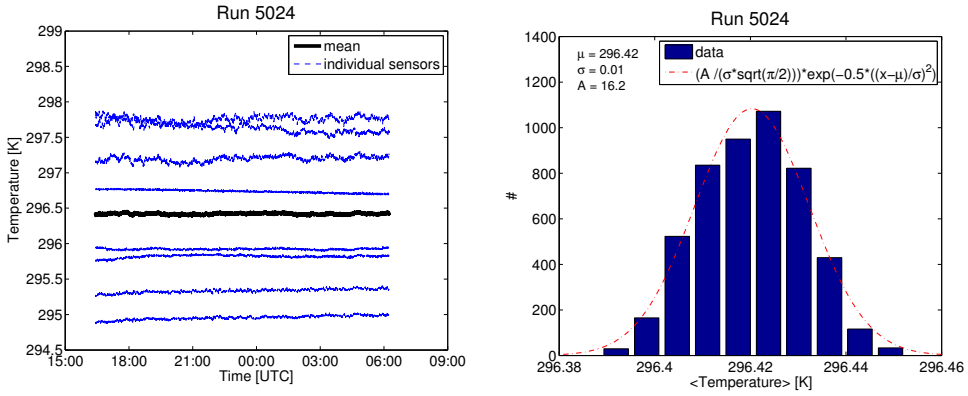

(a) (b)

Figure 2.12: Typical temperature behavior during one night, measured with an array of eight temperature sensors and the mean of all sensors (a). Note that the sensors have unknown offsets so that the absolute temperature reading of each sensor is of limited significance. A histogram (b) of the mean temperature shows, that the temperature is overall very stable and seems to be dominated by random fluctuations of the sensors.

2.4.2 Surrounding field compensation

Centered around the precession chamber[8], the experiment is surrounded by six large rectangular coils, as visible in Fig. 2.11. The coils are about 8 m times 6 m in dimension. Each of these has its own power supply, delivering up to 10 A (x and y direction) or 20 A (z direction) of current, and give six degrees of freedom to regulate the environmental magnetic field around the spectrometer. Using a static current in these coils the constant magnetic field, that is created by the Earth, concrete, and iron radiation shielding of the UCN source etc., can be compensated, so that the magnetic shield, that surrounds the experiment, is situated in a very low field. In addition ten

[8]The center of each coil pair actually differs up to 20 cm from the center of the precession chamber.

three-axis fluxgate magnetometers (so a total of 30 sensors) are installed around the magnetic shield. They serve as input to an active feedback loop, that controls the currents in the six coils. Thus, also changes in the surrounding magnetic field can be attenuated. The optimization of the performance of the SFC is studied in another PhD thesis [Fraon].

2.4.3 Magnetic shield and the degaussing system

The magnetic field around the experiment is attenuated with a four-layer magnetic shield surrounding the vacuum tank. Each layer has a cylindrical shape with removable end caps to allow access to the shielded area. The radii of the shield layers decrease from 1.94 m, 1.58 m, 1.33 m, to 1.15 m and the length decreases from 2.76 m, 2.32 m, 1.88 m to 1.61 m. It consists of a nickel iron alloy[9] with high permeability. This creates a preferred path for magnetic field lines, which reduces the magnetic flux within the shielded area as demonstrated in an exemplary finite element calculation of a magnetic shield and a permanent magnet in Fig. 2.13.

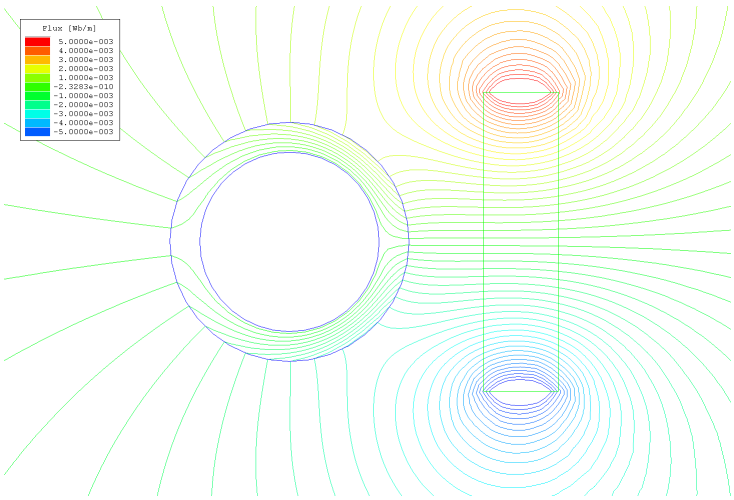

Figure 2.13: An example finite element calculation of a magnet and a magnetic shield. The magnetic flux is confined within the high permeability material, the volume inside the magnetic shield is basically field free. (The calculation was done using Ansoft Maxwell SV version 3.1.04)

The shielding factor has been measured using the SFC coils to create known static and dynamic fields, while measuring the magnetic field inside using a fluxgate magnetometer (Tab. 2.1).

[9] Mumetall®, Vacuumschmelze (Hanau).

Direction	Shielding factor
x	13300(600)
y	1600(20)
z	8600(300)

Table 2.1: Shielding factors for small static perturbations (μT) of the nEDM four-layer magnetic shield measured at PSI [BKGS+09].

To create a low and stable field within the shield it is important to degauss the magnetic shield, i.e. randomize its magnetic polarization, after large field changes inside or outside the shield. It has been shown that otherwise the shield is very sensitive to mechanical influences like vibrations that can change the magnetic field inside up to $\mathcal{O}(1\,\mathrm{nT})$ [BKGS+09]. A scheme of the degaussing system is shown in Fig. 2.14.

To degauss the shield a laptop with a 16 bit DAC card (NI DAQCard-6036E) produces a sinusoidal signal that is fed to a power amplifier (ROHRER PA2088A). The shield is magnetized into saturation using an alternating current of 62 A and 10 Hz in a coil of 14 windings that is wrapped around all four shield layers. Once in saturation the amplitude of the current, hence the magnetization in the shield, is slowly reduced with each polarity change, over 2500 polarity changes. This way the magnetic domains freeze out in a randomized way. To avoid a small magnetization of the shield, caused by the degaussing itself, it is important to reduce the amplitude truly to zero and prevent any DC offset. A transformer between the power amplifier and the degaussing coil is used to prohibit a possible DC offset. To further optimize the degaussing result, a set of potentiometers is installed parallel to the coil serving as a bypass (see Fig. 2.14). During degaussing the resistance in this bypass is high compared to the $0.5\,\Omega$ of the degaussing coil, so that the current is solely flowing through the coil. After the degaussing signal has been sent, there is still noise from the power amplifier going through the coil. If the coil would now be opened, the noise current at the time of opening would magnetize the shield. By slowly reducing the resistance of the potentiometers, the noise current in the coil reduces until it is zero. Now all noise current is flowing through the bypass and the coil can be opened without the danger of magnetizing the shield. To monitor the degaussing process the hysteresis curve $M(H) = \chi_\mathrm{m} H$ of the shield can be checked on an oscilloscope. The magnetization M is measured using a pickup coil around the inner three shield layers connected to a low pass filter and an low noise, battery powered, amplifier. The power amplifier provides a control voltage that is

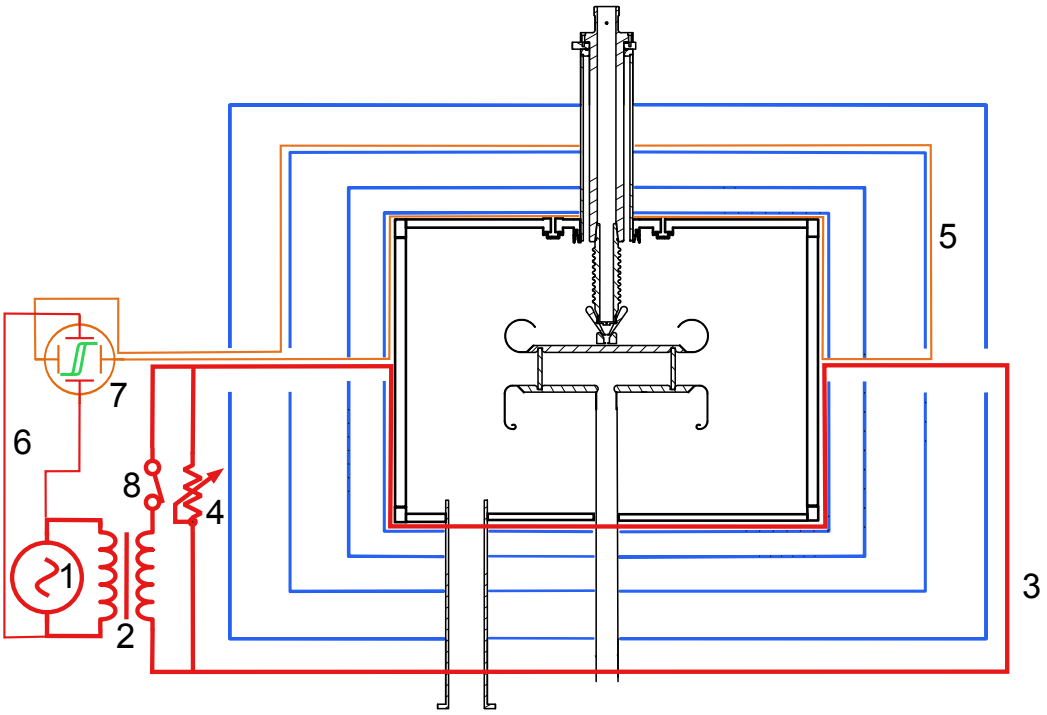

Figure 2.14: A scheme of the system used to degauss the shield. An amplifier (1) is fed from a high resolution DAC converter in a computer that generates the sinusoidal degaussing signal. A 1:1 transformer (2) is used to eliminate any DC offset. The secondary transformer coil is connected to the degaussing coil (3) that has 14 windings and is wrapped around all four shield layers. A bypass with a potentiometer (4) is used to avoid any magnetization due to amplifier noise. Using a pickup coil (5) and an output reference signal (6) coming from the amplifier, the hysteresis curve of the magnetization can be checked on an oscilloscope (7). The coil is opened after degaussing using a switch (8), to minimize noise inside the experiment.

proportional to the output current and therefore also proportional to the magnetic field (H) created inside the shield. As the degaussing coil penetrates the shield and can serve as an antenna for magnetic noise it needs to be opened after the degaussing procedure.

2.4.4 Vacuum and gas system

The experiment is performed in a He atmosphere of $\mathcal{O}(10^{-3}\,\text{mbar})$ to optimize high voltage performance. A simplified sketch of the vacuum system is shown in Fig. 2.15. Inside the magnetic shield an cylindrical aluminum vacuum tank is installed. Four turbo pumps backed by a scroll pump are used to evacuate the tank to about $2{\times}10^{-6}$ mbar. The precession chamber (Sec. 2.4.6), the switch (Sec. 2.4.5), and the neutron guides (Sec. 2.4.5) form a separate vacuum system within this tank. The two systems are not fully tight against each other due to the fact that e.g. the quartz windows for the Hg readout light beam are only tightened with polytetrafluoroethylene (PTFE) tape.

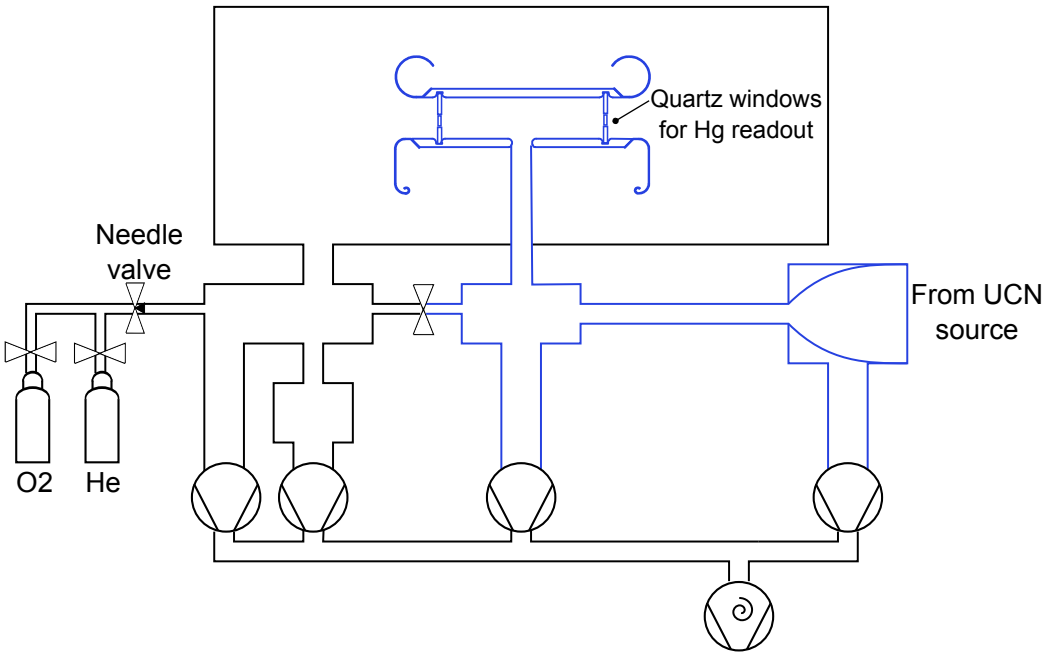

Figure 2.15: A simplified sketch of the vacuum system of the nEDM-experiment. The different vacuum systems are depicted in different colors (see text for details).

A motorized needle valve connected to the tank is used to set a defined pressure of He or O_2 for stable HV operation or discharge cleaning (see Sec. 2.5.3). If the system has to be vented, dry nitrogen from a bottle is

used instead of ambient air. This reduces the amount of water introduced in the system and maintains the performance of the Hg magnetometer.

2.4.5 UCN system

The UCN system includes all components used to guide and confine UCN. These are the neutron guides that guide the UCN between the components, the UCN switch that diverts neutrons into different parts of the experiment, and the neutron shutter that closes the precession chamber after the filling with UCN.

Neutron guides

The neutron guides used in the experiment are made from glass that has been coated with a nickel molybdenum (NiMo) alloy[10]. Handling the glass guides requires great caution as they are very fragile and many guides were actually damaged during the (un)mounting. However, glass has two advantages with respect to our requirements:

1. Glass guides have a low surface roughness. In combination with the NiMo coating that has an optical potential of about 215 neV the guides have a high transmission. This allows us to get a high density of polarized UCN into the precession chamber.

2. Due to the very small thickness of the NiMo coating of a few hundred nanometer there is almost no skin effect that would reduce the amplitude of the oscillating fields used for spin flipping of the neutrons in front of the analyzing foil and after the superconducting magnet.

UCN switch

The UCN switch is used to divert neutrons within the experiment. As the switch is a central part of the UCN system it is of great importance that it has a high transmission and a low loss rate (e.g. due to slits). The switch consists of different small guide pieces that sit in a vacuum housing on a rotating disk. By rotating this disk the different parts of the experiment can be interconnected. A CAD exploded view drawing and a picture of the

[10]Nickel has a fairly high optical potential for UCN but is also magnetic and would depolarize the neutrons. By adding about 15 % of Molybdenum the Curie temperature of pure Nickel is reduced from about 630 K to below room temperature.

device are given in Fig. 2.16. The positions/guide pieces are named by their functionality:

1. *Fill*, a 90°upwards bend made from aluminum and coated with nickel vanadium (NiV, with an optical potential of about 220 neV [ADH$^+$10]), that connects source to chamber. The bend of the fill position has a small hole of 5 mm diameter with an stainless steel insert. Via this hole a small amount of UCN can fall into the detector. This allows to monitor the UCN flux during the filling.

2. *Monitor*, a similar 90 degree downwards bend, that connects source to detector.

3. *Empty*, a straight glass guide also coated with NiV, that connects precession chamber to detector.

Initially it was planned to have a fourth position (the *Test* position) that would connect the source to the backside of the switch. This would give the possibility to have another experiment connected to the same beam port of the source as the nEDM-experiment. As the place for such an experiment is very limited, this guide was removed from the switch to allow better vacuum pumping.

Aluminum inserts are used for the transition between the glass guides that connect to the switch and have a straight edge, and the movable guide pieces, that have a curved edge to match the rotating moving disc they are mounted on. These inserts are coated with NiMo and can be adjusted to minimize slits between the fixed and movable parts of the switch.

The switch is driven by four non-magnetic vacuum compatible piezo motors (Nanomotion HR2). A relative encoder with an index position (MicroE Mercury 1000V) and a motor controller card (Galil DMC-1816) operating in closed loop PID[11] feedback, control these motors. A careful tuning of a set of parameters improved speed and precision of the movement as seen in Fig. 2.17.

As the encoder only detects relative motions it is important to zero it using the index position. The motor controller card has an automatic procedure to do that. In addition an optical setup using a webcam and a window can be used to check the correct zero position by verifying the alignment of a marking in the window and a marking on a mirror on the rotational disc in the *Visual Check* position.

In 2012 transmission and storage properties of the switch were measured in a dedicated setup using unpolarized UCN. All measurements were done

[11] proportional integral derivative

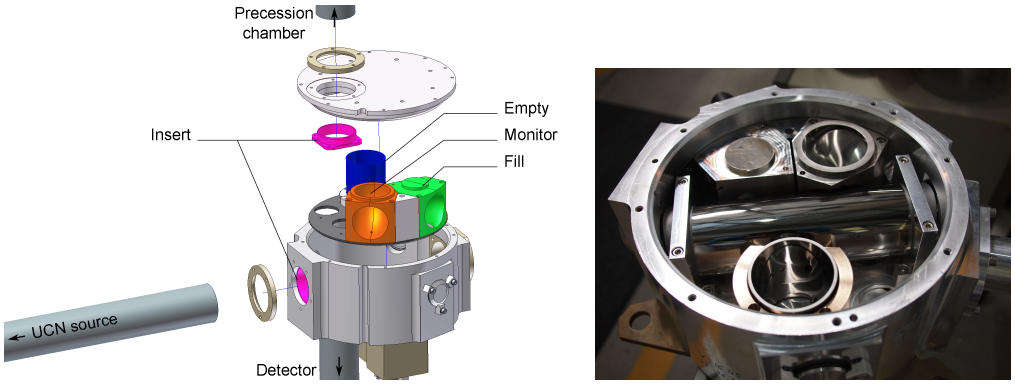

(a) (b)

Figure 2.16: Drawing of the switch (a). The different guide pieces as well as the inserts are visible. The picture of the switch (b) shows the open device with the *Test* guide piece still installed. This was abandoned later for better pumping properties.

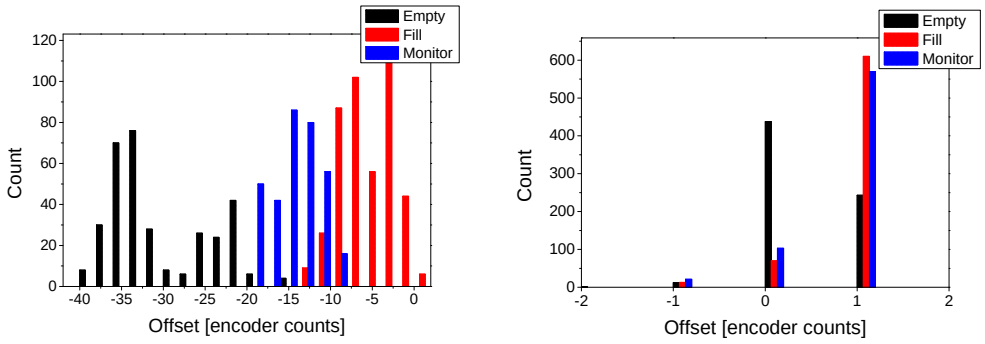

(a) 2011 (b) 2012

Figure 2.17: Position accuracy of the switch in 2011 (a) and after optimization of the PID parameters of the motor controller in 2012 (b). With correctly tuned PID values the positioning is as good as ± 1 encoder count corresponding to about ±0.95 mrad or ±0.13 mm for the fill and monitor and ±0.09 mm for the empty position.

Position	Transmission
Fill	0.675±0.008
Monitor	0.654±0.041
Empty	0.809±0.005

Table 2.2: Transmission of the switch in different positions. The errors are purely from counting statistics.

on the WEST 1 beam line of the UCN source using a ^{10}B-based Cascade detector. The following two paragraphs have been also presented in [BKGS$^+$12].

Transmission properties The transmission of the switch affects the filling and emptying time as well as the density of UCN in the precession chamber. The transmission T of the different switch positions was measured as a ratio $T = {}^{N_\mathrm{s}}/_{N_0}$ with N_s the neutron counts, integrated over the period of $1 - 400\,\mathrm{s}$ after the proton pulse, with the switch in the respective position and N_0, the integrated neutron counts without switch. The transmission values obtained (Tab. 2.2) are lower than one would expect, as NiMo glass guides have been measured to have a transmission of $0.98\,\mathrm{m}^{-1}$ [Göl12]. This is especially true for the *Empty* position, which is straight and consists of only one NiMo-coated 100 mm long glass guide and two short NiMo-coated aluminum inserts, 20 mm and 35 mm in length. After these measurements the inserts, which account for almost 50 % of the guiding surface, have been polished and reacoated with NiMo. This might have improved the transmission properties of the switch but is was not possible to repeat the measurement due to a lack of time.

Storage properties The storage properties of the *Empty* position are of special interest, as during the emptying of the UCN at the end of a cycle, this position is part of the storage volume. For the measurements the slits between inserts and guides, needed to move the switch, were reduced to almost zero. In this condition it is not possible to rotate the switch. However, the result obtained this way is more likely to describe the quality of the coating and not the size of the slits.

The storage time was measured for several different variations of the setup depicted in Fig. 2.18, including and excluding the switch in *Empty* position, and with or without the insert in the top lid. Each of the assembled volumes was filled with UCN (both shutters open). When the highest density was reached, both shutters were closed and neutrons were stored inside the volume

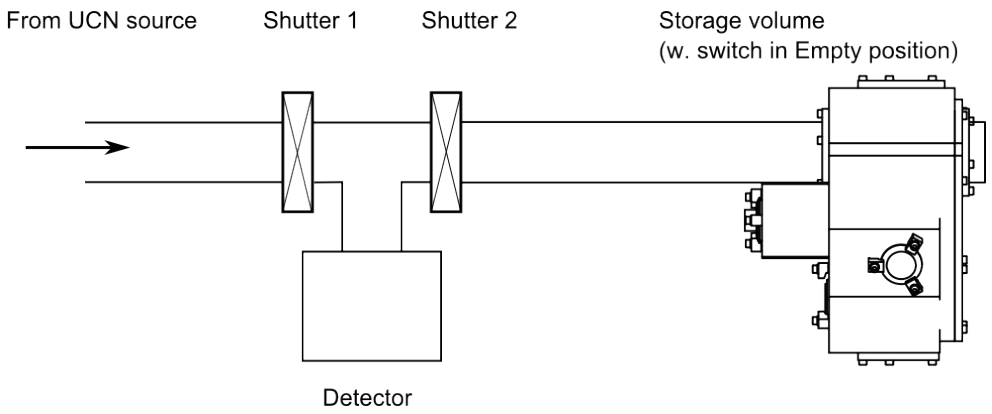

Figure 2.18: Setup to measure the storage properties of the switch, consisting of two shutters, a detector and a storage volume. The latter was always composed of a 1000 mm stainless steel tube with 66 mm inner diameter, a 300 mm long NiMo coated glass tube with 73 mm inner diameter and a stainless steel plug that served as mirror. The storage time was measured with and without the switch in empty position in between the glass tube and the plug.

behind shutter 2. After different storage times, shutter 2 was opened and the neutrons were released into the detector. The count rate in the detector during the filling period was used to normalize the stored neutrons for each cycle.

In Tab. 2.3 the loss per bounce $\mu = \frac{\lambda}{\overline{v}\tau}$ has been calculated using a mean free path $\lambda = \frac{4V}{S}$ of a UCN in the storage volume V with a surface S and a mean velocity of $\overline{v} = 4\,\mathrm{m\,s^{-1}}$. From these numbers one can also estimate the loss per bounce in the switch alone. As the total loss rate $\Gamma = \frac{1}{\tau}$ is given by

$$\begin{aligned}\Gamma_{\mathrm{tot}} &= \Gamma_{\mathrm{filling-guide}} + \Gamma_{\mathrm{switch}} \\ &= \mu_{\mathrm{filling-guide}} \frac{\overline{v}}{\lambda_{\mathrm{filling-guide}}} \eta_{\mathrm{filling-guide}} \\ &\quad + \mu_{\mathrm{switch}} \frac{\overline{v}}{\lambda_{\mathrm{switch}}} \eta_{\mathrm{switch}} \end{aligned} \tag{2.10}$$

with a weighting factor η_{Surface} which is the probability for a UCN to bounce in the switch or in the filling guide. η_{Surface} can be estimated with the ratio of the surfaces in question to the total surface. As $\mu_{\mathrm{filling-guide}}$ has been measured in the setup without switch, the only unknown is μ_{switch}. This result shows that the loss per bounce in the switch is about a factor of four higher than in a standard stainless steel / glass guide combination. Assigning this additional losses to gaps in the switch, one would need a gap of about

Storage volume	λ (mm)	τ (s)	$\mu_{\text{total}} \times 10^{-3}$	$\mu_{\text{switch}} \times 10^{-3}$
filling-guide	135.3	11.2(2)	3.02(5)	
add switch (both inserts)	136.4	8.6(2)	3.97(9)	11.7(9)
add switch (one insert)	136.2	9.3(2)	3.66(8)	9.9(8)

Table 2.3: Storage time (τ) and loss per bounce (μ) assuming a mean velocity of $\overline{v} = 4\,\mathrm{m\,s^{-1}}$ for different setups. All setups always include the filling guide.

0.75 mm to explain the results. This means that the coating of the switch might have holes and should be redone.

UCN shutter

The UCN shutter closes the storage volume of the precession chamber towards the neutron guide. In the closed position it should be tight to not loose Hg or UCN, and in the open position it must have a good transmission for UCN. The shutter used during all measurements in this thesis is based on the old Sussex–RAL–ILL design. A plate with a DLC coated disc (closed) and a DLC coated brass ring (open) is moved so that either the disc or the short guide piece is aligned with the neutron guide (see Fig. 2.19(a)). To reduce gaps, the DLC coated disc is pressed against the bottom electrode in the closed position. The nonmagnetic actuator is driven by pressurized air and situated outside the vacuum tank below the experiment. A polyether ether ketone (PEEK)[12] rod and a vacuum feedthrough transmit the force to the shutter. The shutter needs about 1 s to open or close fully. Although the design of the shutter has not been changed, many of the parts in the shutter have been replaced by PEEK parts to guarantee a nonmagnetic shutter.

For the future a more advanced shutter, build fully from PEEK has been developed that closes the hole in the bottom electrode not with a simple disc, but with a plug (see Fig. 2.19(b)). This shutter needs a much more complicated mechanism, but it fills the hole in the bottom electrode to reduce systematic effects [BDG+06].

2.4.6 Precession chamber

The precession chamber is the heart of the experiment. Everything else is built around this chamber in order to create the conditions needed to perform a high precision measurement inside. The precession chamber stores

[12] A high performance plastic with good mechanical properties.

(a) (b)

Figure 2.19: A close up view from above of the two existing UCN shutter systems mounted to the electrode. (a) The shutter based on the original design of Sussex–RAL–ILL. It is shown here in a position halfway between closed (left) and open (right). (b) The newly design plug shutter in its closed position fills the opening hole inside the bottom electrode.

Figure 2.20: The precession chamber before installation into the experiment. Two corona rings are mounted onto the electrodes for high voltage performance.

the neutrons and the Hg during the period of free precession. It needs to be nonmagnetic at a very high level, and have good storage properties for UCN and Hg. It is formed by two electrodes and an insulating ring to create the electric field. The upper electrode is connected to the high voltage system (see 2.4.11) and can be charged up to ±200 kV. The lower electrode is connected to the leakage current system and has two holes: The larger one (inner diameter 73 mm) in the center is needed to fill and empty UCN, the smaller one (inner diameter 14.5 mm) is used to fill Hg into the chamber. The electrodes are separated by 120 mm with an insulator ring of 150 mm height and an inner radius of 235 mm, situated in two grooves in the electrodes. These components form a volume of $\pi r^2 h \approx 20810\,\mathrm{cm}^3$. The electrodes are made from aluminum coated with diamond like carbon (DLC) which has been proven to have good storage characteristics for UCN and Hg. The insulator ring is made from polystyrene (PS) coated with deuterated PS and was developed within the collaboration [Kuź08]. It has two UV transparent quartz windows on the side, coated with deuterated polyethylene, for the read out light beam of the Hg comagnetometer (see 2.4.9). The center of these windows is located 40 mm above the lower and 80 mm below the upper electrode.

High voltage considerations For the measurement of the electric dipole moment an electric field has to be applied to the chamber. To guarantee a good high voltage performance some design considerations have to be applied to the electrodes. This can be easily seen with the example of an isolated sphere of radius r carrying charge Q. The electric field created by such a sphere is simply given as $E(r) = \frac{1}{4\pi\epsilon_0}\frac{Q}{r}$. Therefore the smaller the radius, the larger the electric field strength at the surface. Practically this means for the design of electrodes to avoid all sharp edges and have very smooth polished surfaces. Sharp edges are avoided inside the spectrometer by the use of so-called corona rings. These are bent aluminum pieces that have large curvature and hide sharp edges. All surfaces are either polished, or in the case of the electrodes, diamond milled to have a smooth, mirror like surface. For the electrodes the connection towards the corona ring remains problematic. Due to the coating process of the electrode it is not practical to make the electrode and the corona ring from one piece. In the original Sussex–RAL–ILL design, the two pieces where welded together after the coating to avoid sharp edges. This practice however has the danger of deforming the electrodes due to the heat stress. This could result in a distorted electric field which leads to systematic effects (see 3.1.2). On the other hand, a simple screw connection does not fully shield all edges (see Fig. 2.21).

In a new developed design, the connection between the electrode and a slightly modified corona ring is moved into the groove of the insulating ring. This has the additional advantage that the two pieces can be insulated against each other and grounded separately, allowing a position sensitive (inside or outside the precession chamber) measurement of leakage currents.

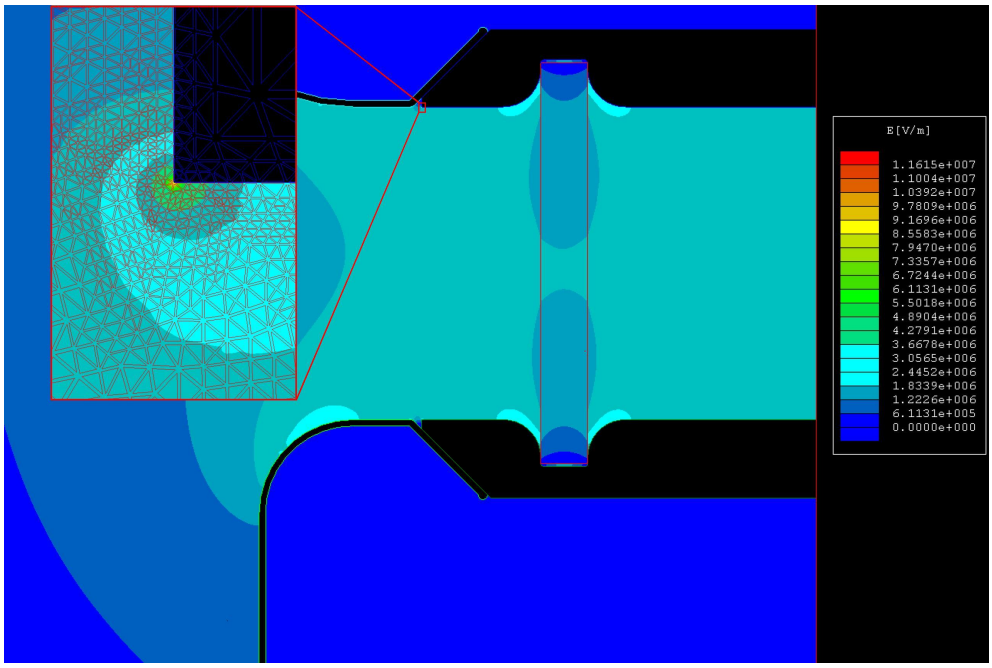

Figure 2.21: A finite element calculation (Ansoft Maxwell SV, V3.1.04) of the original design of the electrodes. In the calculation the maximum possible voltage of 200 kV was used. The transition to the corona ring had a sharp edge that leads to extremely high electric fields and promotes electric discharges. As an intermediate solution the existing electrode had been re-machined and a radius of 15 mm had been applied to the connection between corona and electrode. A new design of the interconnection of corona ring and electrode, moves this in the groove of the insulator ring.

2.4.7 Neutron detector

All detectors in particle physics are based on the creation of charge. Therefore uncharged neutrons cannot be detected directly but need to be converted. For UCN this is realized by a nuclear reaction. An appropriate isotope will capture a UCN and undergo a nuclear reaction into several charged particles that can then be detected. The detector used in the nEDM-experiment consists of nine identical units. This has the advantage that the count rate

is distributed among these units. During the direct emptying of the UCN source into the detector, up to $1.75 \times 10^5\,\mathrm{s}^{-1}$ UCN per unit are expected, which can be counted with only 6.2 % of pileup events [BKGS+10]. Each unit has a sensitive area of $28 \times 28\,\mathrm{mm}^2$ and they are arranged in a square pattern. Each single detector of the modules consists of three parts (Fig. 2.22):

1. A scintillator stack composed of a ^{6}Li depleted layer, followed by ^{6}Li enriched, layer that captures the UCN and transforms the nuclear reaction products into light.

2. A light guide that transports the light to a PMT. It also ensures that the PMT has enough distance from the permanent magnet of the spin analyzing system and matches the shape of the square scintillators to the round PMT.

3. A PMT that transforms and amplifies the light into a current signal.

The scintillator consists of a stack of 57 µm ^{6}Li depleted ($\approx 0.01\%$ ^{6}Li GS30) and 117 µm ^{6}Li enriched ($\approx 95\%$^{6}Li GS20) scintillator. ^{6}Li and neutrons react in the following process:

$$n + {}^6\mathrm{Li} \rightarrow \alpha\,(2.05\,\mathrm{MeV}) + {}^3\mathrm{H}\,(2.73\,\mathrm{MeV}). \tag{2.11}$$

UCN will pass through the depleted layer of the scintillator before they will be captured by ^{6}Li [Rog09]. Therefore the back-to-back emitted α and ^{3}H particles will deposit almost all their energy in the scintillator. This has the advantage of a better signal-to-noise separation compared to a single layer of enriched scintillator material, in which one would loose one of the two reaction products. It is important to keep in mind that the optical potential of such a scintillator, is around 100 neV [BBL+09] and that only UCN with energies above this optical potential can be efficiently detected. Due to the position of the detector 1.6 m below the storage chamber, it is guaranteed that all stored neutrons have high enough energies (see Sec. 1.4.2) to be detected. The detector is read out by a data acquisition (DAQ) system called FASTER. It is an FPGA based system developed for generic nuclear physics experiments by the University of Caen and has been tested in combination with the neutron detector to be able to handle high count rates of up to 4×10^5 counts/s [BKGS+10].

2.4.8 The neutron spin handling system

In order to measure the nedm one needs polarized neutrons, i.e. neutrons which all have their spins aligned parallel or antiparallel with respect to a

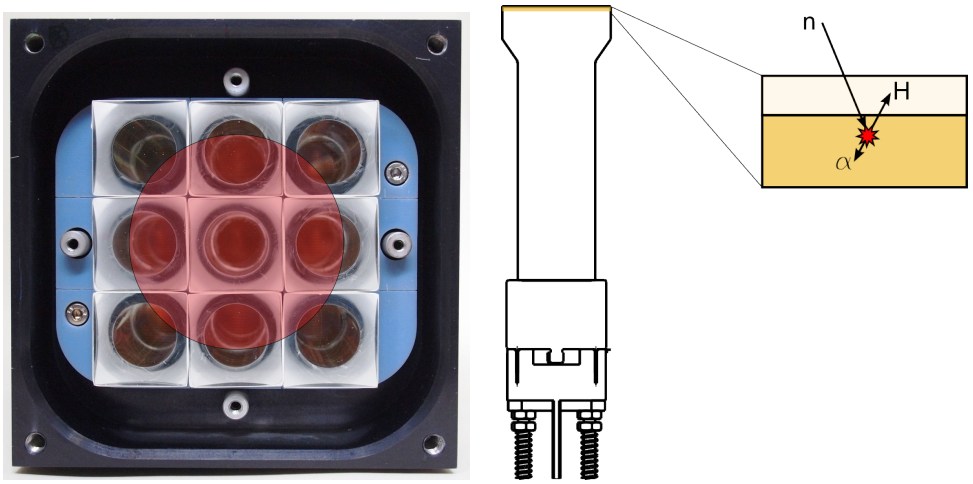

(a) (b)

Figure 2.22: (a) A face-on picture of the UCN detector. The nine individual scintillators are visible in the anodized aluminum housing. Overlaid is the diameter of the neutron guide that covers the individual segments differently. (b) A sketch of an individual detector module and the scintillator stack.

magnetic field. As the UCN source produces unpolarized neutrons, it is an important task to polarize the neutrons, keep the polarization through-out the experiment, and manipulate the orientation of the spin with regard to the holding field. This is achieved by a superconducting polarizer magnet, fast adiabatic spin flippers and an analyzing foil. To avoid loss of polarization it is also important to provide good magnetic field conditions and choose proper materials that have a low depolarization probability per bounce for all guiding surfaces.

Superconducting polarizer magnet

The first component in the south beam line coming from the source is the superconducting polarizer magnet (SCM). It consists of a superconducting solenoid and a central bore at room temperature with a diameter of $D = 221\,\mathrm{mm}$. The SCM provides a strong magnetic field that is used to polarize the UCN (see Sec. 1.4.3). The magnetic field of the SCM can be chosen to be parallel or antiparallel to the UCN beam line. It has a maximum value of 5 T corresponding to an optical potential of 300 neV or a critical velocity of 7.7 m/s in the center of the magnet (see Fig. 2.23). UCN that have a spin parallel to this magnetic field gradient will be accelerated towards the

center of the magnet, whereas UCN with the opposite spin orientation are decelerated and finally reflected from the magnetic potential if their velocity is smaller than the critical velocity. The UCN that are reflected back towards the source can be depolarized with an RF field to increase their possibility to pass the SCM in a later attempt. As the optical potential of the guides and the storage volume of the UCN source is lower than 300 neV the UCN transmitted through the SCM are nearly 100% polarized. For security reasons it is unavoidable to separate the vacuum system of the UCN source from the vacuum system of experiments permanently. This is achieved with a 100 µm thick aluminum foil in the center of the magnet which has an optical potential of about 54 neV. The transmission of one spin component through the foil is increased due to the energy boost in the center of the magnet.

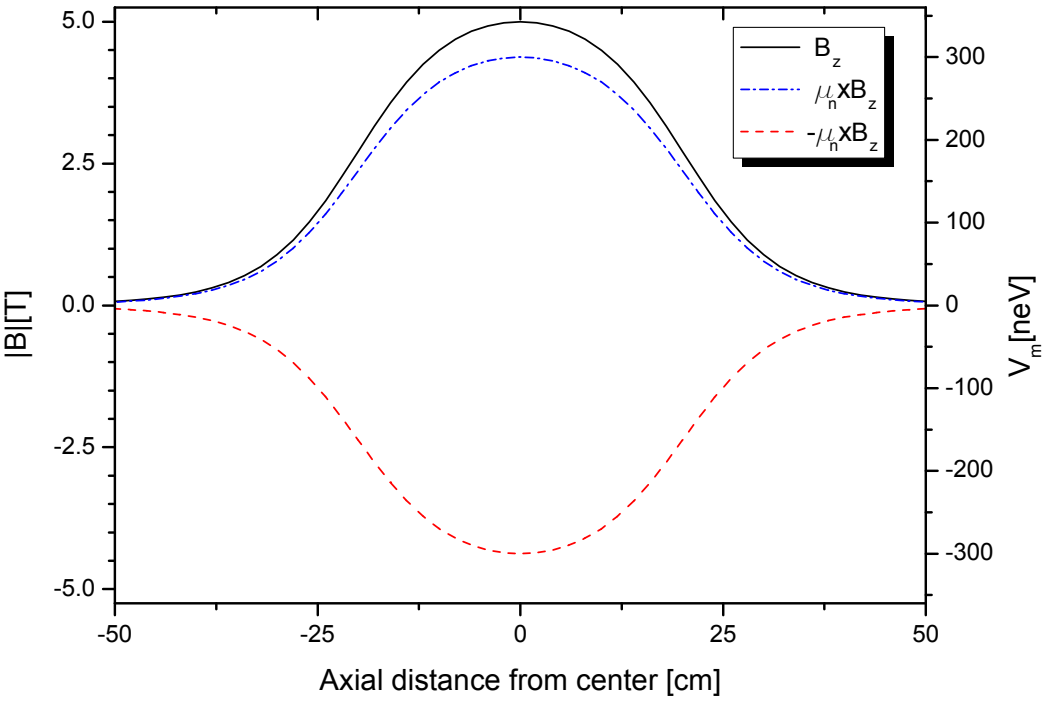

Figure 2.23: The absolute magnetic field ($\sqrt{B_x^2 + B_y^2 + B_z^2}$, solid line) in the center of the magnetic bore and the corresponding magnetic potential $V_m = \boldsymbol{\mu_n} \times \boldsymbol{B_z}$ for UCN with antiparallel (- ·) and parallel (- -) spin and magnetic field. The plot shows the simulated field as supplied from the manufacturer. Measurements of the actual field created by the magnet are in very good agreement with the simulated data [Pie12]. The aluminum foil that serves as a vacuum window is installed at 0 cm.

Guiding field

Non adiabatic field changes along the neutron guides can lead to a depolarization of UCN. The adiabaticity of a magnetic field can be described by the adiabatic parameter k. It is defined as the ratio of the Larmor precession frequency of the UCN, f_L and the change of magnetic field in the rest frame of the UCN, Ω

$$k = \frac{f_L}{\Omega} = \frac{\gamma_\mathrm{n} B^2}{dB/dt}. \tag{2.12}$$

For $k \gg 1$ the change of the field is slow enough for the neutron spin to follow the magnetic field and the neutrons will not depolarize. Equation (2.12) shows that this condition is difficult to fulfill in low fields. A set of guiding field coils is used to provide a magnetic field suitable to keep the polarization of the UCN on their way from the SCM to the precession chamber. The guiding field is descriped in greater detail in [Pie12].

Main field coil and correction coils

Main magnetic field The main magnetic field (B_0) is aligned along the z-axis of the experiment. It needs to be homogeneous over the volume of the precession chamber ($\Delta \mathrm{B}/B_0 \leq 10^{-3}$) in order to keep the polarization of the stored UCN. The B_0 field is created by a cosine-theta coil wound around the vacuum tank (see Fig. 2.24) and is largely enhanced due to the innermost magnetic shield layer. A current of about 17 mA creates the magnetic field of $B_0 \approx 1\,\mu\mathrm{T}$ inside the tank.

The current is provided by a highly stable power supply. To avoid current drifts originating in temperature changes of the power supply, it is installed in a massive aluminum container which is situated in a thermally insulated box (see Fig. 2.25). The aluminum also reduces any influence of electro-magnetic noise on the source. The typical relative current fluctuations of the source at 1000 s are around 4×10^{-7}, which corresponds to a magnetic field change of about 400 fT.

Correction coils The vacuum tank and the magnetic shield cannot be perfectly symmetric with respect to the precession chamber. First, holes are needed for the UCN guide, the high voltage feedthrough, etc. Second, the permeability of the shield is not necessarily homogeneous all over its surface. Therefore the magnetic field created by the main coil cannot be ideal. In addition to the B_0-coil, 33 correction coils are placed on the vacuum tank to correct for inhomogeneities. There are in general four classes of correction coils labeled with three letter acronyms:

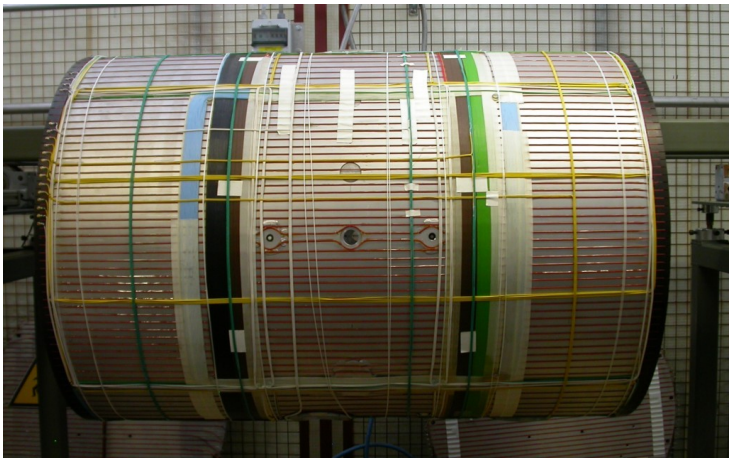

Figure 2.24: A side view of the vacuum tank with the cosine-theta coil (red) and some of the correction coils before its re-installation into the magnetic shield at PSI.

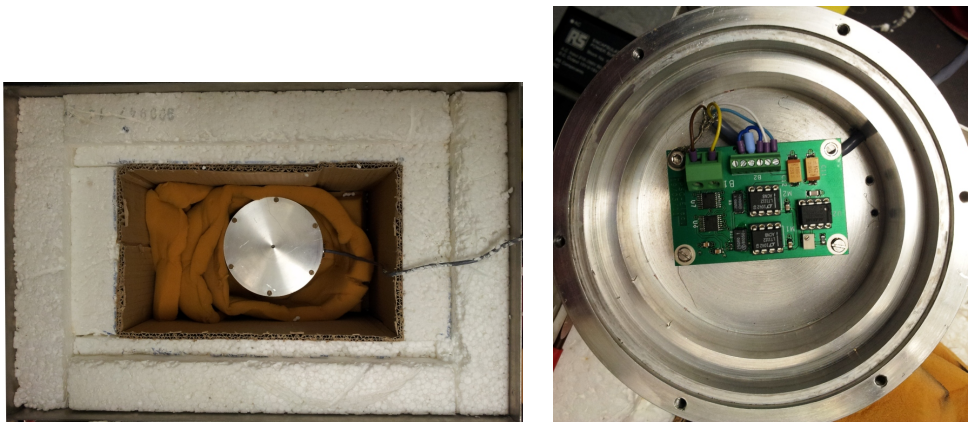

(a) (b)

Figure 2.25: (a) The aluminum block (diameter = 124.5 mm) containing the B_0-power supply inside the thermal insulation. (b) Close up of the power supply within its shielding. The wall thickness of the aluminum is 18 mm at the top and the sides and 55 mm at the bottom.

1. Chimney coils (X X K): Small solenoids inside the holes of the shield needed for inserting the feedthrough for high voltage, the mercury and the UCN.

2. Transversal coils (T X X): Saddle coils wrapped transversally around the vacuum tank, with a dimension of $(500-550)\,\mathrm{mm} \times 860\,\mathrm{mm}$. There are in total 12 of these coils, three on the top, bottom, left and right side of the tank each.

3. Axial coils (A X X): Saddle coils wrapped axially along the vacuum tank, with a dimension of $(300-305)\,\mathrm{mm} \times 1530\,\mathrm{mm}$. There are again 12 coils, three on the top, bottom, left and right side of the tank each.

4. Helmholtz-like coils (H X X): Three Helmholtz like coil pairs at $\pm 150\,\mathrm{mm}$, $\pm 300\,\mathrm{mm}$, and $\pm 550\,\mathrm{mm}$

Further information about the correction coils can be found in [Qué09]. All these coils are powered by bi-polar temperature stabilized power supplies able to deliver up to $\pm 196\,\mathrm{mA}$ of current. The Allan standard deviation (ASD) [AWJ91] of the power supplies is generally of the order of 10^{-5} at around 1000 s (see Fig. 2.26) which at a typical field of $B = 10\,\mathrm{nT}$ created by the correction coils, translates to a magnetic field stability of 100 fT.

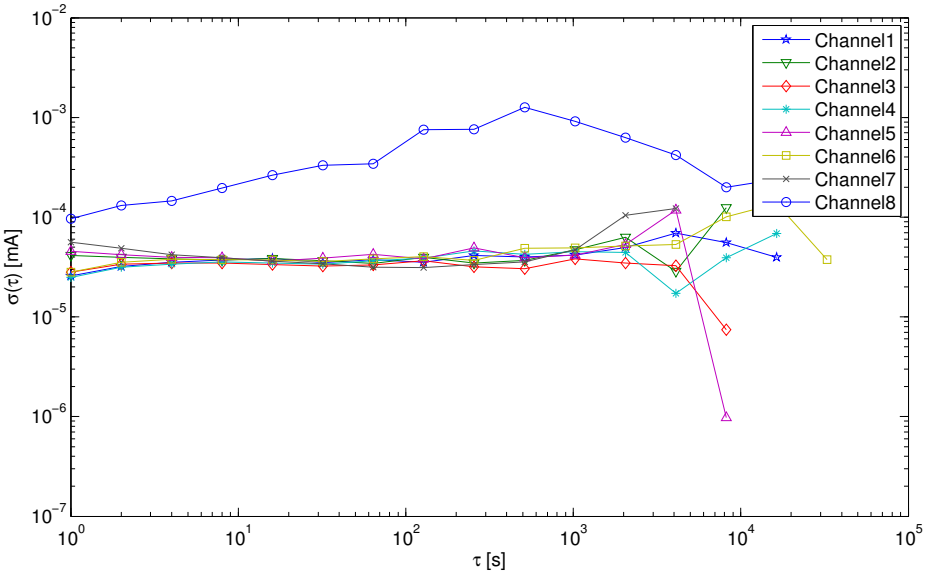

Figure 2.26: Allan standard deviation (ASD) of all eight channels of one of the correction coil power supplies. Measured at 20 mA current with a 11 Ω resistor.

Spin analyzer

To measure the polarization at the end of a cycle a spin analyzing system is used, that is situated between the switch and the detector. It consists of a spin flipper and a 25 µm thick aluminum foil coated with 400 nm of iron in a strong magnetic field created by permanent magnets and an iron yoke.

The iron coated aluminum foil inside the magnetic field of a permanent magnet operates in a way similar to the SCM polarizer, but can be realized in a much more compact way than a superconducting magnet. The downside is a lower field and thus a lower efficiency, although the iron foil used has been measured to have a polarization of 96% [BKGS+12]. The permanent magnet is creating a magnetic field to saturate the iron layer. Thus, during the emptying period the UCN will see a spin dependent optical potential $V = V_{\mathrm{Fe}} \pm \mu_{\mathrm{n}} B$ of $V_{\uparrow\uparrow} = (351 \pm 14)\,\mathrm{neV}$ and $V_{\uparrow\downarrow} = (72 \pm 8)\,\mathrm{neV}$ [ABD+07] respectively for parallel and antiparallel alignment of spin and magnetic field in the iron.

Sequential spin counting For sensitivity reasons, a nedm measurement is performed at a point of the Ramsey curve where an almost equal number of N_{up} and N_{down} will be detected at the end of the cycle (see Sec. 2.1.2). However only one spin state (N_{up}) is able to penetrate the analyzer foil. Thus a fast adiabatic spin flipper is installed above this foil. The working principle of such a device can be found e.g. in [KGR+03]. By turning the spin flipper on and off, one spin state can be counted in the detector while the other is stored above the analyzer foil. For all data presented in this thesis this sequential counting method was applied.

Simultaneous spin counting The UCN spin state that is not counted during a part of the sequential counting is stored in the volume formed by the precession chamber, the vertical guide, the switch and the analyzer foil. The time constant for losses in this volume was measured to be about 20 s [BKGS+12] resulting in large losses during the spin counting sequence. By adding a second analyzing system (iron coated foil, magnet, spin flipper) as well as a second detector in parallel to the first one, both spin states can be detected simultaneously if the two channels are in opposite state. This would have the advantage, that less UCN will be lost during the storage and would increase the total number of counted UCN. Such a simultaneous spin detector is currently under development [Helon].

2.4.9 Mercury comagnetometer

The nEDM-experiment uses several magnetometer systems to monitor the magnetic field. This is important as several cycles are needed to extract the precession frequency of the neutron with a fit (see Sec. 2.1.1). Any random change of the magnetic field over time will thus reduce the performance of the UCN magnetometer. Moreover a magnetic field change correlated with the electric field directions will influence the measurement of the electric dipole moment systematically (see Sec. 3). Therefore the Sussex–RAL–ILL collaboration had used a mercury magnetometer (Hg comagnetometer)[13]. In [GHI+98] a detailed explanation of the system can be found. Only a brief summary of the most important points will be given here. The working principle and all components of the magnetometer are illustrated in Fig. 2.27.

The magnetometer uses ^{199}Hg that is polarized using the optical pumping technique. This is achieved by illuminating Hg vapor in a small storage container, the polarizing chamber, with circular polarized light from a ^{204}Hg discharge lamp. The polarizing chamber is situated in the B_0 field underneath the bottom electrode. Once polarized, the ^{199}Hg is filled into the precession chamber after the UCN shutter has been closed. A rotating magnetic field in the plane normal to the main magnetic field at the Larmor frequency of the Hg is used to apply a $\pi/2$ spin flip, so that the Hg precesses around the main magnetic field with $\omega_L \approx 7.8\,\mathrm{Hz}$ in the $1\,\mu\mathrm{T}$ magnetic field. A circularly polarized readout light beam from a second ^{204}Hg discharge lamp shines through UV transparent quartz windows in the vacuum tank and the precession chamber and its intensity is measured with a photomultiplier tube (PMT). From the DC and AC signal measured on this PMT one can extract the important performance parameters of the magnetometer:

- The amount of mercury in the precession chamber is determined by the difference of the DC signal before the filling of Hg and after the filling but before the spin flip, as the light intensity drops exponentially with the number of Hg atoms. It is therefore referred to as absorption (A).

- The absorption cross section for polarized light depends on the relative angle of the Hg polarization (P) and light polarization. Thus the PMT will measure a sinusoidal signal. From the frequency the mean magnetic field as seen by the Hg can be determined. The signal will decay as the

[13] As the mercury is precessing in the same volume as the UCN it is often referred to as cohabiting magnetometer or simply comagnetometer.

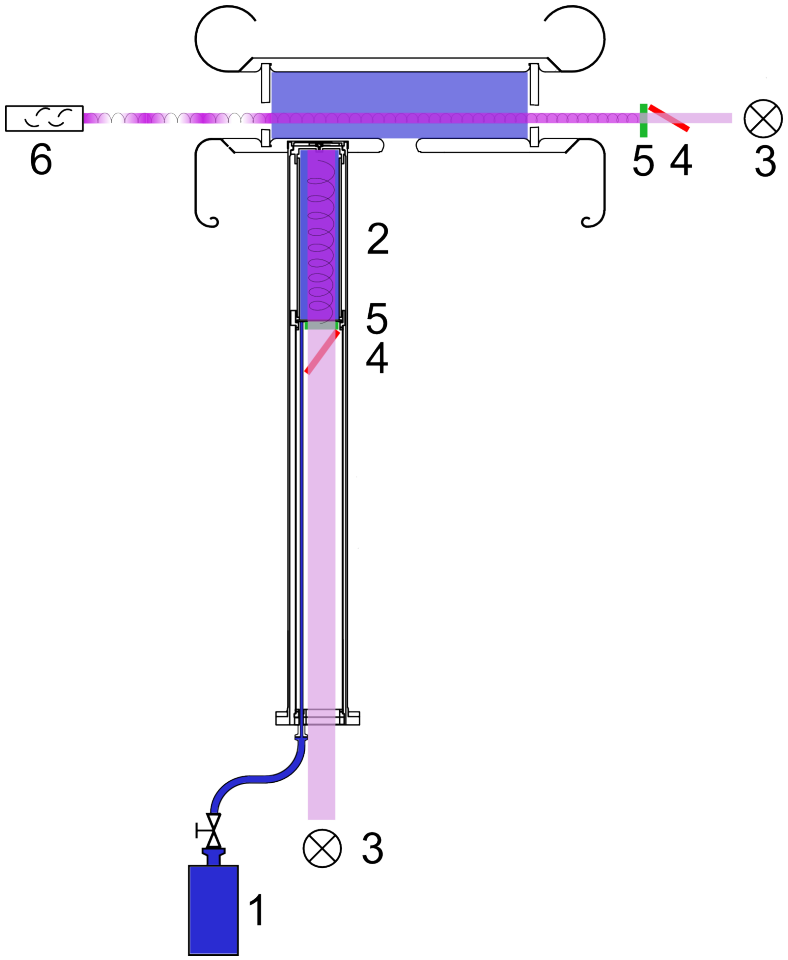

Figure 2.27: Sketch of the ^{199}Hg cohabiting magnetometer and its components: ^{199}Hg is produced by heating metallic Hg or HgO in the source container (1) and is filled into the polarizing chamber (2). A ^{204}Hg discharge lamp (3) powered by a microwave generator together with a thin film polarizer (4) and a quarter wave plate (5) produce circularly polarized light that is used to optically pump the Hg in the polarizing chamber. At the beginning of a measuring cycle the polarized ^{199}Hg is filled into the precession chamber. A rotating magnetic field is applied to spin flip the mercury. A second ^{204}Hg discharge lamp, polarizer, and quarter wave plate are used to create the readout beam, that is send through the chamber. A photomultiplier tube (6) detects the spin dependent absorption of the precessing ^{199}Hg.

Hg depolarizes with the time constant $T2$[14] and can be described by $I = I_0 \times \exp\left(\frac{-t}{T2}\right) \times \sin\left(f_{\mathrm{L}} \times t + \Phi\right)$.

- The (initial) polarization is estimated from the amplitude of this signal.
- The tightness of the chamber for Hg is estimated by the change of the DC level over the length of the precession time of the Hg. This value is called leakage time t_L and is a good indicator of the correct assembly of the chamber, and the proper function of the UCN and Hg shutters.

An example of a Hg signal as seen on the PMT is given in Figure 2.28. The sensitivity of this measurement depends on the signal (a_{s}), which is the product of P and A, to noise (a_{n}) ratio of the precession signal, the length of the free precession time (T) and on the signal decay time τ_{Hg} that is a combination of the $T2$ time and the leakage time t_L as $\frac{1}{\tau_{\mathrm{Hg}}} = \frac{1}{T2} + \frac{1}{t_L}$. Some parameters like P and τ_{Hg} are correlated with the amount of mercury in the polarizing/precession chamber (Fig. 2.29).

The sensitivity of the magnetometer can thus be tuned via the absorption. The temperature of the mercury source defines the production rate of ^{199}Hg and together with the cycle length also the absorption.

2.4.10 Cesium magnetometers

In addition to the Hg comagnetometer an array of optically pumped cesium magnetometers (CsM) is used to monitor the magnetic field at several points above and below the precession chamber. This allows us to measure the vertical gradient of the magnetic field across the precession chamber which is an important parameter for several systematic effects like the uncompensated B-drift (see Sec. 3.1.5). Details of the working principle can be found in [Grö05] and only a short description will be given here.

The magnetic and optical properties of ^{133}Cs are defined by its unpaired electron and allow to measure a magnetic field. The working principle is similar to the Hg comagnetometer system. But whereas the Hg comagnetometer produces a free induction decay of a precession signal, the CsM can be compared to a driven oscillator. ^{133}Cs in a glass bulb of 2 cm diameter is optically pumped using circular polarized laser light that traverses the bulb under an angle of $\pi/4$ with respect to the quantization axes given by the magnetic field. This creates a net magnetization along

[14] The so called transverse relaxation time, that describes the depolarization of the magnetization perpendicular to the holding field. The relaxation of the magnetization along the magnetic field is called longitudinal depolarization time and denoted as $T1$.

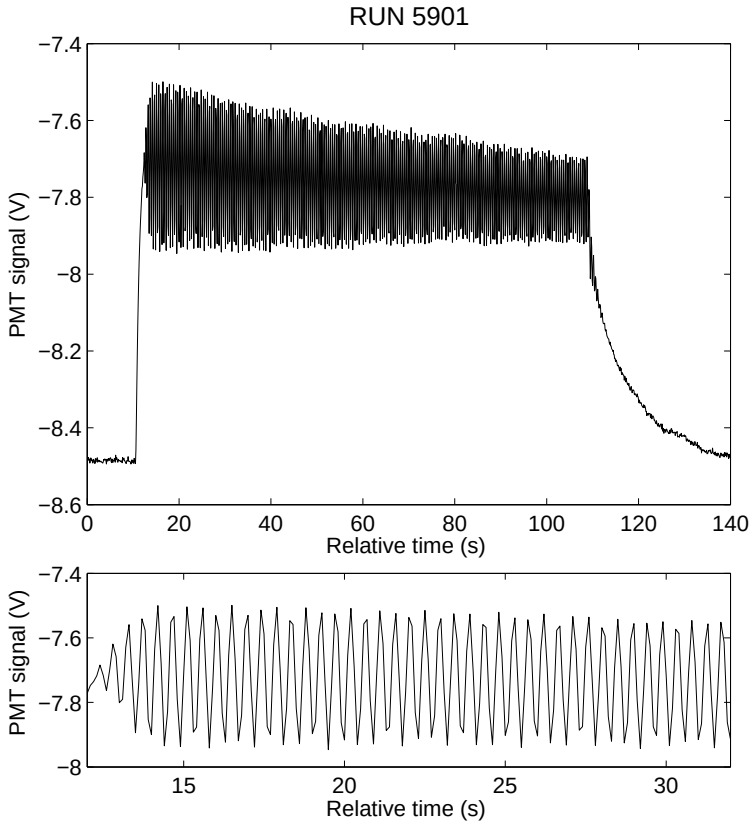

Figure 2.28: A typical Hg signal as seen on the PMT. This data was not recorded with the usual DAQ but with a NI-4070 DMM sampling with only 10 Hz.

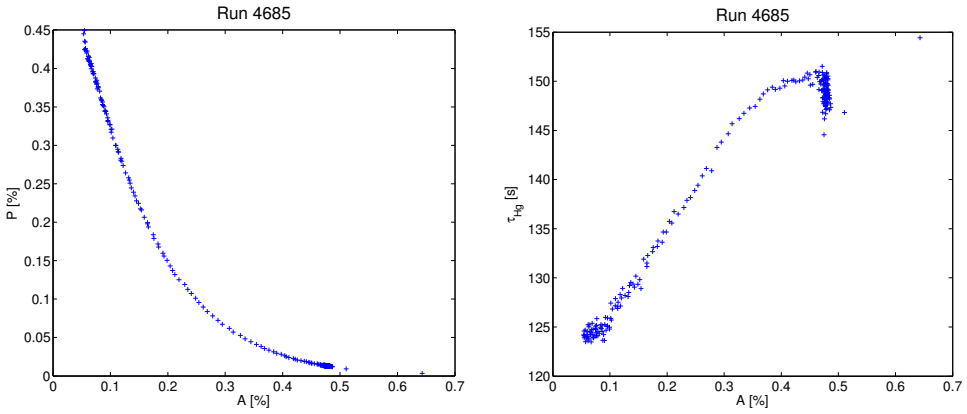

(a) P vs. A (b) τ_{Hg} vs. A

Figure 2.29: Performance of the ^{199}Hg as a function of the absorption A (the amount of Hg in the precession chamber). There is a clear dependence on the polarization P (a) and the τ_{Hg}-time (b).

the light beam. A small radio frequency (RF) field $B_1(t) = B_1 \sin(f_{\mathrm{RF}} t)$ is used to spin flip the ensemble of polarized atoms, so that the Cs starts to precess around the magnetic field B_0 with the driving frequency ω_{RF}. The precession will change the projection of the polarization onto the light vector and therefore lead to a modulated transmission of light. The same light beam that is used for pumping can also be used to read out the precession as the transmission through the glass bulb is measured with a photo diode. Like a classical oscillator the phase and amplitude of this signal measured with the photo diode depend on the difference between the driving frequency and the Larmor frequency $f_{\mathrm{L}} = \gamma_{\mathrm{Cs}} B_0$

$$\delta f = f_{\mathrm{RF}} - f_{\mathrm{L}}. \tag{2.13}$$

If applied on resonance ($\delta f = 0$), the phase difference $\phi \propto \arctan(\delta f)$ between the applied RF and the measured modulation is 90 ° and the amplitude of the modulation is maximal. By measuring ϕ, the magnetic field can thus be calculated.

The laser light beam and the RF-field are aligned parallel to each other to overcome the systematic effect of the so called projection phase error which leads to an artificial offset of the magnetometer reading if the magnetic field was not perfectly aligned by 45 ° to the light vector.

Laser light is brought to a total of 16 CsM that are installed in the nEDM-experiment, via a fiber splitter and 31 individual vacuum

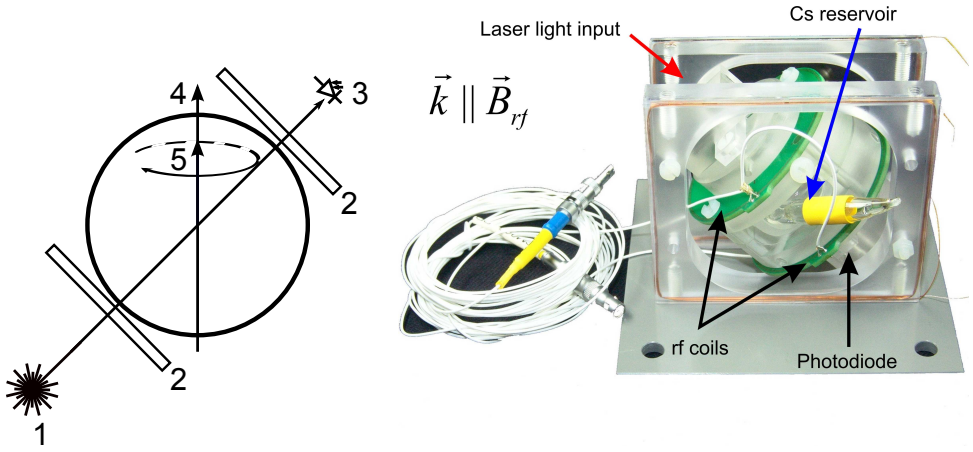

(a) (b)

Figure 2.30: (a) Working principle of a CsM. Circular polarized laser light (1) passes through a glass cell filled with ^{133}Cs vapor. Small coils (2) generate a RF-field to spin flip the magnetization (5) that has been built up by optical pumping with the laser. The precession of the magnetization around the magnetic field (4) will lead to an intensity modulation seen on the photo diode (3). By measuring the amplitude and phase relation to the RF-field the magnetic field can be determined. (b) Photograph of an opened CsM (from [BKGS+11]).

feedthroughs. Six high voltage compatible magnetometers are installed on top of the high voltage electrode. These magnetometers are connected to the electronics purely by optical fibers and the edges of their aluminum housing are shielded with an additional corona plate fixed at the high voltage feedthrough. Ten CsM are installed below the bottom electrode: Usually eight CsM are mounted directly underneath the electrode, and two CsM are screwed onto the bottom plate of these (see Fig. 3.7 for an example). The horizontal distance between the center of the glass bulb containing the ^{133}Cs of the high voltage and the ground CsM is 226 mm for the CsM installed directly under the electrode and 301 mm for the CsM that are installed below each other.

A typical performance of the CsM is shown in Fig. 2.31. The data was collected in December 2012 following the nedm data taking. At 1000 s the Allan standard deviation (ASD) of individual sensors is around 10^{-2} nT, while the ASD of the gradient is lower than $\frac{10^{-3}}{22.6}$ nTcm^{-1}.

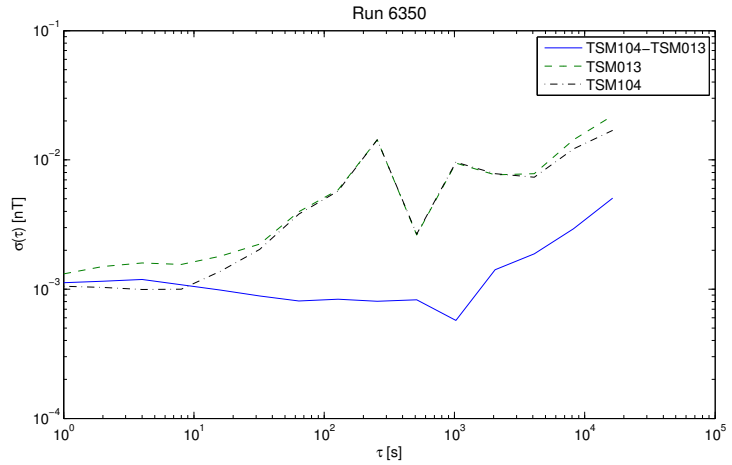

Figure 2.31: ASD of an example pair of CsM. The measurement was performed with a μTimer (see Sec. 2.3.1) where no mechanical action was applied, but with a constant change of the high voltage to measure the systematic effect of uncompensated field drifts.

Offset Although the ASD in Fig. 2.31 shows that relative measurements with the CsM are precise, the absolute value might suffer from systematic effects due to e.g. electronic phase offsets. Comparing the measurements of the CsM in the driven mode explained above, with measurements in a pulsed

mode[15] have shown that offsets of $\mathcal{O}(10\,\mathrm{pT})$ can be expected.

2.4.11 High voltage system

The high voltage (HV) system of the experiment consists of a high voltage power supply, an 1 MΩ resistance, a high voltage vacuum feedthrough, and a leakage current measuring device. A scheme of the electrical layout is shown in Fig. 2.32.

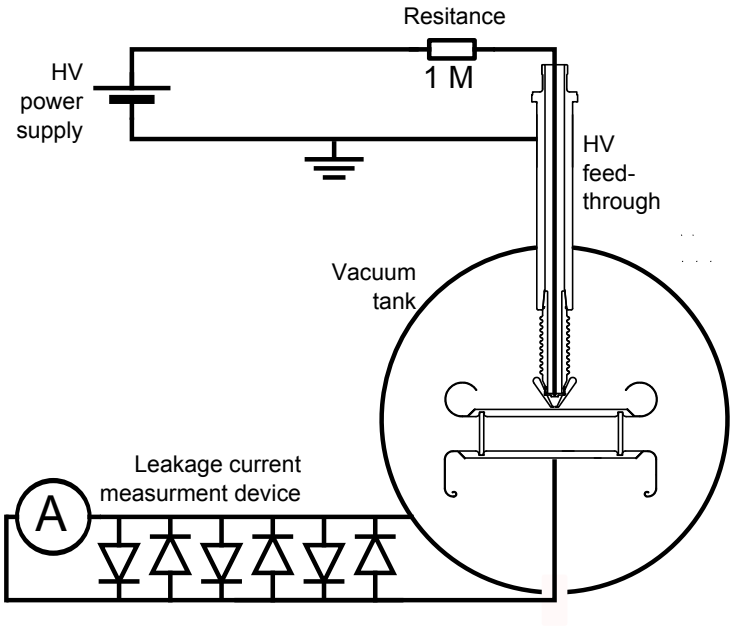

Figure 2.32: Scheme of the HV system that is used to create the electric field in the experiment.

The return path of the current during charging of the electrodes as well as during discharges is of great importance. No closed current loops around the shield should be formed in order to minimize the magnetization that can lead to systematic effects (see Sec. 3.1.5). Also an uncontrolled current during a sudden electric breakthrough can influence and damage electronic components of the experiment. Therefore it is of great importance to have a proper grounding scheme and a controlled flow of all currents. The vacuum tank and the outer hull of the feedthrough serves as ground line and are

[15] In this mode a RF pulse is applied only for a short time ($\mathcal{O}(1\,\mathrm{ms})$) and the decaying free precession signal of the ^{133}Cs is measured. This avoids a whole class of systematic effects related to the PID driven RF feedback in the normal mode, but also needs larger RF amplitudes, which make it unattractive during an nedm measurement.

insulated from the rest of the system. This is achieved by adding insulating pieces in all parts that connect the vacuum tank to the rest of the experiment like neutron guides, magnetometer systems, vacuum connections, etc.

High voltage power supply

A high voltage power supply is needed to create an electric field for the measurement of the electric dipole moment. The old high voltage power supply used at ILL was a mono-polar Cockcroft-Walton generator. It was replaced in 2010 with a modern bipolar high voltage power supply (FUG HCB 40M-200000), which can deliver up to $\pm 200\,\mathrm{kV}$ at a maximum current of $200\,\mu\mathrm{A}$. The maximum ramping speed of the power supply is $1\,\mathrm{kV}\cdot\mathrm{s}^{-1}$. It has an internal controller that can be connected with a RS232 interface to a PC. The manufacturer guarantees the stability of the power supply to be better than 2×10^{-4} over eight hours in optimal conditions (constant temperature, humidity, etc.) [FuG]. Measurements have shown that the performance of the device is actually much better (see Fig. 2.33).

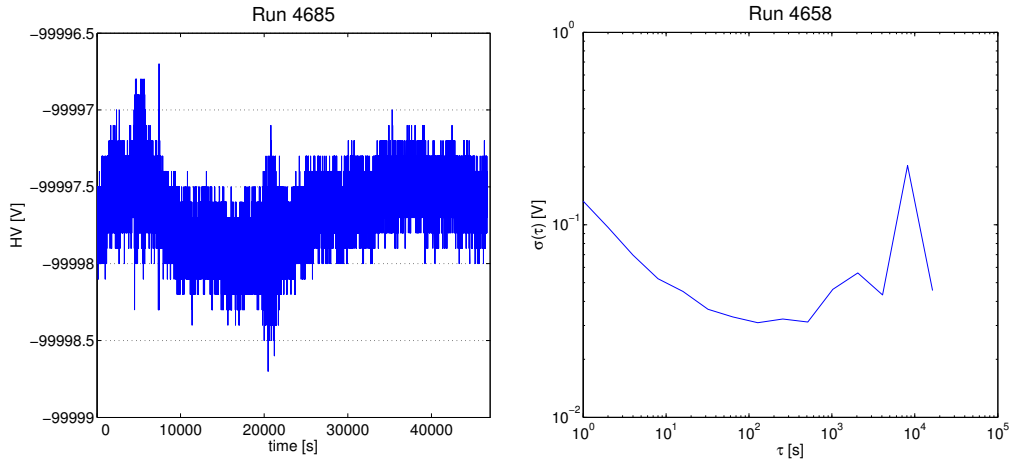

(a) (b)

Figure 2.33: Long time stability of the high voltage power supply measured over $\sim 13\,\mathrm{h}$ at $-100\,\mathrm{kV}$ (a). The corresponding ASD (b) shows that the power supply actually exceeds the specifications from the manufacturer of $10^{-4}\times 100\,\mathrm{kV} = 10\,\mathrm{V}$.

Resistor

A 1 MΩ resistor is installed close to the feedthrough. It divides the high voltage cable that has a capacitance[16] of about $100\,\mathrm{pF}\cdot\mathrm{m}^{-1}$ into a longer piece ($\sim 3\,\mathrm{m}$) from the power supply to the resistor and a shorter piece ($\sim 2\,\mathrm{m}$) from the resistor into the feedthrough. This limits the current in case of a breakthrough as the capacitance of the cable which is directly connected to the electrode is reduced.

Feedthrough

A specially designed oil-insulated vacuum feedthrough is used to charge the top electrode in vacuum (see Fig. 2.34). The main part of the feedthrough is made from aluminum. Onto a ceramic insulator with rippled surface a special non-magnetic end piece made of beryllium copper (BeCu) is glued. The interconnection of the HV - cable with this end piece had to be made with a specially designed plug. Originally, springs were used to connect the BeCu end piece with the cable on one side and the electrode on the other side, to adjust for any dimensional mismatch. A spring however is an almost perfect coil that is powered with very big currents in the case of a discharge[17]. We discovered that the magnetic fields created in the springs can actually magnetize parts of the experiment (see Fig. 5.2). On the oil-insulated side a special sliding connection has been designed to guarantee a firm connection of the HV cable to the BeCu end piece. On the vacuum side of the feedthrough a second connector has been designed to replace the previously used spring for the connection of the feedthrough with the electrodes. During the setup of the experiment the feedthrough is lowered onto the top electrode after the rest of the installation has been finalized. The electrostatic shielding of the CsM array on the top electrode makes it impossible to adjust the connection piece during the installation for the various heights of the electrode stack. A vacuum compatible non-conducting rubber hose and a sliding pin guarantee a secure contact to the electrode without interference from the outside.

Leakage current measurement

The bottom electrode is not directly connected to ground but to a leakage current measurement device. The purpose of this is to measure any leakage current that might flow during a measurement as these currents could create magnetic fields that would lead to a systematic effect (see Sec. 3.1.1).

[16] Which is quite large compared to the capacitance of the electrodes of only $\sim 37\,\mathrm{pF}$.

[17] The current for a discharge of the capacitance of 240 pF charged to 100 kV during a time of 1 µs will result in a current of 24 A.

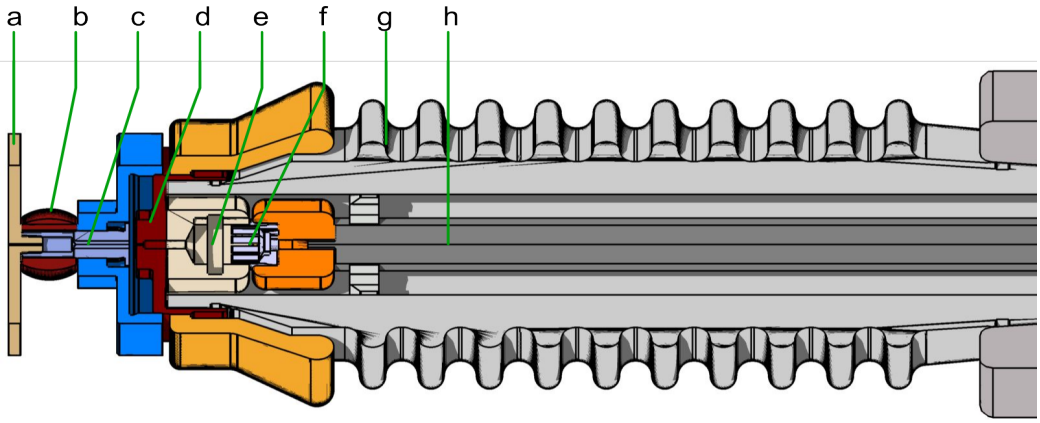

Figure 2.34: CAD image of the high voltage feedthrough. The cut shows the different connections inside the high voltage feedthrough. Between the high voltage cable (h) and the BeCu end piece (d) glued onto a ceramic insulator (g) a spring clip (f) fits firmly into a connector piece (e) that has been screwed to the end piece. On the vacuum side an aluminum plate (a) is lowered onto the electrode. A rubber tube (b) and a sliding pin (c) have replaced the previously used spring and guarantee the electrical contact to the top electrode.

The current is measured with very sensitive, customized, low noise current amplifiers (FEMTO LCA-S) with an amplification of $10^9\,\mathrm{V}\cdot\mathrm{A}^{-1}$. Their bandwidth has been reduced to DC...10 Hz and the maximum allowed input voltage was increased to prevent any damage in case of a sudden discharge of the high voltage system. To further protect the amplifier from too big currents that could destroy it, an array of ten transient voltage suppressor diodes (Diotec 5KP 12A) is installed in front of the amplifier. A 16-bit ADC (NI-USB 6210) digitizes the output signal of the amplifier and sends it via an opto-insulated USB connection to the PC (Fig. 2.35). There are two identical channels, not only for redundancy, but also to be able to determine where current is flowing using a split bottom electrode (see Sec. 2.4.6). The amplifier and the ADC have an maximum range of ±10 V which corresponds to ±10 nA. As typical charging currents of the system at $1\,\mathrm{kV}\cdot\mathrm{s}^{-1}$ are on the order of ±40 nA the system cannot measure them. The ASD of the system for a typical cycle length of 200 s is below 10 pA (Fig. 2.36). It is interesting to note, that the movement of the UCN and Hg shutter can be detected as current signals. As both of these shutters are using friction bearings a possible explanation is that the movement is creating electrostatic charge.

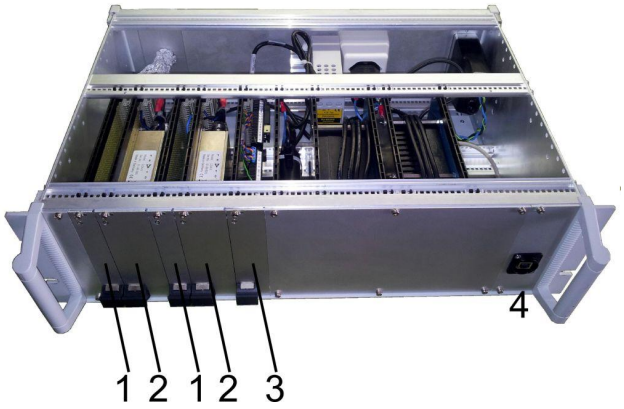

Figure 2.35: The leakage current DAQ with two channels in an electromagnetic shielded box. The amplifiers (2) are protected with an array of transient voltage suppressor diodes (1). Both channels are digitized by a 16 bit ADC (3) and transmitted via an opto-insulated USB connection (4) to a PC.

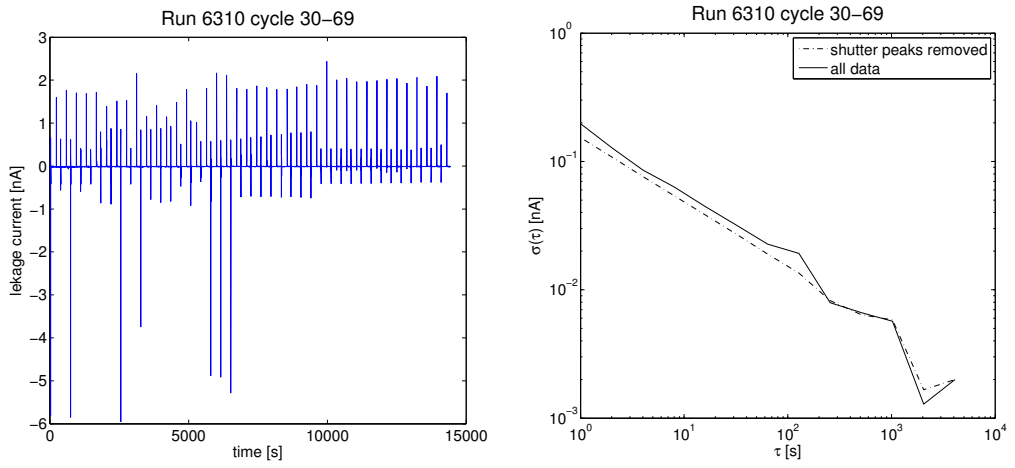

(a) (b)

Figure 2.36: Typical performance of the leakage current DAQ during an nedm run for one polarity of the electric field at $-8.3\,\mathrm{kV}\cdot\mathrm{cm}^{-1}$. In the time series (a) one can see a periodic structure of signals that is correlated with the movements of the UCN and Hg shutter. Also some small sparks up to $-6\,\mathrm{nA}$ have been measured. The ASD of this time series (b) shows an excellent performance of the device even with the shutter induced spikes, and a slightly better performance if the spikes are removed from the time series. The spikes do not appear in the time of free precession which is of interest for the later analysis.

2.4.12 Data acquisition system

The task of data acquisition is split among three computers[18], that are synchronized using a GPS based IRIG B time code and communicate via TCP/IP protocol with each other. As each computer and each subsystem creates its own data- and/or log files, a time stamp is attached to each data point to correlate the data from different data files with each other.

All systems that need to be regularly changed during a cycle/run of a nedm measurement are controlled by the main DAQ computer (nedm-zeus). The computer is running Windows 7 and is connected to the DAQ board via USB. This FPGA based board controls the UCN and Hg shutters, reads the Hg precession signal from the PMT, and produces all needed alternating magnetic fields for the different spin flippers (UCN and Hg). To adapt these spin flipping signals to magnetic field changes, the DAQ program performs an online fit of the Hg precession signal after each cycle. Nedm-zeus also controls the UCN switch, the high voltage power supply, and all pneumatic valves that are part of the vacuum system.

The UCN detector is read out by an independent computer (nedm-faster), which is running Linux. It records the binary data of all detected events and does an online analysis of the data with timing information that it receives from nedm-zeus to calculate the sum of UCN counts in each step of a cycle. The analysis result is sent to nedm-zeus.

The so-called slow control computer (nedm-mars) runs Labview under Windows 7 and controls all subsystems that have a monitoring character via a wide range of buses. Via a USB connection the Cs magnetometer electronics are configured from nedm-mars and the PC averages the magnetometer readings it receives. The currents in the correction coils and guiding field coils are adjusted from this machine and the reading of the internal current meter of the correction coil power supplies is recorded. A serial connection is also used to read the vacuum sensors and configure the electric needle valve needed to generate an O_2 or He atmosphere inside the experiment. The light output of the Hg discharge lamps used in the Hg comagnetometer is controlled via the microwave power in the cavity of these lamps. The reading of a UV sensitive photo diode measuring the intensity of these lamps is recorded. It records the data from the leakage

[18]There are some systems that are still not implemented into this scheme. This concerns the SC magnet, the laser system of the Cs magnetometers and the degaussing of the magnetic shield. These systems are usually running all the time with the same parameters.

current measurement device. The frequency standards from a Rb atomic clock and the GPS that are distributed within the experiment are logged using a frequency counter. The SFC system is controlled by nedm-mars. It reads the fluxgate magnetometers connected to PXI[19] crate and calculates from these readings the currents that the SFC power supplies should send through the SFC coils. The power supplies are connected via GPIB to nedm-mars. The ambient temperature is send via a TCP connection from an MSCB[20] node.

Each subsystem creates its own data file, usually in human readable ASCII, and the synchronization between different data files is based on timestamps, that are using the IRIG B timebase. The data is stored locally on each of these machines and a backup is saved onto a Network-attached storage drive (nedm-jupiter) after the end of each run as well as once a day to a server provided by the PSI AIT where it is accessible from outside PSI to the collaboration.

A notebook running Windows 7 and Evernote is used as an electronic replacement of a paper log book. This is available online within the collaboration.

2.5 Performance and expected sensitivity

The performance of the experiment hence the sensitivity for an electric dipole moment, depends on several parameters for the different subsystems. A short overview of these parameters and their influence on the expected sensitivity will be given in this section.

2.5.1 UCN performance

The statistical sensitivity of the Ramsey cycle (2.8) is almost purely defined by the performance of UCN handling. That is the ability to fill a high density of polarized neutrons into the precession chamber, have them precess without losing them or their polarization, and finally analyze the polarization with high efficiency. As almost all of these parameters are time depended it is perspicuous to formulate (2.8) as a function of the free precession time T, with the electric field E as a parameter, and include also the number of cycle

[19]PCI eXtensions for Instrumentation
[20]Midas Slow Control Bus, developed at PSI.

repetitions M' per day and the number of measuring days n_{days} as

$$\sigma(T,E) = \frac{\hbar}{2E\alpha(T)T\sqrt{N(T)M'(T,E,n_{\text{B}},n_{\text{E}})n_{\text{days}}}}. \tag{2.14}$$

The number of repetitions per day M' does depend on the free precession time, the number of polarity changes of the electric(n_{E}) and magnetic(n_{B}) field and the time that such a polarity change takes. Making some assumptions, an optimal cycle structure for an nedm measurement can be developed as well as an estimate of the attainable sensitivity can be made.

The length of a cycle T' and the proton pulse length t_{p} The precession time is only one part of the complete cycle. Additional time is needed for filling UCN, filling Hg, spin flips, shutter operations, spin counting and pumping. This 'offset' needs to be added to the free precession time T to determine the cycle length, and therefore the repetition frequency of cycles

$$T' = T + t_{\text{offset}}. \tag{2.15}$$

The times contributing to t_{offset} are constant (see also Fig. 2.9). Taking a security margin of 10 s between cycles to allow the online analysis of UCN counts, Hg frequency fit, etc. we end up with $t_{\text{offset}} = 139\,\text{s}$.

The UCN source has a fixed duty cycle of 0.83% that has been aproved by federal authorities (see Sec. 1.4.5). In addition the maximum length of the proton beam on target is limited to 6 s due to the cryogenic system[21]. Using the Heaviside function (Θ) the proton pulse length can be formulated as a function of the cycle length T'(and therefore as a function of T using (2.15)) with the assumption that there should be no time gap between cycles:

$$t_{\text{p}}(T') = 0.0083\,T'\,\Theta(T'_{\text{max}} - T') + 6\,\text{s}\,\Theta(T' - T'_{\text{max}}), \tag{2.16}$$

with $T'_{\text{max}} = {}^{6\,\text{s}}/_{0.0083}$. The number of neutrons produced depends on the duration of the proton pulse. This will influence the initial number of UCN filled into the chamber and therefore also the number of UCN at the end of the cycle.

[21] In principle up to 8 s of proton beam on target are possible with the kicker magnet deflecting the proton pulse onto the UCN target. The cryogenic system however has proven to be slightly unstable for pulses longer than 6 s so this is the limit for operation of the source.

UCN number $N(T)$ at the end of the cycle The number of neutrons N at the end of the cycle depends on the initial density of neutrons N_0 and the storage time constant t:

1. The initial density N_0 is influenced by the filling time and the number of neutrons produced in the UCN source. For a filling time around 30 s the maximum density of neutrons is achieved. This has been measured by varying the filling time and count the neutrons after a fixed storage time. As this is a property of the geometry of the filling guide, the optimal filling time is constant. Hence the only influence on N_0 is related to the initial UCN density in the source, that scales with the length of the proton pulse and thus with the total cycle length $N_0 = N_0(t_\mathrm{p}) \stackrel{\wedge}{=} N_0(T')$.

2. The number of neutrons will decay exponentially due to loss processes (see Sec. 1.4.4) and imperfections in the storage chamber (gaps). The storage time constants t_f and t_s (see below) influence the number of neutrons after the storage time which is essentially the free precession time T.

The storage properties of UCN depend on their energy, due to the properties of the wall material (see Tab. 1.5) and the higher wall collision rate for faster neutrons. This fact is approximated by describing the storage curve for neutrons with two exponential decays for the f(ast) and the s(low) UCN

$$N(T) = N_{0,\mathrm{f}}(T')\exp\left(\frac{-T}{t_\mathrm{f}}\right) + N_{0,\mathrm{s}}(T')\exp\left(\frac{-T}{t_\mathrm{s}}\right). \tag{2.17}$$

A storage time measurement, that includes a 2 s opening of the Hg shutter to fill mercury, resulted in $N_{0,\mathrm{s}}(T') = (14741 \pm 1149)$, $N_{0,\mathrm{f}}(T') = (19041 \pm 1718)$ for $t_\mathrm{p}(T' = 480\,\mathrm{s}) = 4\,\mathrm{s}$, $t_\mathrm{f} = (35 \pm 6)\,\mathrm{s}$ and $t_\mathrm{s} = (175 \pm 13)\,\mathrm{s}$ (see Fig. 2.37).

The initial density $N_{0,\mathrm{f}}(T')$ and $N_{0,\mathrm{s}}(T')$ is assumed to scale linearly with the length of the proton pulse. This has been measured to be true when the main shutter of the UCN source (see Fig. 1.6) is not closed, in the context of a PhD thesis [Göl12]. Thus also the initial number of neutrons can be formulated as a function of T' and therefore T

$$\begin{aligned} N_{0,\mathrm{f}}(T') &= \frac{19041}{4\,\mathrm{s}}\, t_\mathrm{p}(T'), \\ N_{0,\mathrm{s}}(T') &= \frac{14741}{4\,\mathrm{s}}\, t_\mathrm{p}(T'). \end{aligned} \tag{2.18}$$

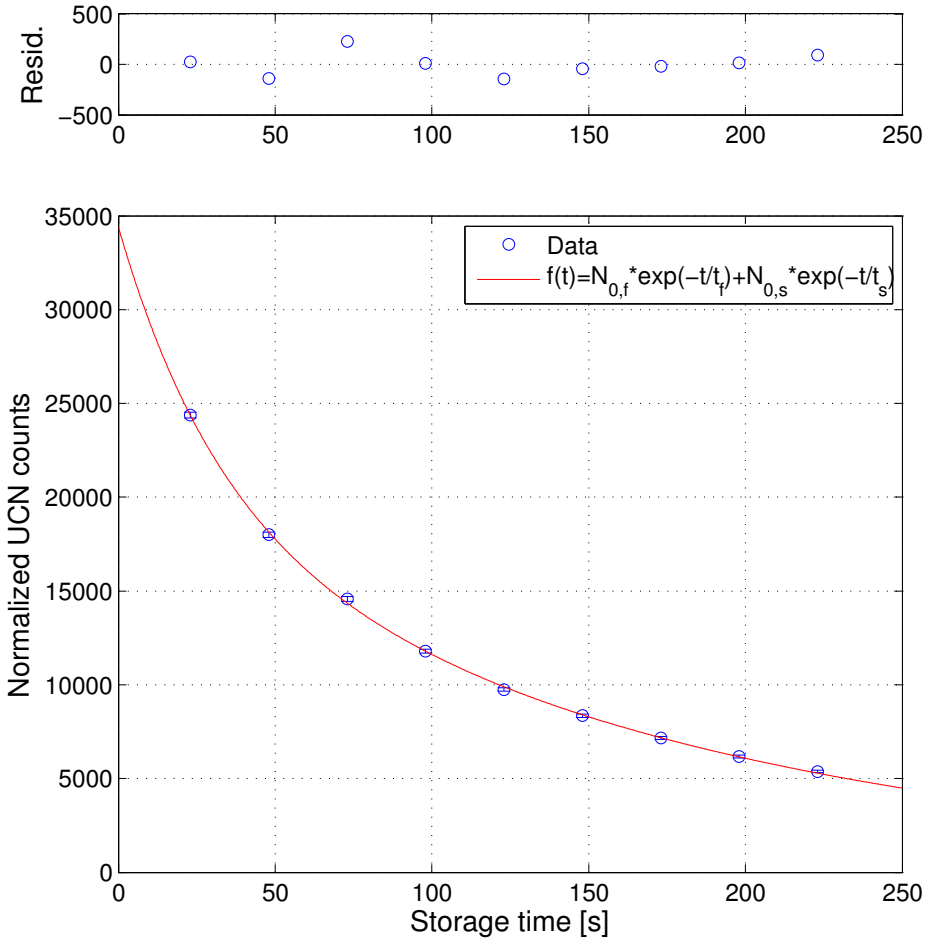

Figure 2.37: Run 5486: Measurement of the storage time for UCN in the precession chamber. The fit (χ^2/d.o.f. =6.3/5) yields $N_{0,\mathrm{f}} = (14741 \pm 1149)$ UCN, $N_{0,\mathrm{s}} = (19041 \pm 1718)$ UCN, $t_\mathrm{f} = (35 \pm 6)$ s and $t_\mathrm{s} = (175 \pm 13)$ s. The UCN counts are normalized to the monitor counts.

UCN polarization at the end of the cycle The visibility α depends on the polarization of the neutrons at the end of a cycle. The 5 T magnetic field polarizes the UCN coming from the source to $\approx 100\,\%$. For the sensitivity it is of great importance to keep as much of this polarization through out the measurement. Depolarization can occur due to bad magnetic field conditions and wall collisions. Already during the filling depolarization was observed.

The polarization loss is dominated by the transversal depolarization of the spins due to field gradients over the volume of the precession chamber. These gradients can be influenced by adjusting the correction coils (see Sec. 2.4.8). A measurement of the depolarization time (T2) for an optimized field of the correction coils and B0 up is is shown in Fig. 2.38.

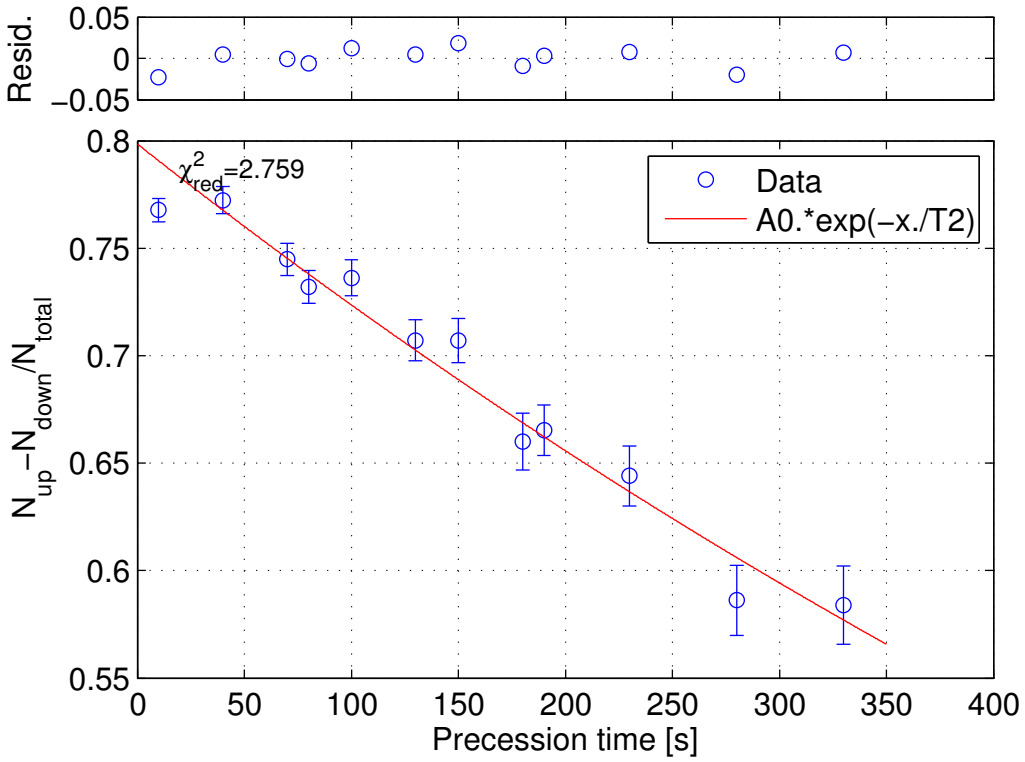

Figure 2.38: Measurement of the T2 time for UCN. Polarized neutrons are filled into the precession chamber, and a $\pi/2$ flip is applied. After a free precession time a second $\pi/2$ flip is applied in resonance with the first one and the number of spin 'up' and 'down' neutrons are measured sequentially. The T2 time determined with the fit is T2 = (1015 ± 63) s and the initial polarization (assymetry) $A_0 = -0.798 \pm 0.009$.

Cycle repetitions $M(T, E, n_\mathrm{E}, n_\mathrm{B})$ Finally the number of repetitions of cycles is important. We assume that during a day there are in average 16 h of effective measuring time (taking into account 2×2 h of SULTAN ramping up and down during weekdays, degaussing after the ramp, and encountering minor problems with operating the apparatus). This time is further reduced by the time it takes to change the electric field direction or the magnetic field configuration times the number of changes per day (n_E and n_B). The time it takes to change the magnetic field is constant and dominated by the time for degaussing including possible drifts afterwards, and assumed to be 3600 s. The time for an electric field change depends on the ramping speed of the high voltage and on the field strength. For a stable operation without (smaller) discharges, a maximum ramping speed of $0.5\,\mathrm{kV \cdot s^{-1}}$ should not be exceeded. Therefore we get for the number of cycles per day

$$\begin{aligned} M'(T, E, n_\mathrm{B}, n_\mathrm{E}) = & \lfloor \frac{16 \cdot 3600\,\mathrm{s}}{T'} \rfloor \\ & - \lfloor \frac{n_\mathrm{B}\, 3600\,\mathrm{s}}{T'} \rfloor \\ & - \lfloor \frac{n_\mathrm{E}\, 2\, E\, 12\,\mathrm{cm}}{T'\, 0.5\,\mathrm{kV \cdot s^{-1}}} \rfloor, \end{aligned} \tag{2.19}$$

and for the total number of cycles $M = n_\mathrm{days} \times M'$.

Using (2.15) to (2.19) one can estimate the total sensitivity of the apparatus as a function of the free precession time T for a given set of parameters n_days, E, n_B, and n_E. Figure 2.39 shows this plot for 10, 100, and 400 days of data taken with an electric field of $E = 8.3\,\mathrm{kV \cdot cm^{-1}}$ two changes of the magnetic field per day and three changes of the electric field for each of the magnetic field configurations.

2.5.2 Hg comagnetometer

The estimation in Sec. 2.5.1 was done under the assumption of constant magnetic field conditions and neglected the required performance of the Hg comagnetometer. As the neutron frequency is later corrected with the Hg frequency, the Hg comagnetometer should work with higher accuracy than the neutron magnetometer to not corrupt the result. The error of the corrected neutron frequency is

$$\Delta f_\mathrm{n,corr} = \left| \frac{\gamma_\mathrm{n}}{\gamma_\mathrm{Hg}} \Delta f_\mathrm{Hg} \right| + |\Delta f_\mathrm{n}|\,. \tag{2.20}$$

Here $\gamma_\mathrm{Hg}$is the gyromagnetic ratio of ^{199}Hg which is $\sim 7.59\,\mathrm{Hz \cdot \mu T^{-1}}$. With the parameters mentioned in Sec. 2.5.1, the neutron magnetometer would

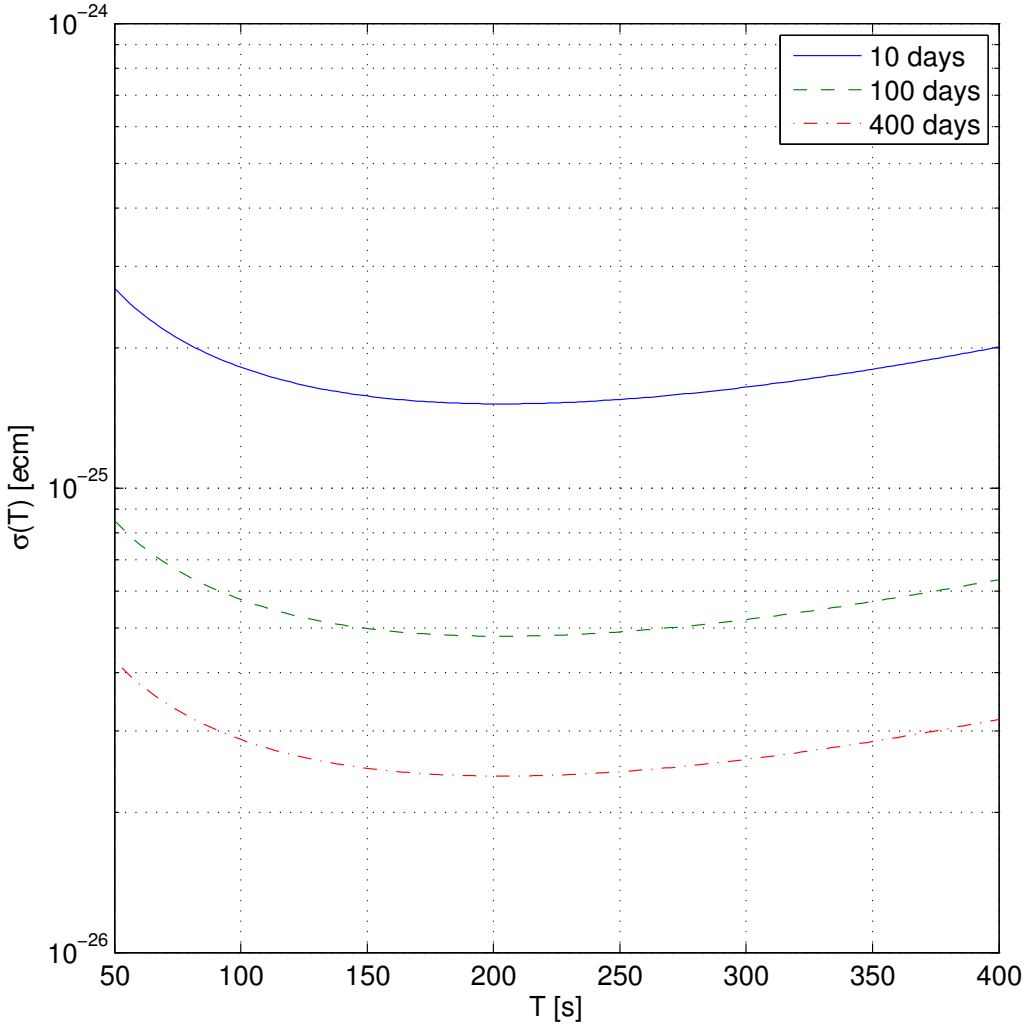

Figure 2.39: Estimated statistical sensitivity for 10, 100, and 400 days of measurement as a function of the free precession time. The electric field is assumed to be $8.3\,\mathrm{kV}\cdot\mathrm{cm}^{-1}$ and the mean $\overline{\mathrm{T2}}$ time (B_0 up and down with various gradients) is assumed to be 500 s. The maximal sensitivity is reached for a free precession time of $T \approx 200\,\mathrm{s}$.

have a sensitivity of $\Delta f_{\mathrm{n}} \approx 2.5{\times}10^{-5}\,\mathrm{Hz}$, corresponding to $\Delta B_{\mathrm{n}} \approx 0.9\,\mathrm{pT}$, per cycle. If the Hg comagnetometer performs a factor ten better, the sensitivity of the neutron result will be $\Delta f_{\mathrm{n,corr}} = |{}^{\gamma_{\mathrm{n}}}\!/_{\gamma_{\mathrm{Hg}}}\, 0.1\,\Delta f_{\mathrm{n}}| + |\Delta f_{\mathrm{n}}| \approx 3.5{\times}10^{-5}\,\mathrm{Hz}$, an increase of about 40 %. This motivates the cutting of cycles with bad Hg precision in the later analysis (see Sec. 4.3.2). The sensitivity of the Hg comagnetometer depends on various performance parameters described in Sec.2.4.9. The depolarization time will decrease by the influence of the electric field changes (see Sec. 2.5.3).

2.5.3 High voltage

The high voltage should be, of course, as high as possible as the sensitivity is linearly dependent. Several factors however limit the high voltage that can be applied to the system besides the limitations of the power supply itself. The electric field is limited by the leakage current, which flows over the resistive storage ring, or more often due to micro discharges. The latter depend on the assembly of the chamber, particularly the arrangement of the fibers for the CsM magnetometers on the top electrode, or abrasion from the UCN shutter. Although very high electric fields above $E = 15\,\mathrm{kV \cdot cm^{-1}}$ have been achieved at low leakage currents in the experiment under optimal conditions, and $E \approx 12\,\mathrm{kV \cdot cm^{-1}}$ has been reached regularly, the electric field performance during the nedm data taking in 2012 was limited to $E = 8.3\,\mathrm{kV \cdot cm^{-1}}$. For the last runs it had to be even further reduced to $E = 5.8\,\mathrm{kV \cdot cm^{-1}}$.

A second issue is the performance of the Hg comagnetometer that decreases under the influence of polarity changes of the electric field (see Fig. 2.40) already observed by [GHI+98]. The only way to recover the performance is a so-called oxygen discharge cleaning. In this operation, an oxygen pressure of about $p \approx 1\,\mathrm{mbar}$ is built up in the chamber, and with a steady electric discharge a plasma is ignited.

Besides the absolute value of the electric field, also the difference in the field strength for both polarities is of importance, to suppress systematic effects that scale with E^2. The electric field strength for the two polarities, measured with the internal voltage meter of the HV power supply, shows that the difference is below 0.3 ‰(see Fig. 2.41).

2.5.4 Summary

A comparison of the 2012 performance of the apparatus with typical performance at ILL is shown in Table 2.4. Although the UCN source is not yet delivering the goal UCN densities, the statistical sensitivity of the

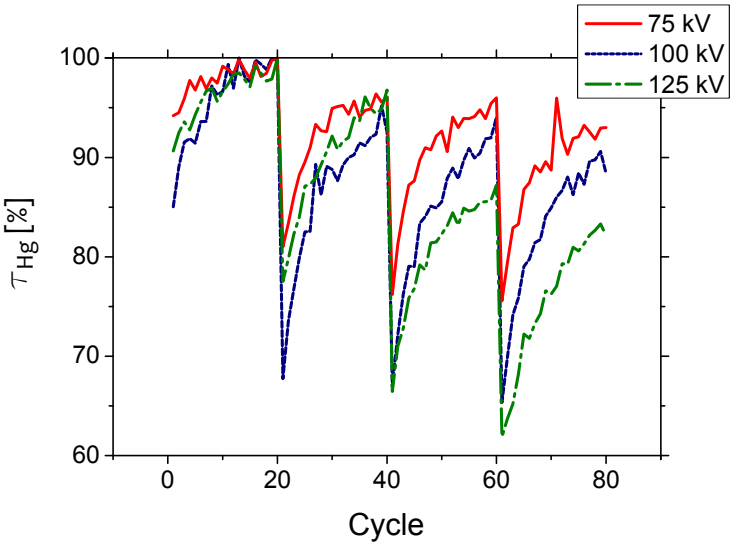

Figure 2.40: Depolarization time of Hg as a function of the cycle number for different runs recorded in 2011 for a measurement of the geometric phase of Hg [Hor12]. The depolarization time is normalized to the maximum for each run. Every 20 cycles the polarity of the HV was changed leading to a immediate reduction in τ_{Hg}, that recovers slowly over the next cycles with constant HV. The higher the voltage, the more severe is the decrease in the depolarization time.

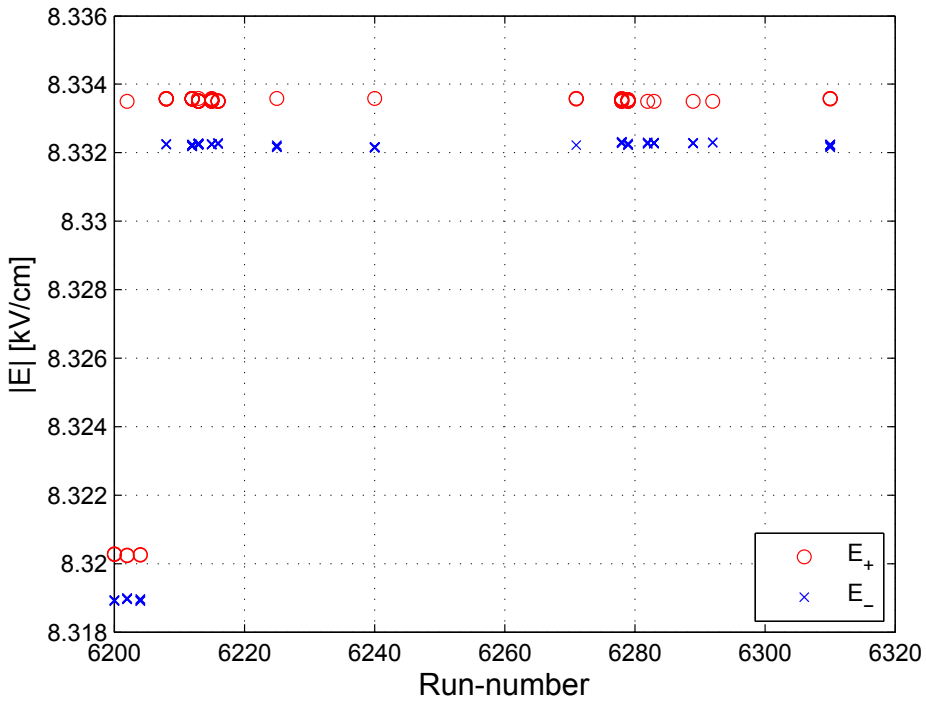

Figure 2.41: The electric field applied during the nedm measurement campaign of 2012. The plot shows absolute values of the electric field (individual for each cycle, not a mean electric field over each run, resulting in slightly blurred symbols for some runs), as a function of the run number for both polarity directions. Only cycles with an electric voltage above 90 kV are plotted to omit the cycles w.o. electric field. The graph shows, that the same electric field can be reproduced over many cycles. It also demonstrates that the electric field has a low asymmetry for the two electric field directions of $\Delta|E| = |E_+| - |E_-| = (2.00 \pm 0.02)\,\mathrm{V \cdot cm^{-1}}$ which is below 0.3 ‰.

	Sussex–RAL–ILL	PSI
Electric field	11	8.3
UCN (end of cycle)	14000	8000
visibility α (end of cycle)	0.453	0.68
Free precession time	130	200
Repetition time	240	360

Table 2.4: The relative sensitivity of the spectrometer at PSI compared to the experiment at ILL $\sigma_{\mathrm{PSI}}/\sigma_{\mathrm{ILL}} \approx 1.08$ shows, that the nEDM-experiment has a competitive performance. Improvements in the electric field strength, the visibility α, and the UCN density can be expected over the next years.

apparatus is comparable to the performance of the Sussex–RAL–ILL-experiment.

Chapter 3

Systematic effects

As mentioned before (see Sec. 2.1.2) the statistical sensitivity is in principle only limited by counting statistics. In order to reach the desired goal of $5\times10^{-27}\,e\cdot\mathrm{cm}$ with 95 % confidence level in case of a zero result or a five σ discovery for an electric dipole moment as big as $1.3\times10^{-26}\,e\cdot\mathrm{cm}$, the sum of systematic effects, leading to a false neutron edm $d_{\mathrm{n,f}}$, needs to be smaller than

$$d_{n,f} < 1.3\times10^{-27}\,e\cdot\mathrm{cm}.$$

In this section an overview of known systematic effects for the experiment will be given with a focus on the systematics that are related to the creation of the electric field.

The origin of systematic effects lies in the coupling of the magnetic moment to magnetic fields. While any statistical fluctuation of the magnetic field will just reduce the sensitivity of the measurement and finally average out, any magnetic field change $\Delta B_{\mathrm{E}} = B_{\mathrm{E},\uparrow\uparrow} - B_{\mathrm{E},\uparrow\downarrow}$ that is correlated to the electric field direction could result in an additional term in (2.3)

$$d_{\mathrm{n}}^{\mathrm{measured}} = d_{\mathrm{n}} + d_{\mathrm{n,f}} = d_{\mathrm{n}} + \frac{\mu_{\mathrm{n}}}{2E}\Delta B_{\mathrm{E}} = d_{\mathrm{n}} + \frac{\hbar\gamma_{\mathrm{n}}}{4E}\Delta B_{\mathrm{E}}, \tag{3.1}$$

from which we can approximate $d_{\mathrm{n,f}} = 2.5\times10^{-18}\,\Delta B_{\mathrm{E}}\,e\cdot\mathrm{cm}\cdot\mu\mathrm{T}^{-1}$ for an electric field of $E = 12\,\mathrm{kV}\cdot\mathrm{cm}^{-1}$. This electric field will be assumed throughout the chapter to scale all systematic effects. In other words: A magnetic field change of the B_0 field that is correlated with the electric field needs to be smaller than

$$\Delta B_E \approx 1.6\,\mathrm{fT} = 1.6\times10^{-9}\,\mu\mathrm{T} \Leftrightarrow 1.3\times10^{-27}\,e\cdot\mathrm{cm}, \tag{3.2}$$

in order to reach the desired sensitivity goal.

The ^{199}Hg comagnetometer is used to correct for the random magnetic fluctuations and increases the sensitivity of the experiment by an order of magnitude compared to former measurements without a comagnetometer [GHI+98]. However, the way that neutrons and mercury atoms are influenced by the magnetic field in the precession chamber is different due to their different energy. In addition there are effects that only influence the Hg, creating a false mercury edm $d_{\mathrm{Hg,f}}$ which will transform into a false neutron edm in the same way as a real d_{Hg} would

$$d_{\mathrm{n,f}} = \left| \frac{\gamma_{\mathrm{n}}}{\gamma_{\mathrm{Hg}}} \right| d_{\mathrm{Hg,f}} \approx 3.84\, d_{\mathrm{Hg,f}}. \tag{3.3}$$

The following section is separated into **direct** systematic effects that influence the neutron magnetometer creating a false magnetic dipole moment ($d_{\mathrm{n,f}}$) that is not (fully) compensated with the normalization of the comagnetometer and **indirect** systematic effects that create an edm-like signal in the Hg channel ($d_{\mathrm{Hg,f}}$) and only result in a false nedm signal through the normalization with Hg.

Effect	class (d/i)	Shift and σ [BDG$^+$06] [$10^{-27}\ e\cdot$cm]	Shift and σ this work [$10^{-27}\ e\cdot$cm]
Leakage currents (Sec. 3.1.1)	d	0.0±0.1	0.00±0.13
$v \times E$			
- First order (Sec. 3.1.2)	d	0.0±1.0	0.00±1.70
- Second order (Sec. 3.1.2)	d	0.00±0.02	0.00±0.00
Electric forces (Sec. 3.1.3)	d	0.0±0.4	0.00±0.00
AC fields (Sec. 3.1.4)	d	0.00±0.01	0.00±0.00
Uncompensated B drifts (Sec. 3.1.5)	d	0.0±2.4	-1.51±1.06
^{199}Hg atom edm (Sec. 3.2.1)	i	-0.40±0.30	0.02±0.06
^{199}Hg light shifts (Sec. 3.2.3)	i	3.50±0.82	0.00±0.27
Geometric phase effect			
- Dipole fields (Sec. 3.2.2)	i	-5.60±6.32	0.00±0.00
- Quadrupole difference (Sec. 3.2.2)	i	-1.30±2.00	0.56±0.90
Total		-3.8±7.2	-0.95±2.22

Table 3.1: Known systematic effects of the nEDM-experiment. The table lists for each systematic effect the classification (direct or indirect), the value estimated by the Sussex–RAL–ILL collaboration, and the current estimations. For the latter, a possible shift and error on this shift in the case of a known effect, or just the error in the case of an unknown influence of an effect. Values below $10^{-29}\ e\cdot$cm are disregarded, see according section for details.

3.1 Direct systematic effects

3.1.1 Leakage currents

Material imperfections in the insulator ring might result in a lower resistivity and create a preferred path for currents flowing from the charged to the grounded electrode. These leakage currents are a potential source of systematic effects as they can produce magnetic fields which are correlated with the direction of the electric field. Current flowing azimuthally along the insulator ring will create a magnetic field in z direction that influences the precession frequency f_{n}. This is to first order canceled by the Hg magnetometer. The remaining source for a systematic error could come from the different averaging of the field by UCN and Hg, due to their different velocities. The actual path of the current is unknown and only the current itself can be measured, and the systematic effect must be scaled under different assumptions. Several scenarios are studied with the method of finite elements (FEM). These are a closed loop, and a scenario, established by the Sussex–RAL–ILL collaboration [BDG+06]. They assumed a travel of the current over an azimuthal distance of 10 cm. For this case different paths are calculated. The models and the labeling convention of the calculation is shown in Fig. 3.1.

Each of the models consists of about 300000 elements V_i from which about half are within the volume of the precession chamber, each with the full field information $\boldsymbol{B}_i$. Due to their different velocities, Hg and UCN will probe a different average magnetic field. While the UCN are slow enough to follow field changes adiabatically, the Hg is not. Thus magnetic fields due to leakage currents will be seen differently by the two species. The UCN will precess in an average field with frequency

$$\omega_{\mathrm{n}} = \gamma_{\mathrm{n}} B_{\mathrm{UCN}} = \gamma_{\mathrm{n}} \sqrt{(B_x + B_y + B_z)^2}, \tag{3.4}$$

while the mercury will have a precession frequency

$$\omega_{\mathrm{Hg}} = \gamma_{\mathrm{Hg}} B_{\mathrm{Hg}} = \gamma_{\mathrm{Hg}} \sqrt{B_x^2 + B_y^2 + B_z^2}. \tag{3.5}$$

For each model the volume average of B_{UCN}, B_{Hg}, the mean magnetic field

$$\overline{B} = \left| \frac{1}{n} \sum_{i=1}^{n} B_i \right|, \tag{3.6}$$

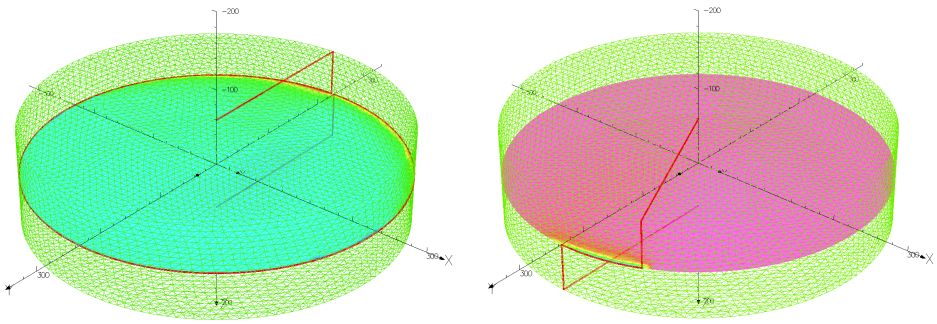

(a) loop1 (b) straight1

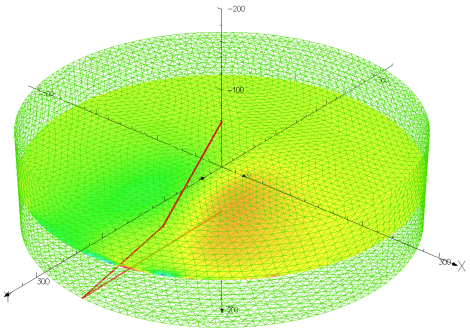

(c) straight2

Figure 3.1: FEM calculations for different leakage current scenarios: The model of the inner volume of the precession chamber (green), the conductor for the current (red) and a color map with the magnetic field B_z in a plane at the center of the precession chamber. A current of $I_l = 100\,\mathrm{pA}$ was used for the calculation. For the cases (a) and (c) the calculation was also done without the conductors on the planes of the electrodes on top and on bottom as a comparison (loop0 and straight0), as the influence of these currents should in principle cancel each other. Not shown is the background volume that defines the boundary of the model and had about twice the size of the precession chamber volume. (Calculations were performed using Opera version 13.0)

as well as the volume average of the gradient

$$\overline{G_z} = \left| \frac{1}{n} \sum_{i \neq j}^{\forall x_i = x_j \& y_i = y_j} \frac{B_{z,i} - B_{z,j}}{z_i - z_j} \right|, \tag{3.7}$$

over the inner volume of the precession chamber has been calculated. The results can be found in Tab. 3.2.

Model	$\overline{B}_x$ 10^{-11} [μT]	$\overline{B}_y$ 10^{-11} [μT]	$\overline{B}_z$ 10^{-9} [μT]	$\overline{B}_{\mathrm{UCN}}$ 10^{-9} [μT]	$\overline{B}_{\mathrm{Hg}}$ 10^{-10} [μT]	$\overline{G}_z$ 10^{-11} [μT cm^{-1}]
l0	0.64(1)	0.11(5)	0.049(1)	0.286(2)	0.2011(5)	0.2(3)
l1	0.68(8)	0.68(8)	0.127(2)	0.73(1)	0.2017(8)	0.2(3)
s0	0.35(1)	0.01(1)	0.021(1)	0.130(2)	0.0224(1)	0.01(6)
s1	0.97(6)	2.13(6)	0.100(2)	0.57(1)	0.0050(6)	0.02(5)
s2	0.81(5)	1.94(6)	0.085(1)	0.491(8)	0.0076(6)	0.01(5)

Table 3.2: FEM calculations for different leakage current paths (l=loop, s=straight, see Fig. 3.1) and a leakage current of 100 pA. The calculation result shows that the components $\overline{B}_x$ and $\overline{B}_y$ which could enhance a geometric phase effects are small compared to gradient fields usually applied in the nedm measurement (see e.g. Sec. 4.4.2).

Without the Hg comagnetometer the magnetic field change $\overline{B_z}$ would according to (3.1), result in a false edm of the neutron of up to $d_{\mathrm{n,f}} = 0.50 \times 10^{-27}\, e \cdot \mathrm{cm}$ for the model loop1 and for the more likely assumption of the model straight2 the false edm would be $d_{\mathrm{n,f}} = 0.06 \times 10^{-27}\, e \cdot \mathrm{cm}$. Due to the correction with the Hg magnetometer this effect cancels out in first order and only the difference $\Delta\overline{B} = \overline{B}_{\mathrm{UCN}} - \overline{B}_{\mathrm{Hg}}$ and the average gradient $\overline{G_z}$ in combination with the center of mass offset Δh between Hg and UCN will create an uncorrected field $B_E = \Delta\overline{B} + \Delta h \overline{G}_z$ that will result in a systematic effect smaller then

$$d_{\mathrm{n,f}} = 0.13 \times 10^{-27}\, e \cdot \mathrm{cm},$$

for the model loop1 with an typical center-of-mass offset of $\Delta h = 0.3\,\mathrm{cm}$.

3.1.2 $v \times E$ effect

The principles of special relativity for UCN moving through an electric field $\boldsymbol{E}$ result in an additional magnetic field $\boldsymbol{B}_{v\times E}$ in the rest frame of the UCN, perpendicular to the motion. Thus, under certain conditions, this field could add up to the main magnetic field B_0 and create a systematic effect via

$$\boldsymbol{B}_{v\times E} = \gamma\left(\boldsymbol{B_0} - \frac{\boldsymbol{v}\times\boldsymbol{E}}{c^2}\right), \tag{3.8}$$

with $\gamma = (1 - v^2/c^2)^{-\frac{1}{2}}$. This was actually limiting the sensitivity of nedm experiments using cold neutron beams. Two points will reduce the effect in the case of stored UCN by orders of magnitude:

1. The particles stored are strongly non-relativistic particles with $v_{\mathrm{UCN}} < v_{\mathrm{Hg}} \ll c$.

2. Unlike the geometric phase effect (see Sec. 3.2.2) only an ordered motion like a shift of the center-of-mass or a rotation of the UCN within the chamber will result in a net effect.

First order

In principle two ordered motions of the UCN in the chamber are imaginable that would result in a field $\boldsymbol{B}_{v\times E}$ aligned with B_0: an ordered net rotation due to specular reflections of UCN on the walls, or a change in the center of mass due to heating or cooling of the UCN ensemble during storage.

Rotational motion Any net rotational flow of the UCN in the storage chamber together with transversal components in the electric field $\boldsymbol{E}_{\mathrm{r}}$[1] could create a magnetic field that is aligned with B_0:

$$\boldsymbol{B}^{\mathrm{rot}}_{v\times E} = \frac{\boldsymbol{v}_{\mathrm{t}}\times\boldsymbol{E}_{\mathrm{r}}}{c^2}. \tag{3.9}$$

Specular reflections on the wall of the insulator ring could maintain any initial net rotational flow v_t of UCN within the chamber. In principle the same amount of UCN should move clockwise and counter clockwise through the chamber resulting in no net ordered motion. In addition, any departure from this symmetry will be diluted by diffuse scattering of UCN. Monte Carlo simulations for different diffuse scattering probabilities and different initial net rotation, show that the mean velocity $\overline{v}_{\mathrm{t}}$, averaged over the free precession time, is below $\overline{v}_{\mathrm{t}} = 0.03\,\mathrm{m}\cdot\mathrm{s}^{-1}$ for a rather extreme and unlikely scenario (see Fig. 3.2).

Results of FEM calculations showed, that the transversal electric field components due to the different shape of bottom and top electrode is about

[1] Only a radial symmetric component will add to this effect, as contributions from a field such as $\boldsymbol{E} = E\boldsymbol{x}$ would cancel out.

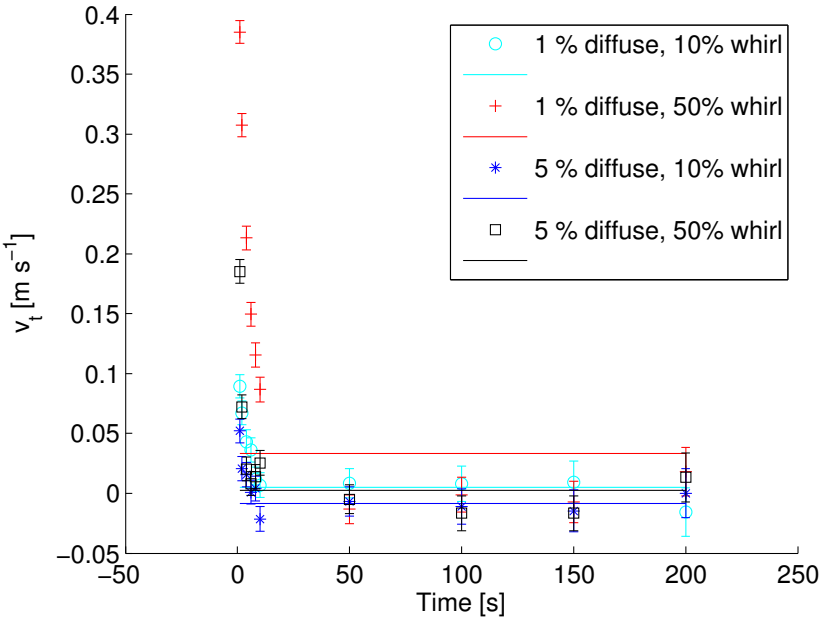

Figure 3.2: Monte Carlo simulations of the average translational velocity as function of the free precession time for different simulation parameters: '% diffuse' is the amount of diffuse scattering on the walls of the insulator ring. '% whirl' characterizes the amount of ordered motion of the initial UCN ensemble used for the simulation. The straigt lines are the average net velocity over the time period $6 \cdots 200\,\mathrm{s}$. The first six seconds are disregarded as in the actual experiment, this time is needed to prepare the Hg-comagnetometer.

$E_\mathrm{r} = 0.001\,\mathrm{E}$ [Kuź08]. Assuming $\overline{v}_\mathrm{t} = 0.005\,\mathrm{m}\cdot\mathrm{s}^{-1}$ we end up with a false edm of

$$d_\mathrm{n,f} = 1.69\times10^{-27}\,e\cdot\mathrm{cm}.$$

A short delay of some seconds of the first spin flip for the UCN could help to reduce this systematic error.

Center-of-mass shift If the energy spectrum of the UCN changes during the storage time, the center-of-mass of the ensemble will move parallel to gravity. Together with a misalignment of the magnetic field with respect to gravity by an angle ψ and a misalignment of the electric field with respect to gravity by an angle φ (see Fig. 3.3) this could create an additional magnetic field

$$\boldsymbol{B}^\mathrm{trans}_{v\times E} = \sin\psi\,\boldsymbol{B}^x_{v\times E} = \sin\psi\,\sin\varphi\frac{\boldsymbol{v}\times\boldsymbol{E}}{c^2}. \tag{3.10}$$

The tilt of the field with respect to gravity is influenced by the alignment of the electrodes and the B_0-coil. The electrodes are aligned with a bubble level with a resolution of 0.3 mrad. After the initial alignment additional tilts due to e.g. the closing of the tank have to be expected. Measurements of the precession chamber tilt with a laser (see Sec. 3.1.3) have shown, that the weight of an average physicist climbing into the tank, lead to an additional tilt of the electrodes of $1-2\,\mathrm{mrad}$. Thus we can assume that $\varphi \leq 10\,\mathrm{mrad}$ when adding additional weight to the front by closing the vacuum tank and the shield. The vacuum tank has been aligned using a theodolite and fixed markings on the tank. However, as the floor of the thermohouse, on which the theodolite was positioned, is not very stable and the magnetic field is not purely created by the coil but is influenced by the magnetic shield and the correction coils, we assume a tilt as large as $\psi \leq 100\,\mathrm{mrad}$. The change of the center-of-mass has been measured via the change in $R = f_\mathrm{n}/f_\mathrm{Hg}$ for different storage times and gradients. The average velocity of this movement is

$$v = \frac{\Delta h(t=0) - \Delta h(t=T)}{T} \approx \frac{1\,\mathrm{mm}}{200\,\mathrm{s}} = 5\times10^{-4}\,\mathrm{m}\cdot\mathrm{s}^{-1}.$$

With these values the resulting field is as small as $B^\mathrm{trans}_{v\times E} = 7\times10^{-13}\,\mu\mathrm{T}$ resulting in a false edm of

$$d_\mathrm{n,f} = 0.16\times10^{-27}\,e\cdot\mathrm{cm}.$$

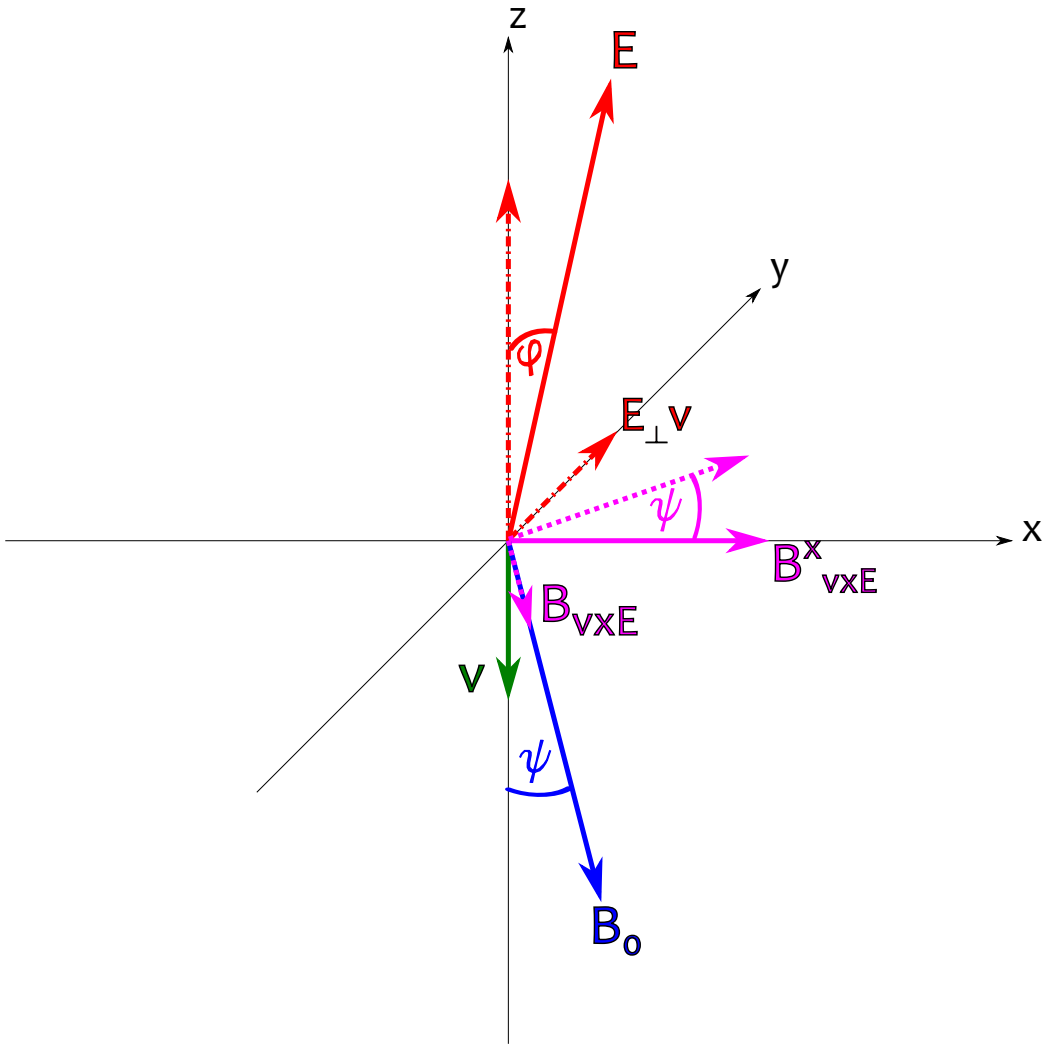

Figure 3.3: A change in the energy spectrum of the UCN during storage could lead to a center-of-mass shift along the gravitational axis (z axis). Together with a misaligned electric and magnetic field this could lead to an additional magnetic field $\boldsymbol{B}_{v\times E}$. In this example for $B_0 \uparrow\downarrow E$ the electric field is tilted by an angle φ towards the y axis, and the magnetic field is tilted by an angle ψ towards the x axis. Note: If the two fields are tilted with respect to gravity in the same plane, there is no systematic error from this effect.

Second order

Apart from the direct influence of ordered motion, any motion perpendicular to B_0 will increase the magnitude of the magnetic field

$$B = \sqrt{B_0^2 + B_{v\times E}^2} \approx B_0 + \frac{B_{v\times E}^2}{2B_0}. \tag{3.11}$$

Thus a change in the magnetic field correlated with E is given by

$$B_{v\times E}^2 = \frac{v_{xy}^2}{2B_0c^4}\Delta E^2. \tag{3.12}$$

As this effect is not proportional to $\boldsymbol{E}$ but only to $\boldsymbol{E}^2$ a false edm could only occur if the absolute field strength is different for the two electric field polarities. Measurements of the voltages show that $|E^+| - |E^-| < 0.001E$ (see Fig. 2.41). The faster moving Hg atoms are more influenced compared to the slow UCN. Assuming a velocity of $v_{xy} = 150\,\mathrm{m}\cdot\mathrm{s}^{-1}$ for the Hg atoms at room temperature we get $B_{v\times E}^{Hg} \approx 5{\times}10^{-12}\,\mu\mathrm{T}$ which is completely negligible.

3.1.3 Electric forces

A deformation of the chamber due to electrostatic forces could lead to additional systematic effects as it would increase the transverse electric fields as well as the tilting angle between the electric and magnetic field, thus increasing the $v \times E$ effect (see Sec. 3.1.2).

The force between the two electrodes with the surface $S = 0.26\,\mathrm{m}^2$, a distance $l = 0.12\,\mathrm{m}$ apart, and with an applied voltage U is given by

$$F = \frac{\epsilon_0 U^2 S}{2l^2}, \tag{3.13}$$

under the assumption of a perfectly homogeneous field without edge effects. To measure the influence of electrostatic forces, the tipping of the electrode stack under the influence of different weights has been measured[2]. Masses of $m = 10\ldots1140\,\mathrm{g}$ are used to simulate electrostatic forces corresponding to electric fields of $E = 2.9\ldots31.2\,\mathrm{kV}\cdot\mathrm{cm}^{-1}$. The relative tilt with and without weight was measured with a laser beam, bouncing off a mirror fixed to the upper electrode and registered with a photo diode after passing through an optical chopper (see Fig 3.4).

[2]The force from a mass on the top electrode is of course different from electrostatic attraction of the two electrodes as it pushes the whole precession chamber down. Thus the measurement can be looked at as an upper limit.

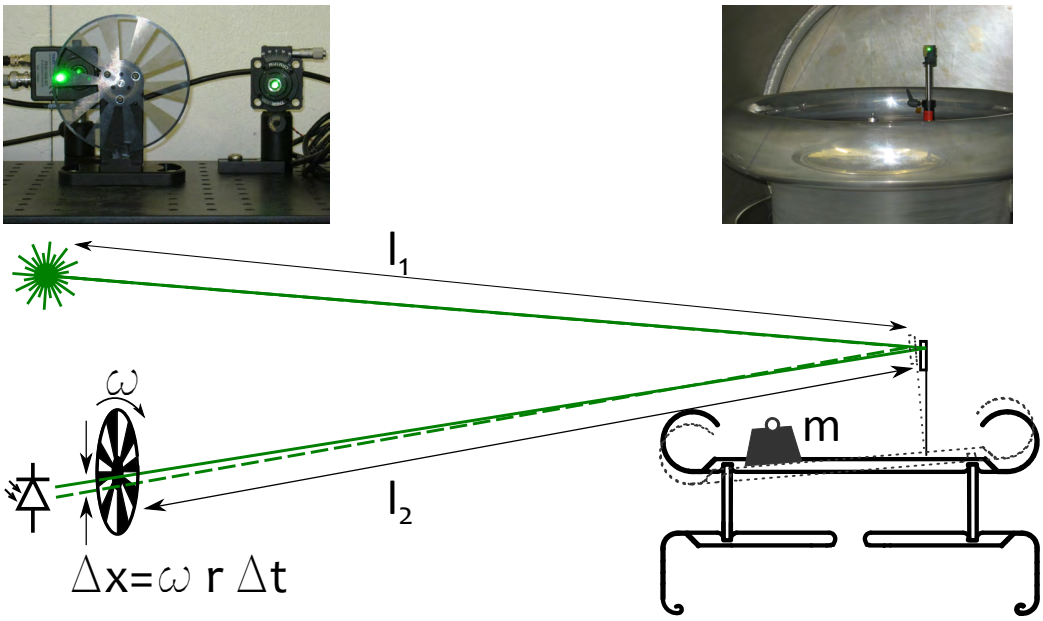

Figure 3.4: Measurement of the tilt of the electrode stack under the influence of different weights (m). A laser beam bounces off a mirror mounted on the top electrode. Any tilt of the top electrode or the precession chamber as a whole, would result in a change of the position Δx of the laser beam. The distance $l_1 = 4437\,\mathrm{mm}$ and $l_2 = 4369\,\mathrm{mm}$ have been measured using a laser rangefinder.

A tilt of the upper electrode or the precession chamber as a whole will result in a change of the position of the laser beam on the photo diode Δx. Thus the chopper plate will cover the beam Δt later or earlier with respect to the trigger signal of the chopper which can be measured with a scope (see Fig. 3.5).

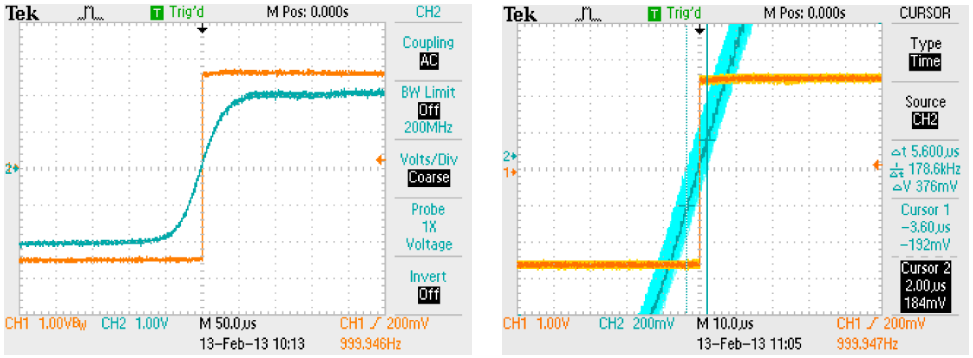

(a) (b)

Figure 3.5: Scope screen shots of the chopper trigger (CH1) and the photo diode signal (CH2). The width of the photo diode signal due to the finite diameter d of the laser beam is shown in (a). The delay of 110 µs between fully open and fully closed corresponds to $d = 3.3$ mm. A different time scale was used in (b). Vibrations of the setup lead to a jitter in CH2. To measure the time delay, a persistence of 5 s was chosen, and the width of the averaged signal is used as the error of the time delay. To avoid movement and reduce the jitter to a minimum, the weights were placed onto the electrode from afar using a pulley.

If the chopper frequency ω as well as the radius r on which the beam hits the chopper plate is known, the distance Δx is simply

$$\Delta x = r\omega\Delta t, \tag{3.14}$$

and the relative tilt α is

$$2\alpha = \frac{\Delta x}{l} \Leftrightarrow \alpha \approx \frac{\Delta x}{l_1 + l_2} = \frac{r\omega\Delta t}{l_1 + l_2}. \tag{3.15}$$

The error of the chopper frequency is negligible, the error of the length measurement due to alignment errors is estimated to be 10 mm. For the error of r the laser beam diameter of 3.3 mm, and for the timing error the width of the signal of the photo diode over 5 s is taken. The results of the measurement are listed in Tab. 3.3. The tilt is minimal even for electric

Mass [g]	E equivalent [$\mathrm{E}\cdot\mathrm{cm}^{-1}$]	$\Delta\alpha$ [mrad]
10.2	2.9	0.00±0.02
99.8	9.23	0.00±0.02
1040	31.2	-0.02±0.02

Table 3.3: Measurement results of precession chamber tilt due to weights, simulating electrostatic forces. The measured angles lead to a $d_{\mathrm{n,f}}$ below the SM predictions for d_{n}.

fields much greater than what is achievable in this experiment, resulting in a

$$d_{\mathrm{n,f}} < 3\times10^{-35}\ e\cdot\mathrm{cm}$$

far below SM predictions for the nedm.

3.1.4 AC fields

Any ripple of the high voltage power supply would result in an alternating magnetic field within the precession chamber. A oscillation frequency of this field close to the Larmor frequency of the neutrons could influence the precession due to a Bloch-Siegert shift (see also Sec. 3.2.2 for a detailed explanation).

The test protocol of the HV power supply (see Fig. B.1) states an overall ripple of $V = V_0\sin(\omega_{ac}t)$ of $V_0 = 1\,\mathrm{V_{p2p}}$. This translates into a current of $I = \frac{V_0}{R}\sin(\omega_{ac}t)$ with $R = 1\,\mathrm{M\Omega}$. The magnetic field lines inside a capacitor (in our case the precession chamber) will form concentric circles and the field strength is given by (see Fig. 3.6)

$$B_r = \frac{V_0}{R}\frac{\mu_0}{2\pi}\frac{1}{r}\sin(\omega_{ac}t). \tag{3.16}$$

Let us assume a homogeneous distribution of the UCN over the radius of the chamber, and up to 10% difference in the ripple for negative and positive electric fields (allthough the test protocol does not show a different ripple). Thus the difference for both polarities in the radius averaged magnetic field is $\Delta B_{r0} = 1.5\times10^{-12}\,\mathrm{T}$. This field would generate a shift of the precession frequency away from the Larmor frequency ω_0 of

$$\Delta\omega = \frac{(\gamma_{\mathrm{n}}\Delta B_{r0})^2}{2\omega_0 - 2\omega_{ac}}. \tag{3.17}$$

For the ripple being maximal at $\omega_{ac} = 50\,\mathrm{Hz}$ due to the frequency of the power grid, the shift will be $\Delta\omega = 5\times10^{11}\,\mathrm{Hz}$, resulting in a false edm of

$$d_{\mathrm{n,f}} = 0.002\times10^{-27}\ e\cdot\mathrm{cm}.$$

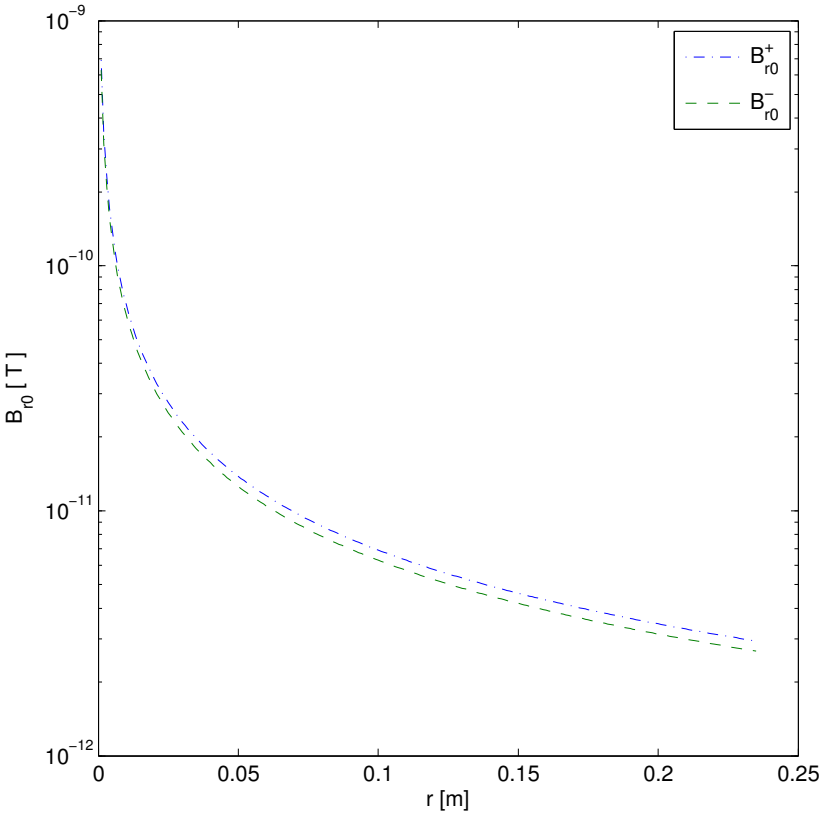

Figure 3.6: Magnetic field strength due to charging currents of the electrodes as a function of the radius within the precession chamber. The two lines correspond to a ripple of $V_0^+ = 1\,\mathrm{V}$ and $V_0^- = 0.9\,\mathrm{V}$. Under the assumption of a homogeneous distribution of the UCN over the radius of the chamber ($R = 0.235\,\mathrm{m}$) the mean magnetic fields are $\overline{B}^+_{r0} = 1.6\times10^{-11}\,\mathrm{T}$ and $\overline{B}^-_{r0} = 1.45\times10^{-11}\,\mathrm{T}$.

3.1.5 Uncompensated B drift

For an electric field direction, currents due to charging or smaller discharges, will flow in a preferred direction which is reversed together with the electric field direction. These currents will produce magnetic fields that are correlated with the electric field direction. Unlike leakage currents (see Sec. 3.1.1) these magnetic fields will not occur during the measurement, as charging is done between cycles, and a cut is applied to data for currents exceeding a certain limit during the measurement (see Sec 4.3). However, despite the fact that great care has been taken in the choice of materials within the experiment not to be ferromagnetic, it is possible to create a small net magnetization. A likely candidate would be the magnetic shield, close to the feedthrough. Let us take a closer look at this example to estimate the size of this effect: A dipole $\boldsymbol{m}$ creates a magnetic field at the position $\boldsymbol{r}$ of

$$\boldsymbol{B}_{\mathrm{dip}} = \frac{\mu_0}{4\pi}\left(\frac{3\boldsymbol{r_e}\left(\boldsymbol{r_e}\boldsymbol{m}\right) - \boldsymbol{m}}{|\boldsymbol{r}|^3}\right), \tag{3.18}$$

with $\boldsymbol{r_e} = \frac{\boldsymbol{r}}{r}$. The innermost shield layer has a distance of about $L = 55\,\mathrm{cm}$ from the center of the precession chamber. Thus the magnitude of the field in z direction created by a dipole $\boldsymbol{m} = m\frac{\boldsymbol{z}}{z}$ in this shield layer close to the high voltage feedthrough will be

$$B_{\mathrm{dip}} \approx \frac{\mu_0}{4\pi}\left(\frac{2m}{L^3}\right) = \frac{\mu_0 m}{2\pi L^3}. \tag{3.19}$$

To first order the magnetic field created by the dipole will be canceled due to the normalization with the Hg magnetometer. Due the center-of-mass offset $\Delta h \approx 0.3\,\mathrm{cm}$ between Hg and UCN however, the two species will see a slightly different B_{dip} of

$$\Delta B = B_{\mathrm{dip}}(D + \Delta h) - B_{\mathrm{dip}}(D) \approx B_{\mathrm{dip}}\frac{3\Delta h}{D} \approx 0.016 B_{\mathrm{dip}}. \tag{3.20}$$

Therefore a dipole correlated with the electric field of e.g. $m = 0.25{\times}10^{-7}\,\mathrm{Am}^2$ will lead to an uncompensated magnetic field[3] of $\Delta B = 0.016{\times}30\,\mathrm{fT} \approx 0.5\,\mathrm{fT}$ resulting in an false edm according to (3.1) of $d_{\mathrm{n,f}} = 1.25{\times}10^{-27}\,e\cdot\mathrm{cm}$, which should not be exceeded.

This field difference ΔB over the vertical distance Δh corresponds to a vertical gradient of the magnetic field of $\Delta G = {}^{\Delta B}/_{\Delta h} \approx 1\times10^{-4}\,\mathrm{nT}\cdot\mathrm{cm}^{-1}$. With the CsM we have a method to measure the vertical gradient independently. It is therefore possible to operate the experiment in a mode

[3]Hence the name of this systematic effect.

in which the electric field is frequently reversed, and the CsM are used to find any correlation of the change in the vertical gradient ΔG_{CsM} with the direction of the electric field. Under the assumption that the gradient as seen by the CsM is the same as the one seen by the mercury and the UCN (see Sec. C for an argumentation of this), the false edm can be estimated as

$$d_{\mathrm{n,f}} = \frac{\hbar\gamma_{\mathrm{n}}}{4E}\Delta B_E = \frac{\hbar\gamma_{\mathrm{n}}}{4E}\Delta G_{\mathrm{CsM}} \times \Delta h. \tag{3.21}$$

Uncompensated B drift measurements 2011 A first set of data using four CsM was recorded in 2010 [Bec11]. Because of limited statistics the result of this measurement could not exclude a false edm due to high voltage correlated gradients of $d_{\mathrm{n,f}} = (2.8 \pm 8.9) \times 10^{-27}\, e \cdot \mathrm{cm}$. The experiment was therefore repeated in 2011 with a slightly changed timing and more CsM to improve on this result. The magnetic field of $B_0 \approx 1020\,\mathrm{nT}$ was kept constant. The high voltage of the system was regularly changed between $U = \pm 110\,\mathrm{kV}$ corresponding to an electric field of $E = \pm 9.17\,\mathrm{kV \cdot cm^{-1}}$ at a ramping speed of $1\,\mathrm{kV \cdot s^{-1}}$. The field changes followed a $+--+-++-$ pattern to compensate for common gradient drifts up to second order. For each polarity the voltage was kept constant for 30 s to measure the magnetic field with an array of 12 CsM sensors: Four on top of the top electrode and 8 below the bottom electrode (see Fig. 3.7) forming gradiometers.
From each of the gradiometers the magnetic gradient was calculated as

$$G_{\mathrm{CsM}} = \frac{B_{\mathrm{CsM,top}} - B_{\mathrm{CsM,bottom}}}{d}, \tag{3.22}$$

with the distance distances d between the sensor pairs of $d = 23.5 \cdots 31\,\mathrm{cm}$. Finally the difference of the gradients with respect to electric field direction

$$\Delta G = G_{\mathrm{CsM}}^{E+} - G_{\mathrm{CsM}}^{E-}, \tag{3.23}$$

for different gradiometers was calculated to estimate the systematic effect according to (3.21).

Results In September 2011 a first data set of two days and 554 polarity changes was taken, and a second in December 2011 of nine days and 2570 polarity changes. For the December data also the direction of B_0 was changed for about half of the data. A plot of the time series with the data actually used for the analysis (after removing e.g. SULTAN ramps, see Sec. 2.3) for the different data sets is shown in Figure 3.8. Table 3.4 gives an overview of the results obtained from this data. Combining the 2011 data with the

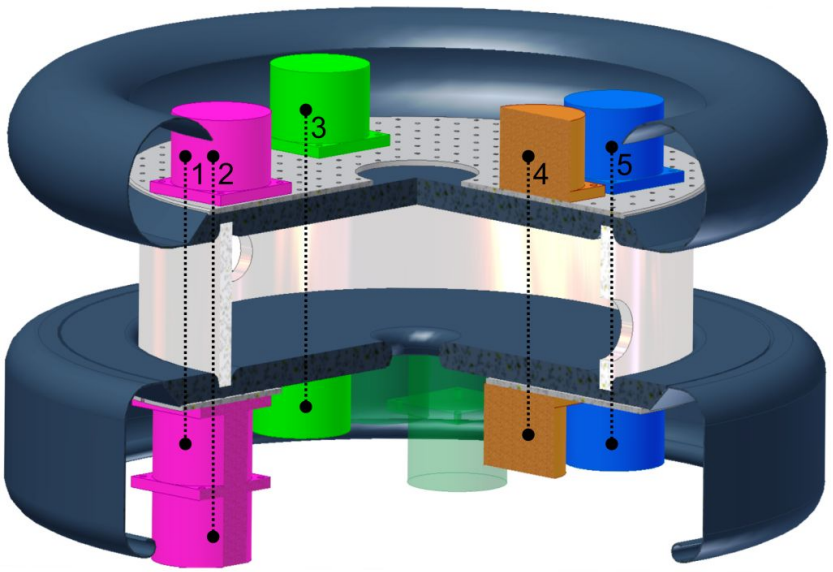

Figure 3.7: Setup of the CsM array for the measurement of the uncompensated B drift. Four sensors above the top and eight below the bottom electrode form gradiometers (1 - 5, color coded) with vertical distances between them of $d = 23.5 \ldots 31\,\mathrm{cm}$.

results from 2010 one gets as result for the false edm due to high voltage correlated gradient changes of

$$d_{\mathrm{n,f}} = (-1.51 \pm 1.06) \times 10^{-27}\, e \cdot \mathrm{cm}.$$

Remark on this kind of measurement The measurement of the uncompensated B drift as described above might not be fully sensitive to the systematic effect as it could happen in the actual nEDM-experiment for the following reason: A short time of constant electric field was chosen for the measurement, matching the sensitivity performance of the Cs magnetometers at that time (minimum of the ASD). However this is different from the situation in a nedm measurement, in which the electric field will be kept constant for thousands of seconds. The chance to have small electrical discharges, as well as the number of discharges, will increase with this time. Thus, in the measurement as described above, mainly the influence of the charging current has been measured.

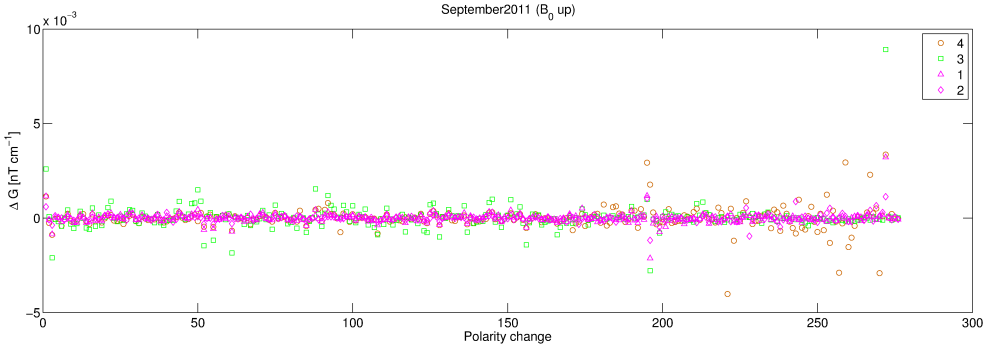

(a)

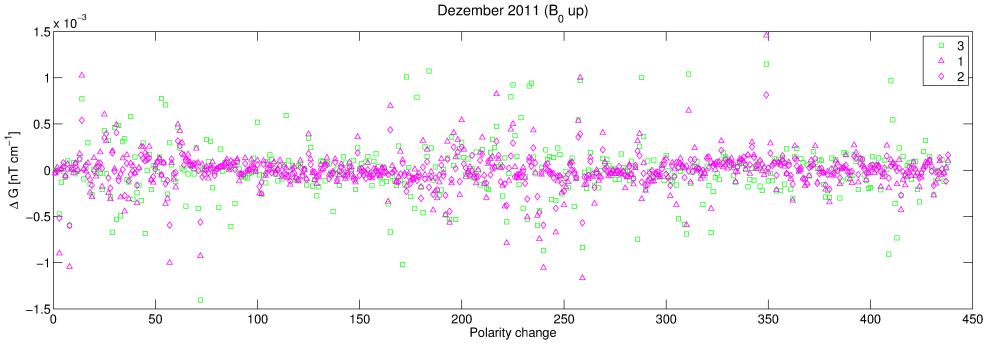

(b)

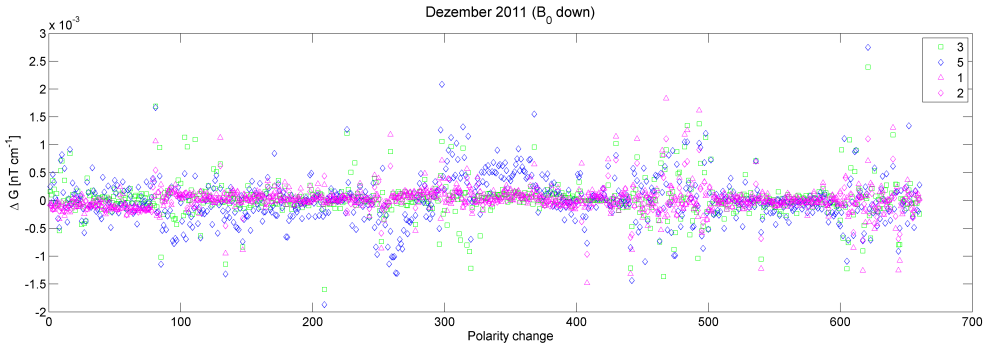

(c)

Figure 3.8: Time series of the gradient changes measured in September (a) and December (b) and (c). Not all CsM were giving reliable data at all times, thus not all gradiometers are used for the analysis (compare Fig. 3.7 for the naming convention and color coding). Error bars are omitted for clarity.

		September B_0-up	December B_0-down	December B_0-up
$\overline{\Delta G}_1$	$[10^{-4}\,\mathrm{nT}\cdot\mathrm{cm}^{-1}]$	-0.10 ± 0.19	-0.19 ± 0.11	-0.04 ± 0.11
$\overline{\Delta G}_2$	$[10^{-4}\,\mathrm{nT}\cdot\mathrm{cm}^{-1}]$	0.06 ± 0.12	0.12 ± 0.07	-0.06 ± 0.07
$\overline{\Delta G}_3$	$[10^{-4}\,\mathrm{nT}\cdot\mathrm{cm}^{-1}]$	0.27 ± 0.43	0.26 ± 0.13	-0.06 ± 0.14
$\overline{\Delta G}_4$	$[10^{-4}\,\mathrm{nT}\cdot\mathrm{cm}^{-1}]$	-0.09 ± 0.36	-	-
$\overline{\Delta G}_5$	$[10^{-4}\,\mathrm{nT}\cdot\mathrm{cm}^{-1}]$	-	0.10 ± 0.17	-
$\overline{\Delta G}_\mathrm{m}$	$[10^{-5}\,\mathrm{nT}\cdot\mathrm{cm}^{-1}]$	0.19 ± 0.52	1.6 ± 0.3	-0.46 ± 0.07
$d_\mathrm{n,f}$	$[10^{-27}\,e\cdot\mathrm{cm}]$	0.9 ± 2.5	8.2 ± 1.6	-1.9 ± 0.3

Table 3.4: Mean gradient changes correlated to polarity changes in the electric field for the different data sets. As not all CsM were working all the time, not all gradiometers are contributing to all data sets. $\overline{\Delta G}_\mathrm{m}$ is the weighted mean of the individual gradiometer channels (for labeling convention see Fig. 3.7). For estimating the false effect (3.21) an electric field of $12\,\mathrm{kV}\cdot\mathrm{cm}^{-1}$ and a center-of-mass offset of $\Delta h = 0.3\,\mathrm{cm}$ is assumed.

3.2 Indirect systematic effects

3.2.1 ^{199}Hg atom edm

Recent measurements have shown that the intrinsic EDM of ^{199}Hg is as small as $d_\mathrm{Hg} = (0.49 \pm 1.29_\mathrm{stat} \pm 0.76_\mathrm{syst}) \times 10^{-29}\, e\cdot\mathrm{cm}$ [GSL+09]. Hence the indirect systematic effect due to d_Hg is only

$$d_\mathrm{n,f} = (0.02 \pm 0.06) \times 10^{-27}\, e\cdot\mathrm{cm},$$

which is negligible and makes ^{199}Hg an almost ideal comagnetometer.

3.2.2 Geometric phase

One of the major systematic effects has its origin in the so called geometric phase effect that occurs for particles that move through inhomogeneous fields. As the effect increases for particles on closed trajectories it is of utmost importance for our experiment that uses stored particles. A detailed explanation of this effect for trapped particles in a cylindrical trap with a uniform gradient can be found in [PHS+04]. A description for arbitrary fields has been developed within the collaboration [PR12].

The origin of the geometric phase in the nEDM-experiment lies in transverse field components $B_{xy} = B_\perp$ that are perpendicular to the main magnetic field aligned with the z-axis, B_0. There are two main contributions to $B_\perp$:

- A gradient in the main magnetic field ${}^{\partial B_{0z}}/_{\partial z}$ will directly produce a transversal field due to the Maxwell equation $\nabla B = 0$

$$B_{0\perp} = -\left(\frac{\partial B_{0z}}{\partial z}\right)\frac{r}{2}, \tag{3.24}$$

  which is of the order $\mathcal{O}(B_{0\perp}) = 10^{-3}\,\mu\mathrm{T}$ for typical gradients during an edm measurement (${}^{\partial B_{0z}}/_{\partial z} \approx 10\,\mathrm{nT}\cdot\mathrm{m}^{-1}$) and a trap radius of $R = 10^{-1}\,\mathrm{m}$.

- The movement in the electrical field will create a motional magnetic field that is perpendicular to the electric field, thus perpendicular to B_0

$$B_{v\perp} = \frac{E \times v}{c^2}, \tag{3.25}$$

  that is of the order $\mathcal{O}(B_{v\perp}) = 10^{-3}$ / $10^{-5}\,\mu\mathrm{T}$ for typical speed in our chamber of $v \approx 100$ / $1\,\mathrm{m\,s^{-1}}$ for Hg / UCN and electric fields of $E = 10^6\,\mathrm{V}\cdot\mathrm{m}^{-1}$.

- Transverse fields due to leakage currents are many orders of magnitude smaller (see Tab. 3.2) and can therefore be neglected.

Hence we get

$$B_\perp = B_{0\perp} + B_{v\perp} = \left(\frac{\partial B_{0z}}{\partial z}\right)\frac{r}{2} + \frac{E \times v}{c^2}. \tag{3.26}$$

A particle moving through the chamber will therefore see a time dependent transverse field $B_\perp = \gamma_\mathrm{n}\omega_r$. In the rest frame of the particle rotating with ω_r we thus get a precession frequency ω_L of

$$\omega_L = \sqrt{(\gamma_\mathrm{n}B_0 + \omega_r)^2 + (\gamma_\mathrm{n}B_\perp)^2}. \tag{3.27}$$

Transferring back to the lab frame we see that the precession frequency is

$$\omega_L = \sqrt{(\omega_0 + \omega_r)^2 + (\gamma_\mathrm{n}B_\perp)^2} - \omega_r, \tag{3.28}$$

with $\omega_0 = \gamma_\mathrm{n}B_0$. The shift $\Delta\omega = \omega_L - \omega_0$ is called the Ramsey Bloch Siegert shift and is in first order given by

$$\Delta\omega \approx \frac{(\gamma_\mathrm{n}B_\perp)^2}{2(\omega_0 - \omega_r)}. \tag{3.29}$$

With (3.26) we see that

$$\begin{aligned} B_\perp^2 &= (B_{0\perp} + B_{v\perp})^2 \\ &= B_{0\perp}^2 + B_{v\perp}^2 + 2\, B_{0\perp}\, B_{v\perp} \\ &= B_{0\perp}^2 + B_{v\perp}^2 + \frac{\partial B_{0z}}{\partial z}\frac{v_{xy}}{c^2} r E, \end{aligned} \tag{3.30}$$

where the last term is linear in E and the geometric phase therefore mimics a true edm value. Due to the higher mean velocity of the Hg atoms inside the trap, the false effect is an order of magnitude higher for Hg atoms as for UCN. In [PR12] the false edm of Hg for a cylindrical trap with diameter D in a uniform gradient has been derived to be

$$d_{\mathrm{Hg,f}} = \frac{\hbar \gamma_{\mathrm{Hg}}^2}{32 c^2} D^2 \frac{\partial B_{0z}}{\partial z}. \tag{3.31}$$

Measurement of the geometric phase for Hg

The geometric phase effect of Hg was measured in 2011 [Hor12]. The electric field polarity was alternated every 20 cycles between $8.3\,\mathrm{kV \cdot cm^{-1}}$ and $-8.3\,\mathrm{kV \cdot cm^{-1}}$ and the difference in the precession frequency of the mercury $\Delta f_{Hg} = f_{Hg\uparrow\uparrow} - f_{Hg\uparrow\downarrow}$ was measured. The experiment was repeated for different gradients $G = \frac{\partial B_z}{\partial z}$ created with two correction coils (BTC and TTC in anti Helmholtz configuration). The gradient was estimated using the average of the CsM on the top electrode minus the average of the CsM below the bottom electrode. The result is shown in Fig. 3.9. A linear fit of (3.31) to the data gives

$$d_{\mathrm{Hg,f}}(\frac{\partial B_{0z}}{\partial z}) = (9.94 \pm 0.25) \times 10^{-27}\, e \cdot \mathrm{cm} \cdot \mathrm{nT^{-1}} \cdot \mathrm{m}, \tag{3.32}$$

for B_0 down. For B_0 up the result is

$$d_{\mathrm{Hg,f}}(\frac{\partial B_{0z}}{\partial z}) = (-9.96 \pm 0.33) \times 10^{-27}\, e \cdot \mathrm{cm} \cdot \mathrm{nT^{-1}} \cdot \mathrm{m}. \tag{3.33}$$

Crossing point analysis

In contrary to an electric dipole moment the geometric phase scales linearly with the vertical gradient of the magnetic field. This allows us to make a first order correction and extract the true edm with the so-called crossing point analysis as it was introduced by the Sussex–RAL–ILL-collaboration

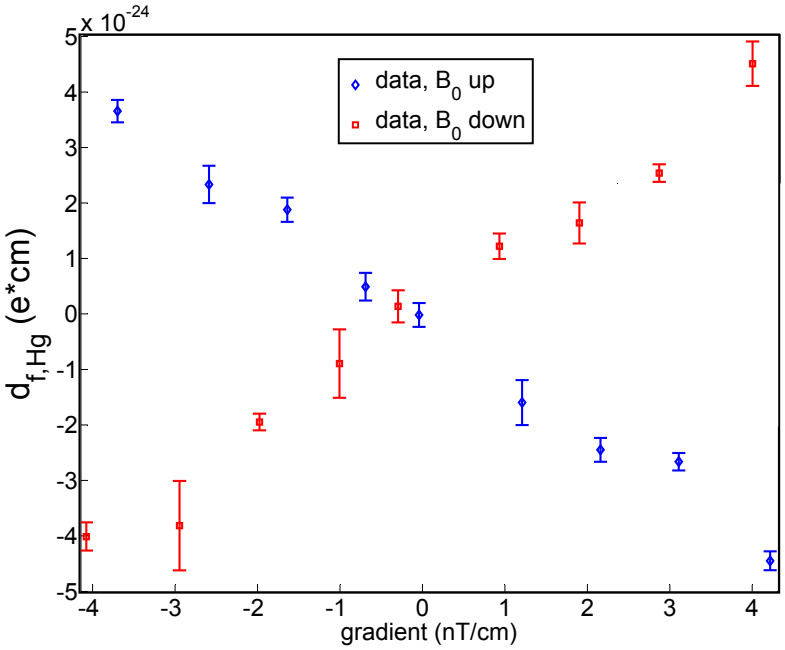

Figure 3.9: Geometric phase measurement of the Hg comagnetometer as a function of the gradient. The gradient has been measured using the CsM (from [Hor12]).

([BDG+06]). With the center-of-mass offset Δh between Hg and UCN the vertical gradient can be expressed as a function of the frequency ratio

$$\mathcal{R} = \frac{f_\mathrm{n}}{f_\mathrm{Hg}} \frac{\gamma_\mathrm{Hg}}{\gamma_\mathrm{n}} = \mathcal{R}_0 \pm \frac{\Delta h}{B_0} \frac{\partial B_{0z}}{\partial z} \approx 1 \pm \frac{\Delta h}{B_0} \frac{\partial B_{0z}}{\partial z}. \tag{3.34}$$

With (3.3), (3.31) and (3.34) we get for the false edm of the neutron

$$\begin{aligned} d_\mathrm{n,f} &= d_\mathrm{n,f}^\mathrm{other} + d_\mathrm{n,f}^\mathrm{geo} \\ &= d_\mathrm{n,f}^\mathrm{other} \pm |\gamma_\mathrm{Hg}\gamma_\mathrm{n}| \frac{\hbar B_0}{32c^2\Delta h} D^2(\mathcal{R} - \mathcal{R}_0) \qquad (3.35) \\ &= d_\mathrm{n,f}^\mathrm{other} \pm k(\mathcal{R} - \mathcal{R}_0), \qquad (3.36) \end{aligned}$$

with the $\pm$ sign corresponding to B_0 down/up. $\mathcal{R}_0$ is the ratio of the precession frequencies at zero gradient, normalized with gyromagnetic ratios and is usually close to unity. However, there are effects that will shift $\mathcal{R}_0$ away from one (Sec. 3.2.2). Measuring the edm for different gradients and thus different values of $\mathcal{R}$, one gets two slopes for the two B_0 directions when plotting $d_\mathrm{n,meas.} = d_\mathrm{n} + d_\mathrm{n,f}$ as a function of $\mathcal{R}$. At the crossing point of the two slopes $d_\mathrm{n,f}^\mathrm{geo} = 0$ and one is left only with other systematic effects.

However, any effect that changes $d_{\mathrm{n,f}}^{\mathrm{geo}}$ independently of $\mathcal{R}$ or changes $\mathcal{R}$ but does not create a false edm according to (3.36) will lead to a false effect that is not considered by this crossing point analysis.

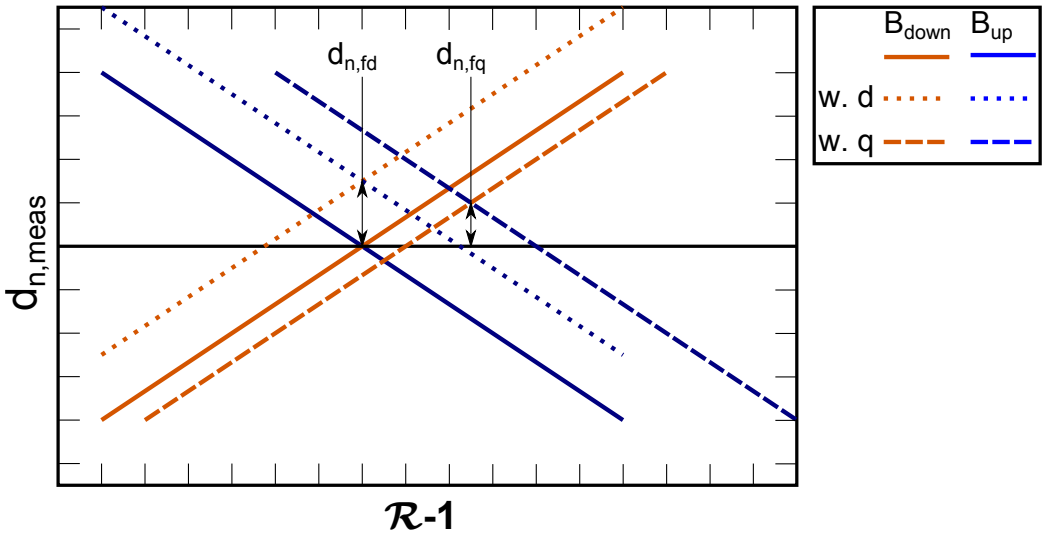

Figure 3.10: Illustration of the crossing point analysis. The value $d_{\mathrm{n,meas.}}$ is measured as a function of $\mathcal{R}$. Ideally, all geometric phase effects cancel and one is left only with other systematic effects effects due to a local dipole (w. d) and a quadrupole difference (w. q) at the crossing point. For details see text.

Local dipoles

Local dipoles will create an additional gradient (and thus additional vertical field components), independent of the gradient in the main field and thus independent of $\mathcal{R}$ [HP06, PR12]. This is not included in (3.31) and will enhance the geometric phase effect due to the average gradient created by the dipole

$$d_{\mathrm{Hg,f}} = \frac{\hbar\gamma_{\mathrm{Hg}}^2}{32c^2} D^2 \frac{\partial B_{0z}}{\partial z} + d_{\mathrm{Hg,f}}^{\mathrm{dip}} \left(\overline{\frac{\partial B_{0z}^{\mathrm{dip.}}}{\partial z}} \right) . \tag{3.37}$$

As the dipole field does not change when changing the B_0 directions, the two slopes in Fig. 3.10 are shifted upwards and result in an remaining false edm $d_{\mathrm{n,fd}}$.

The electrodes, used in the experiment, are sent to Physikalisch-Technische Bundesanstalt (PTB) Berlin to be surveyed every year during the winter shutdown of the proton accelerator. Possible dipoles due to magnetization of the electrodes are measured there. After the 2012

edm measurement campaign, the measurement revealed as strongest magnetization one of the titanium screws, used to attach the high voltage corona ring to the top electrode. The magnetic signal corresponded to a dipole of $m \approx 22\,\mathrm{nA}\cdot\mathrm{m}^2$ or $0.02\,\mathrm{nT}\cdot\mathrm{cm}^3$ which would result in a false edm of

$$d_{\mathrm{n,f}} = (0.000 \pm 0.004)\times 10^{-27}\, e\cdot\mathrm{cm}.$$

Quadrupole fields

Any transverse magnetic field $\boldsymbol{B}_\perp$ that does not create a vertical gradient is seen by the UCN as they will follow the field adiabatically while moving through the chamber. An example of such a $\boldsymbol{B}_\perp$ is a quadrupole field of strength q aligned with the z-axis ($B_x = -qx$,$B_y = qy$). Due to their high velocity, the Hg-atoms will not see such a field when averaging over the precession chamber. Such a field will shift the ratio [PHS+04]

$$\mathcal{R}_\perp \approx \mathcal{R} + \frac{\overline{B}_\perp^2}{4B_0^2}, \tag{3.38}$$

with $\overline{B}_\perp^2 \approx q^2R^2$ the mean vertical magnetic quadrupole field. This changes $\mathcal{R}_0$ which moves the slopes in Fig. 3.10 to the right. If the quadrupole field is different for the two B_0 directions a false edm due to the quadrupole field $\boldsymbol{B}_\perp$ remains

$$d_{\mathrm{n,fq}} = \frac{\hbar\gamma_{\mathrm{n}}\gamma_{\mathrm{Hg}}D^2}{128c^2B_0\Delta h}\left(\overline{B}_{\perp,\downarrow}^2 - \overline{B}_{\perp,\uparrow}^2\right). \tag{3.39}$$

Scanning the field inside the vacuum tank with a flux gate magnetometer, between measurements, has so far been the only way to determine the quadrupole component of the B_0-field and reduce it with the correction coils. The development of multi-beam vector cesium magnetometers [BKGS+12] could give an online measure of this value in the future. From the $\mathcal{R}$-curve analysis of the 2012 edm data taking (see Sec. 4.4.2) a quadrupole difference of $\overline{B}_{\perp,\downarrow}^2 - \overline{B}_{\perp,\uparrow}^2 = (-5.5 \pm 8.9)\,\mathrm{nT}^2$ and a center-of-mass offset of $\Delta h = (3.0 \pm 0.2)\,\mathrm{mm}$ could be extracted. This would correspond to a false edm of

$$d_{\mathrm{n,f}} = (0.56 \pm 0.90)\times 10^{-27}\, e\cdot\mathrm{cm}.$$

However, a malfunction in the CsM-electronics might have provoked an unknown systematic error in the CsM data used for this result (see Sec. 4.5). A comparison with the results of the 2013 magnetic field mapping, should help to clarify these measurements.

3.2.3 Mercury light shift

Non resonant light absorption from the circularly polarized ^{204}Hg readout light beam will influence the precession frequency of ^{199}Hg due to its interaction with the electron shell that will broaden and shift the energy levels in the atoms. A theoretical description as well as an experimental study of light shift effects can be found in [CTDR72]. There an effective Hamiltonian is formulated to describe the interaction of the light beam with the atom, which can be interpreted in our case (assuming perfectly circular polarization) as a fictitious magnetic field along the direction of the light beam $\boldsymbol{k}$:

$$\boldsymbol{B}_{\mathrm{ls}} \propto B_{\mathrm{ls}}(I,\omega)\boldsymbol{k}. \tag{3.40}$$

The magnitude of this magnetic field depends on the intensity of the light I and its frequency ω. A component of B_{ls} along the B_0 field can be the result of a misalignment of the readout beam by an angle ζ or reflections of a divergent light beam. The change in the precession frequency $f_{\mathrm{Hg}} = \gamma_{\mathrm{Hg}}B_0 \pm \gamma_{\mathrm{Hg}}\sin(\zeta)B_{ls}$ is not dependent of the electric field and thus will not directly contribute to a false edm. However, as the influence of the light shift is opposite for the two B_0 directions a false effect will remain in the crossing point analysis (see Sec. 3.2.2). As the systematic effect can be reduced by reducing the magnitude B_{ls} or aligning $\boldsymbol{k}$ with respect to B_0, two steps are taken to reduce light shifts:

- On a short time scale an improved optical system has been implemented in 2012, that allows a better alignment, thus reduce ζ, and reduce the divergence of the beam.
- On a longer time scale a UV laser system will be installed to replace the ^{204}Hg discharge lamp. The narrow laser line width and a good frequency control will allow us to reduce B_{ls} [Feron].

With the new probe light optic the systematic error has been estimated to be as small as [Reb12]

$$d_{\mathrm{n,f}} = (0 \pm 0.27) \times 10^{-27}\, e \cdot \mathrm{cm}.$$

High voltage induced light intensity shifts

The Sussex–RAL–ILL-collaboration observed a linear dependency for the light intensity of the Hg readout light with the electric field [Doy04] $I = I(E)$. This could lead to a direct systematic effect due to (3.40) for unequal magnitudes of $\boldsymbol{E}$. For our setup the dependence of light intensity

with the electric field could not be confirmed. The systematic error arising from intensity shifts in the light level was found to be smaller than [Hor12]

$$d_{\mathrm{n,f}} = 0 \pm 0.04 \times 10^{-27}\, e \cdot \mathrm{cm}.$$

Chapter 4

Data Analysis

This chapter will focus on a possible strategy for data analysis and some first results of nedm data taken in November 2012.

4.1 Analysis strategy

The data analysis is performed separately by two independent analysis groups. The first group consists essentially of collaborators from LPC (Caen), LPSC (Grenoble), and CSNSM (Orsay). The second group comprises collaboration members from PSI (Villigen), ETH Zürich, University of Fribourg, and Jagellonian University (Cracow). Inside the groups, subtasks are then distributed among the members of each group.

The work presented in the following sections is part of the second analysis group. Within this group it was decided to concentrate on the use of the commercial software MATLAB for the analysis.

4.1.1 Preprocessing the data

As mentioned in Sec. 2.4.12 the data of each subsystem is written to an individual ASCII data file. Data files greater than 10 MB are split into separate files. For the analysis the different files need to be collected, synchronized, and combined based on their timestamps. As an experiment is organized usually into runs and cycles (see Sec. 2.3.1) this defines a natural structure for organizing the data. Figure 4.1 shows an illustration of the processed data structure. Per run a binary MATLAB file is created containing general information about the run, like the run number, the μTimer(s)[1] and a (1 × number of cycles)-structure array that contains the

[1]It is possible to define two μTimer (0,1), that will be executed after each other.

data of all subsystems for each cycle. In addition already during the import of the data, some analysis is performed. This includes e.g. comparing the set and reached positions of the switch for each cycle, averaging slow control data that is taken every second over the period of free precession or integrate the neutron counts over dedicated time periods of each cycle defined by the μTimer. The data of the neutron detector is saved in a separate binary file, as the data of a whole run is several 100 MB large. Only the integrated UCN counts are stored in the main file.

4.1.2 The nEDM data plotter

Once the data is imported into a MATLAB compatible structure, it is useful to have the possibility of quick visualization. An easy to use multi-purpose tool with a graphical user interface was written to look at trends, stability, correlations, etc. The functionality is described in the caption of Fig. 4.2.

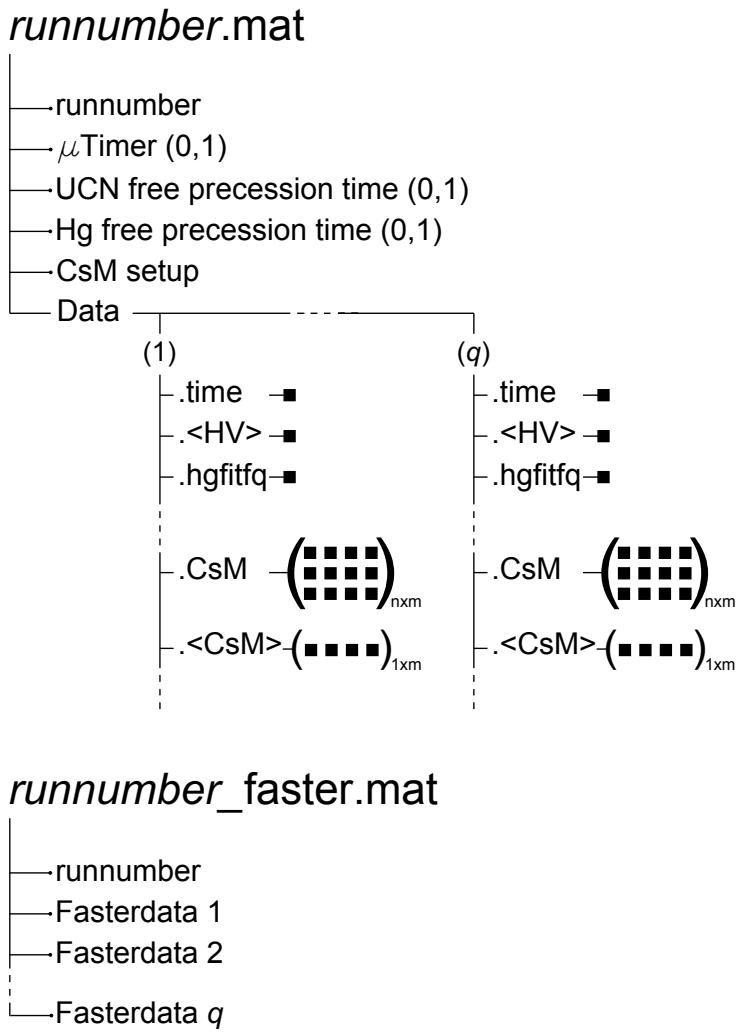

Figure 4.1: Illustration of the data structure after the import into MATLAB. The general layout is defined by the separation of any experiment into runs and cycles (1 to q). For each run two files are created. Information concerning the whole run, e.g. the information on the steps of each cycle in the μTimer, are stored as variables in the first file. Based on the time stamp, the different data files are then sorted into the cycle structure and stored with their name in the *Data* structure array. In addition, data that is recorded n-times per cycle (vacuum, CsM, temperature, ...) is averaged over the time period of the free precession (symbolized by <>) for each cycle. For performance reasons, the UCN detector files (faster) are stored, separated for each cycle, in a second file.

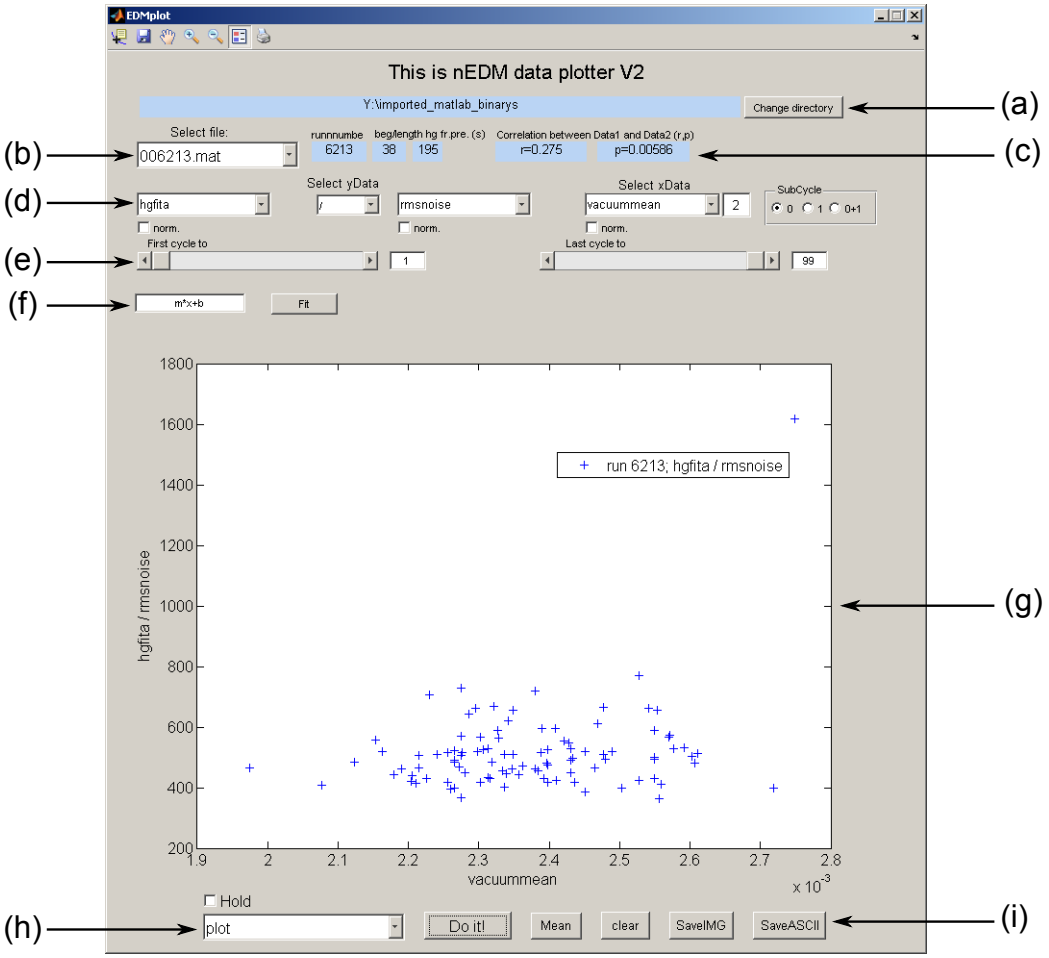

Figure 4.2: Screen shot of the nedm data plotter. (a) Select working directory where imported data is stored. (b) Drop-down menu to select a run. (c) Timing information used for the averaging and correlation parameters of currently plotted data. (d) Selection of data to be plotted. Simple mathematical operations $(+ \; - \; \times \; /)$ as well as a normalization to the mean of the selected data is optional. Also the sub-cycle can be selected. (e) Two sliders allow the selection of limited number of cycles to be plotted. (f) Nonlinear fitting of the currently plotted data. (g) Plot window showing the result. (h) Drop-down menu to select the plot type: xy-plot, xyy-plot, histogram (only first y data set), Allan deviation (only first y data set). The hold option allows to plot different data sets or different runs together. (i) Exporting the results as an ASCII or image file.

4.2 Blind analysis

In most fields of modern science it is nowadays common to blind the analysis of an experiment. Particularly in medical science, where in a clinical trial of new drugs, not only the patient but also the ones who apply a new medicine, do not know if they administer a placebo or not (so-called double blind test). The reason for this effort is to reduce any bias of the experimenters conduction of the experiment towards their own expectations[2].

In modern nuclear and particle physics the method of blind analysis has become common since the last decades. Most past particle physics experiments have been conducted open and were therefore susceptible to bias: An experimenter who already 'knows' the result of his experiment during analysis, e.g. because he remeasures a value that is known with a certain precision, might unconsciously influence his analysis to achieve the expected results. Two possible factors of human bias are to apply cuts to the dataset with the knowledge of how the cuts influence the final result (selection bias) and to disregard systematic effects, as one might stop looking for them once the result agrees with expected result (ending bias).

An example in the field of physics is the measurement of the speed of light (c). Figure 4.3 shows the history of the measured values of c. It is clearly visible that during certain periods in time, all measurement results were in agreement with measurements made before rather than with the real value. Although this can be no proof for biased analysis it gives a strong hint towards it.

4.2.1 Common methods of blind analysis

Following [KR05] a short overview of common blind analysis techniques is given that are used in particle physics experiments. The principle idea in all methods is to hide certain aspects of the data until the analysis method is set. Thus the result of the analysis should not influence the analysis itself. Only after the analysis is completed, the hidden aspect of the data is revealed, and the data is unblinded. This certainly makes the analysis more difficult, and also it might become more difficult to cope with unexpected results.

(i) Hidden signal box In this method the data, as a function of one or more experimental parameters, is divided into two subsets: the signal region which is hidden and the sidebands, which are analyzed immediately. This

[2]Many articles concerning blind analysis give the very instructive yet amusing example of Clever Hans (Kluger Hans) [Pfu11].

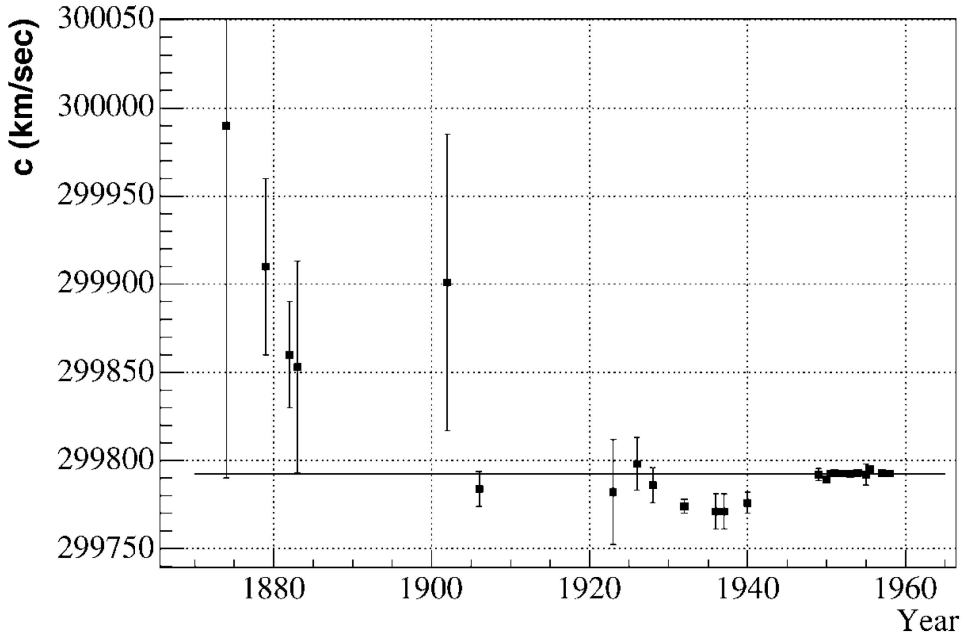

Figure 4.3: History of measurements of the speed of light together with the real value. It is conspicuous, that measurements seem to rather agree with the value measured before, than with the real value (especially in the measurements around 1930). From [KR05].

is a feasible method if the signal region is well known before hand. Also the expected background in the signal region must be known as a result of the analysis of the side bands. This is usually the case in experiments searching for rare decays. Once the signal region is unblinded, the estimated background is compared with the events found.

(ii) Hidden answer methods The method of hidden answer separates the analysis of the data from the numerical value that is the result of the data analysis. This is in general possible if a certain parameter is measured with high precision and the parameter does not depend on the number of observations. This can be achieved for example by hiding a certain parameter of the detector, providing that the experiment can be performed without this knowledge and that the parameter can be obtained later on. For most experiments this simple approach is not possible. In this case it is possible to add an additional (random) offset to the data to hide the real result. Usually a Gaussian distributed offset with a standard deviation big enough to cover e.g. theoretical predictions and an additional random sign is a reasonable approach. If not only the numerical result, but also the distribution of the data should be hidden to avoid bias, in addition to an offset an asymmetry might be added to the data. In this case great care has to be taken in constructing the blinding to not make the data analysis impossible. If the final physical result can be only obtained by several analysis results that can be obtained by independent analyzes, the data might be split. Independent groups can perform an individual analysis on a specific subgroup of the whole data set and add an offset to their intermediate result for communication among each other. Only at the end all final results are combined to get the physically meaningful result.

(iii) Adding or removing events If the result of an experiment directly depends on counting the number of events, it is possible to add artificial events, remove a certain part of all events or even do both. If events are added it is important that they are as alike as possible to the real signal. This can be done by simulated events or by adding a real signal to the detector. The added events are tagged and only removed after the analysis has been completed. Of course a good simulation or a source of signal like events that can be tagged is not always available. In this case it is also possible to remove a certain percentage of all events, so that the deriving of a meaningful result is not possible. This might even be preferable, as by adding events some bias can evolve for the case, that less events are detected despite the fact that some have been added by hand. By the combination,

adding and removing events at the same time, it remains unknown which effect is bigger and possible bias is reduced greatly.

(iv) Data prescaling By analyzing only a subset of the whole data set or by applying analysis methods only on Monte Carlo data, a majority of the data set can be hidden. This requires of course that either the subset of data selected for the analysis is a good representation of the whole data set, or that the Monte Carlo simulation is trustworthy enough to base the analysis on it. A further drawback is that only the biased adjustment of cuts, enhancing non statistical background fluctuations, can be suppressed. The search for systematic effects is not addressed. If the data set is big enough it is however possible to divide it into several pieces that can be unblinded bit by bit. The prescaling has to be done unbiased, it must be a good representative of the whole data set and the size must be large enough to develop an analysis strategy but small enough to not bias the complete data set. Usually if the prescaled data set has a considerable size of the total data set, it should be disregarded for the final result. This blinding method can of course be combined with one of the earlier mentioned methods.

4.2.2 Blinding the nedm experiment

The measurement of the nedm is particularly susceptible to bias. Depending on the belief of the person analyzing the data that either the electric dipole moment is given by the SM (and therefore zero within the sensitivity of the experiment), or the data gives a hint to physics beyond the SM, one could be inclined to tune the value of the nedm to be zero or not. The problem of a blind analysis for the nedm is that it must be possible to still investigate (unknown) systematic effects, which are in principle at the same level as the nedm value. Of the above described methods for blind analysis only the hidden answer method and the data prescaling method seem to be appropriate for the nedm experiment. The figure of merit of the experiment is a frequency shift correlated with the electric field. Thus any hidden parameter or added offset needs to be correlated with the electric field in order to mimic a true edm.

The most simple approach would be to blind the value of the electric field. Care must be taken that the electric field strength cannot be determined from the charging current measured with the leakage current DAQ. However, as the nedm is so small only a big offset in the electric field would lead to a proper blinding, which leads to a psychological issue: as the sensitivity is correlated to the electric field strength, it is hard to make people believe that the experiment was running at a lower electric field.

The only other parameter that could be hidden is the frequency of the UCN and Hg comagnetometer (The CsM do not need to be considered as they are not exposed to an electric field). Any offset (random or fixed) would need to be correlated with the electric field. The UCN and Hg channels can be analyzed independently as well as combined, and might make it necessary, to add an 'artificial' edm in both channels. In addition, a random offset might not only mimic an edm but also systematic effects. It seems however plausible to simply add a constant artificial edm of considerable size (e.g. $1.005 \times 10^{-25}\, e \cdot \mathrm{cm}$) to the Hg channel. It would shift the Hg precession frequency and due to the corrections also the nedm result away from zero. Even if the value of this artificial result can be determined from the neutron channel, it will be limited by statistical fluctuations of the magnetic field and therefore not be very precise[3].

Finally it is always possible to analyze only a subset of data that has a statistical sensitivity above the current best limit. Care must be taken only in the selection of the data subset as it needs to be a good representative for the whole dataset. In particular changes or upgrades of the experiment (implement a new UCN shutter, use a laser based Hg readout system, etc.) need to be considered. Of course this would only prevent a certain statistical bias and some systematic studies might only be performed after the unblinding.

It should be stated here that a blind analysis is no guarantee for a correct result (nor does an open analysis need to be false). Also the analysis does not need to stop if after the unblinding an unreasonable result is achieved. A non blind analysis could always be performed later on, and both the blind and open analysis result can be published together with a possible explanation of what has lead to the wrong blind analysis result.

4.3 nedm data analysis

In November 2012 a first set of edm data[4] was taken with the spectrometer at PSI. The data set is not large enough to have a discovery potential yet, but the per-cycle sensitivity of the apparatus was excellent. The data is of highly valuable to gain experience in operating the apparatus and train data analysis algorithms. The data set recorded was not blinded. Over a period

[3] This holds only if the CsM can not be used to correct magnetic field fluctuations.

[4] Actually a single run of six hours was recorded in December 2011 just before the yearly shutdown of the proton accelerator.

of 14 days[5], a total of 24 runs with 2362 cycles have been recorded. Half of the data set was recorded with B_0 up, the other half with B_0 down. In addition the TTC and BTC correction coils were powered with currents of $(0, \pm 250, \pm 500)$ µA to measure at gradients of $\mathcal{O}(\pm 10\,\mathrm{nT \cdot m^{-1}})$. The electric field was altered in a $+++0-----0+++$ (or reversed) pattern where each of the symbols $(+\,0\,-)$ represents seven to eight cycles, so that a typical run consisted of about 100 cycles and had a duration of about 10 h. The net sensitivity of the data, after applying cuts (see Sec. 4.3.2), adds up to

$$\sigma_{d_\mathrm{n}} = 1.28 \times 10^{-25}\, e \cdot \mathrm{cm}. \tag{4.1}$$

To determine d_n from the data a series of steps has to be performed first to extract the neutron frequency f_n and from that the frequency difference with respect to the electric field polarity.

4.3.1 Extraction of neutron counts

The FASTER data acquisition system, connected to the neutron detector, records a binary datafile for every cycle. For every charge event that exceeds a validation time (charge over threshold of 3 mV) of 6 ns this file contains two integrated charges of the event (integration time $0 \ldots 8$ ns and $8 \ldots 200$ ns), referred to as QDC[6] gates. Each entry gets a time stamp relative to the starting time of the file. The data file not only contains UCN events but also low charge events due to e.g. Čerenkov events in the acrylic glass light guides. The separation between UCN and background, at the moment done in a simple cut on the QDC value of the second gate is shown in Fig. 4.4.

The FASTER DAQ has a non-extensible dead time of $\tau_\mathrm{dt} = 80$ ns [Fon12]. For a constant count rate a dead time correction for each channel can be performed according to

$$N \approx \frac{M}{1 - (M \times \tau_{dt}/t)}, \tag{4.2}$$

with N the real UCN counts, M the registered UCN counts and t a time interval of $t \leq 0.5\,\mathrm{s}$[7] during which the count rate can be assumed to be constant. As the count rates currently do not exceed $\approx 40000\,\mathrm{s^{-1}}$, the dead

[5] The actual data recording period was 17 days, including 3 days during which the proton accelerator was switched off for maintenance.

[6] Charge-to-Digital converter.

[7] The time binning of the analysis script is adaptive, to divide a given µTimer step into an integer number of intervals t but also to have as few time intervals as possible to save computing time.

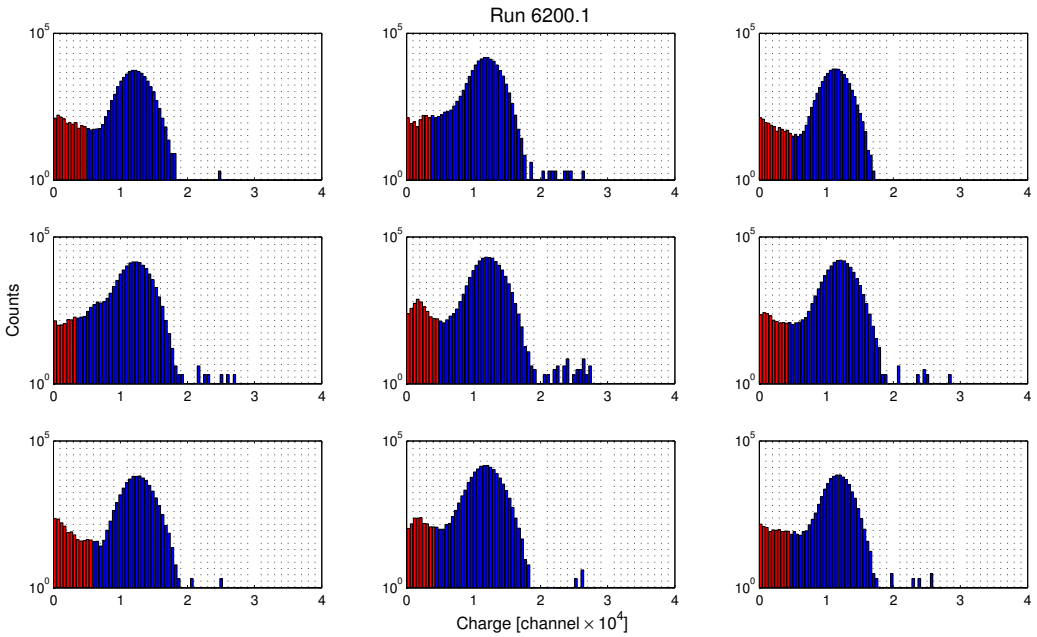

Figure 4.4: Double logarithmic plot of the QDC distribution of the nine UCN detector channels. The red distribution, below the threshold is accounted as background, the blue distribution as Signal.

time correction is usually below 3 ‰. So far no pile-up treatment is performed in the analysis which might become necessary when higher count rates are achieved in the future.

After the mentioned corrections are performed the relevant UCN counts of different steps of the μTimer of each cycle are summed up (see Fig. 4.5). Two timestamps are written to a separate log file, containing the start of the FASTER file (ExtEvU 0) and the start of the cycle[8] (ExtEvU 1). With this time difference and the timing information of the μTimer it is possible to sum up all events that occurred during the single steps of the μTimer and allot the summed up counts to the different UCN counting periods 'monitoring', 'spin up', and 'spin down'.

4.3.2 Cuts

A series of cuts was performed to select reasonable data out of the data set recorded. The cut criteria are based on systematic considerations, hardware malfunctions, or statistical considerations:

[8]More precisely the command to open the main neutron beam line shutter which marks the first action of any cycle with the intention to count neutrons.

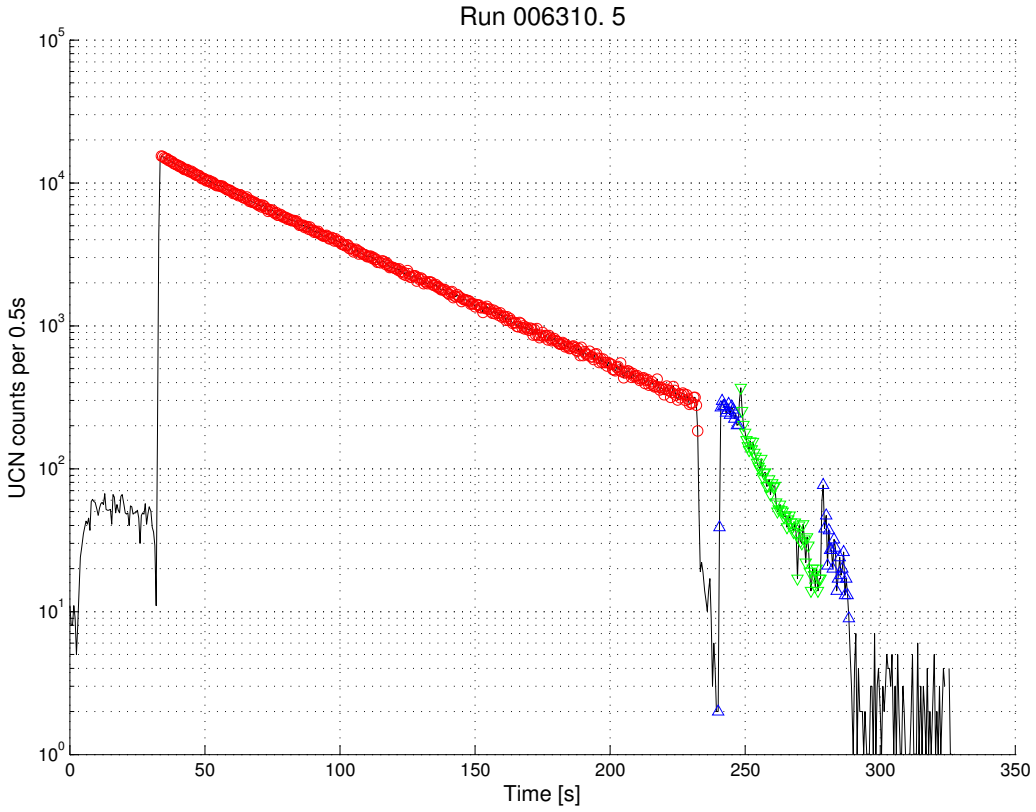

Figure 4.5: UCN time series of a typical nedm cycle. Plotted is the summed count rate of all nine detector channels. During the first 30 s UCN are filled into the chamber. The small increase in the count rate is due to the monitoring hole in the fill position (see Sec. 2.4.5). During the free precession time of 200 s UCN from the source are directly guided to the UCN detector. Around $t = 240$ s, the stored UCN are emptied into the detector with the spin flipper above the analyzer switched on for 30 s. The different UCN counting periods that are integrated are marked with: ○-'monitoring', △-'spin up', ▽-'spin down'.

- **Leakage currents** produce a systematic shift of the magnetic field (see Sec. 3.1.1). Thus any data with a measured current above 1 nA is rejected.

- If the **switch** is not in the correct position during the emptying period, the storage time above the foil will change, influencing the measured polarization due to the spin sequence. The usual position accuracy is 1 encodercount(e.c.) $\approx$ 1 mrad (see Fig. 2.17). Therefore all cycles with a position error bigger than 1 e.c. are considered as a switch malfunction and are rejected.

- Cycles with large **changes in the B_0-field** are disregarded, as these occur usually when the SULTAN magnet is ramping. Cuts are performed on changes between two consecutive cycles by looking at the difference between $f^i_{\mathrm{Hg}} - f^{i-1}_{\mathrm{Hg}} > 30\,\mu\mathrm{Hz}$ and deviations from the average field of the run larger than 150 pT.

- Significantly lower numbers in the **UCN counts** mean usually that the UCN source, or one of the valves towards the experiment did not work as expected, or that the network connection between the Faster-PC and Zeus-PC was interrupted (see Sec. 2.4.12). Therefore cycles with less than 50 UCN and cycles with a deviation of the monitor counts larger than three standard deviations from the run averaged monitor counts are rejected.

- The performance of the **Hg comagnetometer** needs to meet the specifications defined in Sec. 2.5.2 in order to effectively correct the UCN magnetometer from magnetic field changes. Thus the result of the online fit (which is used for this analysis) is used as a cut criterion. Cycles which have a χ^2/dof greater than two or smaller than 0.5 as well as cycles with an error on the fitted f_{Hg} larger than 5 µHz are removed from the data set.

To find reasonable values for the criteria concerning the Hg comagnetometer and the B_0-field, the χ^2/dof of the Ramsey resonance fit was studied. With the values stated above, 27 % of the data was rejected. 80 % of the cycles that were rejected do fulfill one cut criteria (see Fig. 4.6), showing that the choosen criteria are relativly independent. Most cuts are related to the performance of the Hg comagnetometer as shown in Figure 4.7. This also becomes apparent when looking at the cycle number of the cut cycles. The histogram in Fig. 4.8 shows that cycles around number 30 and 80 are more often rejected. This coincides with the polarity change

of the electric field that reduces the Hg comagnetometer performance (see Sec. 2.5.2). Hopefully more data can be accepted when using an offline fit of the Hg precession data.

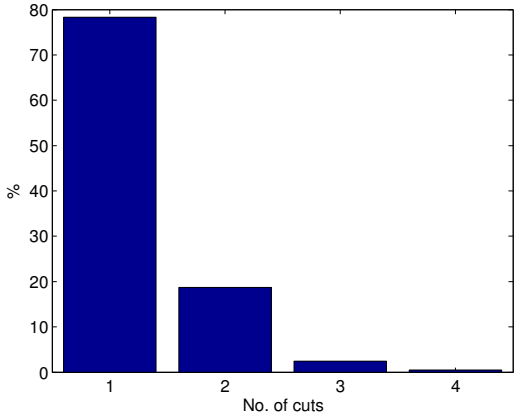

Figure 4.6: Most cycles that were cut, fulfilled only one or two cut criteria.

4.3.3 Correction of the data

The raw data is affected by magnetic field drifts and fluctuations of the neutron flux. These flaws however can be corrected using the Hg comagnetometer and the UCN monitor counts. The effect of these corrections is shown in Fig. 4.9. The analysis in this work is performed using the online analysis results of the Hg precession frequency which is based on the fitting method described in [GHI+98]. The raw Hg precession data is stored and can be reanalyzed at any time.

4.3.4 Extraction of the neutron frequency

Close to the resonance, the central fringe of the Ramsey resonance curve can be approximated with a cosine function. Comparison to numerical results have shown that the relative error in the resonance frequency due to the approximation is below 2×10^{-7} [May98] and thus is negligible. The number of neutrons in the different spin states at the end of a cycle is described in this approximation as:

$$N^i_{\uparrow\downarrow} = N^{\mathrm{avg}}_{\uparrow\downarrow}\left[1 \mp \alpha_{\uparrow\downarrow}\cos\left(\pi\frac{f_\mathrm{n} - f^i_\mathrm{RF}}{\upsilon}\right)\right], \tag{4.3}$$

with the average number of neutrons $N^{\mathrm{avg}} = \frac{N_{\max}+N_{\min}}{2}$ at the end of the cycle, $\alpha = \frac{N_{\max}-N_{\min}}{N_{\max}+N_{\min}}$ the visibility of the Ramsey resonance, f_n the resonance

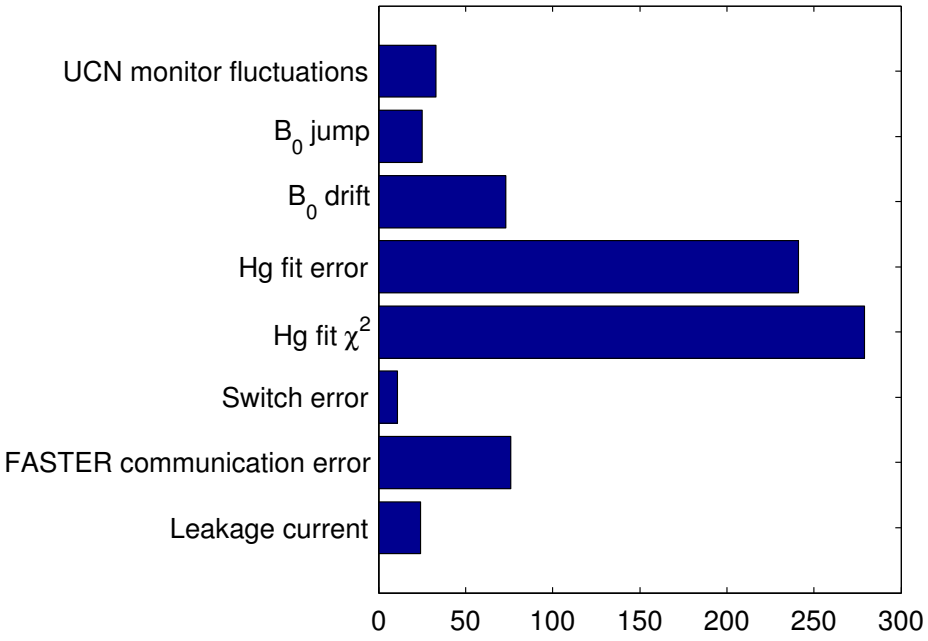

Figure 4.7: Visualization of the number of cycles cut by different criteria. Clearly, the Hg online fit together with the choosen cutting limits is the most influential cut. Using offline fitting of the Hg data might reduce the number of discarded cycles.

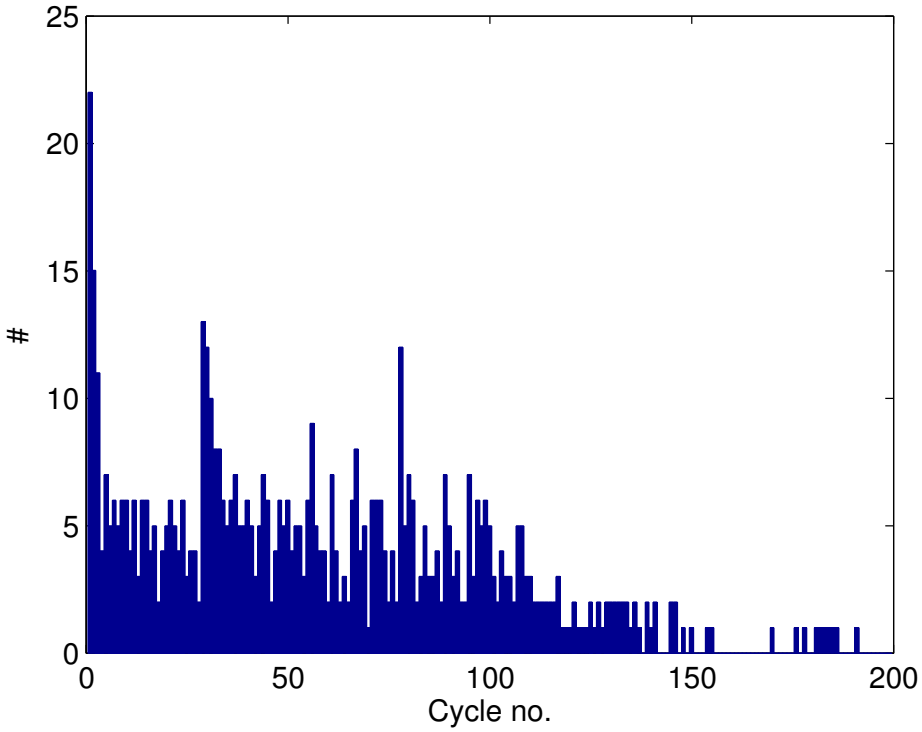

Figure 4.8: Histogram of the cycle number of cycles that have been cut. The general trend of lower entries towards higher cycle numbers is expected if one keeps in mind that most runs have less than 100 cycles. The peaks around cycle 30 and cycle 80 correspond to the polarity change of the E-field that leads to a decreased Hg performance. Also the current magnetic field is unknown when starting a run, leading to a rejection of the first cycle.

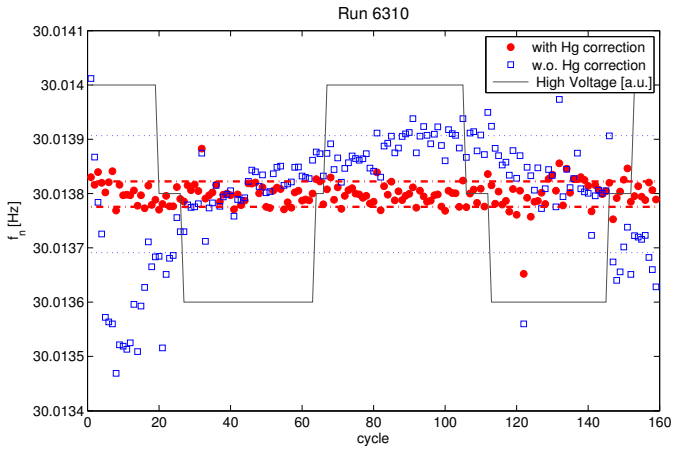

(a)

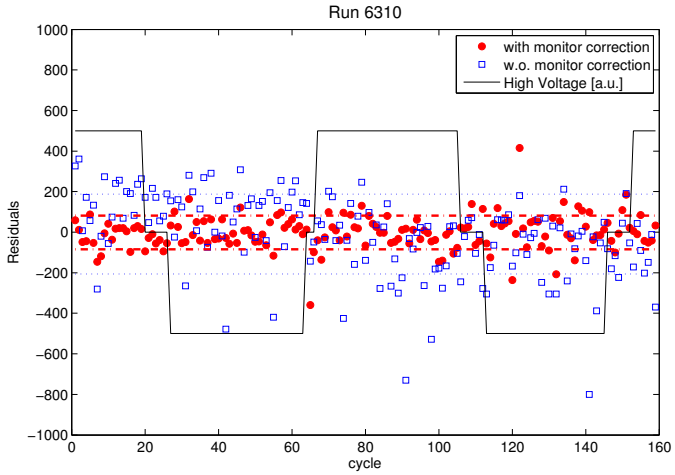

(b)

Figure 4.9: Example of the influence of corrections on data quality. Plotted is the corrected (○) and uncorrected (□) data for magnetic field drifts with the information of the Hg comagnetometer (a), and the correction of UCN counts using the UCN monitor information(b). The respectively other correction is preformed. The improvement is best seen by comparing the standard deviations of the corrected (- · -) and uncorrected (· · ·) data set. The fluctuations are (on this scale) independent of the direction of the electric field.

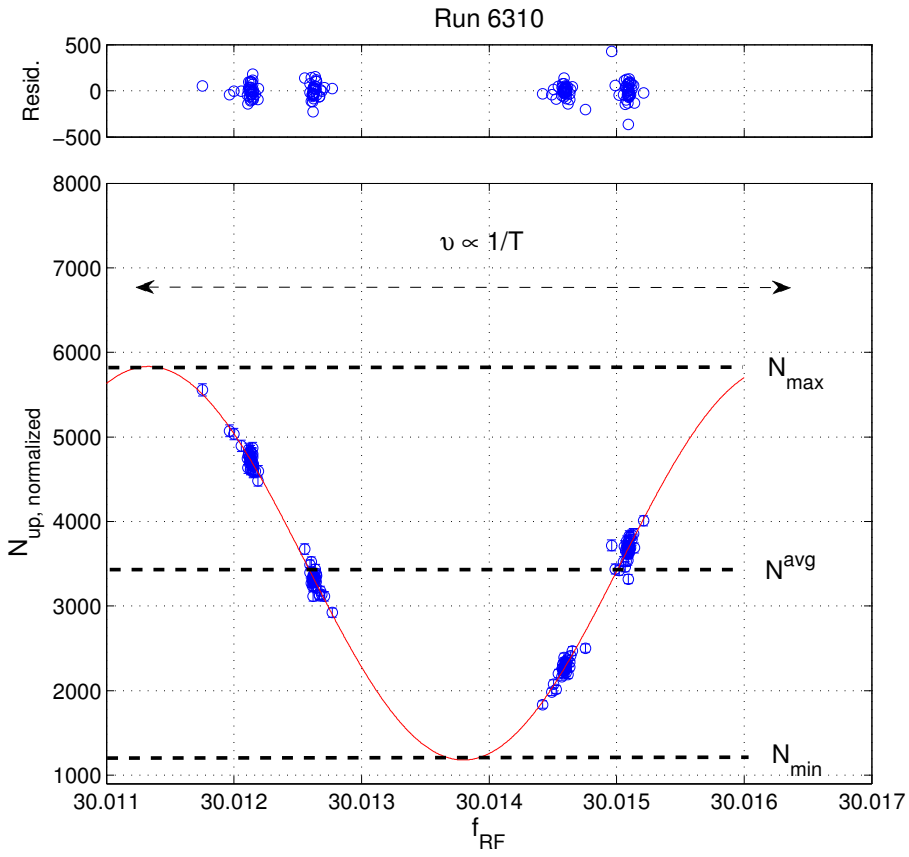

Figure 4.10: Illustration of cosine approximation fit. For details see text.

frequency of the neutrons and f^i_{RF} the frequency of the applied spin flip in cycle i and the width of the resonance $\upsilon = \frac{1}{2(T+4t_{\mathrm{RF}}/\pi)}$ as illustrated in Fig. 4.10. In addition also the asymmetry A between N_{up} and N_{down} counts is fitted to extract the neutron frequency:

$$A^i = \frac{N^i_\uparrow + N^i_\downarrow}{N^i_\uparrow - N^i_\downarrow} = A_0 + \alpha \cos\left(\pi \frac{f^i_{\mathrm{n}} - f^i_{\mathrm{RF}}}{\upsilon}\right). \tag{4.4}$$

For the rest of the document, the fit performed to the corrected data to extract the neutron precession frequency, is called 'Ramsey fit'. It is performed on the whole data of each run, as well as on parts grouped by the electric field status $(+\,0\,-)$.

4.3.5 Extraction of the electric dipole moment

The last step in the analysis is the extraction of the measured edm of the neutron. The simplest method to extract the frequency difference $\Delta f_\mathrm{n} = f_\mathrm{n}\uparrow\uparrow - f_\mathrm{n}\uparrow\downarrow$ would be a simple subtraction of the two values obtained from the fit of the Ramsey resonance. In order to also make use of the data taken without electric field, a different approach was used. As we can see from (2.1) f_n shifts linearly with the electric field strength, thus a linear fit of

$$f_\mathrm{n}(E) = \frac{2}{h} d_\mathrm{n} E \mathrel{\hat{=}} mE, \tag{4.5}$$

results in a slope m from which d_n can be extracted as $d_\mathrm{n} = \frac{mh}{2}$. An example is shown in Fig. 4.11. This method can also be used to extract d_Hg, with the average frequency f_Hg at different electric fields, calculated in the individual runs.

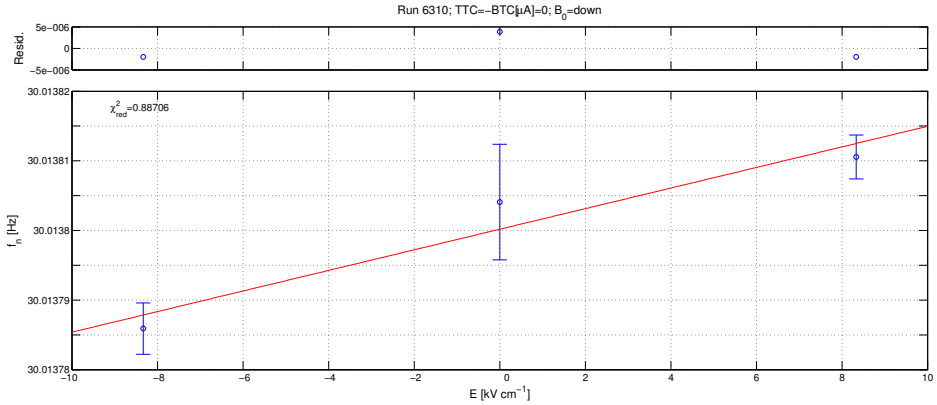

(a)

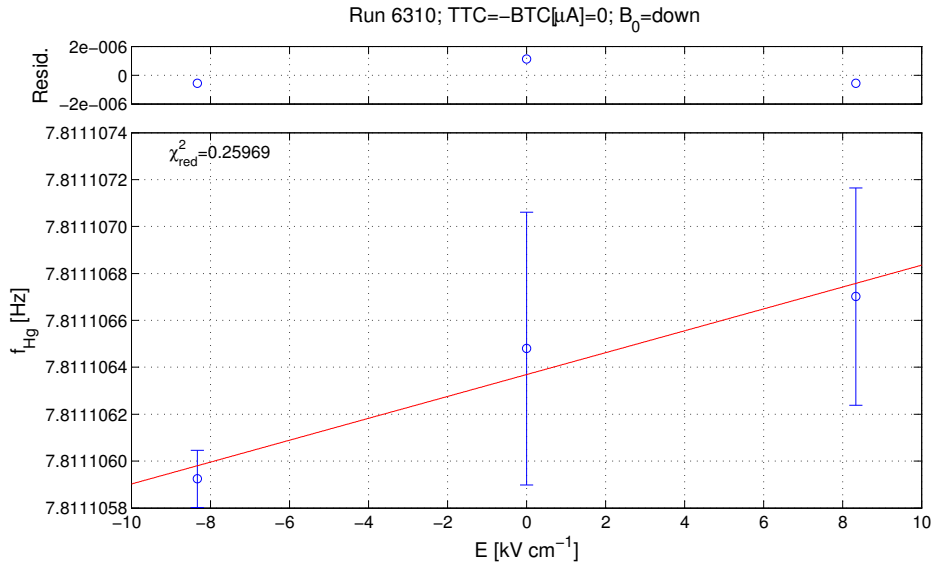

(b)

Figure 4.11: Extraction of d_n with a fit of (a) $f_\mathrm{n}(\mathrm{E})$ and (b) $f_\mathrm{Hg}(\mathrm{E})$. The neutron frequency is a combination of the fit results of N_up, N_down, and A.

4.4 Combining different runs

After performing the analysis steps above, a database is created, containing all data and results from the steps above. This database can be further analyzed and interpreted. In the following section we will look at some of the results and give a first upper limit of d_n that has been measured at PSI, which also is the first result of the nEDM-experiment since [Kne09].

4.4.1 Statistical analysis of the Ramsey fit

It is important to understand if the cosine approach is a good representation of the data, or if additional systematic errors are hidden in the data, that would lead to a wrong result. This can be done e.g. by looking at the distribution of the residuals of the Ramsey fit or by checking the distribution of χ^2:

Residuals The residuals (UCN counts) of the Ramsey fit to the complete run should be normally distributed if the fit is a good representation of the data. The statistical moments (mean, skewness, and kurtosis) of a set of n residuals r_i are defined as

$$\text{mean} : \mu = \frac{1}{n}\sum_{i=1}^{n} r_i, \tag{4.6}$$

$$\text{skewness} : \gamma_1 = \frac{\frac{1}{n}\sum_{i=1}^{n}\left(r_i-\mu\right)^3}{\sigma^3}, \tag{4.7}$$

$$\text{kurtosis} : \gamma_2 = \frac{\frac{1}{n}\sum_{i=1}^{n}\left(r_i-\mu\right)^4}{\sigma^4} - 3, \tag{4.8}$$

with σ the standard deviation of r_i. A negative/positive skewness means that the distribution is asymmetric towards the values smaller/larger than the mean. The kurtosis characterizes the amount of data in the center or among the shoulders of the distribution. All three moments should be zero for a normal distribution. An overview of these values for all runs is shown in Fig. 4.12.

The distribution of the statistical moments of the residuals can be compared to the output of the MATLAB *randn* function. This function produces normally distributed pseudorandom numbers for which the statistical moments were calculated. The results are compared in Tab. 4.1. It is obvious that residuals are not fully normal-distributed. Some runs have statistical moments much larger than zero (see Fig. 4.12). These are

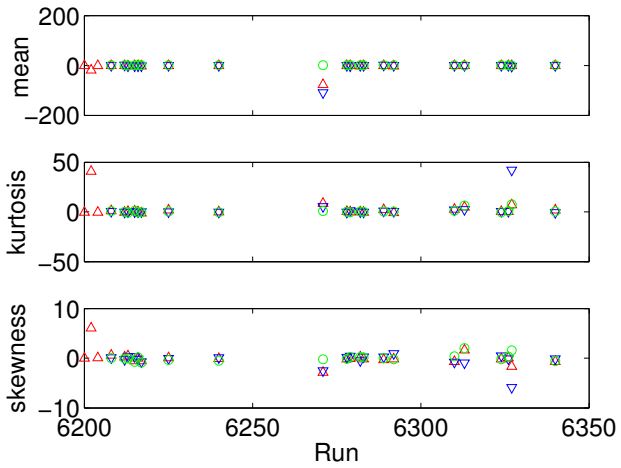

(a)

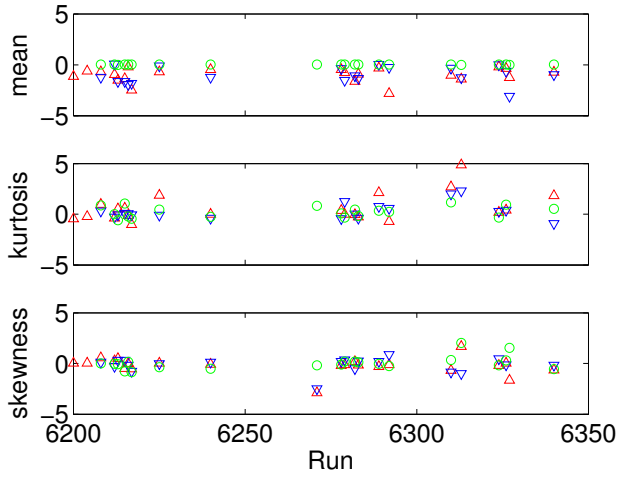

(b)

Figure 4.12: Mean, skewness and kurtosis of the Ramsey fit residuals (a), and a zoom of these values(b). The different symbols show the results for the fit of N_{up}(△), N_{down}(▽) and the asymmetry(◯).

6204, 6271 (switch malfunction and an ill log file was created on which a cut could be made) and 6326 (magnetic field change which passed the selected cut criteria). Excluding these runs from $\overline{\mu}$, $\overline{\gamma_1}$, and $\overline{\gamma_2}$ brings the values closer to expectations, but they are still incompatible with zero.

	$\overline{\mu}$	$\overline{\gamma_1}$	$\overline{\gamma_2}$
N_{up}	-4.3±3.3	0.8±0.4	-0.06±0.15
N_{down}	-5.5±4.6	0.3±0.2	-0.09±0.13
Asym.	0.0004±0.0005	0.43±0.25	-0.049±0.114
N_{up}*	-1.03±0.15	0.55±0.31	-0.023±0.111
N_{down}*	-1.03±0.16	0.23±0.19	0.007±0.116
Asym.*	-0.0001±0.00003	0.48±0.31	-0.06±0.14
randn(100×20)	0.005±0.02	-0.008±0.10	-0.022.±0.061

Table 4.1: Statistical moments of residuals and MATLAB *randn* of size (cycles×runs). Calculated is always the mean of the distribution of the statistical moments. The values with asterisk are calculated without runs 6204, 6271, and 6326.

χ^2 distribution The distribution of the χ^2 of the different Ramsey fits can be compared to the χ^2 probability density function defined by

$$\mathrm{pdf}_\nu(x) = \frac{x^{\frac{\nu-2}{2}} e^{-\frac{x}{2}}}{2^{\frac{\nu}{2}} \Gamma\left(\frac{\nu}{2}\right)}, \tag{4.9}$$

for ν degrees of freedom (dof). Here Γ is the Gamma function. For each run N_{up}, and N_{down}, as well as the asymmetry are fitted for the three electric fields conditions (+,-,0). So in total each run has six plus three χ^2 values. As all fits have a different ν_i, they were normalized to the mean $\overline{\nu}$ of all fits

$$\chi_i^2 = \frac{\chi_i^2}{\nu_i}\overline{\nu}. \tag{4.10}$$

A histogram of this quantity was then fitted with (4.9) (see Fig. 4.13). The normalized χ^2 values from the Ramsey fits are roughly distributed according to (4.9). However the ν_{fit} one obtains from the distribution, is different from $\overline{\nu}$ obtained from the individual dof.

4.4.2 $\mathcal{R}$-curve measurement

As mentioned in Sec. 4.3, a small part of the data was measured at zero electric field. This data can be used to determine the ratio of precession

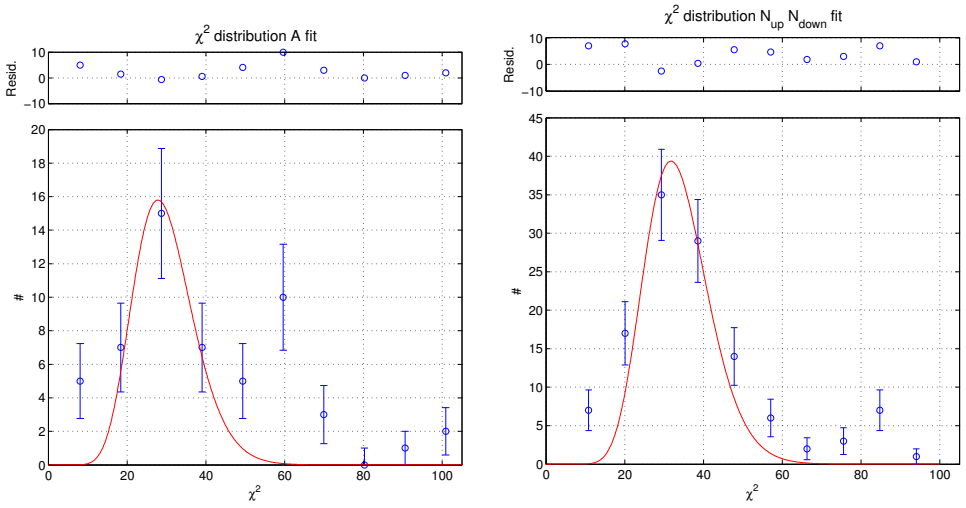

(a) (b)

Figure 4.13: χ^2 distribution of the Ramsey fits. The result of the fit yields a different ν_{fit} than the $\overline{\nu}$ used for the normalization. For the asymmetry (a) we get $\nu_{\text{fit}} = 29$ and $\overline{\nu} = 23$. For the N_{up}, N_{down} fits (b) the difference is $\nu_{\text{fit}} = 34$ to $\overline{\nu} = 23$.

frequency of Hg-atoms and UCN. Figure 4.14 shows the data for both B_0 directions together with a linear fit. Using (3.34) one can see that from the linear fit the center-of-mass offset between UCN and Hg can be extracted. With

$$\mathcal{R} = \mathcal{R}_0 \pm \frac{\Delta h}{B_0}\frac{\partial B_{0z}}{\partial z} \mathrel{\hat{=}} b + m \times x, \tag{4.11}$$

we can extract

$$\Delta h = \pm m \frac{\gamma_{\text{Hg}}}{\gamma_{\text{n}}} B_0, \tag{4.12}$$

with the plus (minus) sign for B_0-up (B_0-down). Taking the average B_0-field of all runs used for the fit one gets

$$\begin{aligned} \Delta h_{\text{up}} &= (3.0 \pm 0.1)\,\text{mm}, \\ \Delta h_{\text{down}} &= (3.0 \pm 0.3)\,\text{mm}, \\ \overline{\Delta h} &= (3.0 \pm 0.2)\,\text{mm}. \end{aligned}$$

Also the shift of $\mathcal{R}_0 = \left(\frac{f_{\text{n}}}{f_{\text{Hg}}}\right)_{G=0} \times \left|\frac{\gamma_{\text{Hg}}}{\gamma_{\text{n}}}\right|$ away from unity can be studied. Attributing the difference to a quadrupole field one also has a measure of the

systematic effect described in Sec. 3.2.2. From the fit to the data we get

$$\begin{aligned}\mathcal{R}_{0\,\mathrm{up}} &= (1.0000241 \pm 0.0000008),\\ \mathcal{R}_{0\,\mathrm{down}} &= (1.0000228 \pm 0.0000019),\\ \Delta\mathcal{R}_0 &= (1.3 \pm 2.1)\times 10^{-6}.\end{aligned}$$

Rewriting (3.38), the difference $\Delta\mathcal{R}_0$ corresponds to a quadrupole field $\Delta\overline{B}_\perp$ of

$$\Delta\overline{B}_\perp^2 = \overline{B}_{\perp,\downarrow}^2 - \overline{B}_{\perp,\uparrow}^2 = 4\,\Delta\mathcal{R}_0\,B_0^2. \tag{4.13}$$

With $B_0 = 1.030\,\mu\mathrm{T}$, the average magnetic field magnitude of all measurements, this results in a quadrupole difference of

$$\Delta\overline{B}_\perp^2 = (-5.5 \pm 8.9)\,\mathrm{nT}^2.$$

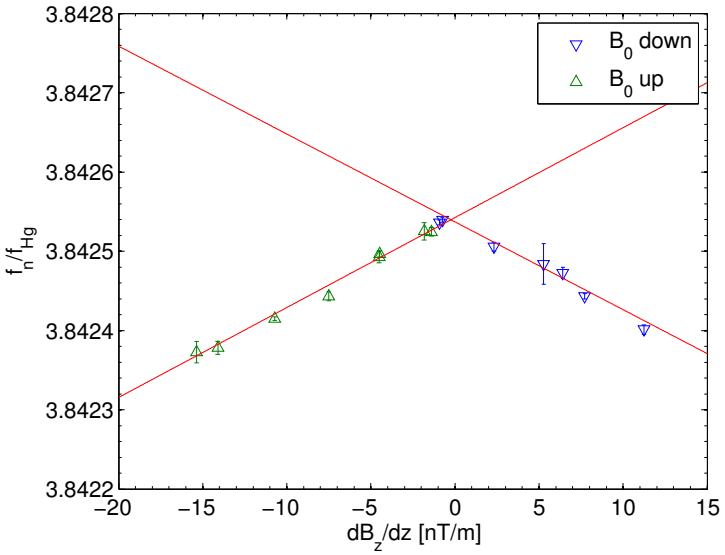

Figure 4.14: $\mathcal{R}$-curve extracted from the subset of the 2012 nedm data set measured without electric field. Only runs with working CsM were used, as these were used to extract the vertical gradient. The linear fits $f(x) = m\times x + b$ to the data results in $m_{\mathrm{up}} = 1.13(5)\times 10^{-5}\,\mathrm{m\cdot nT^{-1}}$, $b_{\mathrm{up}} = 3.8425424(4)$, $m_{\mathrm{down}} = -1.1(1)\times 10^{-5}\,\mathrm{m\cdot nT^{-1}}$, and $b_{\mathrm{down}} = 3.842537(1)$.

4.4.3 Neutron and ^{199}Hg edm for all runs

Figure 4.15(a) shows the value of d_{n} as a function of the run number. As already seen in Sec. 4.4.1, the runs that gave a bad fit result (6271 and 6326), also lead to a large error on d_{n}. A weighted average of all runs result in $d_{\mathrm{n}} = (0.2 \pm 0.9) \times 10^{-25}\, e \cdot \mathrm{cm}$. The same analysis can be performed with the Hg channel alone (see Fig. 4.15(b)). Here the weighted average of all runs is $d_{\mathrm{Hg}} = (-0.6 \pm 0.2) \times 10^{-25}\, e \cdot \mathrm{cm}$. It is interesting to notice that the run 6271 also has the largest error in the Hg channel.

4.4.4 Crossing point analysis

The value above now should still contain the geometric phase effect for the Hg comagnetometer. The average gradient extracted with the CsM (see Fig. 4.14) is $\overline{G} = 1.57\,\mathrm{nT} \cdot \mathrm{m}^{-1}$ and the maximum gradient is $G_{\mathrm{max}} = 15.3\,\mathrm{nT} \cdot \mathrm{m}^{-1}$. From the measurements of the geometric phase (see Sec. 3.2.2) one expects this gradient to result in an average false effect of $d_{\mathrm{n}} = 0.15 \times 10^{-25}\, e \cdot \mathrm{cm}$, and a maximum of $d_{\mathrm{n}} = 1.5 \times 10^{-25}\, e \cdot \mathrm{cm}$. Thus the crossing point analysis described in Sec. 3.2.2 is applied to the data set and the measured d_{n} is analyzed as a function of $\mathcal{R}$. Figure 4.16 shows the data and global linear fit with a common value for the absolute slope, but different intercepts.

The fit result of $k = (1.02 \pm 0.62) \times 10^{-20}\, e \cdot \mathrm{cm}$ is, within the errors, in agreement with the theoretical slope from (3.36) of $k^{\mathrm{theo}} = 1.54 \times 10^{-20}\, e \cdot \mathrm{cm}$. At the crossing point of the data taken at B_0-down and B_0-up of $\mathcal{R} - 1 = (-2.8 \pm 1.5) \times 10^{-5}$ the nedm is

$$d_{\mathrm{n}} = (1.42 \pm 2.54) \times 10^{-25}\, e \cdot \mathrm{cm}.$$

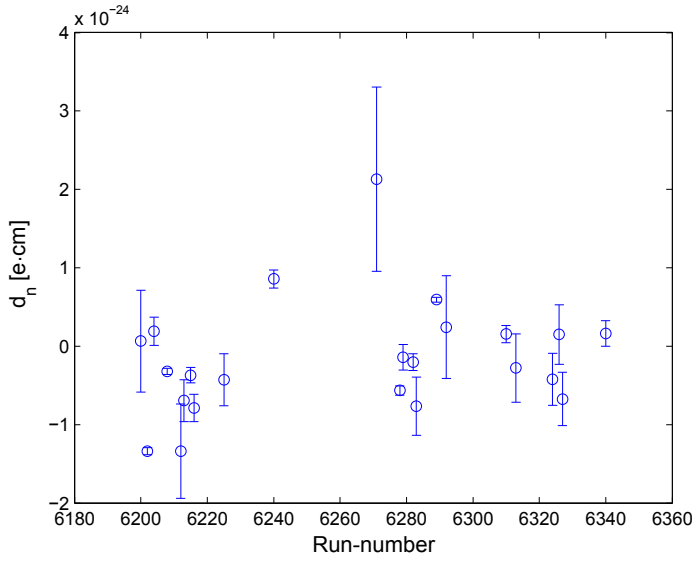

(a)

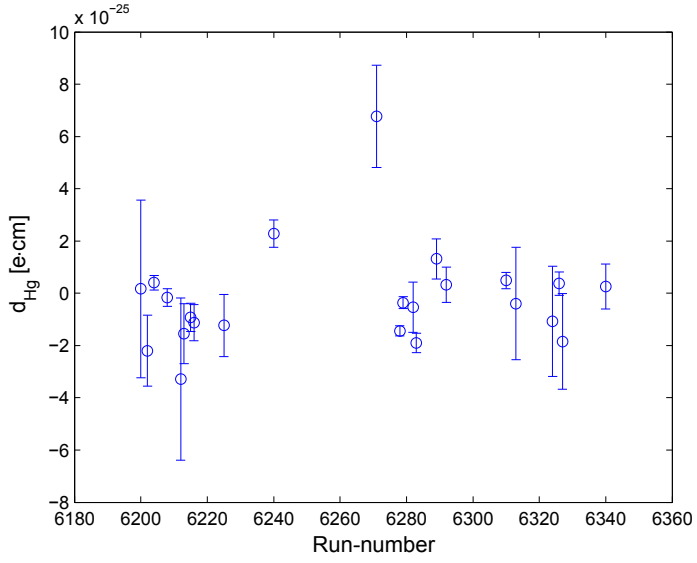

(b)

Figure 4.15: The extracted edm of the neutron (a) and ^{199}Hg (b) for the different runs.

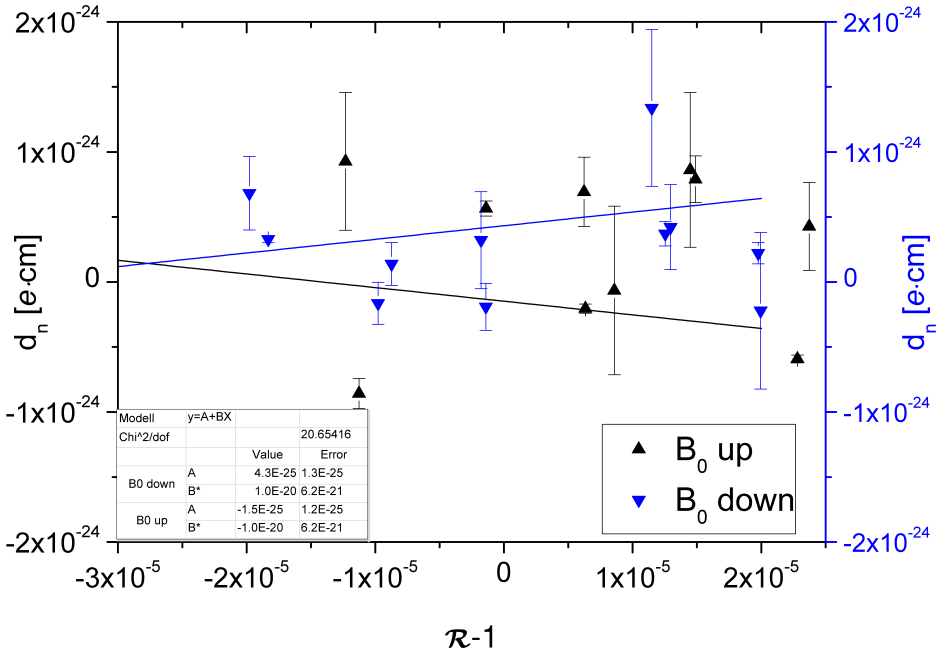

Figure 4.16: Measured nedm as a function of the relative frequency shift between UCN and Hg-atoms. A global linear fit with a common slope $|k|$ but different intercepts is performed to the data.

4.5 Results and discussion

The results of the analysis are summarized and discussed in the following section.

Technical remarks The data taken in November 2012 suffered from two technical issues, that might influence its quality. Due to a firmware error in the CsM-control electronics, the amplitude of the spin flip signal applied to the sensors became distorted and was not a perfect sine function. In general the absolute value of the CsM is known to some 10 pT. The distorted RF could however not only lead to an unknown offset in the CsM readings, but also might influence the precession frequency of the UCN and the Hg-atoms. The malfunction was only discovered in the middle of the data taking, and thus the data after run 6310 was taken with the CsM switched off. About 60% of all runs where recorded with the CsM electronic switched on. As the effect on the actual CsM values is hard to estimate, in the analysis the error on the CsM measurements itself is assumed to be as small as usual. The results however might have an unknown systematic effect, and the interpretation might be incorrect.

A second issue concerns the applied $\pi/2$-pulse for the UCN in the precession chamber. The gating module inside the main DAQ board (see Sec. 2.4.12) malfunctioned and produced an unwanted envelope around the UCN sine spin flip signal. Using a simple relay the shape could be recovered as depicted in Fig. 4.17. However a mechanical relay is always suffering from contact bounce and the timing is not as precise as with purely electronic devices. The relay used was measured by opening and closing it more than 50000 times. The relay needs about (1.3885 ± 0.0001) ms to open and (2.4767 ± 0.0003) ms to close, so the $\pi/2$-pulse is actually not 2 s but only (1.9989118 ± 0.000004) s long, which is a deviation of 0.5‰(see Fig. 4.18).

Results $\mathcal{R}$, extracted from the subset of data taken with zero electric field, as a function of the magnetic field gradient, measured with the CsM was analyzed. The linear fit to the data had a large χ^2/dof of 5.7 for B_0-down and 2.2 for B_0-up. This could be due to technical difficulties the CsM firmware created at that time. With this fit the center-of-mass offset of UCN and Hg-atoms was determined to be $\Delta h = (3.0 \pm 0.2)$ mm. Also the quadrupole difference could be estimated to be $\Delta\overline{B}_{\perp}^{2} = (-5.5 \pm 8.9)\,\mathrm{nT}^2$. If this value is confirmed by magnetic field mapping with a fluxgate and vector CsM magnetometer, the systematic effect arising from this, is one of the major systematic errors. However, the field can be optimized using correction coils.

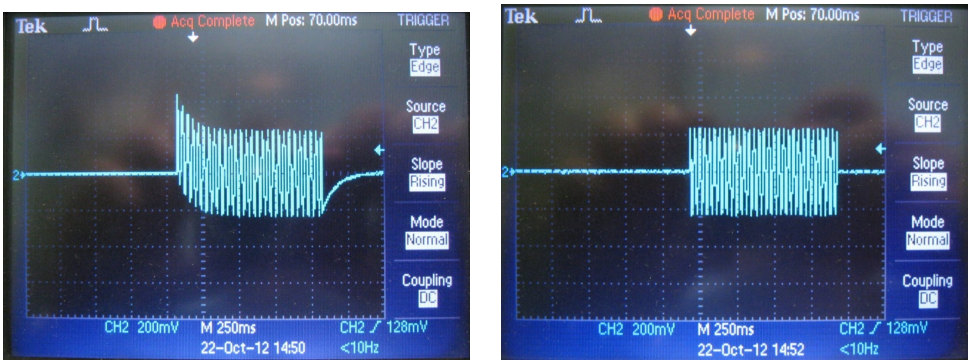

(a) (b)

Figure 4.17: Usage of a relay to gate the UCN spin flip signal in and out. The two screen shots show the 2 s long RF signal used for the $\pi/2$-pulse for the UCN as measured with a scope in parallel to the coil. The gate module of the DAQ board (a) produces a distorted signal. Using a mechanical relay to cut out the middle of a longer signal results in the desired shape.

Figure 4.18: A function generator turned the relay on and off, used for the $\pi/2$-pulse of the UCN, every second. The time delay between the signal of the generator and the actual opening or closing was measured for more than 50000 cycles. The relay needs (2.4767 ± 0.0003) ms to close (shown here) and (1.3885 ± 0.0001) ms to open.

For the sensitivity of the present data set, systematic errors as appraised in Sec. 3, are insignificant for the total error.

A simple averaging of the edm over all runs results in $d_{\mathrm{Hg}} = (-0.6 \pm 0.2) \times 10^{-25}\, e \cdot \mathrm{cm}$ and $d_{\mathrm{n}} = (0.2 \pm 0.9) \times 10^{-25}\, e \cdot \mathrm{cm}$. This value can be compared to the last result that was achieved in 2007, with the nEDM-experiment still at Ill. In that measurement a simple average of data collected gave a result of $d_{\mathrm{n}} = (0.17 \pm 6.57) \times 10^{-25}\, e \cdot \mathrm{cm}$ [Kne09] from a data set of three days.

Analyzing the values of d_{n} as a function of $\mathcal{R}$ resulted in a slope of $k = (1.02 \pm 0.62) \times 10^{-20}\, e \cdot \mathrm{cm}$ which is in agreement with the theoretical expectations of $k^{\mathrm{theo}} = 1.54 \times 10^{-20}\, e \cdot \mathrm{cm}$ derived from (3.36). At the crossing point, this translates to an edm of $d_{\mathrm{n}} = (1.42 \pm 2.54) \times 10^{-25}\, e \cdot \mathrm{cm}$ and together with the systematic effects listed in Tab. 3.1 the final result is

$$d_{\mathrm{n}} = (1.43 \pm 2.54_{\mathrm{stat.}} \pm 0.02_{\mathrm{sys}}) \times 10^{-25}\, e \cdot \mathrm{cm}, \tag{4.14}$$

which corresponds to an upper limit of $|d_{\mathrm{n}}| \leq 6.4 \times 10^{-25}\, e \cdot \mathrm{cm}$ (95%C.L.).

Discussion This result (4.14) is not fully satisfactory, as the reduced χ^2 of the linear fit is surprisingly large. This seem to point to the fact, that there is a remaining unknown systematic which was missed in the analysis. Looking at Fig. 4.15(a) one can see that there are several runs with $|d_{\mathrm{n}}| \approx (1.0 \pm 0.1) \times 10^{-24}\, e \cdot \mathrm{cm}$. An example is run 6289. Figure 4.19 shows the leakage current and the high voltage data for this run. Apart from the usual peaks in the leakage current data that are expected due to ramping and shutter movements there are additional peaks. This could be a hint for discharges that influence the magnetic field in a way that is not compensated with the Hg comagnetometer (uncompensated B drift). The fact that for the last third of the data taking the electric field of only $E = 8.3\,\mathrm{kV} \cdot \mathrm{cm}^{-1}$ had to be reduced by another 30 %, is also a sign that the HV conditions were not ideal.

Moreover the whole data analysis is performed with the online fit results of the Hg comagnetometer signal. Any error in the frequency extracted could result in the observed problems like the non-Gaussian distribution of the Ramsey fit residuals, the large χ^2 in the $\mathcal{R}$-curve fit and the nedm result. The relative error however would need to be of the order $\mathcal{O}(10^{-5})$, which is not very likely. It is anyway interesting to redo the analysis once the offline analysis of the Hg comagnetometer data is ready.

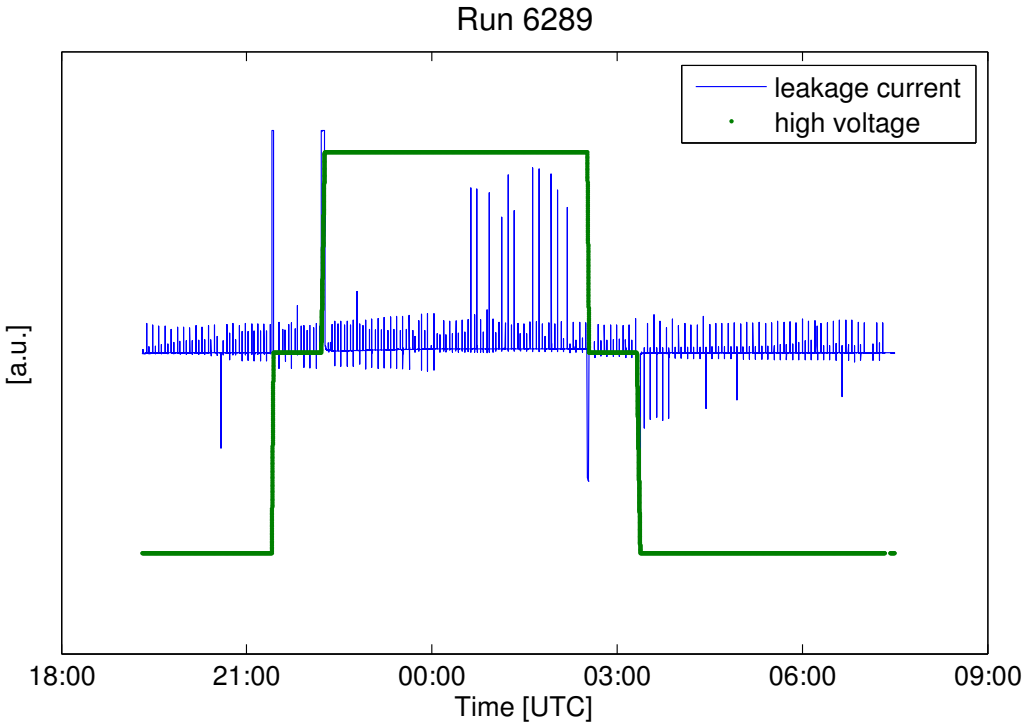

Figure 4.19: Leakage current and high voltage of run 6289. Apart from the expected peaks for the ramping of the HV and the shutter movements, there are other events. In particular the signals between midnight and 3 a.m. could be a series of short sparks that might have influenced the magnetic field. The 10 Hz filter in the leakage current could suppress sparks on a shorter time scale.

Chapter 5

Non-metallic electrodes

This chapter will describe the investigations made in order to build non-metallic electrodes. The term 'non-metallic' can be misleading and will be explained. Of course electrodes need to be conductive in order to be charged up and create an electric field that is required for the measurement of the edm. At the same time, any conductor will create noise due to the thermal movement of charge carriers. To diminish this noise, the amount of conducting material (metal) has to be reduced. A possible solution is to create a composite structure from an insulating material that defines the shape and the mechanical properties of the electrode and a thin conducting surface layer. This is referred to in the following as non-metallic.

5.1 Motivation for investigating non-metallic electrodes

Johnson-Nyquist noise Any form of random magnetic signal or noise will influence the measurement of the nedm. As the noise is not correlated with the direction of the electric field no systematic effect or false edm arises from it. However, the sensitivity of a magnetometer is limited by the environmental noise. Figure 5.1 shows the sensitivity of the UCN magnetometer as a function of the counted UCN according to (2.6).

In the design goal of the n^{2}EDM-experiment, the sensitivity of the UCN magnetometer will be of around $\sigma(B) \approx 0.2\,\mathrm{pT}$. A comagnetometer like ^{199}Hg (or possible external magnetometers like superconducting quantum interference devices (SQUIDs), ^{133}Cs, or ^{3}He magnetometers) need to be about a factor 10 better in order not to lose the sensitivity of the UCN magnetometer due to corrections for magnetic field drifts. In the following,

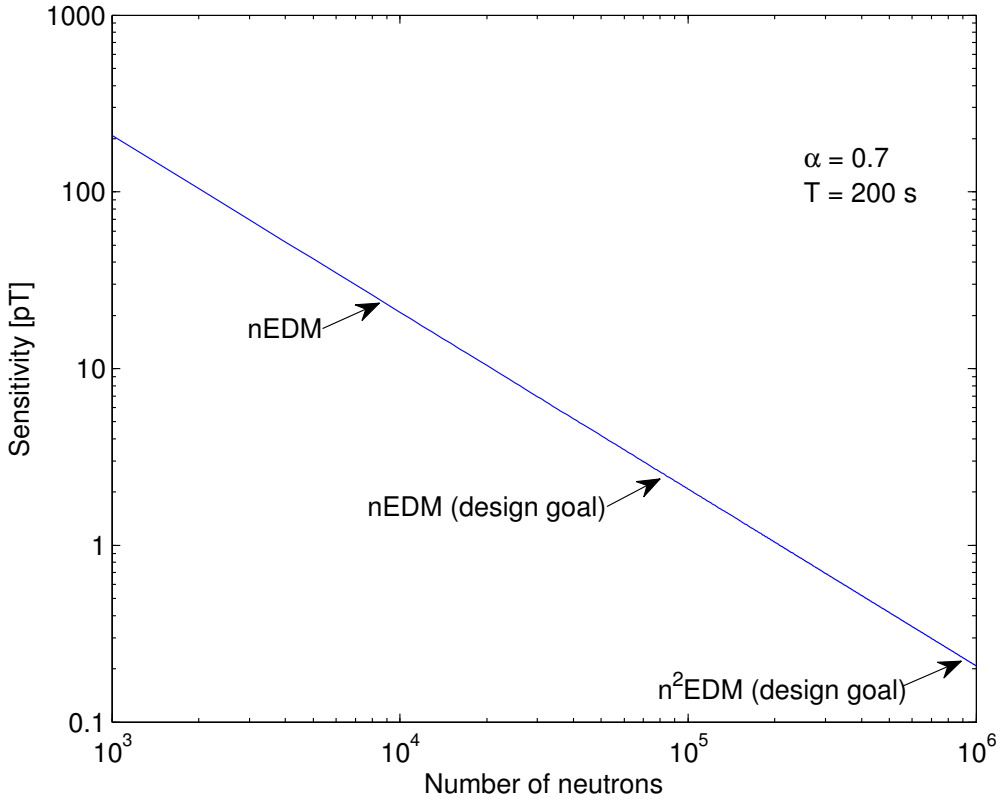

Figure 5.1: Sensitivity of the UCN magnetometer per cycle as a function of the UCN counts at the end of a cycle with 200 s free precession time and $\alpha = 0.7$.

magnetic noise of

$$B_{\mathrm{n}} \leq 0.02\,\mathrm{pT}/\sqrt{\mathrm{Hz}}$$

will be the noise limit that should be achieved. At this sensitivity level the intrinsic Johnson-Nyquist noise (JNN) coming from conductors close to the magnetometers can limit the sensitivity, as numerical calculations showed (see Sec. 5.2). The metallic electrodes are a fundamental part of the experiment and their distance to the Hg and UCN magnetometer is not adjustable at will. Thus reducing the noise is only possible by changing the material composition.

Magnetization Apart from noise considerations, ferromagnetic and paramagnetic impurities are more common in metals than in e.g. organic polymers, due to the production process. A measurement of magnetic properties for different materials can be found e.g. in [SJB+09]. Materials with ferromagnetic impurities (e.g. Fe or Ni) can be magnetized during the experiment by currents related to the creation of the electric field (see Fig. 5.2). Systematic effects like the uncompensated B drift (see Sec. 3.1.5) are directly related to magnetization of material close to or even within the precession chamber. These systematics can be suppressed by a carefull selection of materials like carbon fiber reinforced plastic (CFRP) as measurements showed (see Fig. 5.3).

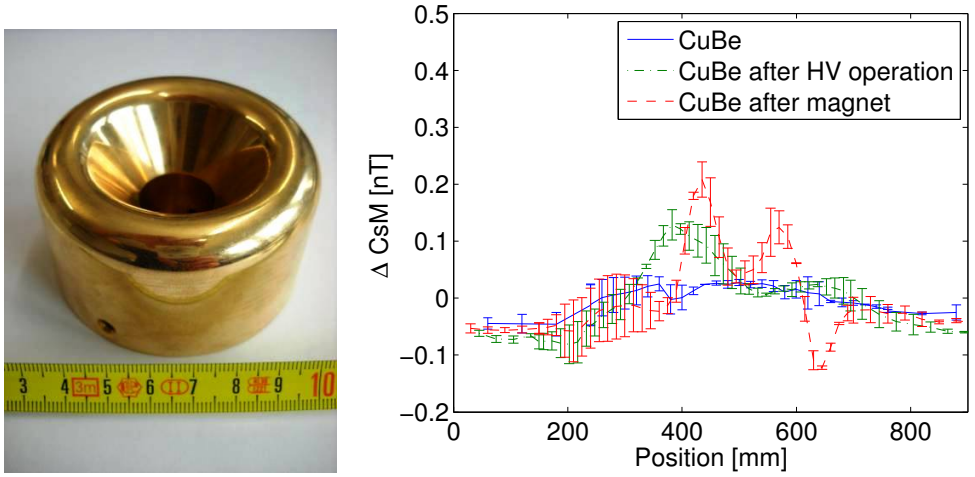

(a) (b)

Figure 5.2: (a) Shows a CuBe piece of the original high voltage system that connected the feedthrough with the top electrode. (b) Measurements in a gradiometer (see Sec. A) showed that this piece got magnetized after several weeks of high voltage operation. Exposing it to a permanent magnet ($B \approx 1.3\,\mathrm{T}$) gave an even stronger signal.

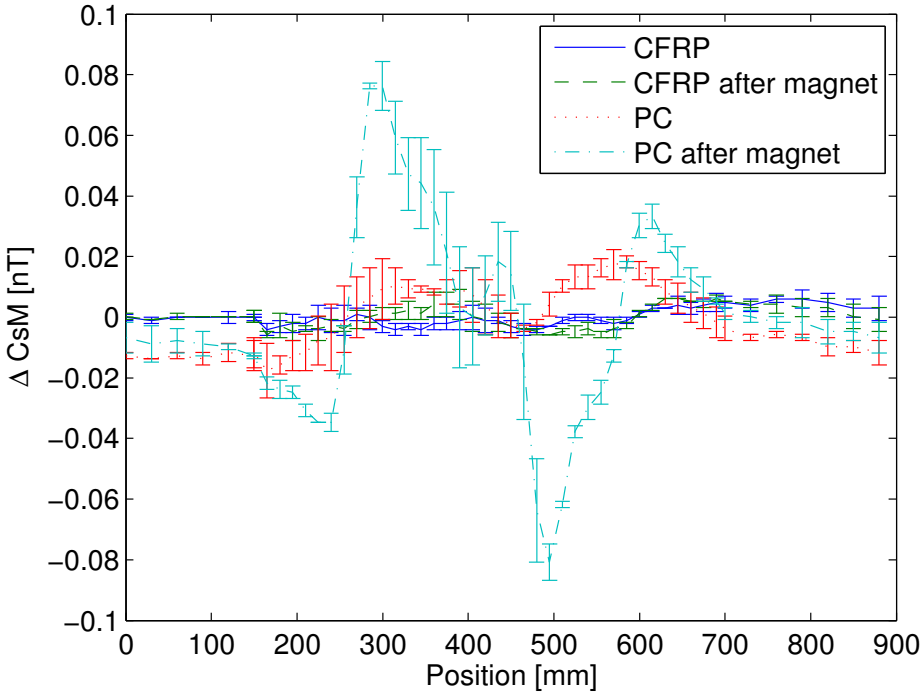

Figure 5.3: Magnetization of PC and CFRP: After a first measurement in a gradiometer (see Sec. A) the samples were exposed to a permanent magnet with $B \approx 1.3\,\mathrm{T}$. Carbon fiber reinforced plastic (CFRP) is less influenced by the magnetic field than polycarbonate (PC).

5.2 Numerical calculations of Johnson-Nyquist noise

The source of noise that has its origin in all metallic parts of the experiment is called Johnson-Nyquist noise (JNN). It was discovered first by J.B. Johnson in 1927 [Joh28] when investigating the noise of amplifier tubes as a dependence of the connected amplifier and one year later theoretically explained by N. Nyquist [Nyq28]. In their initial work they found that a resistor at a temperature T, with the real part of its impedance $R(\omega) = \Re(Z(\omega))$, connected to an amplifier with a transmission function $Y(\omega)$ showed a mean square noise current of:

$$\bar{i}^2 = \frac{2kT}{\pi} \int_0^\infty d\omega \, R(\omega)|Z(\omega)|^2, \tag{5.1}$$

with the Boltzmann constant k. Thus the noise they measured was a simple function of the resistance and the temperature of the conductor connected to the amplifier, and independent of shape or material. This current will create a magnetic field that will influence the sensitivity of magnetometers as used in edm experiments. In connection with biomagnetic measurements using SQUIDS, several papers developed models to describe this magnetic field for different geometric shapes. The phenomenological model for infinite conducting slabs, developed by [VP84], not only agreed with measurements, it also formed the basis for later work e.g. [NMK96, MT05]. A script[1] was developed based on [VP84] using numerical integration to calculate the noise of the electrodes in the nEDM, and n^{2}EDM-experiment. In the following the general concept of the model is recapitulated shortly.

Let us consider a volume with a conductivity σ at a temperature T that can be divided into small volume elements $\Delta V = \Delta x \Delta y \Delta z$ (see Fig. 5.4). In the case of a shortened resistor for a frequency interval Δf (5.1) becomes

$$\bar{i}_j^2 = \frac{4kT\Delta f}{R_j}, \tag{5.2}$$

for the mean current in direction $j = [x, y, z]$ of the volume element ΔV. The resistivity R_j in e.g. x-direction is given as

$$R_x = \frac{1}{\sigma}\frac{l}{A} = \frac{1}{\sigma}\frac{\Delta x}{\Delta y \Delta z}. \tag{5.3}$$

[1] Wolfram Mathematica, version 7.0.1.0

One can now define a current dipole $P_j = i_j \Delta j$ in each ΔV and with (5.2) and (5.3) we see that the mean square current dipole is

$$\overline{P}_x^2 = \bar{i}_x^2 \Delta x^2 = 4kT\sigma\Delta f \Delta V = \overline{P}_y^2 = \overline{P}_z^2. \tag{5.4}$$

Using Maxwell equations it is in principle possible to find a transfer function $\boldsymbol{g}_j(\boldsymbol{r}, \boldsymbol{r}', f)$, i.e. a Green's function, so that

$$B_j(\boldsymbol{r}) = \boldsymbol{g}_j(\boldsymbol{r}, \boldsymbol{r}', f)\boldsymbol{P}. \tag{5.5}$$

However, $\boldsymbol{g}$ can be derived analytically only for certain geometries, like an infinite slab. Under the assumption that the JN currents in all ΔV are uncorrelated, integrating over the volume of the conductor will result in the RMS spectral density of the magnetic field noise of

$$B_{n,j} = \sqrt{\frac{\overline{B}_j^2}{\Delta f}} = \sqrt{\int_V d\boldsymbol{V}' 4kT\sigma\Delta f |\boldsymbol{g}_j(\boldsymbol{r}, \boldsymbol{r}', f)|^2}. \tag{5.6}$$

5.2.1 Results of numerical calculations

In the following section results will be presented that were obtained with the Mathematica script (see Sec. F) based on the model described above. Calculated is always the JNN perpendicular to the slope $B_{n,z} = \sqrt{2}B_{n,x} = \sqrt{2}B_{n,y}$ [VP84]. The dependency of the JNN on different parameters like distance, thickness, or conductivity of the slab are investigated. In all examples a temperature of $T = 293\,\mathrm{K}$ and a relative permeability of $\mu/\mu_0 = 1$ is assumed.

Comparison to measured data

The electrodes used in the nEDM-experiment are regularly investigated at the Physikalisch-Technische Bundesanstalt (PTB) Berlin. In the highly magnetically shielded room [BHKS01] a SQUID system can be used to measure magnetization in the electrodes due to e.g. electrical discharges. In 2011 also the JNN was measured with this system as a function of frequency. This data can be used as a comparison with the calculations (see Fig. 5.5). The results obtained with the Mathematica script agree with the measurement in amplitude and shape. Thus the following calculations can be trusted as well.

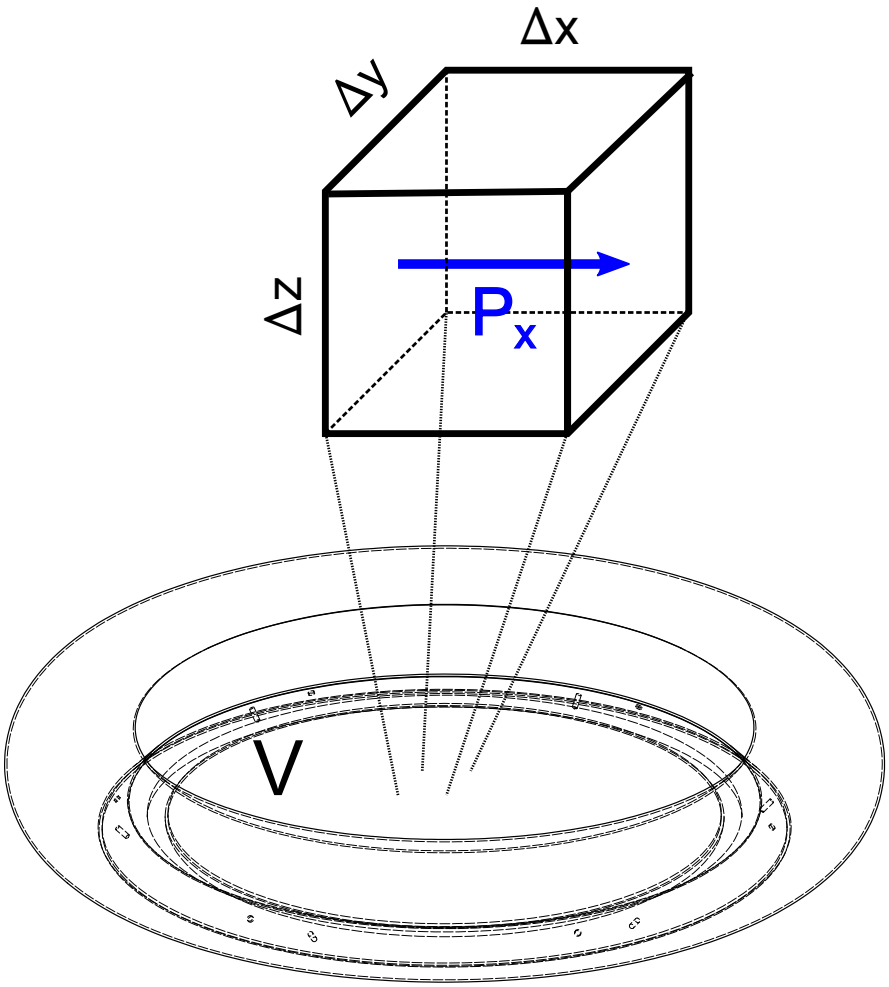

Figure 5.4: A volume V (like the top electrode) is divided into infinitesimally small rectangular volume elements ΔV. To each of these elements a current dipole P due to JN current is assigned. For certain simple geometries and under the assumption of uncorrelated P, one can integrate over the volume to calculate the mean magnetic noise using a Green's function.

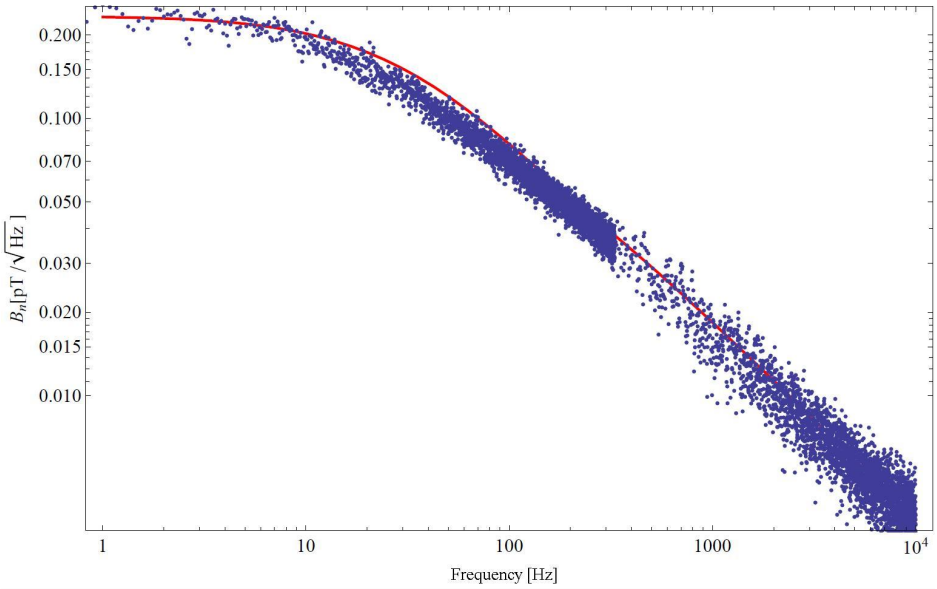

Figure 5.5: Comparison of a JNN calculation (solid line) and data measured at PTB Berlin.

Distance dependency

As expected, the JN noise of a slab reduces with the distance to the slab (see Fig. 5.6). Thus mainly the electrodes are of concern for noise considerations. In all current designs the vacuum tank is less important in terms of noise, but might be considered depending on the position of local magnetometers.

Thickness dependency

The idea of non-metallic electrodes is to reduce the thickness of the metallic layer. Figure 5.7 shows the calculated spectral density of JNN as a function of the thickness of an aluminum slab at a fixed distance of 1 mm. The noise can be reduced, as expected, if the slab is thinner.

Conductivity dependency

The conductivity of a conductor like aluminum is many orders of magnitude higher than that of a typical insulator (see Fig. 5.8) due to the reduced mobility of the electrons. Thus any insulating material can be neglected with regard to JNN considerations.

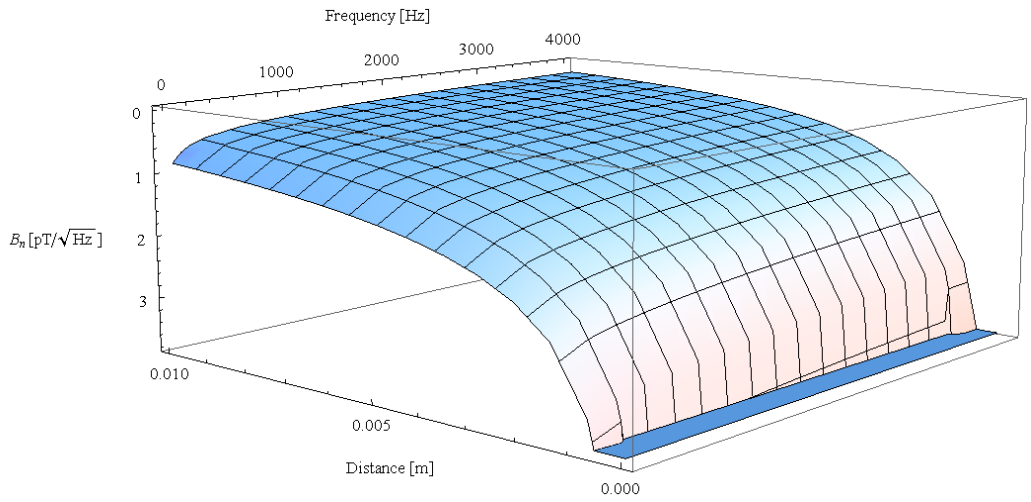

Figure 5.6: Spectral density of JNN as a function of the distance of an aluminum conductor (25 mm thickness).

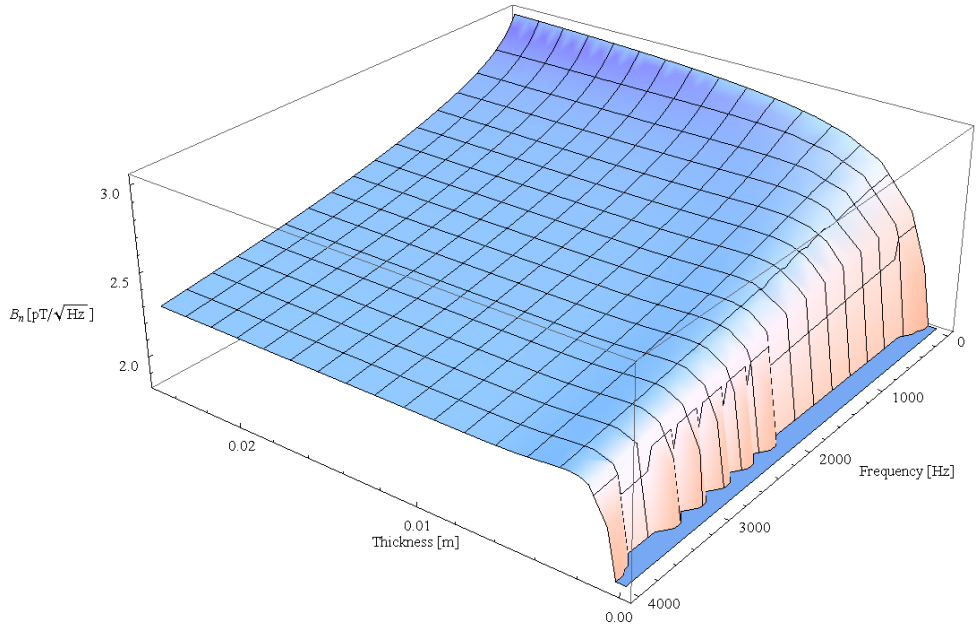

Figure 5.7: Spectral density of JNN as a function of the thickness of an aluminum conductor (in 1 mm distance).

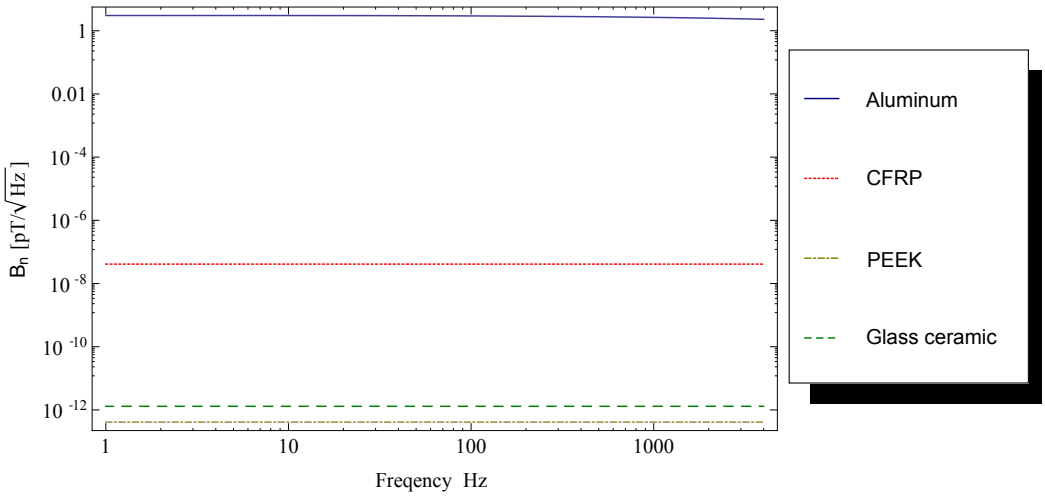

Figure 5.8: JNN for different materials of 25 mm thickness at a distance of 1 mm. The conductivity changes over many order of magnitude from aluminum ($\sigma_{\mathrm{Al}} \approx 10^{8}\,\mathrm{S}\cdot\mathrm{m}^{-1}$), over CFRP ($\sigma_{\mathrm{CFRP}} \approx 10^{-6}\,\mathrm{S}\cdot\mathrm{m}^{-1}$) to glass ceramic ($\sigma_{\mathrm{GK}} \approx 10^{-15}\,\mathrm{S}\cdot\mathrm{m}^{-1}$) and PEEK ($\sigma_{\mathrm{PEEK}} \approx 10^{-16}\,\mathrm{S}\cdot\mathrm{m}^{-1}$).

Calculations for the n^{2}EDM-experiment

Noise for magnetometers outside the precession chamber In the n^{2}EDM-experiment, the implementation of a ^{3}He magnetometer is discussed. Close to the electrodes it shall measure gradients over the precession chamber for several cycles. A crude picture of the situation in the n^{2}EDM-experiment using a ^{3}He gradiometer is depicted in Fig. 5.9. Also marked is the position of infinite slabs, that were calculated to estimate the JNN coming from the vacuum tank and the electrodes.

The result of the calculation (see Fig. 5.10) shows, that the main influence of the noise is coming, as expected, from the electrode. If the electrode can be replaced with a non-metallic one, the noise situation would improve. The vacuum tank as a source of JNN is less important in the scenario presented here. This might change if the design of the experiment changes, and a non-metallic vacuum tank (e.g. CFRP coated with Cu) might be needed. For non-metallic electrodes with a thin metallic coating on the micrometer level, the noise can be expected to be lower than $0.02\,\mathrm{pT}/\sqrt{\mathrm{Hz}}$, which is acceptable for the designed sensitivity of the experiment.

Noise inside the precession chamber The precession chamber is defined by the two electrodes and an insulator ring. The electrodes dominate the noise contribution for UCN and ^{199}Hg. To estimate the noise experienced

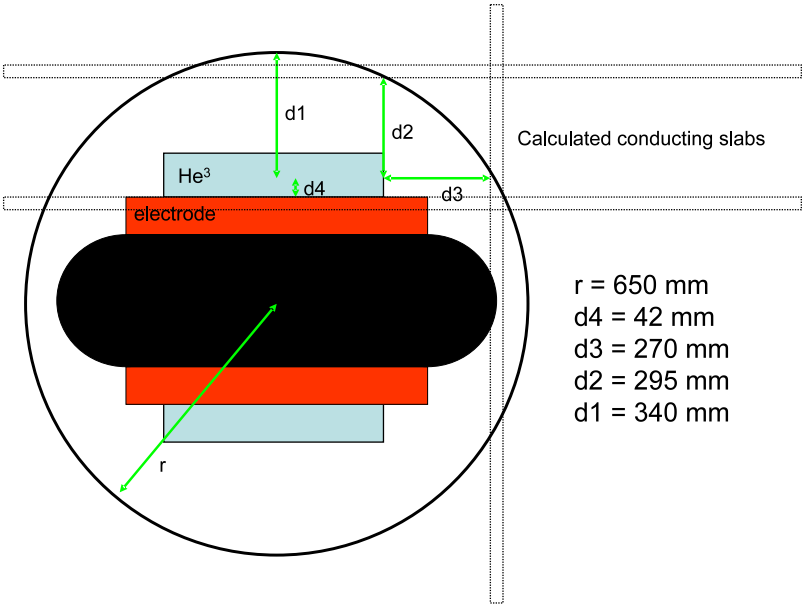

Figure 5.9: Simplified sketch of the n^{2}EDM-experiment. The double precession chamber (black) is situated in between two electrodes on ground potential. Next to the electrodes a ^{3}He-cell will be positioned. At typical distances (d1 - d4) of the ^{3}He-cell to the vacuum tank and the electrode, slabs have been calculated to estimate the noise in the magnetometer.

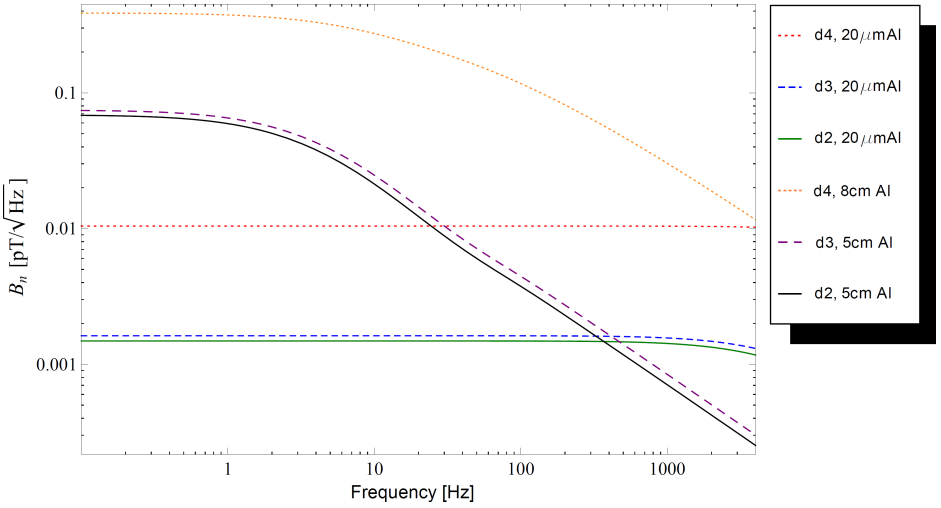

Figure 5.10: JNN experienced by the He magnetometer in the n^{2}EDM-experiment. At the precession frequency in a $B = 1\,\mu\mathrm{T}$ field of $f_{\mathrm{L,He}} \approx 30\,\mathrm{Hz}$ the noise is dominated by the electrodes. With non-metallic electrodes their noise is on the same level as that of the vacuum tank.

by UCN and ^{199}Hg inside the chamber, the noise over the chamber has been averaged over the height z in the chamber, so that

$$\overline{B}_{\mathrm{n}} = \overline{B_{\mathrm{n}}(z) + B_{\mathrm{n}}(0.12 - z)}. \tag{5.7}$$

The results for a 25 mm and a 20 µm thick electrode are shown in Fig. 5.11. Using metallic electrodes the noise is more than thirty times higher than acceptable at the precession frequency of ^{199}Hg of about 8 Hz in a 1 µT field.

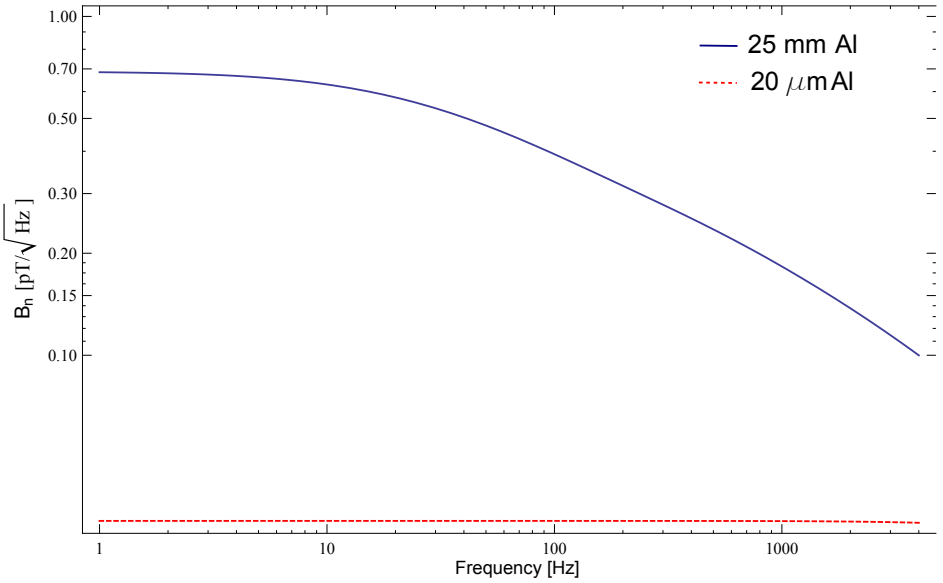

Figure 5.11: Mean noise according to (5.7) for metallic and non-metallic electrodes.

5.3 Research and development

The electrodes together with the insulator ring form the precession chamber. Thus stringent requirements are made to the material and the surface of the electrodes to allow a reliable measurement. A non-metallic electrode will be a composite of different materials: A nonconducting substrate will define the shape and the mechanical properties of the electrode. A thin metallic layer, that can be charged to create a uniform electric field. Finally a diamond-like carbon (DLC) or diamond coating is needed to guarantee good UCN and Hg properties of the surface.

5.3.1 Substrate

The insulating substrate from which the main body of the electrodes is machined needs to be:

- Nonmagnetic: In order to be used within the experiment any material needs to be nonmagnetic[2] to reduce systematic effects.

- Vacuum compatible: The electrodes represent a considerable amount of the surface within the vacuum chamber. To maintain a clean high vacuum environment, the out-gassing of the electrodes needs to be at least comparable with DLC-coated aluminum from which the current electrodes are made.

- Machinable: The surface must be smooth in order to create high electric fields (see e.g. [SGK03]) and the material must be machinable to create the desired design of the electrode. Also a robust electrode is preferable.

- Heat-resistant: During the high voltage conditioning in the experiment and in the coating process, resistive heating in the conducting layer can be expected. First samples made from acrylic glass (upper working temperature (UWT) 75 °C) melted after several hours of conditioning (see Fig.5.12).

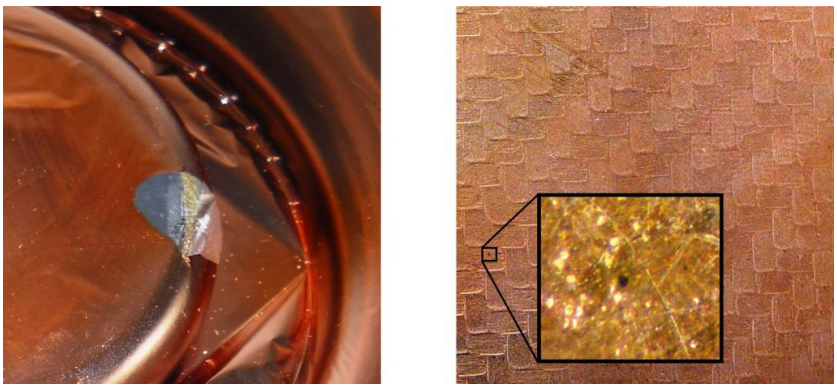

Figure 5.12: Acrylic glass (left) and CFRP (right) samples, coated with 20 µm Cu, after several hours of conditioning. The acrylic glass sample partly melted and the Cu layer de-laminated, while the CFRP only shows microscopic damages in the metallization (the black spot in the CFRP sample has a diameter of about 0.1 mm).

[2]Very weakly para-, or diamagnetic.

Material	G_{p2p} [pT]
Epoxy (EPO 752, Axon)	1800(1100)
Epoxy (Durapot863, Cotornics)	21(18)
Eltimid (Handtmann)	30(4)
Graphit	62(14)
CFRP (Brühlmeier)	20(10)
CFRP (PaukoPlast)	37(15)
PEEK (Ketron®, Quadrant)	31(14)
PEEK (TECAPEEK®, Ensinger)	60(20)
Glass-ceramic (Macor®, Corning)	50(20)
Glass-ceramic (Robax®, Schott)	30(10)
Glass-ceramic (Zerodur®, Schott)	40(20)
Borosilicate glass	150(10)

Table 5.1: Gradiometer measurement of different materials that were investigated as substrate for non-metallic electrodes. The peak-to-peak value of the gradient as function of the cart position is listed. The error on each measurement is based on the reproducibility between forward and backward movement of the cart. The background of the cart itself, $G^b_{p2p} = 12\,\mathrm{pT}$, has not been subtracted from the measurements above.

Several types of material classes have been tested: Epoxy, plastics [polyether ether ketone (PEEK), carbon fiber reinforced plastic (CFRP)], and glass ceramics.

Magnetic properties The magnetic properties of potential materials were tested in the gradiometer at PSI (see Sec. A). In Tab. 5.1 the peak to peak value of the gradient as a function of the position is listed.

Apart from the epoxy (EPO 752), which has been colored black using iron oxide, none of the tested materials showed a clear magnetic signal. Particularly CRFP, Durapot863, and Robax seem to be promising candidates. However the mechanical properties of Durapot863 (brittle) do not meet our demands.

Outgassing To measure the outgassing of different materials, samples have been placed in a vacuum chamber and pumped for several thousand seconds. The outgassing rate per surface S is defined as

$$Q_l = \frac{\Delta p V}{\Delta t S}, \tag{5.8}$$

with the pressure change Δp over the time Δt in a volume V. The tested materials can be compared to the empty, stainless steel, vacuum chamber in which they are placed for the test. Results of these measurements are listed in Tab. 5.2. CRFP showed the worst vacuum properties if it has no metallic coating. Assuming a surface of the two electrodes for the n^{2}EDM of $S = 4 \times (\pi r^2) = 2 \times 25^2 \pi\,\mathrm{cm}^2 \approx 3926\,\mathrm{cm}^2$, and a volume of the storage chamber of $V = 20000\,\mathrm{cm}^3$, during the time of free precession where the chamber is not pumped a outgassing of $Q_l = 10^{-6}\,\mathrm{mbar}\cdot\mathrm{l}\cdot(\mathrm{s}\cdot\mathrm{cm}^2)^{-1}$ would result in a pressure change of

$$\Delta p = \frac{Q_l S \Delta t}{V} = 4 \times 10^{-2}\,\mathrm{mbar}, \tag{5.9}$$

corresponding to a mean free path (5.11) of the order $\mathcal{O}(10^{-2}\,\mathrm{m})$. This is about the same as the mean free path of a UCN in the chamber in vacuum (5.10) and thus will influence the storage time[3] and reduce the sensitivity. Also the high voltage properties will be influenced in this pressure regime (see Sec. 5.5.3). However, the experience with the dPS storage ring showed, that baking at 60 deg C can reduce the outgassing by an order of magnitude [Kuź08]. As all tested materials withstand temperature well above 100 °C, the outgassing results do not exclude any of the tested samples.

Machinability Producing a complex form like the electrodes is especially easy with CFRP where a mold can be machined to high precision. The surface roughness of a CFRP test electrode has been measured using a profilometer (Hommel T1000E). The mean roughness $R_a = 0.4\,\mu\mathrm{m}$ is worse than the currently used diamond milled Al electrodes (the company doing the milling guarantees $R_a < 0.01\,\mu\mathrm{m}$). However this is in principle still acceptable for the electric fields used in the experiment. Also PEEK has been used for different constructions within the nEDM-experiment (e.g. a new UCN shutter was designed and build using only PEEK) and has shown good results. The surface can also be diamond milled with a roughness of $R_a < 0.03\,\mu\mathrm{m}$ on samples of $(50 \times 50)\,\mathrm{mm}^2$. Based on the experience gained with the quartz insulator ring and the glass guides, brittle glass-ceramic is not a material of first choice. The handling of these components lead to a lot of damaged surfaces.

[3] and also the depolarization time, if polar molecules are outgassing.

Material	outgassing after 10000 s pumping $\left[\frac{\text{mbar}\cdot\text{l}}{\text{cm}^2\cdot\text{s}}\right]$
Empty chamber	3×10^{-8}
CFRP	2-3$\times10^{-6}$
CFRP (sputtered)	2-3$\times10^{-6}$
CFRP (galvanic)	1×10^{-7}
Glass ceramics	0.8-1$\times10^{-7}$
PEEK	7×10^{-7}
PEEK (galvanic)	2×10^{-7}
Graphite	4×10^{-7}

Table 5.2: Vacuum properties of selected materials to be used for non-metallic electrodes. As the vacuum properties are greatly influenced by the surface, measurements have been repeated for plastic material after coating with a metallic layer. 'Galvanic' refers to a galvanically applied Cu layer of 20 µm thickness , 'sputtered' to a 200 nm thick layer of NiMo, Ti, Cu, or Al.

5.3.2 Metallic coating

The metallic coating of the substrate should be thin enough to reduce JNN. However, a thicker coating can help to improve vacuum properties. Also the surface resistance in the case of an electric discharge is lower. Two methods of metallization have been tested that have been proven not to influence the magnetic properties of a substrate:

1. An electrochemical deposition technique (galvanization) of Cu developed by Galvanic Wädenswil [Feu]. The typical thickness of the Cu layer applied in this process is 20 µm.

2. Sputtering of NiMo, Ti, Al, or Cu in facilities within the collaboration (Mainz and PSI). The thickness of these coatings is in the 100 . . . 500 nm range.

Both methods result in an evenly conducting layer.

5.3.3 DLC coating

The current Al electrodes are coated with DLC. It has a high optical potential, a low loss probability (see Tab. 14), and a low depolarization probability of $\beta = 0.8 \times 10^{-6}$ per wall collision [Fie05]. Also the Hg magnetometer shows reasonable performance (depolarization times of

$T_{2,\mathrm{Hg}} > 200\,\mathrm{s}$ have been achieved in the current precession chamber) with DLC coated electrodes. It is thus desirable to have also non-metallic electrodes coated with DLC to preserve these good qualities. The coating is done by the Fraunhofer-Institut für Werkstoff- und Strahltechnik by means of a physical vapor deposition (PVD) [Fra]. The process consists of several steps: first a discharge cleaning of the samples is performed, then a 10 nm thick chromium bond coat is applied. The ionized carbon is then applied in several steps, each step at a lower accelerating voltage.

5.4 Test samples

To investigate the feasibility of non-metallic electrodes, test samples of about $10 \times 10\,\mathrm{cm}^2$ surface have been produced from different substrates and with different coating techniques for the metallic coating. In total three batches of samples were then coated with DLC. The samples in the first batch were made from low tech plastics (PC, acrylic glass) and melted during the coating process. This led to the initial requirement for the substrate to be heat-resistant, hence this batch was not considered further. The last batch was coated with slightly altered coating parameters: the initial carbon layer was applied at a lower accelerating voltage to reduce thermal stress on the sample and its metallic coating. Images of the coating results can be seen in Figs. 5.13 to 5.16. The DLC coating batch number is given as (B2) or (B3) below each sample.

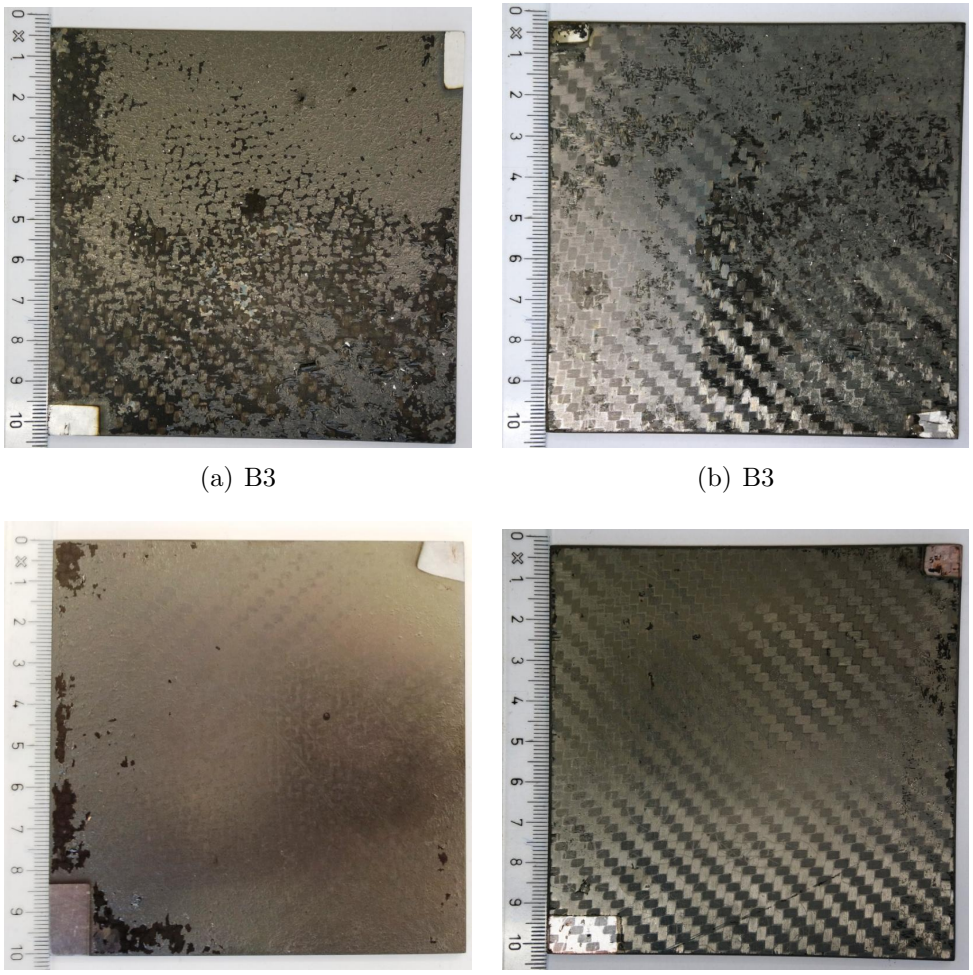

(a) B3 (b) B3

(c) B3 (d) B3

Figure 5.13: DLC coating on CFRP samples from PaucoPlast [Pau] (left) and Brühlmeier [Bru] (right). A 500 nm thick layer of Al (top) and Cu (bottom) was sputtered onto the samples.

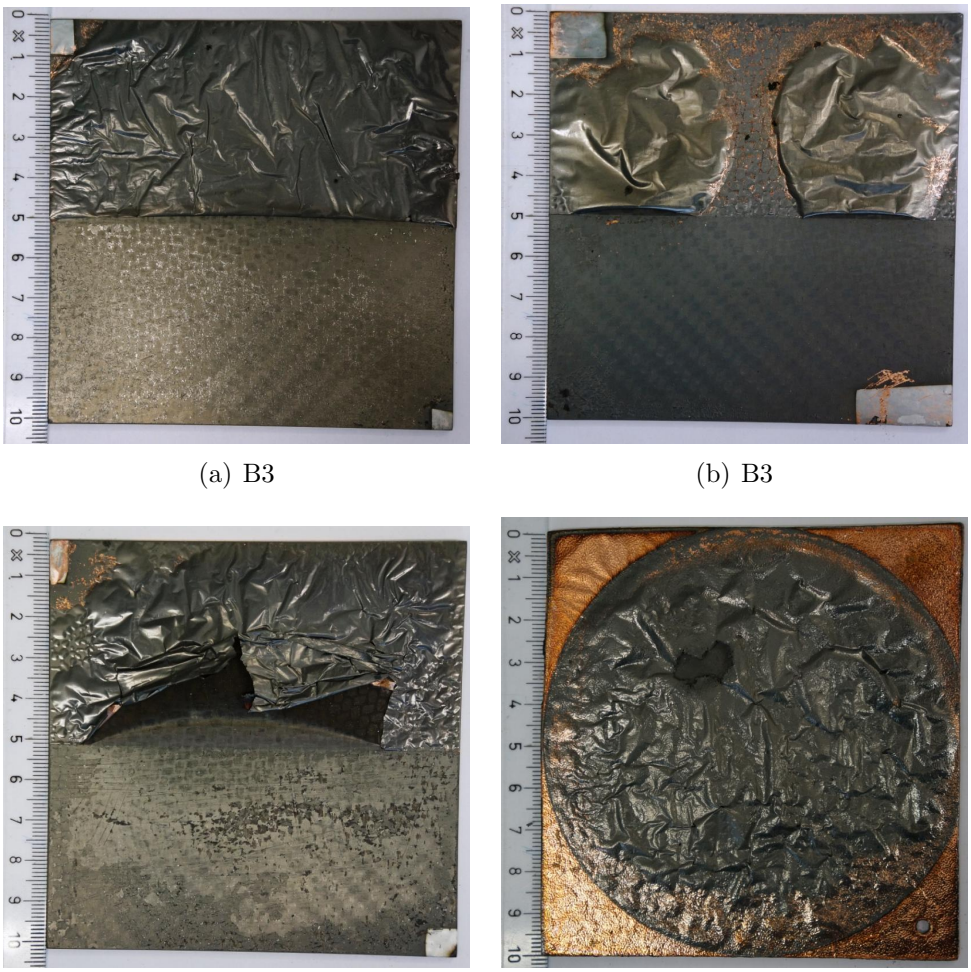

(a) B3 (b) B3

(c) B3 (d) B2

Figure 5.14: DLC coating on CFRP samples from PaukoPlast. The metallic layer applied by sputtering is: 100 nm Ti (a), 200 nm Cu (b), 150 nm NiV (c). (The upper) half of each of the three samples was in addition coated electrochemically with 20 µm Cu. Unfortunately this process damaged the initially sputtered metall layer at the edges opposite to the Cu layer (see Fig. 5.17). Sample (d) was coated electrochemically with 20 µm Cu.

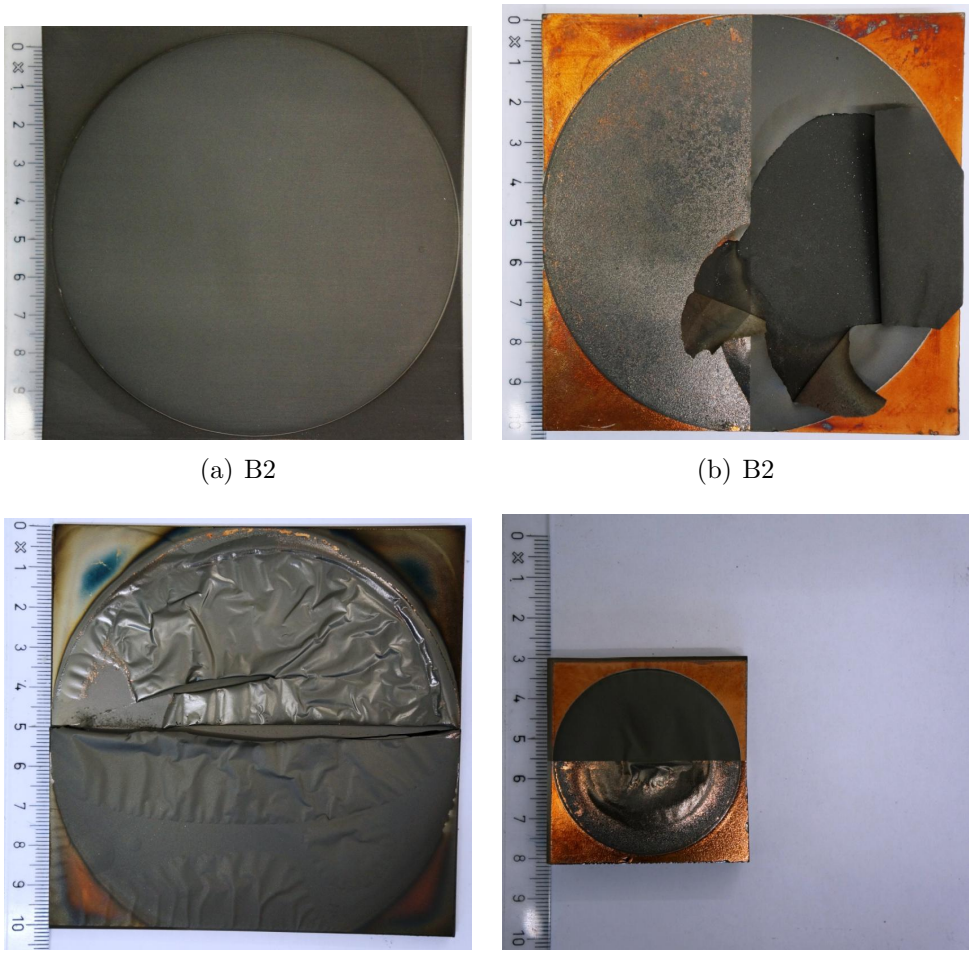

(a) B2 (b) B2

(c) B2 (d) B2

Figure 5.15: Graphite samples without (a) and with (b) a layer of 20 µm Cu. The DLC coated glass ceramics, metallized electrochemically with 20 µm Cu, are Robax (c) and Zerodur (d). Sample (c) broke in half during the transport back after coating. Half of the surface of all samples with Cu layer had been bead-blasted to improve the sticking of the DLC coating (see Sec. D).

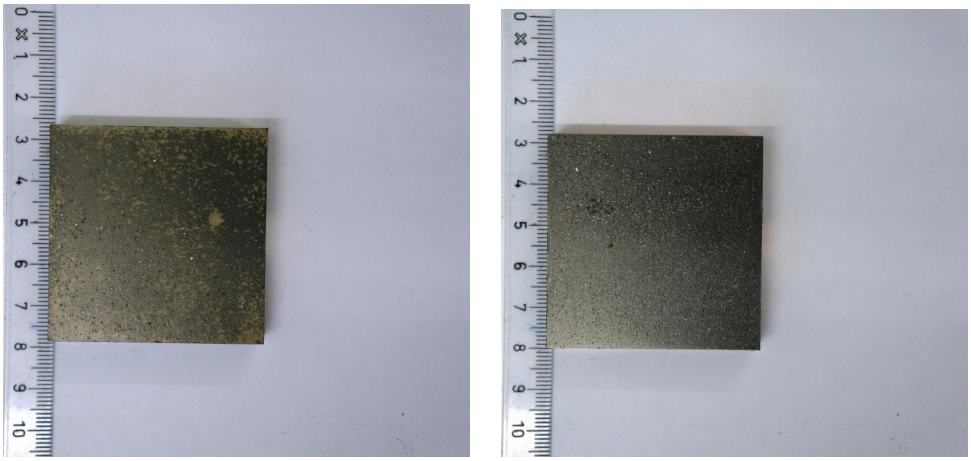

(a) B3 (b) B3

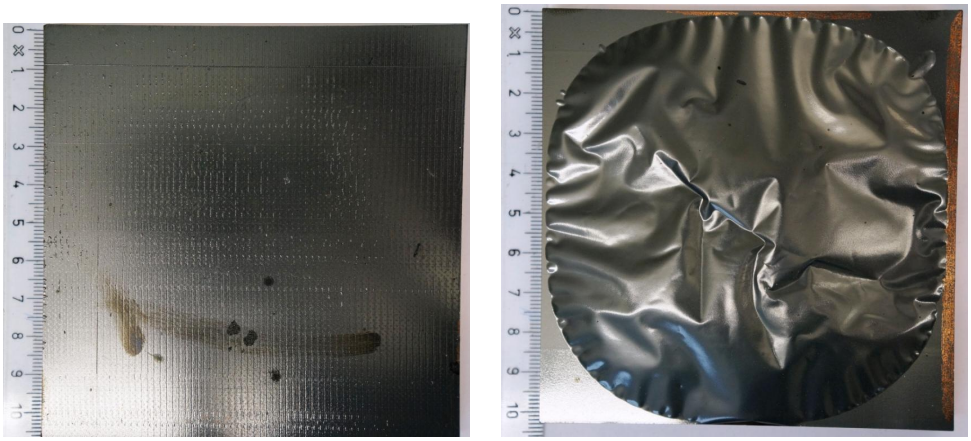

(c) B3 (d) B3

Figure 5.16: Coating results for different PEEK samples. The smaller samples were diamond milled before they were metallized with 500 nm Al (a), and 500 nm Cu (b) respectively. Sample 5.16(c) had an untreated rough surface and was coated with 20 µm Cu. Sample (d) is made from Eltimid and was also coated with 20 µm Cu.

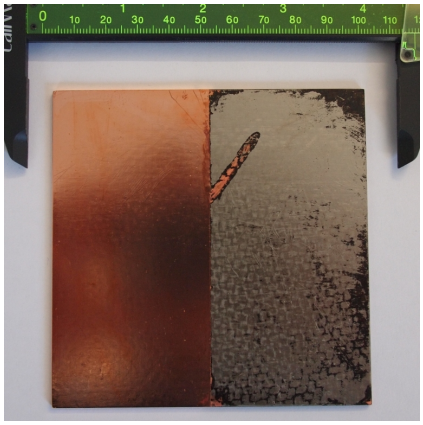

Figure 5.17: Example of the damage of the sputtered Ti layer due to the electrochemical process. The NiV sample was influenced more, the Cu sample less than the Ti sample.

Summary of test sample results From the experience gained, some conclusion for further developments can be made:

Substrate All tested substrates were nonmagnetic and usable in the vacuum environment of the nEDM or n^2EDM-experiment, although e.g. CFRP probably needs to be baked if the conducting metallic layer is not thick enough. As CFRP can sustain up to $\approx 150\,^{\circ}\mathrm{C}$, which is the lowest of all considered materials, it seems to be sufficient for the DLC coating process and the use in the experiment. Experiences with brittle materials in the experiment (quartz insulating ring, glass guides), as well as during the coating tests presented here (broken Robax sample (see Fig. 5.15(c)) showed, that the handling of glass ceramics is not easy. Thus plastics like PEEK and CFK are preferable. Both of them seem to be equally suited as material for non-metallic electrodes, if produced in injection molding technique.

Metallization Both metallic coating techniques resulted in nonmagnetic, conducting surface layers, that could be used as electrode. While the electrochemical coating results in a thicker, hard-wearing layer, the adhesion on the substrate is not as good as sputtered samples, as the DLC coating showed. The combination of a sputtered intermediate layer and an electrochemical added Cu layer did not improve the adhesion.

DLC coating The process of DLC coating can easily destroy the metallization of samples. Particularly the electrochemical layers,

although showing good coating results, de-laminated (see e.g. Fig. 5.16(d)) from surfaces, particularly if they are smooth (which is preferred for electrodes). The best results were obtained with Cu sputtered on CFRP samples (Fig. 5.13(c), 5.13(d), and 5.14(b)). Optimizing the DLC coating process for non-metallic electrodes with the current vendor is very time consuming. An on-site coating facility for DLC is under construction. Once finished it will be much easier to optimize coating parameters.

5.5 The high voltage test setup

A high voltage test setup (HVtest) has been developed in the context of this work. This setup can be used to test high voltage related components that are designed for the nEDM, or n^{2}EDM-experiment.

5.5.1 Motivation

Any newly developed high voltage component, like a feedthrough, electrodes, etc. has to be tested in an environment similar to the one in the experiment. Using a dedicated test setup has the advantage that the running experiment is not disturbed by these tests. HVtest does not require magnetic shields, thus the access is much easier. In addition the risk of damaging sensitive equipment, like magnetometers, by high voltage discharges is excluded.

5.5.2 General design of the high voltage test setup

The high voltage test setup is designed to house full scale models or actual electrodes as they are used in the current nEDM or future n^{2}EDM-experiment. Figure 5.18 shows a photo of HVtest, a CAD image is shown in Fig. 5.19. The large door guarantees easy access. A variety of vacuum flanges allows for flexibility and makes it possible to mount the high voltage feedthrough vertically or horizontally. A height-adjustable table inside the setup can hold samples. The whole setup is mounted on a platform for flexible positioning, e.g. it can be placed behind a concrete radiation shielding if needed. To operate HVtest only pressurized air, electricity, and a local area network need to be connected to this platform.

HV power supply

The high voltage system of HVtest consists of two Spellman SL130 power supplies. These can deliver voltages up to 130 kV with a maximum current of 250 µA. As the supplies are mono polar, manual intervention is needed to change the polarity by plugging the high voltage cable to the according power supply. The high voltage feedthrough used in HVtest is an exact copy of the high voltage feedthrough used in the nEDM-experiment. A diode-protected amplifier[4] is used to measure small currents of the order of $\mathcal{O}(1\,\mathrm{nA})$.

[4]The device was initially used in the nEDM-experiment, but was replaced by components with less noise.

Figure 5.18: Photograph of HVtest. The whole setup is mounted on a platform for flexible positioning. To operate HVtest only pressurized air, electricity, and local area network need to be connected to the platform.

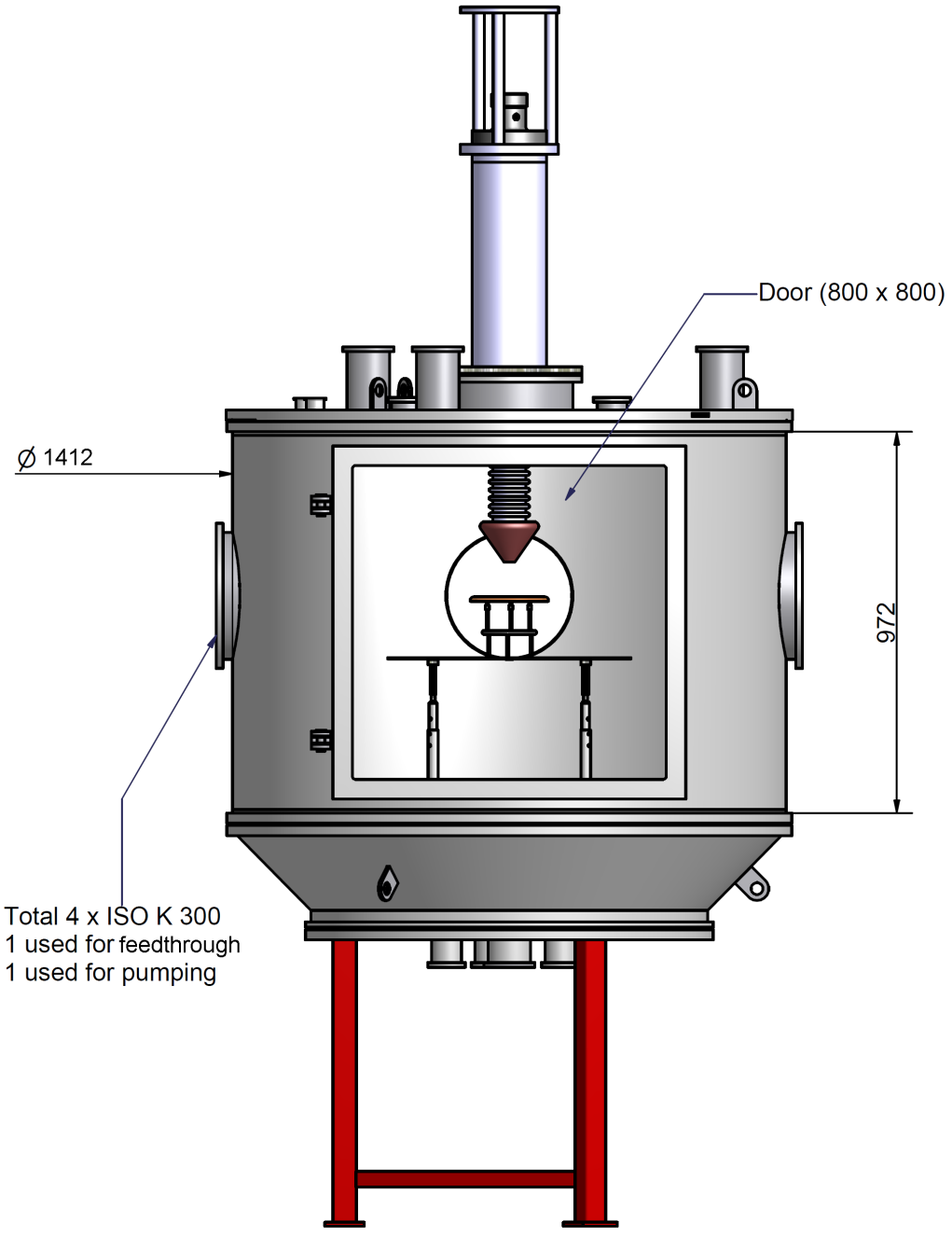

Figure 5.19: CAD image of HVtest. The dimensions in the sketch are given in millimeters.

DAQ and electronics

Figure 5.20 shows the electronic rack of HVtest. The Spellman power supplies used in the setup are designed for front panel operation and only have an analog input/output connector for basic control and surveillance of the unit. On this connector voltages of $\pm 10\,\mathrm{V}$ can be measured for surveillance or have to be applied for controlling. Analog switches had to be replaced by relays to switch the output on or off. These requirements are matched by the SCS 2000 device [Rit], a PSI module that was initially designed for the slow control of the MEG experiment [Rit02]. The base unit can be equipped with a variety of ADC, DAC or other in- and outputs and communicates via Ethernet with a PC. As it was developed for slow control purposes, the sampling frequency is limited to a few 10 Hz. For the use in HVtest, a SCS 2000 node was equipped with an eight channel 14-bit ADC and an eight channel 16-bit DAC cards, as well as four 24 V relays and eight digital inputs. It is not only used to control the high voltage power supplies, but also to read back all other parameters like vacuum pressure, temperature, and leakage current. HVtest can be controlled by any computer running Labview via a local area network connection.

Vacuum and gas handling system

Using a roughing pump with a pumping speed of $13\,\mathrm{m^3 \cdot h^{-1}}$ and a turbo pump with a pumping speed of $0.52\,\mathrm{m^3 \cdot h^{-1}}$, the volume of $\sim 6.8\,\mathrm{m^3}$ can be evacuated to a pressure of 1×10^{-6} mbar within a few hours. The control of the vacuum system has been automated. Like the DAQ for the high voltage, it is based on a SCS2000 module and can be controlled remotely or via front panel operation.

A gas feeding line, connected to a needle valve is used to create defined atmospheres of e.g. He or O_2. It can be connected to the roughing pump via a valve to allow purging of the line after the exchange of gas bottles.

5.5.3 Breakdown voltage of different gases

One of the major systematic errors, the geometric phase effect for Hg (see Sec. 3.2.2), can be reduced by constraining the mean free path λ of the Hg atoms. At low pressure λ is defined by the volume (V) and the surface (S) of the precession chamber via

$$\lambda = \frac{4V}{S}. \tag{5.10}$$

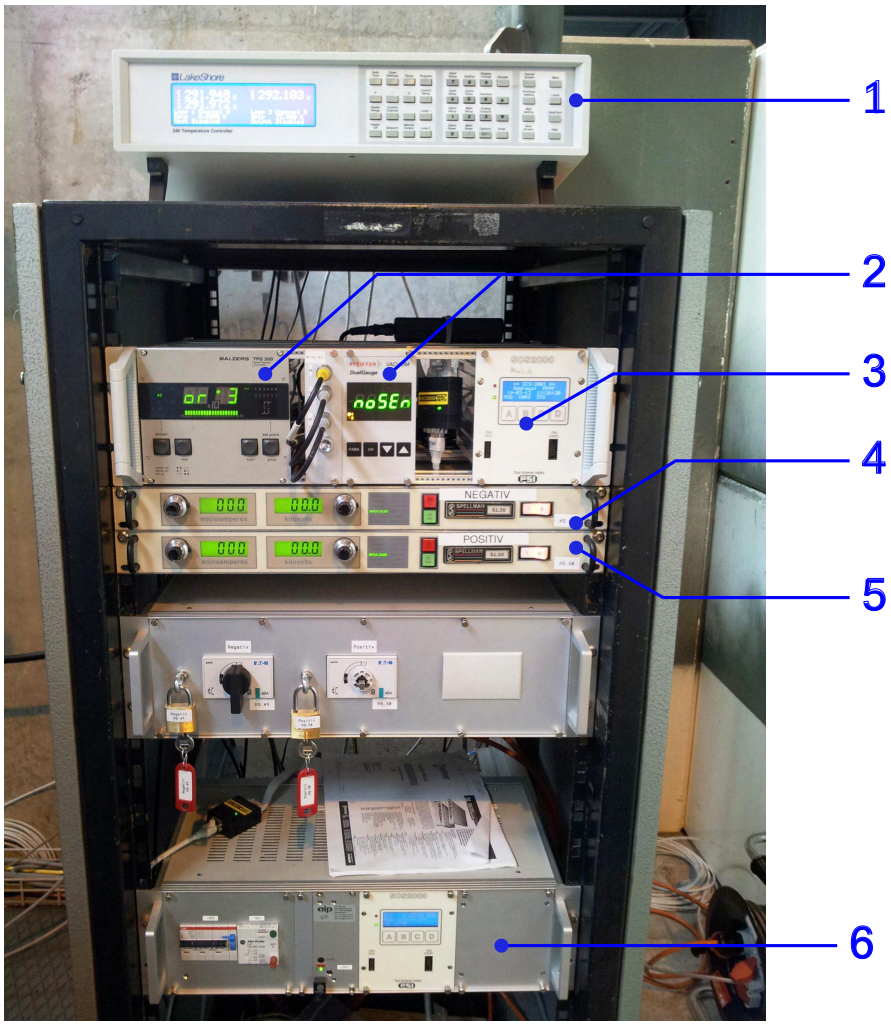

Figure 5.20: Electronics for HVtest: (1) Temperature controller for readout of PT100 sensors, (2) vacuum sensor readout, (3) main DAQ module, (4) negative HV power supply, (5) positive HV power supply, (6) vacuum control and main switch.

Reducing the mean free path by the use of a buffer gas at some intermediate pressure has already been discussed in [PHS+04]. Their estimations showed, that a mean free path of a few centimeter is needed for a significant reduction of the false effect. In a simple model using ideal gas theory, the mean free path of a particle is given by [LS06]

$$\lambda = \frac{RT}{\sqrt{2}\pi\, d^2\, N_\mathrm{A}\, p}, \tag{5.11}$$

with the ideal gas constant R, the temperature T, the diameter of the buffer gas molecule d, the Avogadro number N_A, and the pressure p. Thus a buffer gas pressure in the mbar regime is needed for a sufficient reduction of the mean free path. Buffer gases will, among other things, influence the properties of the high voltage stability in the experiment. To estimate the possibilities of using a buffer gas, the break down voltage of several gases in a nEDM-like setup has been measured. This is of special interest as break down voltages found in the literature are usually measured at smaller electrode separations and without an insulator between them. The following section has been also presented in [BKGS+11].

Setup For the measurement a precession chamber (top and bottom electrode separated by a quartz insulator) consisting of old parts from the nEDM-experiment, was mounted inside HVtest (see Fig. 5.21). In contrast to the original setup, this precession chamber had no quartz windows, UCN shutter or bottom corona ring mounted. The precession chamber was mounted on acrylic glass pieces, insulating it from the tank. The grounding was realized via a copper wire, conneted to a protection array of fast diodes and an amplifier to measure the current.

Measurement In preparation for the measurement the system was operated for 20 h at a goal voltage of 130 kV. With the current limited to 10 µA, the voltage did slowly increase and the system could be operated without any measurable current flow at 125 kV after this conditioning. Using the needle valve, the different gases were filled into the chamber. To guarantee that only the gas of interest is introduced into the system, the gas feeding line was evacuated and flushed several times after each exchange of a gas bottle. The gas pressure was measured with a set of gas-type-independent pressure gauges (Pfeiffer-vacuum CMR 375 and PCR 260). Up to a pressure of about 0.01 mbar the system was operated in a flow-through mode with the turbo pump running while the needle valve was opened to a certain level to reach a chosen, stable pressure. Above a

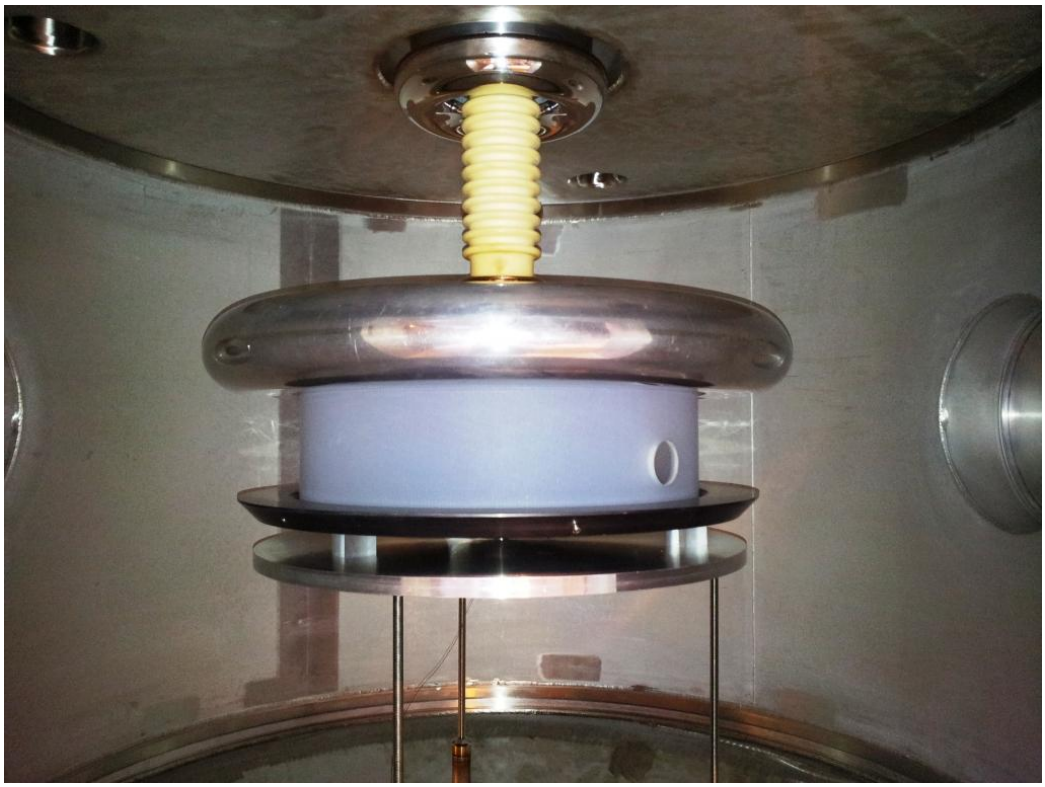

Figure 5.21: Precession chamber inside the HVtest. The bottom electrode was mounted without a corona ring. It rests on three acrylic glass cubes that insulate it from the tank. The grounding is realized via a protection array of fast diodes and an amplifier to measure leakage current.

Gas	pd_{min} [mbar cm]	U_{min} [V]
N_2	0.86	240
O_2	0.93	450
He	5.32	155

Table 5.3: The minimum values of the breakdown voltage (U_{min}) and the corresponding pressures for the measured gas types according to [AM11].

pressure of 0.01 mbar the turbo pump was valved off and gas was only filled via the needle valve until the desired pressure was reached. To determine the breakdown voltage U_{max} at a given pressure, the voltage was ramped up until a current (limited to 60 µA) started to flow. The output of the power supply was then switched on and off each time with a slightly reduced target voltage. The maximum voltage that could be reached without current flowing was taken as the breakdown voltage for this pressure. An alternative method was used in addition for He. A fixed voltage was set, and the pressure was slowly varied until a breakdown occurred. Both methods gave the same result. As the voltage can be faster changed than the pressure, the first method was preferred.

Result The result is shown in Fig. 5.22. As usual for these types of measurements, the breakdown voltage is plotted as a function of the product of pressure and electrode distance of 12 cm. As the HVtest power supply has a maximal voltage of $U = 130\,\text{kV}$ the steep part for low pressures could not be measured up to the target voltage in the nEDM-experiment. The maximal voltage of 130 kV could be reached at pressures below 0.01 mbar of He or 0.001 mbar of N_2, and O_2. Despite the difference in the setup, the minimal voltage U_{min} and pressures agree with values found in the literature (see Tab. 5.3).

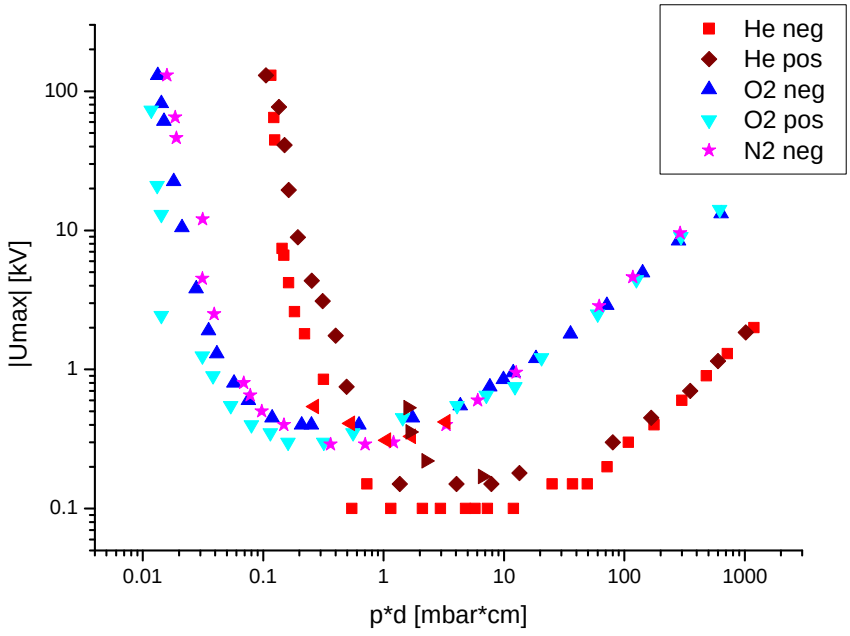

Figure 5.22: Breakdown voltage in the precession chamber for He (purity 6.0), N_2 (purity 5.0), and O_2 (purity 4.8). As usual for Paschen curves, the maximum voltage is plotted against the product of the gas pressure and the distance between the electrodes (12 cm). The minimum of the curves agree with values found in the literature (see Tab. 5.3).

Chapter 6

Conclusion and Outlook

The work presented in this thesis took place during the most interesting phase of building up the nEDM-experiment at PSI. Parallel to the start up phase of the PSI UCN source, the experiment was commissioned. This was a unique opportunity to get to know the experiment and all its components in great detail. Therefore this work tries to give a complete overview of the experiment in Chapter 2.

This work also gives a summary of systematic effects in Chapter 3. Most of the known systematic effects are under control. The sum of all systematic errors is only about two times too large, to reach the goal sensitivity of $5 \times 10^{-27}\, e \cdot \mathrm{cm}$. For the most dominant systematic error, the uncompensated B drift, more data has been recorded in late 2012 and is currently analyzed. This should bring down the uncertainty. A more detailed Monte Carlo simulation might determine if a delay in the first spin flip of the UCN is needed to reduce the systematic error of rotational motion. Also the quadrupole difference, is one of the larger systematic errors at the moment. The reliability of the CsM data used to calculate this result is questionable, due to a distorted RF signal in the CsM sensors. Magnetic field maps recorded with a fluxgate and a vector CsM during spring 2013 will hopefully bring more insight to this issue.

The analysis of the nedm data is discussed in Chapter 4. The final result of the nedm analysis is $d_\mathrm{n} = (1.43 \pm 2.54_\mathrm{stat.} \pm 0.02_\mathrm{sys}) \times 10^{-25}\, e \cdot \mathrm{cm}$, which corresponds to an upper limit of $|d_\mathrm{n}| \leq 6.4 \times 10^{-25}\, e \cdot \mathrm{cm}$ (95%C.L.). The unexpected large reduced χ^2 of the linear fit in the crossing point analysis, might originate in HV discharges, that have not been taken into account during the analysis. High voltage tests and performance optimization are scheduled before the next data taking period and should improve the situation. It might be interesting to reanalyze the data using an offline analysis of the ^{199}Hg precession data.

In parallel the collaboration is preparing the next generation experiment: the n^{2}EDM-spectrometer. Foundations on the development of non-metallic electrodes, to be used in this experiment, have been established in Chapter 5. Such electrodes will have the advantages of lower noise and lower magnetization probability. A parameter optimization for the DLC coating is best done with the in-house coating machine that is currently under construction.

Outlook Over the next years the nEDM-experiment is going to measure about 400 days of nedm data. With the current performance this would correspond to a sensitivity of $\sim 2{\times}10^{-26}\ e \cdot \mathrm{cm}$. However, improvements in the visibility α and the electric field strength can be expected. The investigations concerning the neutron density of the UCN source are ongoing, and we expect that the number of UCN in the nEDM-experiment can be further improved. The design of the next generation experiment should increase the sensitivity by another factor 10. A new upper limit or a discovery of the electric dipole moment of the neutron can thus be expected in the near future.

Appendix A

The PSI magnetic gradiometer

The gradiometer is used to test the magnetic properties of samples (see Fig. A.1).

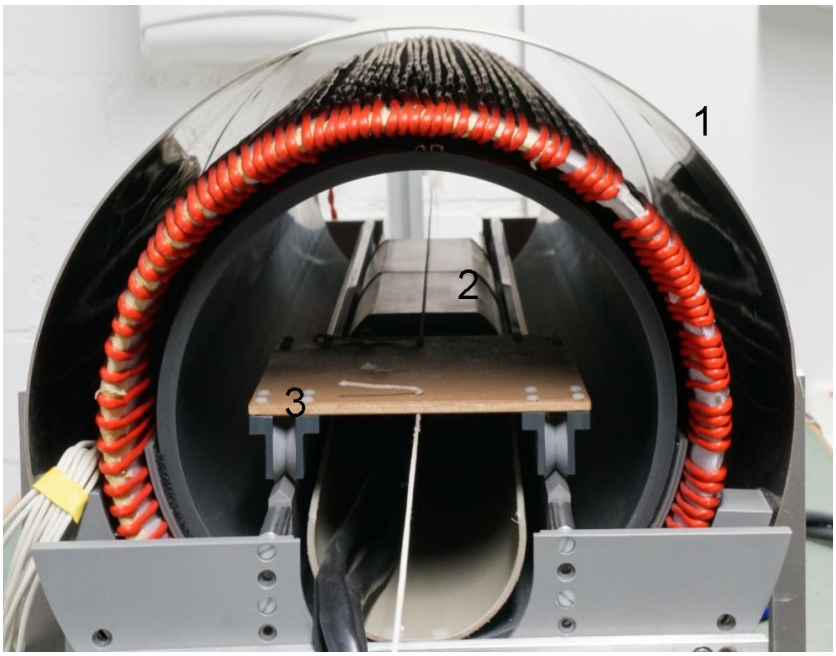

Figure A.1: A view into the two-layer cylindrical shield of the gradiometer (1). The red degaussing coil of the system is visible on the inner shield layer. Two CsM (2) are situated in the center of the shield. A nonmagnetic cart (3) drives through the shield, hauled by a pulley.

A cylindrical two-layer magnetic shield is used to reduce the ambient magnetic field. A solenoid coil produces a magnetic field of about $B = 2.2\,\mu\mathrm{T}$ along the cylindrical axis. Two CsM, that use discharge lamps

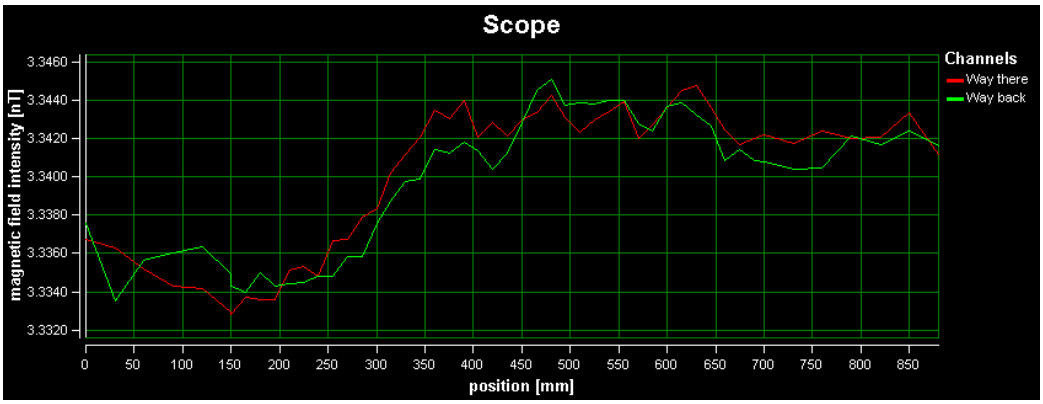

Figure A.2: Background measurement as seen on the online display of the gradiometer. The empty cart is slightly magnetic ($\approx 12\,\mathrm{pT}$). The difference between forward and backward gives the resolution of the measurement of about $2\,\mathrm{pT}$.

and not a laser like the magnetometers in the nEDM-experiment, are placed in the center of the shield with a distance of about $D = 200\,\mathrm{mm}$ between them. A nonmagnetic wooden cart, on which samples can be placed, is hauled through the shield. The differential signal of the two CsM as a function of the position of the cart is measured twice (forward and backward). A typical background measurement (empty cart) in a quiet environment can be seen in Fig. A.2. It shows that the cart is slightly magnetic and that the agreement between forward and backward measurement is about $2\,\mathrm{pT}$.

Appendix B

Test log of the high voltage power supply

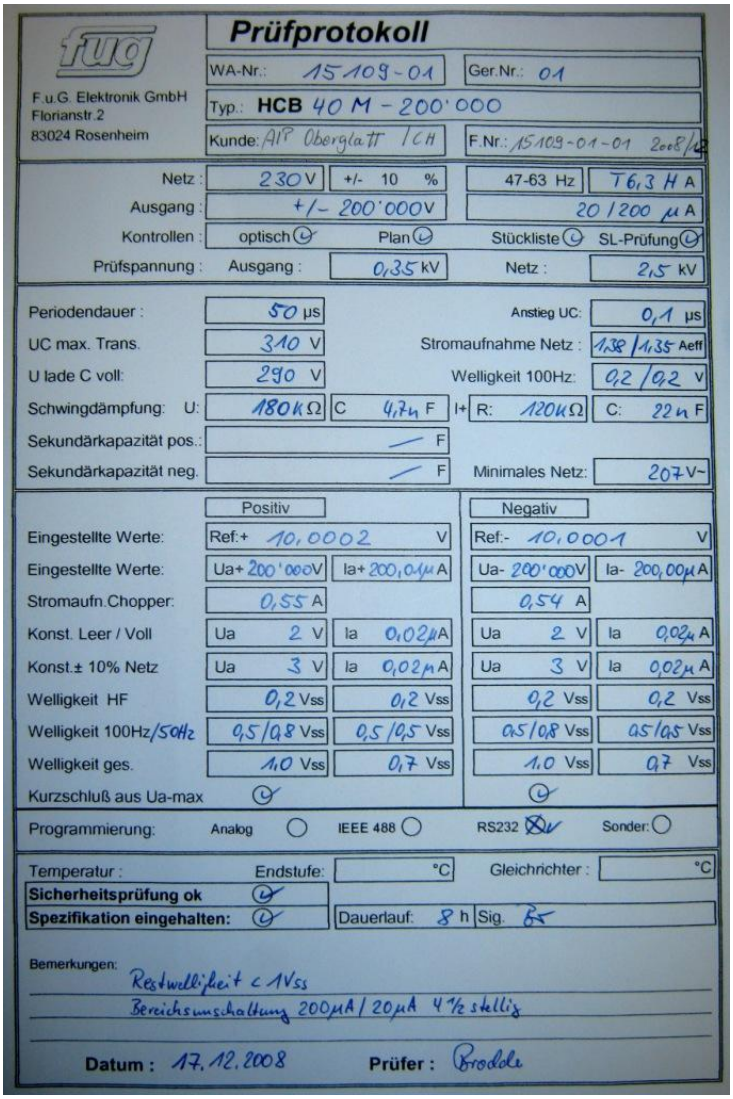

Prüfprotokoll

F.u.G. Elektronik GmbH
Florianstr.2
83024 Rosenheim

WA-Nr.: 15109-01 | Ger.Nr.: 01
Typ.: HCB 40 M - 200'000
Kunde: AIP Oberglatt / CH | F.Nr.: 15109-01-01 2008/

Netz :	230 V	+/- 10 %	47-63 Hz	T6,3 H A
Ausgang :	+/- 200'000V			20 / 200 µ A
Kontrollen :	optisch ✓	Plan ✓	Stückliste ✓	SL-Prüfung ✓
Prüfspannung :	Ausgang :	0,35 kV	Netz :	2,5 kV

Periodendauer :	50 µs	Anstieg UC:	0,1 µs
UC max. Trans.	310 V	Stromaufnahme Netz :	1,38 / 1,35 Aeff
U lade C voll:	290 V	Welligkeit 100Hz:	0,2 / 0,2 V
Schwingdämpfung: U:	180kΩ C 4,7n F	I+ R: 120kΩ	C: 22n F
Sekundärkapazität pos.:	— F		
Sekundärkapazität neg.	— F	Minimales Netz:	207 V~

	Positiv		Negativ	
Eingestellte Werte:	Ref:+ 10,0002 V		Ref:- 10,0001 V	
Eingestellte Werte:	Ua+ 200'000V	Ia+ 200,01µA	Ua- 200'000V	Ia- 200,00µA
Stromaufn.Chopper:	0,55 A		0,54 A	
Konst. Leer / Voll	Ua 2 V	Ia 0,02µA	Ua 2 V	Ia 0,02µ A
Konst.± 10% Netz	Ua 3 V	Ia 0,02µA	Ua 3 V	Ia 0,02µ A
Welligkeit HF	0,2 Vss	0,2 Vss	0,2 Vss	0,2 Vss
Welligkeit 100Hz/50Hz	0,5 / 0,8 Vss	0,5 / 0,5 Vss	0,5 / 0,8 Vss	0,5 / 0,5 Vss
Welligkeit ges.	1,0 Vss	0,7 Vss	1,0 Vss	0,7 Vss
Kurzschluß aus Ua-max	✓		✓	

Programmierung: Analog ○ IEEE 488 ○ RS232 ☒ Sonder: ○

Temperatur : Endstufe: °C Gleichrichter : °C
Sicherheitsprüfung ok ✓
Spezifikation eingehalten: ✓ Dauerlauf: 8 h Sig. BS

Bemerkungen:
Restwelligkeit < 1Vss
Bereichsumschaltung 200µA / 20µA 4½ stellig

Datum : 17.12.2008 **Prüfer :** Brodole

Figure B.1: Test log of the high voltage power supply used in the nEDM-experiment.

Appendix C

Gradient consideration within a model of harmonic polynomials

Some parts of the analysis rely on the assumption that the magnetic field gradient

$$dB_z(\boldsymbol{r}) = \frac{\partial B_z(\boldsymbol{r})}{\partial z}, \tag{C.1}$$

measured with the CsM situated below the bottom and above the top electrode, is a good representation of the gradient inside the precession chamber. This is e.g. of importance when measuring the systematic effect of the uncompensated B drift (see Sec. 3.1.5).

In connection with magnetic field mapping[1] an analytical description of the magnetic field has been formulated [Qué11]. Within this field parametrization, based on harmonic polynomial series expansions, a simple comparison of the average magnetic field gradient seen by CsM and the analytical solution has been performed.

Field parametrization using harmonic polynomials Inside the empty vacuum tank of the experiment, where no current density is present, Maxwell equations describing the magnetic field simplify to

$$\boldsymbol{\nabla} \cdot \boldsymbol{B} = 0, \tag{C.2}$$

$$\boldsymbol{\nabla} \times \boldsymbol{B} = 0, \tag{C.3}$$

and the magnetic field can be described purely by a scalar potential $\boldsymbol{B} = \boldsymbol{\nabla}\Psi$, that fulfills the Laplace equation

[1] Magnetic field mapping refers to a systematic measurement of the magnetic field within the experiment, using a vector magnetometer that is moved along a grid of points by an automatized device, called mapper.

$$\boldsymbol{\nabla}^2\Psi = \Delta\Psi = 0. \tag{C.4}$$

One possible solution for Ψ is a set of **h**armonic **p**olynomials so that $\Psi = \sum_n \mathcal{H}_n Q_n$ and thus

$$\boldsymbol{B}_{\mathrm{hp}}(\boldsymbol{r}) = \boldsymbol{\nabla}\sum_{\mathrm{n}} \mathcal{H}_{\mathrm{n}} Q_{\mathrm{n}}(\boldsymbol{r}) = \sum_{\mathrm{n}} \mathcal{H}_{\mathrm{n}} \boldsymbol{P}_{\mathrm{n}}(\boldsymbol{r}), \tag{C.5}$$

where $\boldsymbol{P}_{\mathrm{n}} = \boldsymbol{\nabla} Q_{\mathrm{n}}$ is the polynomial and $\mathcal{H}_{\mathrm{n}}$ is the harmonic parameter of order n. A set of $\mathcal{H}_n$ for different desired fields with defined gradients can be given, e.g. a homogeneous vertical gradient over the volume of the precession chamber[2]. Using different sets of $\mathcal{H}_{\mathrm{n}}$ up to n=35, the magnetic field seen by the CsM at the positions $\boldsymbol{r} = \boldsymbol{r}_{\mathrm{CsM,1}} \ldots \boldsymbol{r}_{\mathrm{CsM,j}}$ (see Fig. 3.7) has been calculated to be

$$\begin{aligned} B_{\mathrm{CsM}}(\boldsymbol{r}) &= \sqrt{\sum_{\mathrm{i}=1}^{3} B_{\mathrm{i}}^2(\boldsymbol{r})} \\ &= \sqrt{\sum_{\mathrm{i}=1}^{3}\sum_{\mathrm{n}=1}^{35} \mathcal{H}_{\mathrm{n}}^2 \boldsymbol{P}_{\mathrm{n,i}}^2(\boldsymbol{r})}. \end{aligned} \tag{C.6}$$

From these field values a mean CsM gradient $\overline{G}_{\mathrm{CsM}}$ has been calculated according to (3.22). This gradient can now be compared to an analytically calculated gradient within the precession chamber defined as

$$\overline{G}_{hp} = \frac{\int_V d\boldsymbol{r}\, dB_{\mathrm{hp,z}}(\boldsymbol{r})}{\int_V d\boldsymbol{r}} = \frac{1}{V}\int_V d\boldsymbol{r} \sum_{\mathrm{n}=1}^{35} \frac{\partial}{\partial z}\mathcal{H}_{\mathrm{n}}\, P_{\mathrm{n,z}}(\boldsymbol{r}). \tag{C.7}$$

A comparison for different fields solutions can be found in Tab. C.1. Within the model it seems reasonable to assume that a gradient measured with CsM is a good representation of the real gradient.

[2]The idea behind that is the following: Using the information from the magnetic field maps taken for all individual coils as well as the remnant field, a fit to the harmonic series expansion can be done for individual coil. As the harmonic parameters vary with the current in the coil, for a desired set of $\mathcal{H}_n$, the needed current in all coils can be calculated. Unfortunately this optimization is not yet working perfectly as the current dataset of maps is corrupted.

Goal gradient	$\overline{G}_{\mathrm{CsM}}$	$\overline{G}_{\mathrm{hp}}$
20	20.0482	20.0007
10	10.0391	10.0004
-10	-9.9805	-10.0001
0	-0.0098	0.007

Table C.1: Comparison of the gradient calculated with a set of harmonic polynomials. All values are given in $\mathrm{nT} \cdot \mathrm{m}^{-1}$. $\mathcal{H}$ was calculated from a fit to trim coil maps to give the goal gradient.

Appendix D

DLC coating on different aluminum surfaces

The influence of the surface treatment on DLC coatings was investigated. Aluminum samples with different surface qualities were coated with DLC. Figure D.1 shows pictures of the result. The sample holder created an electric field distortion, and caused the coating failures at the edges. This defect can be used at the same time as a measure for the coating quality. The bead-blasted sample has rather rough surface ($R_a \approx 1\,\mu m$) and shows the best coating result. The diamond milled surface ($R_a \approx 10\,nm$) is coated equally well in the center. Attempts to remove the coating, by wiping the samples with a paper wipe, resulted in coating damages for the hand-polished and the hand-sanded sample. All other coatings did stick well to the aluminum. The smoothest surface and an acceptable coating was achieved for the diamond-milled surface.

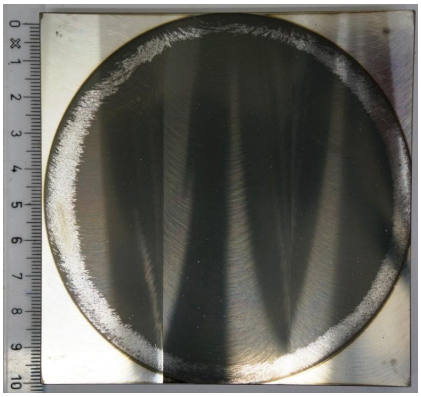

(a) milled

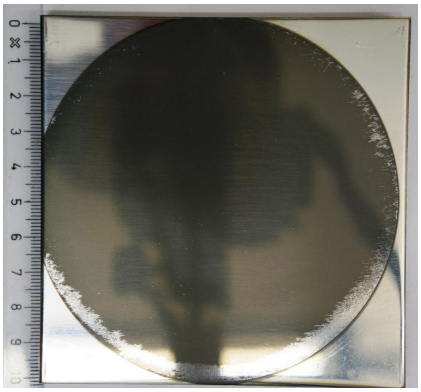

(b) hand-polished

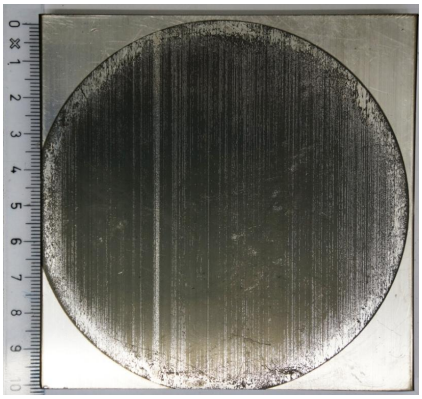

(c) hand-sanded

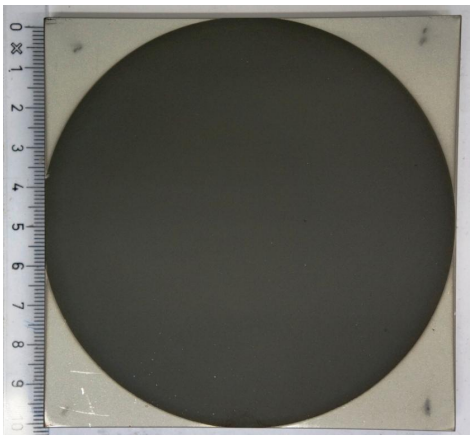

(d) bead-blasted

(e) diamond milled

Figure D.1: DLC coating on Al samples with different surface treatments. For details see text.

Appendix E

SCS2000 connections of HVtest

SCS2000 Software channel	**SCS2000** Backplane	**Purpose**	**Cable**	**SL130** (+) TB1	**SL130** (-) TB1
ground	ground	ground	wh	1	1
0	P0.0	A I	br	5	
1	P0.1	A I	bl	6	
2	P0.2	A I	br		5
3	P0.3	A I	bl		6
4	P0.4	A I			
5	P0.5	A I			
6	P0.6	A I			
7	P0.7	A I			
8	P1.0	A O	pi	8	
9	P1.1	A O	ye	10	
10	P1.2	A O	pi		8
11	P1.3	A O	ye		10
12	P1.4	A O			
13	P1.5	A O			
14	P1.6	A O			
15	P1.7	A O			
16	P2.0	D I	gr	17	
17	P2.1	D I	li	18	
18	P2.2	D I			
19	P2.3	D I			
20	P2.4	D I	gr		17
21	P2.5	D I	li		18
22	P2.6	D I			
23	P2.7	D I			
24	P7.0 P7.1	relay	yebr,yewh	14.15	
25	P7.2 P7.3	relay	brgr,grwh	15.16	
26	P7.4 P7.5	relay	yebr,yewh		14.15
27	P7.6 P7.7	relay	brgr,grwh		15.16
		shield	gy	28	28

Table E.1: SCS 2000 connections to the TB1 connectors of the Spellman power supplies. Color code for the cable is **wh**ite, **br**own, **bl**ue, **pi**nk, **ye**llow, **gr**een, **li**lac, **g**ra**y**, and multicolors like **ye**llow and **br**own.

Appendix F

Script used for noise calculations

```
(*Load packages*)
<< PlotLegends`

(*Set working directory to notebook directory*)
SetDirectory[NotebookDirectory[]];

(*Define constants *)
μ0 = 4 * Pi * 10^ - 7;  (*Permeability of vacuum [H/m]*)
kb = 1.381 * 10^ - 23; (*Boltzmann constant [J/K]*)

(*Properties to define before calculation*)
μr = 1; (*Permeability of material[H/m]*)
T = 293; (*Temperatur [K]*)

(*Frequency range of noise to look at [Hz]*)
ω2[t_, z_]:=1/(4μ0σzt)(*Approx. of frequency of -3 dB point*)
k[ω_, σ_]:=√(iμ0σω)

(*Some conductivities [1/Ωm] *)
σAl = 1/(2.650 * 10^ - 8); (*Aluminium*)
σPl = 1/(10.5 * 10^ - 8); (*Platin*)
σGr = 1/(1375 * 10^ - 8); (*Graphit*)
σSa = 1/(2 * 10^12); (*AL2O3 Saphir*)
σCu = 1/(1.678 * 10^ - 8); (*Copper*)
σCFK = 10^ - 6; (*CFRP*)
σPEEK = 10^ - 16; (*PEEK*)
```

```
σGK = 10^ − 15; (*Glass-ceramic*)
σSi = 1/1000; (*Silicon*)
σTi = 2.5 * 10^6(*Titan*);


(*Define functions (using numerical integration)*)
(*Substitutions*)
u[ω_, ρ_, σ_]:=1/μr + ρ / Sqrt[ρ^2 + k[ω, σ]^2] ;

v[ω_, ρ_, σ_]:=1/μr − ρ / Sqrt[ρ^2 + k[ω, σ]^2] ;


(*Transfer function*)
R[ρ_, z1_, t_, ω_, σ_]:=Exp[−Sqrt[ρ^2+k[ω,σ]^2]*z1]/(π*Sqrt[ρ^2+k[ω,σ]^2])*
(u[ω,ρ,σ]+v[ω,ρ,σ]*Exp[−2*Sqrt[ρ^2+k[ω,σ]^2]*(t−z1)])/(u[ω,ρ,σ]^2−v[ω,ρ,σ]^2*Exp[−2Sqrt[ρ^2+k[ω,σ]^2]*t]);
(*Magnetic noise [pT/Sqrt[Hz]] *)
Bn[t_, z_, ω_, σ_]:=
Re[μ0 * Sqrt[σ * 2 * π * kb * T]*
Sqrt[NIntegrate[Norm[R[ρ, z1, t, ω, σ]]^2 * Exp[−2 * ρ * z] * ρ^3,
{ρ, 0.001, ∞}, {z1, 0, t}, AccuracyGoal → 10, MaxRecursion → 10000]*
10^12];

(* Integral magnetic noise (1 Hz to -3 dB point) [pT] *)
B[t_, z_, σ_]:=
Re[μ0 * Sqrt[σ * 2 * π * kb * T]*
Sqrt[NIntegrate[Norm[R[ρ, z1, t, ω, σ]]^2 * Exp[−2 * ρ * z] * ρ^3,
{ρ, 0, ∞}, {z1, 0, t}, {ω, 1, ω2[t, z]}, AccuracyGoal → 10,
MaxRecursion → 10000] * 10^12];
```

Bibliography

[A+86] I.S. Altarev et al. Search for an electric dipole moment of the neutron. *JETP Letters*, 44(8):360, 1986.

[AAA+01] K. Abe, K. Abe, R. Abe, I. Adachi, Byoung Sup Ahn, H. Aihara, M. Akatsu, G. Alimonti, K. Asai, M. Asai, et al. Observation of large CP violation in the neutral B meson system. *Physical Review Letters*, 87(9):091802, 2001.

[AABA+12] R. Aaij, C. Abellan Beteta, B. Adeva, M. Adinolfi, C. Adrover, A. Affolder, Z. Ajaltouni, J. Albrecht, F. Alessio, M. Alexander, et al. Evidence for CP Violation in Time-Integrated $D^0 \to h^- h^+$ Decay Rates. *Physical Review Letters*, 108(11):111602, 2012.

[ABB+80] I.S. Altarev, Yu. V. Borisov, A.B. Brandin, A.I. Egorov, V.F. Ezhov, S.N. Ivanov, V.M. Lobashov, V.A. Nazarenko, G.D. Porsev, V.L. Ryabov, et al. A search for the electric dipole moment of the neutron using ultracold neutrons. *Nuclear Physics A*, 341(2):269–283, 1980.

[ABB+81] I.S. Altarev, Yu. V. Borisov, N.V. Borovikova, A.B. Brandin, A.I. Egorov, V.F. Ezhov, S.N. Ivanov, V.M. Lobashev, V.A. Nazarenko, V.L. Ryabov, et al. A new upper limit on the electric dipole moment of the neutron. *Physics Letters B*, 102(1):13–16, 1981.

[ABB+92] I.S. Altarev, Yu. V. Borisov, N.V. Borovikova, S.N. Ivanov, E.A. Kolomensky, M.S. Lasakov, V.M. Lobashev, V.A. Nazarenko, A.N. Pirozhkov, A.P. Serebrov, et al. New measurement of the electric dipole moment of the neutron. *Physics Letters B*, 276(1):242–246, 1992.

[ABD+06] F. Atchison, B. Blau, M. Daum, P. Fierlinger, P. Geltenbort, R. Henneck, S. Heule, M. Kasprzak, K. Kirch, K. Kohlik,

et al. Storage of ultracold neutrons in a volume coated with diamondlike carbon. *Physical Review C*, 74(5):055501, 2006.

[ABD+07] F. Atchison, B. Blau, M. Daum, P. Fierlinger, P. Geltenbort, M. Gupta, R. Henneck, S. Heule, M. Kasprzak, A. Knecht, et al. Measurement of the Fermi potential of diamond-like carbon and other materials. *Nuclear Instruments and Methods in Physics Research Section B: Beam Interactions with Materials and Atoms*, 260(2):647–656, 2007.

[ADH+10] F. Atchison, M. Daum, R. Henneck, S. Heule, M. Horisberger, M. Kasprzak, K. Kirch, A. Knecht, M. Kuźniak, B. Lauss, et al. Diffuse reflection of ultracold neutrons from low-roughness surfaces. *The European Physical Journal A*, 44(1):23–29, 2010.

[AM11] Ravindra Arora and Wolfgang Mosch. *High Voltage and Electrical Insulation Engineering*. John Wiley & Sons, 2011.

[AWJ91] David W. Allan, Marc A. Weiss, and James L. Jespersen. A frequency-domain view of time-domain characterization of clocks and time and frequency distribution systems. In *Proceedings of the 45th Annual Symposium on Frequency Control*, pages 667–678. IEEE, 1991.

[BBB+09] G.W. Bennett, B. Bousquet, H.N. Brown, G. Bunce, R.M. Carey, P. Cushman, G.T. Danby, P.T. Debevec, M. Deile, H. Deng, et al. Improved limit on the muon electric dipole moment. *Physical Review D*, 80(5):052008, 2009.

[BBL+09] G. Ban, K. Bodek, T. Lefort, O. Naviliat-Cuncic, E. Pierre, C. Plonka, and G. Rogel. UCN detection with ^{6}Li-doped glass scintillators. *Nuclear Instruments and Methods in Physics Research Section A: Accelerators, Spectrometers, Detectors and Associated Equipment*, 611(2):280–283, 2009.

[BCL98] Patrick D. Bangerty, M. Cooper, and S.K. Lamoreaux. Uniformity of the magnetic field produced by a cosine magnet with a superconducting shield. `http://www.neutrino.lanl.gov/edm/pointers/pat_mag.ps`, 1998.

[BDG+06] C.A. Baker, D.D. Doyle, P. Geltenbort, K. Green, M.G.D. van der Grinten, et al. An improved experimental limit on the electric dipole moment of the neutron. *Physical Review Letters*, 97:131801, 2006.

[BDH+08] K. Bodek, M. Daum, R. Henneck, S. Heule, M. Kasprzak, K. Kirch, A. Knecht, M. Kuźniak, B. Lauss, M. Meier, et al. Storage of ultracold neutrons in high resistivity, non-magnetic materials with high Fermi potential. *Nuclear Instruments and Methods in Physics Research Section A: Accelerators, Spectrometers, Detectors and Associated Equipment*, 597(2):222–226, 2008.

[Bec11] J. Becker. The search for the electric dipole moment of the neutron, investigation of uncompensated magnetic field drifts. Master's thesis, K.U.Leuven, Belgium, 2011.

[BGKM88] J. Baumann, R. Gähler, J. Kalus, and W. Mampe. Experimental limit for the charge of the free neutron. *Physical Review D*, 37:3107–3112, Jun 1988.

[BHKS01] J. Bork, H.D. Hahlbohm, R. Klein, and A. Schnabel. The 8-layered magnetically shielded room of the PTB: Design and construction. In *Biomag2000, Proc. Twelfth Int. Conf. Biomagnetism*, pages 970–73. Helsinki Univ. Technol. Espoo, Finland, 2001.

[BKGS+09] M. Burghoff, S. Knappe-Grüneberg, A. Schnabel, L. Trahms, G. Ban, et al. Progress report. *PSI Proposal R-05-03.1*, 2009.

[BKGS+10] M. Burghoff, S. Knappe-Grüneberg, A. Schnabel, L. Trahms, J. Voigt, et al. Progress report. *PSI Proposal R-05-03.1*, 2010.

[BKGS+11] M. Burghoff, S. Knappe-Grüneberg, A. Schnabel, L. Trahms, J. Voigt, et al. Progress report. *PSI Proposal R-05-03.1*, 2011.

[BKGS+12] M. Burghoff, S. Knappe-Grüneberg, A. Schnabel, L. Trahms, J. Voigt, et al. Progress report. *PSI Proposal R-05-03.1*, 2012.

[BMDR69] J. K. Baird, P. D. Miller, W. B. Dress, and Norman F. Ramsey. Improved upper limit to the electric dipole moment of the neutron. *Physical Review*, 179:1285–1291, Mar 1969.

[Bru] BRÜHLMEIER MODELLBAU AG. Durisolstrasse 8, 5612 Villmergen.

[CCFT64] J. H. Christenson, J. W. Cronin, V. L. Fitch, and R. Turlay. Evidence for the 2π decay of the K_2^0 meson. *Physical Review Letters*, 13:138–140, Jul 1964.

[CNS+69] Victor W. Cohen, Robert Nathans, H. B. Silsbee, Edgar Lipworth, and Norman F. Ramsey. Electric dipole moment of the neutron. *Physical Review*, 177:1942–1945, Jan 1969.

[CTDR72] Claude Cohen-Tannoudji and Jacques Dupont-Roc. Experimental study of Zeeman light shifts in weak magnetic fields. *Physical Review A*, 5:968–984, Feb 1972.

[DMP+77] W. B. Dress, P. D. Miller, J. M. Pendlebury, Paul Perrin, and Norman F. Ramsey. Search for an electric dipole moment of the neutron. *Physical Review D*, 15:9–21, Jan 1977.

[DMR73] W. B. Dress, P. D. Miller, and N. F. Ramsey. Improved upper limit for the electric dipole moment of the neutron. *Physical Review D*, 7:3147–3149, Jun 1973.

[Doy04] Dara D. Doyle. *Systematic Effects in the Neutron EDM Experiment and its Constrains on Physics Beyond the Standard Model*. PhD thesis, University of Sussex, 2004.

[DS11] Dirk Dubbers and Michael G. Schmidt. The neutron and its role in cosmology and particle physics. *Reviews of Modern Physics*, 83:1111–1171, Oct 2011.

[eaPDG12] J. Beringer et al. (Particle Data Group). Review of particle physics. *Physical Review D*, 86:010001, Jul 2012.

[Feron] Martin Fertl. PhD thesis, ETH Zürich, in preparation.

[Feu] Feusi + Federer AG. Galvanic Wädenswil. `http://www.galvanic.ch/index.htm`.

[Fie] Peter Fierlinger. A next generation measurement of the electric dipole moment of the neutron at the FRM-II. `http://www.universe-cluster.de/fierlinger/nedm.html`.

[Fie05] Peter Fierlinger. *Losses and Depolarization of Stored Ultracold Neutrons on Diamond-like Carbon*. PhD thesis, Universität Zürich, 2005.

[FJK+10] V.V. Fedorov, M. Jentschel, I.A. Kuznetsov, E.G. Lapin, E. Lelièvre-Berna, V. Nesvizhevsky, A. Petoukhov, S. Yu. Semenikhin, T. Soldner, V.V. Voronin, et al. Measurement of the neutron electric dipole moment via spin rotation in a non-centrosymmetric crystal. *Physics Letters B*, 694(1):22–25, 2010.

[FKL+08] V.V. Fedorov, I.A. Kuznetsov, E.G. Lapin, S. Yu. Semenikhin, and V.V. Voronin. Diffraction enhancement and new way to measure neutron electric charge and the ratio of inertial to gravitational mass. *Nuclear Instruments and Methods in Physics Research Section A: Accelerators, Spectrometers, Detectors and Associated Equipment*, 593(3):505–509, 2008.

[Fon12] C. Fontbonne. *FASTER-QDC-TDC module user manual*, 2012.

[Fra] Fraunhofer Institute for Material and Beam Technology IWS. SUPER HARD CARBON FILMS. `http://www.iws.fraunhofer.de/content/dam/iws/en/documents/publications/product_sheets/500-1_diamor_en.pdf`.

[Fraon] Beatrice Franke. PhD thesis, ETH Zürich, in preparation.

[FuG] FuG Elektronik GmbH. Data sheet HCB series. `http://www.fug-elektronik.de/webdir/3/special.htm#SeriesHCB`.

[Fuk12] T. Fukuyama. Searching for new physics beyond the standard model in electric dipole moment. *International Journal of Modern Physics A*, 27(16), 2012.

[GHI+98] K. Green, P.G. Harris, P. Iaydjiev, D.J.R. May, J.M. Pendlebury, et al. Performance of an atomic mercury magnetometer in the neutron EDM experiment. *Nuclear Instruments and Methods in Physics Research Section A: Accelerators, Spectrometers, Detectors and Associated Equipment*, A404:381–393, 1998.

[Gie97] Francois Gieres. About symmetries in physics. *Symmetries in Physics: Proceedings of the Fifth Seminaire Rhodanien de Physique*, 1997.

[Göl12] Leonard Göltel. *Characterization of the PSI Ultra-Cold Neutron Source*. PhD thesis, ETH Zürich, 2012.

[GP75] R. Golub and J.M. Pendlebury. Super-thermal sources of ultra-cold neutrons. *Physics Letters A*, 53(2):133 – 135, 1975.

[Grö05] Stephan Gröger. *Laser-pumped cesium magnetometers for the PSI-nEDM experiment*. PhD thesis, Université de Fribourg, 2005.

[GRL91] R. Golub, D.J. Richardson, and S.K. Lamoreaux. *Ultra-Cold Neutrons*. Adam Hilger, 1991.

[GSL+09] W.C. Griffith, M.D. Swallows, T.H. Loftus, M.V. Romalis, B.R. Heckel, and E.N. Fortson. Improved limit on the permanent electric dipole moment of ^{199}Hg. *Physical Review Letters*, 102(10):101601, 2009.

[HBG+99] P.G. Harris, C.A. Baker, K. Green, P. Iaydjiev, S. Ivanov, D.J.R. May, J.M. Pendlebury, D. Shiers, K.F. Smith, M. Van der Grinten, et al. New experimental limit on the electric dipole moment of the neutron. *Physical Review Letters*, 82(5):904–907, 1999.

[Helon] Victor Helain. PhD thesis, Université de Caen Basse Normandie, in preparation.

[HKS+11] J. J. Hudson, D. M. Kara, I. J. Smallman, B. E. Sauer, M. R. Tarbutt, and E. A. Hinds. Improved measurement of the shape of the electron. *Nature*, 473(7348):493–496, 2011.

[Hor12] Marlon B. Horras. *A highly sensitive ^{199}Hg magnetometer for the nEDM experiment*. PhD thesis, ETH Zürich, 2012.

[HP06] P.G. Harris and J.M. Pendlebury. Dipole-field contributions to geometric-phase-induced false electric-dipole-moment signals for particles in traps. *Physical Review A*, 73(1):014101, 2006.

[I+07] Takeyasu M. Ito et al. Plans for a neutron edm experiment at SNS. In *Journal of Physics: Conference Series*, volume 69, page 012037. IOP Publishing, 2007.

[Ign90] V.K. Ignatovich. *The physics of ultracold neutrons*. Oxford science publications. Clarendon Press, 1990.

[Joh28] J.B. Johnson. Thermal agitation of electricity in conductors. *Physical Review*, 32:97–109, 1928.

[K+11] E. Komatsu et al. Seven-Year Wilkinson Microwave Anisotropy Probe (WMAP) Observations: Cosmological Interpretation. *The Astrophysical Journal Supplement Series*, 192:18, 2011.

[KGR+03] W.H. Kraan, S.V. Grigoriev, M.Th. Rekveldt, H. Fredrikze, C.F. de Vroege, and J. Plomp. Test of adiabatic spin flippers

for application at pulsed neutron sources. *Nuclear Instruments and Methods in Physics Research Section A: Accelerators, Spectrometers, Detectors and Associated Equipment*, 510(3):334 – 345, 2003.

[Kne09] Andreas Knecht. *Towards a new measurement of the neutron electric dipole moment*. PhD thesis, Universität Zürich, 2009.

[KR05] J.R. Klein and A. Roodman. Blind analysis in nuclear and particle physics. *Annual Review of Nuclear and Particle Science*, 55:141–163, 2005.

[Kuź08] Marcin Kuźniak. *The Neutron Electric Dipole Moment Experiment: Research and Development for the New Spectrometer*. PhD thesis, Jagiellonian University, 2008.

[KZ82] I.B. Khriplovich and A.R. Zhitnitsky. What is the value of the neutron electric dipole moment in the Kobayashi-Maskawa model? *Physics Letters B*, 109(6):490 – 492, 1982.

[Lab] Oak Ridge National Laboratory. Spallation neutron source. `http://neutrons.ornl.gov/facilities/SNS`.

[Lau13] B. Lauss. private communication. 2013.

[Liu02] Chen-Yu Liu. *A Superthermal Ultra-Cold Neutron Source*. PhD thesis, Princeton University, 2002.

[LL] Institut Laue-Langevin. Description of the ILL HFR (High-Flux Reactor). `http://www.ill.eu/reactor-environment-safety/high-flux-reactor/technical-characteristics/`.

[LPT+12] J.P. Lees, V. Poireau, V. Tisserand, J. Garra Tico, E. Grauges, A. Palano, G. Eigen, B. Stugu, D.N. Brown, L.T. Kerth, et al. Observation of Time-Reversal Violation in the B^0 Meson System. *Physical Review Letters*, 109(21):211801, 2012.

[LS06] H. Lindner and W. Siebke. *Physik für Ingenieure*. Number 10. Fachbuchverlag Leipzig im Carl Hanser Verlag, 2006.

[MAH+12] Yasuhiro Masuda, Koichiro Asahi, Kichiji Hatanaka, Sun-Chan Jeong, Shinsuke Kawasaki, Ryohei Matsumiya, Kensaku Matsuta, Mototsugu Mihara, and Yutaka Watanabe. Neutron

electric dipole moment measurement with a buffer gas comagnetometer. *Physics Letters A*, 376(16):1347 – 1351, 2012.

[May98] Daniel John Robert May. *A high precision comparison of the gyromagnetic ratios of the* ^{199}Hg *atom and the neutron.* PhD thesis, University of Sussex, 1998.

[MDBR67] P. D. Miller, W. B. Dress, J. K. Baird, and Norman F. Ramsey. Limit to the electric dipole moment of the neutron. *Physical Review Letters*, 19:381–384, Aug 1967.

[MT05] J.R. Munger and Charles T. Magnetic Johnson noise constraints on electron electric dipole moment experiments. *Physical Review A*, 72(1):012506, 2005.

[NMK96] Jukka Nenonen, Juha Montonen, and Toiro Katila. Thermal noise in biomagnetic measurements. *Review of Scientific Instruments*, 67(6):2397–2405, 1996.

[Noe18] E. Noether. Invariante Variationsprobleme. *Nachr. d. König. Gesellsch. d. Wiss. zu Göttingen, Math-phys. Klasse, Seite 235-157*, pages 235–257, 1918.

[Nyq28] H. Nyquist. Thermal Agitation of Electric Charge in Conductors. *Physical Review*, 32:110–113, 1928.

[Pau] PaucoPlast AG. Talstrasse 14, 8852 Altendorf.

[Pfu11] O. Pfungst. *Clever Hans:(the horse of Mr. Von Osten.) a contribution to experimental animal and human psychology.* Holt, Rinehart and Winston, 1911.

[PHS+04] J.M. Pendlebury, W. Heil, Yu. Sobolev, P.G. Harris, J.D. Richardson, et al. Geometric-phase-induced false electric dipole moment signals for particles in traps. *Physical Review A*, 70:032102, 2004.

[Pie12] M. Edgard Pierre. *Développement et optimisation dŠun système de polarisation de neutrons ultra froids dans le cadre dŠune nouvelle mesure du moment dipolaire électrique du neutron.* PhD thesis, Université de Caen Basse Normandie, 2012.

[Plü98] Michael Plümacher. Baryon asymmetry, neutrino mixing and supersymmetric SO (10) unification. *Nuclear Physics B*, 530(1):207–246, 1998.

[PR50] E.M. Purcell and N.F. Ramsey. On the possibility of electric dipole moments for elementary particles and nuclei. *Physical Review*, 78, 1950.

[PR05] Maxim Pospelov and Adam Ritz. Electric dipole moments as probes of new physics. *Annals of physics*, 318(1):119–169, 2005.

[PR12] Guillaume Pignol and Stéphanie Roccia. Electric-dipole-moment searches: Reexamination of frequency shifts for particles in traps. *Physical Review A*, 85(4):042105, 2012.

[PSG+84] J. Mo. Pendlebury, K.F. Smith, R. Golub, J. Byrne, T.J.L. McComb, T.J. Sumner, S.M. Burnett, A.R. Taylor, B. Heckel, N.F. Ramsey, et al. Search for a neutron electric dipole moment. *Physics Letters B*, 136(5):327–330, 1984.

[PSKI+10] C. Plonka-Spehr, A. Kraft, P. Iaydjiev, J. Klepp, V.V. Nesvizhevsky, P. Geltenbort, and Th. Lauer. An optical device for ultra-cold neutrons - investigation of systematic effects and applications. *Nuclear Instruments and Methods in Physics Research Section A: Accelerators, Spectrometers, Detectors and Associated Equipment*, 618(1):239–247, 2010.

[Qué09] G. Quéméner. Trim coils pictures library. Internal Notes, 2009.

[Qué11] G. Quéméner. Notes on a new set of harmonic polynomial series expansions to parametrize a magnetic field. Internal Notes, 2011.

[RCSD02] B. C. Regan, Eugene D. Commins, Christian J. Schmidt, and David DeMille. New limit on the electron electric dipole moment. *Physical Review Letters*, 88:071805, Feb 2002.

[Reb12] D. Rebreyend. New optics for the Hg probe light. Internal Notes, 2012.

[Rit] S. Ritt. Midas home page. `http://midas.psi.ch/`.

[Rit02] S. Ritt. Electronics for the $\mu \rightarrow e\gamma$ experiment. *Nuclear Instruments and Methods in Physics Research Section A: Accelerators, Spectrometers, Detectors and Associated Equipment*, 494(1):520–525, 2002.

[Rog09] M. Gwendal Rogel. *Développement de détecteurs de neutrons ultra-froids et d'un système d'analyse de polarisation pour la mesure du moment électrique dipolaire du neutron.* PhD thesis, UNIVERSITÉ DE CAEN BASSE-NORMANDIE, 2009.

[RT99] Antonio Riotto and Mark Trodden. Recent progress in baryogenesis. *Annual Review of Nuclear and Particle Science*, 49:35–75, 1999.

[Sak67] A.D. Sakharov. Violation of CP invariance, C asymmetry, and baryon asymmetry of the universe. *JETP Letters*, 5:24–26, 1967.

[SCP+90] K.F. Smith, N. Crampin, J.M. Pendlebury, D.J. Richardson, D. Shiers, K. Green, A.I. Kilvington, J. Moir, H.B. Prosper, D. Thompson, et al. A search for the electric dipole moment of the neutron. *Physics Letters B*, 234(1):191–196, 1990.

[SGK03] U. Schumann, S. Giere, and M. Kurrat. Breakdown voltage of electrode arrangements in vacuum circuit breakers. *Dielectrics and Electrical Insulation, IEEE Transactions on*, 10(4):557–562, 2003.

[SJB+09] Andrew Sunderland, Li Ju, David G Blair, Wayne McRae, and Howard Golden. Low magnetic susceptibility materials and applications in magnetic gradiometry. *Smart Materials and Structures*, 18(9):095038, 2009.

[SN67] C.G. Shull and R. Nathans. Search for a neutron electric dipole moment by a scattering experiment. *Physical Review Letters*, 19(7):384–386, 1967.

[SNS+86] A. Steyerl, H. Nagel, F.-X. Schreiber, K.-A. Steinhauser, R. Gähler, W. Gläser, P. Ageron, J.M. Astruc, W. Drexel, G. Gervais, and W. Mampe. A new source of cold and ultracold neutrons. *Physics Letters A*, 116(7):347 – 352, 1986.

[SPR57] J.H. Smith, E.M. Purcell, and N.F. Ramsey. Experimental limit to the electric dipole moment of the neutron. *Physical Review*, 108(1):120, 1957.

[vdG09] M.G.D. van der Grinten. CryoEDM: A cryogenic experiment to measure the neutron electric dipole moment. *Nuclear Instruments and Methods in Physics Research Section*

A: Accelerators, Spectrometers, Detectors and Associated Equipment, 611(2):129–132, 2009.

[VP84] Timo Varpula and Torsti Poutanen. Magnetic field fluctuations arising from thermal motion of electric charge in conductors. *Journal of Applied Physics*, 55(11):4015–4021, 1984.

[WAH+57] C. S. Wu, E. Ambler, R. W. Hayward, D. D. Hoppes, and R. P. Hudson. Experimental test of parity conservation in beta decay. *Physical Review*, 105:1413–1415, Feb 1957.

[WG11] Fred E. Wietfeldt and Geoffrey L. Greene. *Colloquium* : The neutron lifetime. *Reviews of Modern Physics*, 83:1173–1192, Nov 2011.